Università degli Studi di Ferrara

DOTTORATO DI RICERCA IN

FISICA

CICLO XXXII

COORDINATRICE Prof.ssa Eleonora Luppi

Cyclotron production of theranostic radionuclides: ^{67}Cu and ^{47}Sc

Settore Scientifico Disciplinare FIS/07

Dottoranda:

Dott.ssa MOU LILIANA

Tutore:

Prof. DUATTI ADRIANO

Co-Tutore:

Dott. ESPOSITO JUAN

Anni 2016/2019

TABLE OF CONTENTS

ABSTRACT

The work described in this Ph.D. thesis was carried out in the framework of the LARAMED (LAboratory of RAdioisotopes for MEDicine) project at the Legnaro National Laboratories of the National Institute of Nuclear Physics (INFN-LNL). The LARAMED project is a branch of SPES (Selective Production of Exotic Species) with the purpose to evaluate the cyclotron-based production of emerging radionuclides to produce innovative radiopharmaceuticals. This work reports the main results obtained in the COME (COpper MEasurement) and PASTA (Production with Accelerator of Sc-47 for Theranostic Applications) projects in which I was involved in the three years of my Ph.D.. Since the accurate knowledge of the reaction cross section is the first step in the optimization of radioisotope production, both projects were focused on these measurements, for ^{67}Cu and ^{47}Sc respectively, by using proton beams up to 70 MeV. ^{67}Cu and ^{47}Sc are theranostic radionuclides as they can decay simultaneously by γ- and β^- emission. This property allows visualization of a specific biological target by γ imaging that, in turn, can be used for applying selectively targeted β^- therapy. Worldwide a real problem to be solved is the lack of ^{67}Cu and ^{47}Sc availability, as underlined by the IAEA CRP (No. F22053) focused on the production of the theranostic radionuclides ^{67}Cu, ^{186}Re and ^{47}Sc. In the COME project the first measurements of the ^{70}Zn(p,x)^{67}Cu, ^{64}Cu, ^{67}Ga, ^{66}Ga, ^{65}Zn, and ^{69m}Zn cross sections in the 45-70 MeV energy range were obtained. These results, compared with the well-known ^{68}Zn(p,x)^{67,64}Cu nuclear reaction, allowed us to find an optimal energy range to maximize the ^{67}Cu production and, in the same time, minimize the co-produced ^{64}Cu; this result is described in the International Patent n° WO 2019/220224 A1 (November 2019). In the PASTA project the proton-induced reactions on ^{48}Ti and ^{nat}V targets were investigated. The cross sections values obtained for the ^{48}Ti(p,x)^{47}Sc, ^{46}Sc, ^{44}Sc, ^{44m}Sc nuclear reactions show a regular trend, in agreement with the previous experimental data. The results of the ^{nat}V(p,x)^{47}Sc, ^{46}Sc, ^{44}Sc, ^{44m}Sc, ^{43}Sc, ^{48}Sc, ^{48}Cr, ^{49}Cr, ^{51}Cr, ^{48}V, ^{42}K, ^{43}K cross sections were also obtained and compared with literature data and theoretical calculations. Calculations of the Thick Target Yield were also performed for both ^{67}Cu and ^{47}Sc to study the feasibility of their real production by exploiting the nuclear reactions investigated and the 70 MeV proton cyclotron installed at INFN-LNL. For the ^{47}Sc case, dosimetric calculations were performed considering the DOTA-folate conjugate cm10 ([^{47}Sc]-cm10) radiopharmaceutical; the effective Dose Increase (DI)

due to the presence of a small amount of the co-produced contaminant ^{46}Sc for E_p<35 MeV was maintained within the 10%, limit required for the radiopharmaceutical clinical use.

RIASSUNTO

Il lavoro descritto in questa tesi di dottorato è stato sviluppato nell'ambito del progetto LARAMED (LAboratory of RAdioisotopes for MEDicine), una branca del progetto SPES (Selective Production of Exotic Species), presso i Laboratori Nazionali di Legnaro dell'Istituto Nazionale di Fisica Nucleare (INFN-LNL). Il progetto LARAMED si propone di studiare la produzione di radionuclidi per la realizzazione di nuovi radiofarmaci, utilizzando il fascio di protoni generato dal ciclotrone SPES. Questo lavoro riporta i principali risultati ottenuti con i progetti COME (COpper MEasurement) e PASTA (Production with Accelerator of Sc-47 for Theranostic Applications) nei quali ho lavorato durante i tre anni di dottorato. Poiché la conoscenza accurata delle sezioni d'urto è il primo step nell'ottimizzazione della produzione di radioisotopi, entrambi i progetti erano focalizzati su queste misure, rispettivamente per il ^{67}Cu e lo ^{47}Sc, usando fasci di protoni di energia fino a 70 MeV. Il ^{67}Cu e lo ^{47}Sc sono radionuclidi teranostici (entrambi emettitori γ- e β^- che possono anche essere accoppiati con isotopi β^+), permettendo la selezione dei pazienti che hanno una buona probabilità di rispondere positivamente allo specifico radiofarmaco con imaging SPECT (o PET) prima della terapia. Un reale problema da risolvere è la mancanza di disponibilità di ^{67}Cu e ^{47}Sc, come sottolineato dal CRP IAEA (No. F22053) focalizzato sulla produzione dei radionuclidi teranostici ^{67}Cu, ^{186}Re e ^{47}Sc. Nel progetto COME sono state realizzate le prime misure delle sezioni d'urto ^{70}Zn(p,x)^{67}Cu, ^{64}Cu, ^{67}Ga, ^{66}Ga, ^{65}Zn and ^{69m}Zn nel range energetico 45-70 MeV. Questi risultati, confrontati con la ben nota reazione nucleare ^{68}Zn(p,x)^{67,64}Cu, mi ha permesso di trovare un range di energia ottimale per massimizzare la produzione di ^{67}Cu e nello stesso tempo minimizzare la produzione dell'isotopo contaminante ^{64}Cu; questo risultato è descritto nel Patent Internazionale n° WO 2019/220224 A1 (Novembre 2019). Nel progetto PASTA sono state investigate le reazioni nucleari indotte da protoni su bersagli di ^{48}Ti e ^{nat}V. I risultati delle sezioni d'urto delle reazioni nucleari ^{48}Ti(p,x) ^{47}Sc, ^{46}Sc, ^{44}Sc, ^{44m}Sc mostrano un trend regolare in accordo con i dati di letteratura. Sono anche stati ottenuti i risultati delle sezioni d'urto ^{nat}V(p,x)^{47}Sc, ^{46}Sc, ^{44}Sc, ^{44m}Sc, ^{43}Sc, ^{48}Sc, ^{48}Cr, ^{49}Cr, ^{51}Cr, ^{48}V, ^{42}K, ^{43}K che sono state confrontate con i dati di letteratura e con alcune stime teoriche. Sono anche stati realizzati dei calcoli di produzione su bersagli spessi, sia nel caso del ^{67}Cu che dello ^{47}Sc per studiare la fattibilità di una reale produzione sfruttando le reazioni nucleari studiate ed il ciclotrone presente presso i LNL. Nel caso dello ^{47}Sc, sono stati effettuati anche calcoli dosimetrici, considerando il radiofarmaco DOTA-

folate conjugate cm10 ([^{47}Sc]-cm10). L'incremento della dose efficace dovuta alla presenza di una piccola contaminazione dovuta alla co-produzione di ^{46}Sc è inferiore al 10%, limite richiesto per uso clinico del radiofarmaco, per E_p<35 MeV.

INTRODUCTION

Nuclear medicine is a fundamental medical methodology that makes use of radiolabelled compounds for diagnostic and therapeutic purposes. These radiocompounds, conventionally called 'radiopharmaceuticals', can be pictured as chemical vectors that are designed to deliver radioactivity to a selected cellular population that has been affected by molecular alterations characteristics of a specific disease. Concentration of a radiopharmaceutical at the target site allows both imaging and therapy of the diseased tissue depending on the type of radioactive decay of the radionuclide incorporated into the radiopharmaceuticals. It turns out that progress in the search of new radiopharmaceutical is critically dependent on the availability of several radionuclides with different physical (half-life, radiation type) and chemical characteristics. Currently, the scientific community is looking forward to personalize the treatment to the specific patient's needs, in order to ideally select the right therapy for the right patient at the right time. This approach aims at selecting the patients with a high chance to positively respond to the therapy, thus avoiding the application of expensive or ineffective (or harming) drugs. One of the pillars of personalized therapy is the use of theranostic radionuclides, i.e. radioisotopes or pair of isotopes that emit radiation useful for both diagnostic and therapeutic purposes. A radiopharmaceutical, labelled with a theranostic radionuclide, can be first used to select the patient prior to therapy by administration of a low dose of radioactivity and by detecting the γ component of the emission. Precise visualization of the disease target site allows subsequently to inject a therapeutic dose to the patient by using the same molecular probe, taking advantage of the concomitant emission of a massive charged particle (electrons or alpha particles). At present, the production of theranostic radionuclides is thus a crucial goal for the international scientific community, as emphasized by the organization of a Coordinated Research Project (CRP) promoted by the International Atomic Energy Agency (IAEA) and focused on "Therapeutic Radiopharmaceuticals Labelled with New Emerging Radionuclides (^{67}Cu, ^{186}Re, ^{47}Sc)" (No. F22053), in which I actively participated thanks to the research work carried out in this thesis.

Indeed, this Ph.D. work aims to study new and more efficient production routes for ^{67}Cu and ^{47}Sc radionuclides, based on the use of intense proton beams.

Recently, the Italian scientific community has demonstrated its involvement and interest in this field by the foundation of a new research facility almost close to completion. At the Legnaro National Laboratories of the National Institute of Nuclear Physics (LNL-INFN) a high-performance, 70p model cyclotron, manufactured by BEST*TM* Theratronics (Ottawa, Ontario, Canada), was installed in May 2015 in the context of the SPES (Selective Production of Exotic Species) project. The core of SPES (SPES-α stage) is the dual-beam operational cyclotron, with a proton beam energy tunable in the range 70-35 MeV, available with a high output current (up to 750 μA). SPES primary goals are focused on both research in Radioactive Ion Beams (RIBs), produced with an ISOL target (SPES-β), and applied nuclear physics, both in medicine and neutron-applications (SPES-γ and SPES-δ respectively). The LARAMED (LAboratory of RAdioisotopes for MEDicine) project is a branch of SPES (SPES-γ) with the purpose to study unexplored production routes for medical radionuclides, and also aiming at the related development (targets, radiochemical procedures, etc) of essential technological tools for the high-yield production of radionuclides. To achieve these goals, it is necessary to have a multidisciplinary working group, comprising experts in different fields, from nuclear physics to radiochemistry, material science, nuclear engineering, medical physics and nuclear medicine. My contribution to the team was mainly focused in the measurement of nuclear cross sections (including stacked-foils target preparation), data analysis and literature compilation. In addition to this, I was member of the team responsible for the LARAMED facility installation under way. In particular, my skills and knowledge were essentials to achieve key equipment such as γ-spectrometry instrumentation and in designing the future laboratory dedicated to spectrometric measurements. To date, despite the infrastructures and laboratory facilities are not yet completed, different studies were carried out, or are still underway, in collaboration with several external laboratories and hospitals. Since 2012, the LARAMED team has started working, through dedicated research projects approved and supported by INFN, on the cyclotron production of conventional radionuclides such as ^{99m}Tc (APOTEMA and TECHN-OSP), emerging radionuclides such as ^{67}Cu (COME), ^{47}Sc (PASTA) and ^{52}Mn (METRICS) and on the development of high power targets (TERABIO).

My Ph.D. work reports the main results achieved during the COME and PASTA projects, funded by the INFN CSN3 and CSN5 scientific commissions in 2016 and in 2017-2018. Such research activities were focused on the production of ^{67}Cu and ^{47}Sc, two theranostic radionuclides under the spotlight of the international scientific community thanks to their favorable physical and chemical properties. ^{67}Cu is the longest-lived isotope of copper ($T_{1/2}$=61.83 h) and emits both a β^- radiation with a mean energy of 141 keV (E_{max} = 580 keV), useful for therapy, and a γ-ray of 184.5 keV, useful for imaging through SPECT camera (Single-Photon Emission Computed Tomography). Moreover, it can be paired with the β^+ emitter ^{64}Cu to perform dosimetric studies with PET (Positron Emission Tomography) imaging, by using the same radiopharmaceutical. Likewise, ^{47}Sc has a relatively long half-life ($T_{1/2}$=3.3492 d) that permits to follow the slow kinetic biodistribution of large molecules in the body and, as ^{67}Cu, has a combined β^- and γ-ray emission, suitable for imaging with SPECT and to treat small-medium sized (mean β^- energy: 162 keV; γ-ray: 159.3 keV). Similarly, ^{47}Sc can also be paired with ^{43}Sc or ^{44g}Sc to perform PET studies prior therapy with the same radiopharmaceutical. The main goal of this thesis was the measurement of different nuclear cross sections to find out the best irradiation parameters, maximizing the production yield of the radionuclide of interest (^{67}Cu and ^{47}Sc). The minimization of the co-produced contaminants was also carefully considered and, for this reason, enriched and expensive materials have been extensively used. This also required the development of a dedicated target manufacturing procedure. In particular, the enriched titanium metallic targets, used in the cross section measurements for ^{47}Sc production, were realized at INFN-LNL within the scope of a dedicated research project, E_PLATE, funded by INFN CSN5 in 2018 and 2019. When needed, the development of a dedicated radiochemical processes, to extract the desired radionuclides from the irradiated material, was carried out in collaboration with the INFN department and the University of Ferrara (Italy) and the Sant'Orsola Hospital in Bologna (Italy). Thanks to another fruitful research collaboration, irradiation runs were always carried out at the ARRONAX facility (Nantes, France), where a Cyclone 70 cyclotron (manufactured by IBA, Belgium) is in operation.

In this work the dissertation is organized as follows.

Chapter 1 describes the use of radionuclides in nuclear medicine, with imaging and therapeutic applications, including also the description of the theranostic approach.

Chapter 2 is focused on the actual radioisotopes production techniques, that exploit both reactor and particles accelerators.

Chapter 3 refers to the theory of radioisotope production, focusing on the definitions of nuclear cross section and thick target yield.

Chapter 4 describes the LARAMED project under construction stage at INFN-LNL and the related research activities carried out within its framework.

Chapter 5 is focused on the production of ^{67}Cu by using ^{70}Zn targets, reporting the main results obtained for the ^{70}Zn(p,x)^{67}Cu,^{64}Cu,^{67}Ga,^{66}Ga,^{69m}Zn,^{65}Zn cross sections.

Chapter 6 is focused on the production of ^{47}Sc by using ^{48}Ti and ^{nat}V targets, reporting the results obtained for the ^{48}Ti(p,x)^{47}Sc, ^{46}Sc, ^{44}Sc, ^{44m}Sc and ^{nat}V(p,x)^{48}Sc, ^{47}Sc, ^{46}Sc, ^{44}Sc, ^{44m}Sc, ^{43}Sc, ^{48}V, ^{43}K, ^{42}K, ^{48}Cr, ^{49}Cr, ^{51}Cr cross sections.

1 RADIONUCLIDES IN MEDICINE

Nuclear Medicine (NM) is a medical technology that uses radionuclides for diagnosis and therapy, and to monitor patient's response to the treatment of a particular disease process [1]. According to the World Nuclear Association's data updated in February 2019, over 10000 hospitals worldwide use radioisotopes in medicine, and about 90% of the procedures are for diagnostic purposes [2]. The physical characteristics of radioactive emission of radionuclides determine their use in NM [3]:

- Emission of γ or β^+ radiation is useful for diagnostic purposes to visualize functional and metabolic processes at the deepest molecular level because of the high detection sensitivity;
- Emission of β^-, Auger-electrons or α radiations is useful for therapy as a result of the biological effects induced by these types of radiation and generated by their high linear energy transfer (LET[1]).

While diagnostic techniques such as Radiography, Computed Tomography (CT) and Nuclear Magnetic Resonance Imaging (MRI) provide morphological information, NM provides also biochemical and physiological functional information by means of radiopharmaceuticals [1]. Radiopharmaceuticals are radioisotopes bound, thanks to special synthesis process called "Labeling", to biological molecules, thus combining nuclear properties of a radioactive isotope with biomolecular probe properties of molecules. A radiopharmaceutical can, therefore, be seen as the union of a radionuclide and a vehicle molecule with high affinity for a tissue or a specific function of a human organ. Because every organ in our body acts differently from a chemical point of view, in this medical field, the cooperation between physics and pharmacology, to provide a wide selection of radiopharmaceuticals, is necessary. The physiological environment in which radiopharmaceuticals shall operate, the human body, requires the application of rigorous selection criteria for the radionuclide to ensure their effective use in nuclear

[1] Linear Energy Transfer (LET): A measure of how, as a function of distance, energy is transferred from radiation to the exposed matter, usually expressed in keV/µm. A high LET indicates that energy is deposited within a small distance; protons, neutrons, and α particles have much higher LET than gamma or x-rays.

medicine. In general, the medical radionuclides employed both for diagnostic and therapeutic purposes should meet the following specific requirements:

- suitable physical properties for selected application in terms of half-life ($T_{1/2}$), decay mode, emission energy;
- suitable chemical properties to allow their incorporation in a vector molecule through a so-called labelling reaction, with high radiochemical yields;
- ability to deliver an appropriate radiation dose to the target tissue (Appendix A) sufficient to accomplish the intended clinical use (diagnosis or therapy), but without harming the patient;
- a reasonable price.

A new frontier of NM is the "theranostic approach" that combines therapy and diagnosis carried out using the same radiopharmaceutical labelled either with a single radionuclide emitting γ photons (or positrons) and a massive particle (α or β^-) simultaneously, or a matched pair of radioisotopes one suitable for imaging and the other for therapy.

In the following paragraphs, the diagnostic, therapeutic and theranostic properties as well as use of radiopharmaceuticals will be further discussed.

1.1 Diagnostic techniques in nuclear medicine

Reliable diagnostic imaging techniques are always necessary in the first step of a clinical study in order to identify and characterize the site of the disease [2]. Therefore, an appropriate diagnosis is essential to establish the subsequent, most appropriate, therapeutic approach. Diagnostic imaging can be divided into two categories:

- methods that define very precisely anatomical details;
- methods that produce functional or molecular images.

The first method is based on the use of CT and MRI scans and it can provide detailed images of lesion location, size, morphology and structural changes to surrounding tissues, but only provides limited information on biomolecular processes underpinning the onset of the disease. The second method, based on the use of imaging technologies such as Positron-Emission Tomography (PET) and Single-Photon Emission Computed

Tomography (SPECT), provides insights into the abnormal physiology of the target tissue down to the molecular level, but are not conceived to disclose precise anatomical details. PET and SPECT are based on the use of radioisotopes that emit gamma rays, in a direct or indirect way (annihilation photons), with enough energy to escape from the body and being subsequently revealed with appropriate detectors. The combination of results, obtained with these two main diagnostic approaches, allows to integrate anatomical, functional, and biomolecular information in a single scan to yield hybrid diagnostic images.

1.1.1 SPECT

Single-Photon Emission Computed Tomography (SPECT) is the most used scanning technology to diagnose and monitor a wide range of medical conditions [3].

The SPECT imaging technique requires the injection to the patient of a γ-emitting radionuclide under a specific chemical form. The out-coming radiation is successively detected through SPECT-cameras (large scintillation crystals connected to Photo-Multiplier Tubes [PMTs] or semiconductor detectors). Usually, a SPECT-camera employs a sodium iodide crystal Tl dropped (or other detectors as cadmium zinc telluride, CZT) and its design must mediate between detection efficiency (which improves with thicker crystals) and intrinsic spatial resolution (which improves with thinner crystals) [4]. A compromise was found using relatively thin crystals (6.4 to 12.7 mm) that guarantee an acceptable detection efficiency while maintaining high intrinsic spatial resolution in the energy range of 100-200 keV. As shown in Figure 1, the photopeak detection efficiency is nearly 100% for energies up to approximately 100 keV for all crystal thickness, while for higher energies the efficiency decreases.

SPECT-cameras are normally provided with collimators, that select a specific direction absorbing almost all γ rays coming from any direction different from the chosen one. To acquire SPECT images, the gamma camera is rotated around the patient and this makes possible to reconstruct the complete 3D distribution of the radio-pharmaceutical used. The speed of acquisition may have an important effect on the quality of the resulting image also because of the unavoidable motion of the patient himself influences the effectiveness of the merging of scans from different angles. In some cases, in order

to increase the speed of the acquisition, multi-headed cameras are used. The acquired signals are further elaborated by back projections and reconstruction algorithms to obtain a 3D image of the radionuclide distribution within the patient body [5]. A schematic representation of the SPECT fundamentals is shown in Figure 2.

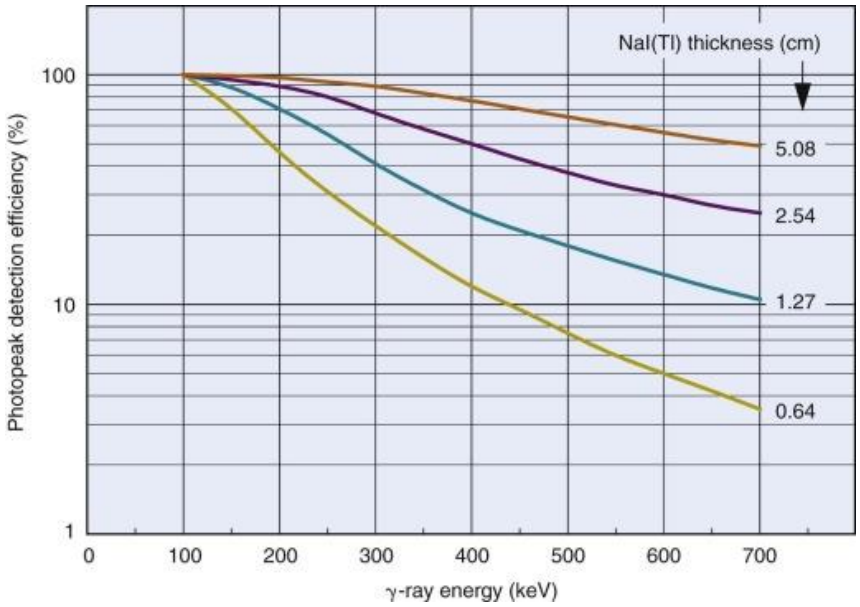

Figure 1: Photopeak detection efficiency versus γ-ray energy for the gamma camera detector for a range of NaI(Tl) crystal thicknesses [4]

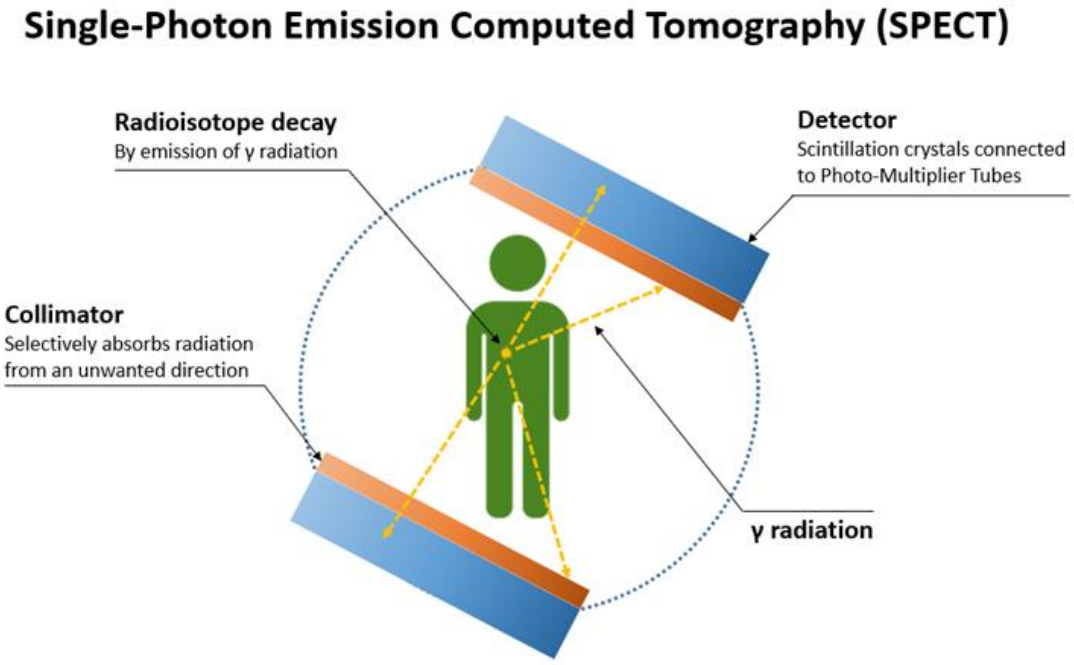

Figure 2: Schematic principle of SPECT

Generally, suitable nuclides are selected according to their half-lives and radiation properties. As a general principle, the γ-ray energy should be high enough to emerge from the patient's body but low enough to be fully absorbed by medium-size crystals, whereas the radiation intensity must be high enough to guarantee the imaging accuracy. In addition, the collimator has to be properly designed considering the energy of the gamma emitted by the selected radionuclide. Nowadays, ^{99m}Tc is the most used γ-emitting SPECT radionuclide [6] involved in over 85% of all diagnostic procedures thanks to its physical and chemical features that makes it the ideal element for the application in nuclear medicine. Indeed, ^{99m}Tc decays, with a half-life of 6.0072 hours, to ^{99g}Tc through isomeric transition (IT) by emitting a 140-keV photon (I=89%) [7], thus causing a lower radiation dose being delivered to patients. Moreover, thanks to its rich coordination chemistry, the establishment of a wide range of compounds and labeling methods allow to cover the diagnostic needs for almost all major organs such as brain, thyroid, lungs, heart, spleen, kidney, stomach, liver, bones.

An additional recent technological improvement has come from the possibility of fusion of CT and SPECT images that led to combine the functional and metabolic information, collected with SPECT, with morphological information recorded by CT [8].

1.1.2 PET

Positron emission tomography (PET) is a nuclear medicine procedure based on the use of tracer molecules radiolabeled with positron-emitting radionuclides. In β^+ decay, the emitted positron propagates into the surrounding matter and undergoes scattering interactions, which change its direction and cause loss of the kinetic energy. The positron combines with an electron of the surrounding matter (annihilation) after traveling a distance of the order of a millimeter, which depends on the initial energy [5]. The conservation of the linear moment implies that annihilation should generate two 511-keV photons emitted simultaneously at an angle of approximately 180°. The perpendicular distance between the line defined by the path of the two opposite photons and the decayed nucleus (effective positron range) places a limit on the spatial resolution that can be achieved with PET systems [9] (Figure 3).

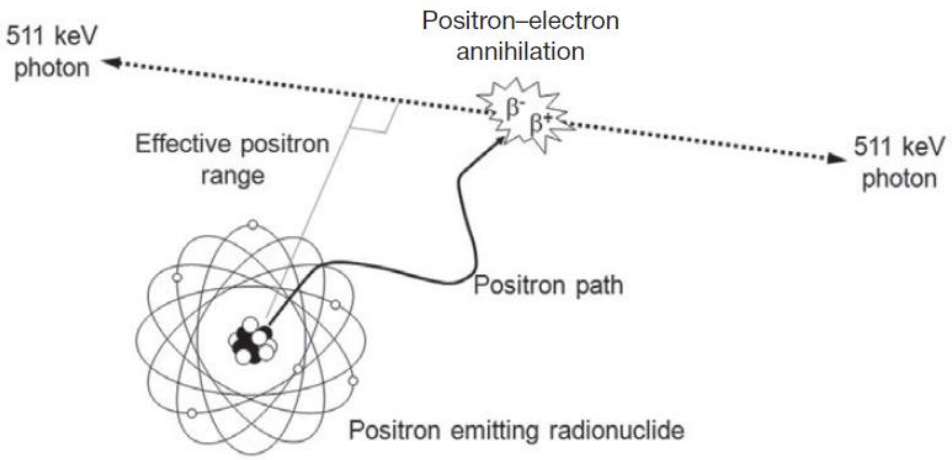

Figure 3: Principle of annihilation coincidence and effective positron range [5]

It is possible to distinguish and select the photon pairs with a coincidence detection method using detectors placed around the source, as shown in Figure 4. Scintillation detectors are the most common to detect 511-keV photons in PET imaging due to their good stopping efficiency and energy resolution [5]. Differently to SPECT, PET does not require a collimator and this elicites a sharp improvement in spatial resolution, statistical quality, and quantitative accuracy [10].

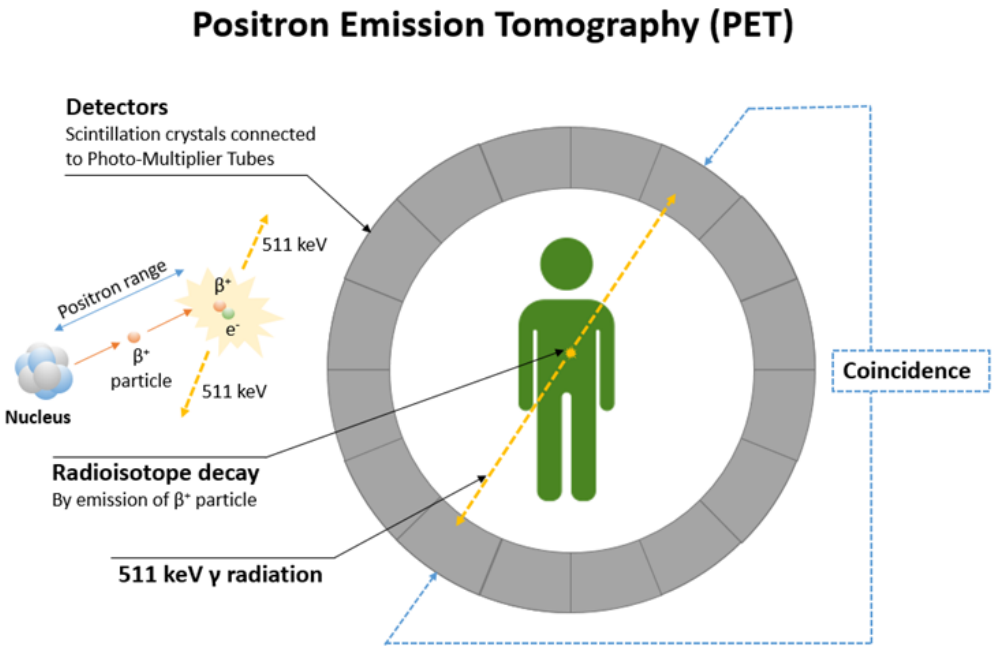

Figure 4: Schematic principle of PET

PET is a nuclear medicine functional imaging technique that allows to observe the metabolic process in the body and helps in the diagnosis of diseases. Currently, the most common radiotracer used in PET is ^{18}F-fluorodeoxyglucose (^{18}F-FDG), a glucose molecule labeled with ^{18}F [11]. In addition to ^{18}F, many other radionuclides are used in PET, such as ^{11}C ($T_{1/2}$ = 20.334 m), ^{13}N ($T_{1/2}$ = 9.965 m) and ^{68}Ga ($T_{1/2}$ = 67.71 m), as well as other non-standard positron emitters, under development [12] [13].

As in the case of SPECT/CT, also for PET hybrid imaging methods have been developed, in particular PET/CT and PET/MRI (Magnetic Resonance Imaging), where the functional PET images are merged with anatomical images. Such solutions allowed to significantly improve the quality of PET diagnostic information. In particular, for oncology applications, PET/CT has completely replaced PET, whereas clinical applications of PET/MRI are currently under development since such technology is not yet fully mature [14].

1.2 Radiotherapy

Different therapeutic strategies involve the use of radiation to treat cancer. There are mainly three types of radiation therapy treatment options [15]:

- *External beam radiation therapy (EBRT)* directs the radiation at the tumor from outside the body. The beam is designed to minimize radiation exposure to healthy cells and maximize the damage to cancer cells. EBRT usually delivers X-rays, electrons or, in case of particle therapy, protons or carbon ions;
- *Brachytherapy* is a type of radiotherapy where a radiation source is placed inside of or next to a specific area of a patient's body that requires treatment;
- *Targeted Radionuclide therapy (TRT)* involves small amounts of radioactive material taken into the body and thanks to a biological vector[2] is transported to the cellular target. The transported radionuclide emits energetic particles (α, β^- or Auger electrons) towards the targeted cell, inducing damage. Ideally, TRT delivers a high amount of radiation dose selectively to cancer cells, sparing, therefore, other healthy tissues.

Since this work is focused on therapeutic radionuclides, it is particularly important to identify the criteria to select the most appropriate ones for a specific purpose. In general, the selection criteria are based on the physical characteristics of the radionuclide decay, the production methods, its chemistry, and biological variables [16]. Moreover, the half-life must be sufficiently long to permit preparation of the radiopharmaceutical, injection and diffusion to the targeted biological site. In comparison with the radionuclides used for SPECT and PET, the half-life of the therapeutic radionuclides must be long enough to deliver sufficient cumulated dose to kill most of the cancer cells. The most convenient half-life usually ranges from a few hours to some days [17]. The particles emitted in the decay (α, β^- or Auger electrons) should have a LET allowing them to release all their energy over a very short distance, thus causing local cellular damage and disruption [18]. As an example, nuclides that decay emitting β^- particles with energies up to 1 MeV, are suitable to treat macro-clusters cells, since such radiation is stopped over 1 to

[2] Biological vector: A chemical construct, of both chemical or biological origin, that can be used to selectively deliver a radioactive payload to a target cellular population as a result of its intrinsic pharmacodynamic and pharmacokinetics properties.

10 mm, having low LET, whereas, α particles with energies up to 6 MeV are more appropriate for isolated metastatic cells or micro-clusters, since such radiation has high LET and it is absorbed within 0.1 mm [19]. Finally, Auger electron emitters are generally used to label carrier molecules that can penetrate through the cell membrane and reach the nucleus, where the emitted low-energy electrons can interact with the nuclear DNA of the target cell, thus sparing the surrounding healthy tissues [19].

The most commonly used therapeutic radionuclides are: iodine-131 (^{131}I) to treat thyroid-related diseases; strontium-89 (^{89}Sr) and samarium-153 (^{153}Sm) labelled radiopharmaceuticals for the treatment of bone metastasis; rhenium-186, -188 ($^{186/188}$Re) and Yttrium-90 (^{90}Y) for the treatment of a variety of malignancies; lutetium-177 (^{177}Lu) for the treatment of neuroendocrine tumors; radium-223 (^{223}Ra) for prostate cancer treatment, etc. (Table 1).

*Table 1: Physical characteristics of commonly available therapeutic radionuclides (RN) [20]. Decay modes: β^- beta electrons; EC electron capture; IT isomeric transition; α alpha particles; *Conversion electron*

RN	$T_{1/2}$	Decay Mode	E_{Max} β^- (keV)	β^- range in soft tissue (mm)		Production Method	Daughter Nuclide
				Mean	Max		
^{32}P	14.3 d	β^-	1710	2.6	7.9	^{31}P(n,γ)^{32}P ^{32}S(n,p)^{32}P	^{32}S
^{89}Sr	50.5 d	β^-	1496	2.4	8	^{88}Sr(n,γ)^{89}Sr ^{89}Y(n,p)^{89}Sr	^{89}Y
^{90}Y	64.1 h	β^-	2280.1	3.6	11	^{89}Y(n,γ)^{90}Y ^{90}Sr/^{90}Y gen.	^{90}Zr
^{117m}Sn	13.6 d	IT	130* 150*	0.22 0.29	0.27	^{116}Sn(n,γ)^{117m}Sn ^{117}Sn(n,n',γ)^{17m}Sn	^{117}Sn
^{131}I	8.02 d	β^-	606	0.4	2.4	^{130}Te(n,γ)^{131m,g}Te→^{131}I	^{131}Xe
^{153}Sm	46.5 h	β^-	808.2	0.7	3.1	^{152}Sm(n,γ)^{153}Sm	^{153}Eu
^{169}Er	9.40 d	β^-	350	0.3	1	^{165}Ho(p,n)^{165}Er	^{169}Tm
^{177}Lu	6.73 d	β^-	497.8	0.28	1.7	^{176}Yb(n,γ,β^-)^{177}Lu ^{176}Lu(n,γ)^{177}Lu	^{177}Hf
^{186}Re	3.72 d	EC, β^-	1069.5	1.2	3.6	^{185}Re(n,γ)^{186}Re	^{186}Os; ^{186}W
^{188}Re	17.0 h	β^-	2120.4	2.1	11	^{188}W/^{188}Re gen.	^{188}Os
^{223}Ra	11.4 d	α	5979.2(α)	<10 μm (α)		^{227}Ac/^{227}Th/^{223}Ra gen.	^{219}Rn (unst.)

1.3 Theranostics and personalized therapy

Theranostic is a clinical approach that is based on the use of radionuclides, or radionuclide pairs, characterized by the combined emission of both diagnostic and therapeutic radiations that allow collecting pre-therapy information with low-dose diagnostic imaging followed by high-dose therapeutic administration to the patient. This approach is getting closer to the realization of personalized medicine in which low-dose molecular imaging performed with SPECT/CT or PET/CT is a necessary step to provide preliminary information on biodistribution, dosimetry, the limiting or critical organ or tissue, and the maximum tolerable dose [21]. If the patient responds positively to the pre-therapy phase, the following step is to administer a higher-dose treatment in the same patient with the same radiopharmaceutical, thus ensuring the same biodistribution. In the theranostic approach it can be used:

- a single radiopharmaceutical that has both diagnostic and therapeutic properties; i.e. a bioactive molecule labeled with an isotope whose radiation is suitable for both diagnosis and therapy, (Table 2);
- a single radiopharmaceutical labeled with a couple of different radioisotopes of the same element, one radionuclide being utilized for diagnosis and the other for therapy (Table 3);
- a single radiopharmaceutical, labeled with a pair of different isotopes each belonging to a different element (surrogate pair), where one radionuclide is utilized for diagnosis and the other for therapy.

The interest of the international community on theranostic radionuclides is highlighted by the IAEA Coordinated Research Project (CRP) on "Therapeutic Radiopharmaceuticals Labelled with New Emerging Radionuclides (^{67}Cu, ^{186}Re, ^{47}Sc)" (IAEA CRP No. F22053) started in 2016. Whatever radionuclide is chosen it is of fundamental importance to know the possible presence of coproduced radionuclidic impurities, the chemical impurity profiles, and the effective specific activity (A_s) [22]. Moreover, a real problem to be solved is the lack of availability of most of the theranostic radionuclides proposed in Table 2 and Table 3. This thesis is focused on the production of ^{67}Cu and ^{47}Sc using proton beams to try to identify the best way to produce these isotopes by reducing, as far as possible, the presence of contaminants.

Radionuclide production processes will be discussed in the following chapter.

Table 2 Theranostic radionuclides. β^- beta electrons; C.E. conversion electrons; α alpha particles; Aug. Auger electrons.

	$T_{1/2}$ (days)	**Principal γ energy for imaging, keV (%)**	**Therapeutic particle(s)**
^{47}Sc	3.35	159 (68)	β^-
^{67}Cu	2.58	186 (40)	β^-
^{67}Ga	3.26	93, 184, 296 (40, 24, 22)	Aug., C.E.
^{111}In	2.8	171, 245 (91, 94)	Aug., C.E.
^{117m}Sn	14	159 (86)	C.E.
^{123}I	13.3 h	159 (83)	Aug., C.E.,
^{131}I	8	365 (82)	β^-
^{153}Sm	1.94	103 (30)	β^-
^{211}At	7.2 h	79 (21)	α
^{213}Bi	46 min	441 (926)	β^-, α (from ^{213}Bi→ ^{209}Tl)
^{186}Re	3.7186	137.157 (9.47)	β^-

Table 3: Theranostic radionuclides pairs. β^+ positrons; β^- beta electrons; C.E. conversion electrons; Aug. Auger electrons.

Imaging/therapeutic pair	**$T_{1/2}$ (days)**	**Imaging**	**Therapeutic particle(s)**
^{44}Sc/^{47}Sc	3.97/3.35	β^+	β^-
^{64}Cu/^{67}Cu	0.53/2.6	β^+	β^-
^{68}Ga/^{67}Ga	68 min/3.26	β^+	Aug; C.E.
^{86}Y/^{90}Y	0.61/2.7	β^+	β^-
^{124}I/^{131}I	4.2/8.0	β^+	β^-

2 PRODUCTION TECHNIQUES OF MEDICAL RADIONUCLIDES

The production of radionuclides used in nuclear medicine is a very crucial step. From a radiopharmaceutical industry point of view, a radionuclide is selected if its production efficiency is acceptable, the starting material is not too expensive, its half-life is suitable for logistics and there is enough demand on the market.

Radionuclides are artificially produced by nuclear reactors, charged particle accelerators and γ-irradiation. In addition, generators can be considered as an additional approach for radioisotopes local supply (i.e. hospitals), particularly used and advantageous for short-lived isotopes. The different radioisotope production methods determine their clinical utility due to the different characteristics of the final product [23]. Some isotopes can have dual production routes, through reactors and accelerators. The choice to select one of the production methods is often determined by economic and political reasons. Indeed, in order to satisfy the needs of a specific radioisotope, the production is not always carried out using the most convenient nuclear reaction. This is generally due to the already available infrastructure (almost always ageing research reactors) built in the past to cover different needs in a given geographical area.

In the next paragraphs, a brief analysis about the three state-of-art approaches are discussed more in detail.

2.1 Radionuclides production in nuclear reactors

A large variety of β^- emitting radionuclides can be produced in nuclear reactors by neutron induced fission processes on strategic fissile material, or by neutron activation reactions. In the latter case, both thermal and fast neutron reactions may properly be exploited.

So far, the current reactor-based mass production for several radioisotopes, (or of their decay products, e.g. $^{99}Mo \rightarrow {}^{99m}Tc$ etc.) useful in nuclear medicine, is indeed based

upon the chemical separation from fission fragments produced by using highly-enriched uranium, weapons-grade (HEU-WG) target material (i.e. ^{235}U enrichment > 80%). Such a productions route was, therefore, subject to the strict international regulations and control actions against the proliferation of nuclear weapons. In order to overcome such a problem, and also to mitigate the recent shortages of $^{99}Mo/^{99m}Tc$ generators on the international market occurred in 2008-2010 and further events happened in 2018 (i.e. the NRU Chalk River reactor –Canada- permanent shutdown) the efforts at international level have moved towards the use of non-strategic LEU (Low-Enriched Uranium) material (i.e. ^{235}U enrichment < 20%)

On the other hand, neutron activation may occur in nuclear reactors with different nuclear reactions, among which are worth to be noted [23]:

- (n,γ) reaction in which the target and product are different isotopes of the same element. In this case, the chemical separation to extract the product desired is useless (i.e. carrier-added radioisotope);
- (n,p) (n,xn) (n,α) reactions, in which the target and product are different elements. In such case the chemical separation procedures may be applied to get high-purity radionuclides (i.e. no carrier-added radioisotope).

In the reactor-based route, targets of specific materials can be placed around the reactor core to be irradiated by the intense reactor neutron flux for an appropriate time to produce a desired radioactive nuclide in a given amount [23] [24]. For both approaches, the irradiated targets are loaded in appropriate shielding containers and transported to hot chemistry labs for further processing. The quality and specific activity of the radioisotopes produced depends on both the target and the irradiation conditions [24].

A list of reactor-based medical radioisotopes, produced through fission and neutron activation, are reported in Table 4:

Table 4: Medical radioisotopes produced in nuclear reactor with some examples of their biomedical applications

RN	Decay mode	Reaction	Application
^{99}Mo	β^-	HEU fission fragment (~6% mass) alternative route: $^{98}Mo(n,\gamma)^{99}Mo$	^{99}Mo is used as a generator of ^{99m}Tc

RN	Decay mode	Reaction	Application
^{131}I	β^-, γ	HEU fission fragment (~3% mass) alternative route: $^{130}Te(n,\gamma)^{131}Te^{\beta^-} \rightarrow {}^{131}I$	Diagnosis and treatment of thyroid disorders
^{90}Y	β^-	$^{89}Y(n,\gamma)^{90}Y$	Therapeutic radionuclide commonly used in radioembolization to treat liver cancer
^{177}Lu	β^-, γ	$^{176}Lu(n,\gamma)^{177}Lu$ $^{176}Yb(n,\gamma)^{177}Yb \rightarrow {}^{177}Lu$	Targeted therapy via peptide labelling (neuroendocrine tumors and metastatic prostate cancer)
^{186}Re	β^-, EC	$^{185}Re(n,\gamma)^{186}Re$	Targeted therapy, including metastatic bone disease
^{32}P	β^-	$^{31}P(n,\gamma)^{32}P$	Brachytherapy label for pancreatic disease; treatment agent for some myeloproliferative diseases
^{125}I	EC, γ	$^{124}Xe(n,\gamma)^{125}Xe^{EC} \rightarrow {}^{125}I$	Brachytherapy (brain tumors, prostate cancer); Labelling of antibodies for nuclear medicine studies (research)
^{67}Cu	β^-	$^{67}Zn(n,p)^{67}Cu$	Labelling of peptides for the treatment of NETs, meningioma (currently under trial)
^{223}Ra	α	$^{226}Ra(n,\gamma)^{227}Ra \rightarrow {}^{227}Ac \rightarrow {}^{227}Th \rightarrow {}^{223}Ra$	Targeted therapy for bone metastases

EC = electron capture

Most of the existing reactors devoted to the medical radionuclides production started operation more than 50 years ago, and are next to be permanently shutdown for some of them is indeed foreseen both for obsolescence and economic and political reasons, as highlighted in Table 5 [25]. For this reason, the international community pushes radionuclides production research to look for alternative production routes to prevent further medical radionuclide shortages [20] [26].

Table 5: Main research reactors involved in the production of medical radionuclides [25]

Reactor	Country	Current targets[3]	Normal operating days/year	Estimated end of operation
BR-2	Belgium	HEU/LEU	147	At least until 2026
HFR	Netherlands	HEU/LEU	275	2026
LVR-15	Czech Rep	HEU/LEU	210	2028
MARIA	Poland	LEU	200	2040
RA-3	Argentina	LEU	230	2027 or earlier based on RA 10 introduction
SAFARI	South Africa	LEU	305	2030
RIAR	Russia	HEU	350	At least until 2025
KARPOV	Russia	HEU	336	At least until 2025
MURR	United States	Natural Mo in CRR	339	2037
OPAL	Australia	LEU	300	2057

2.2 Accelerator-based production

Accelerators are used to bombard production targets with beams of charged particles to produce a wide range of isotopes. The projectile particles are typically protons, deuterons, or helium nuclei ($^{3}He^{2+}$, $^{4}He^{2+}$). The production of radionuclides with an accelerator demands that the beam energy must be high enough to induce nuclear reactions, while the beam current must be sufficient high to give practical yield. There are many types of accelerators and they all share two underlying basic principles:

1. Electric fields, both static and variable at RF (Radio Frequency) regime, are used to accelerate particles (principle required for all the accelerators);
2. Magnetic fields are used to steer the particles (required if the accelerator steers the particle in a non-linear path).

The specific way in which these two principles are implemented determines the two main categories of particle accelerators: linear and circular accelerators.

[3] Abbreviations: LEU—Low-Enriched Uranium (<20%); HEU—Highly-Enriched Uranium (>80%); CRR—Conventional Research Reactor

The Van Der Graaf, Pelletron, Tandetron and other electrostatic accelerators are not discussed in detail in this Ph.D. thesis, since they are not used for radionuclide production due to the low current that they are able to provide (up to tens of μA). However, they are often employed for nuclear physics experiments and various types of applications, as radiobiology, material characterization, archaeometry, etc. On the other hand, linear particle accelerators and cyclotrons may provide a much higher current (up to tens of mA) and are thus used to produce radionuclides for medical applications.

2.2.1 Linear particle accelerators (LINACS)

A linac is a type of particle accelerator that accelerates electrons, protons or ions in a linear structure. A typical linac design, shown in a simplified sketch in Figure 5, include the following parts:

- a straight hollow pipe vacuum chamber which contains all the other components;
- a particle source, that produces a continuous, or pulsed, beam of charged particles which the machine accelerates. The design of the source depends on the type of particle to be accelerated;
- the drift tubes, composed by a series of open-ended cylindrical electrodes which are crossed by the particles coming from the source. The length of each electrode increases progressively with the distance from the source and it is determined by the frequency and the power of the driving power source; it also depends on the particle type to be accelerated. The mass of the particle has a large effect on the length of the cylindrical electrodes;
- an electronic oscillator and amplifier, to generate the required radio frequency (RF) applied to the cylindrical electrodes;
- a target, located at the end of the accelerating electrodes, where the particles collides and the nuclear reactions of interest occur.

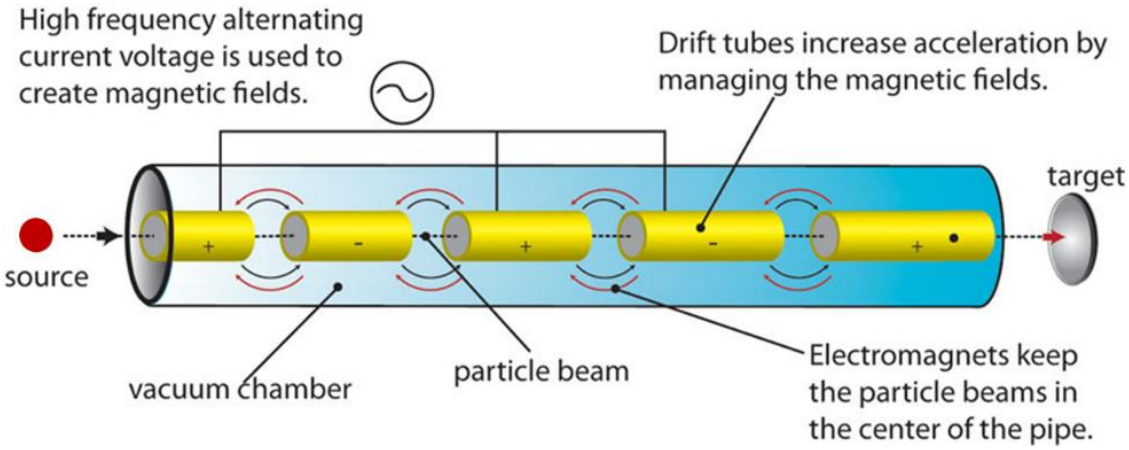

Figure 5: Schematic structure of a linear accelerator [27]

As already mentioned, the particles' kinetic energy increases when they pass through an appropriate electric field. In the linac structure, the energy increase is obtained by applying an oscillating voltage to alternate cylindrical electrodes thus having an opposite polarity (180° out of phase), so adjacent electrodes have opposite voltages. The oscillating electric field is created in the gap between each pair of drift tubes, which causes an electric drive force on particles when they pass through the gap, determining the acceleration. The system is conceived so that only bunched particles, synchronous with the accelerating wave, can achieve the maximum energy provided by each tube. The maximum energy gain in a multi-cell structure corresponds to the condition that the particles inside each bunch travels from one gap to the next in a time equal to half of the RF period (T/2). For a particle travelling at relativistic speed $\beta = v/c$, the time needed to cross one cell is $\tau = l/\beta c$ and the condition $\tau = T/2$ gives the required cell length $l = \frac{\beta c}{2} T = \frac{\beta \lambda}{2}$. Moreover, because of the high mass difference, electrons and ions react differently to an externally applied electric field. For this reason, each linac structure must be designed to the specific beams. In the case of an electron linac where the particles have $\beta = 1$, apart from a short initial section, the structure is composed by a sequence of identical cells of the same length $l = \lambda/2$. Instead, in the case of a proton linac, β increases slowly by order of magnitude and the cell length must follow the precise β profile. Linear accelerators can be split in linear electron accelerators or linear ions accelerators, depending on the type of accelerated particles.

Linear ion accelerators

In the case of linear ions accelerators, protons or heavier ions are generated in the ion source, that has its own high voltage supply to inject the particles into the beamline. Many linacs serve as initial accelerator stage for larger particle accelerators (such as synchrotrons and storage rings) but the accelerated beam can be used directly to hit a target of various materials, depending upon the specific investigation.

Linear ion accelerators are already used for the production of medical radionuclides. An example is the Brookhaven Linac Isotope Producer (BLIP), that consists of a beam line and a proper target for isotope production. Protons up to 200 MeV energy and 110 μA beam current can be obtained from the BNL Linac. Among the isotopes produced, a monthly ^{67}Cu supply is also reported on the dedicated webpage [28].

Linear electron accelerators

In case of linear electron accelerators, the electrons can be generated in the source by using a cold cathode, a hot cathode, a photocathode, or RF. Electron linacs are often used to convert the electron beam into a photon beam by using a high-density target (usually tungsten, for its high melting point) to induce the bremsstrahlung mechanism. For this reason, the target irradiated by the photon beam does not require a proper cooling system (as in the case of proton or deuteron irradiations), since it is not subjected to direct beam heating. This is an advantage in the target design and realization. However, photon-induced reactions require targets with higher masses than charged-particles induced reactions due to their lower attenuation in matter. This may be a drawback, especially if expensive materials are mandatory, as the case of enriched targets (e.g. one of the alterative ^{99}Mo production investigated in the last 10 years for ^{99}Mo/^{99m}Tc generators through the reaction route ^{100}Mo(γ,n)).

Electron linacs are already used in several laboratories also for the production of ^{67}Cu and ^{47}Sc, although in limited amounts, by exploiting photonuclear production by the reactions ^{68}Zn(γ,p)^{67}Cu [29], ^{48}Ti(γ,p)^{47}Sc and ^{49}Ti(γ,pn)^{47}Sc [30] [31].

2.2.2 Circular accelerator: Cyclotrons

The need to achieve high energies by using compact structures (with reasonable costs) has led to the development of a different kind of circular accelerators. Cyclotrons are circular accelerators, where charged particles are accelerated (by using a rapidly varying RF electric field) from the ion source, in the center, along a spiral path (thanks to the magnetic field).

The most frequent circular accelerators used for nuclear medicine are cyclotrons, mainly employed to produce nuclides both for PET and SPECT applications.

There are at least three types of cyclotrons: classical cyclotrons (constant magnetic field, constant frequency), synchrocyclotron (constant magnetic field, variable frequency), and Isochronous cyclotrons (variable magnetic field, constant frequency). Some cyclotrons are able to accelerate positive ions and other negative ions; the extraction technique strongly depends on this specific characteristic of the accelerator: for example, a stripper foil is used in case of accelerated negative ions.

Classical cyclotron

In modern cyclotron technology, ions (H^+ or H^- in the simplest case), once produced in an ion source, are injected into the center part of the cyclotron put inside a vacuum chamber. Soon the acceleration process, starts under the strong electric filed provided by a given number accelerated cavities (usually 2-4 to speed up the increase of the energy gain per turn) powered by a high frequency electric field. A schematic sketch showing the working principle of the spiral-accelerating path is instead portrayed in Figure 6. A RF (usually from a few up to some tens MHz) electric field of several kV is applied alternatively at the so-called "Dees". The acceleration occurs when ions pass from one dee to the next through a gap between the dees. Obviously, a charged particles beam can follow a circular trajectory of radius r only if it is immersed in a magnetic field B (Lorentz force, F_L) and it maintains its circular trajectory only if subjected to a centripetal force (F_c):

$$\begin{cases} \overrightarrow{F_L} = q\vec{v} \times \vec{B} \\ \overrightarrow{F_c} = \frac{mv^2}{r}\vec{n} \end{cases} \quad \rightarrow \quad F_L = F_c \quad \rightarrow \quad qvB = \frac{mv^2}{r} \quad \rightarrow \quad mv = qBr \qquad (2.1)$$

where v is the velocity, q is the electric charge of the particle and m is the mass of the charged particle. Consequently, the charged particles travel a complete circular trajectory with a frequency f given by:

$$f = \frac{qB}{m} = \frac{v}{r} = \omega_P = \omega_{RF} = 2\pi f_{RF} \rightarrow \quad f_p = \frac{qB}{2\pi m} \tag{2.2}$$

Thus, the timing of the RF voltage is switched between the dees, accelerating the particles and increasing the diameter of their circular path with every revolution, turning it into a spiral (Figure 6). For a given particle and energy, the RF frequency, in this simple approach, is thus fixed and constant as the energy increase. However, the latter sentence is, in general, not true when the particle achieves energies larger than a few MeV. In such a case, the condition that the particle mass is kept constant at the rest mass ($m=m_0$) is of course no longer true, thus causing a loss of isochronism. A modification in the vertical magnetic field B intensity is therefore necessary.

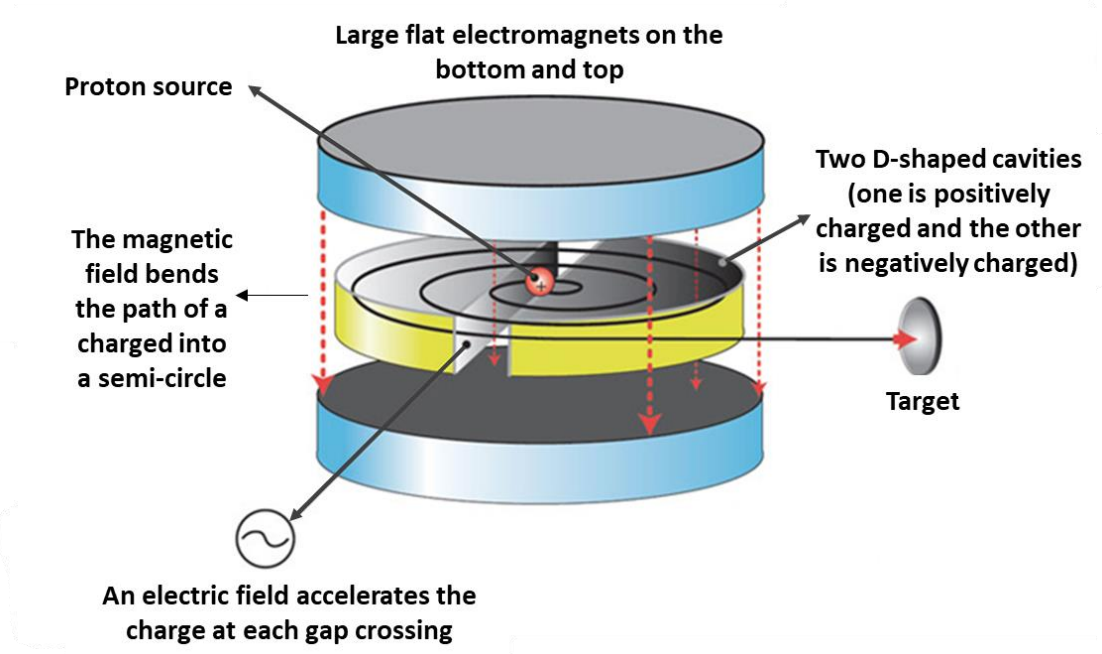

Figure 6: Schematic structure of a cyclotron

The first cyclotrons were equipped with H^+ ion sources while in the more recent decades, usually negative hydrogen (H^-) ion sources were used for proton accelerator facilities (not only for cyclotrons). The electric polarity of the accelerated negative ions can be inverted easily by removing the two electrons with a striper foil. This process is exploited in the beam extraction phase in which, instead of electrostatics deflectors to change the particle's trajectories, is usually employed a carbon foil. A thin carbon foil

removes ("strips") the electrons from the accelerated ions; due to the different *q/m* vector quantity changes the curvature of the trajectory of the beam, thus conducting the particles out of the cyclotron. This type of extraction is very efficient, in some cases it reaches 100%, and it is possible to extract the beam at different energies only by changing the position of the stripping foil which moves along a radial arm, inside the cyclotron. So, given *R* as the extraction radius, the output energy of the particles is:

$$E = \frac{1}{2}mv^2 = \frac{q^2B^2R^2}{2m} \tag{2.3}$$

Therefore, the limit to the cyclotron's output energy for a given type of particle is the strength of the magnetic field *B* and the radius *R*, which is determined by the size of the magnets. Even if some very large cyclotrons have been built, in the most common ones the proton energies are lower than 30 MeV and only in a few cases they reach 70 MeV [32]. Under these conditions it can be assumed that the non-relativistic approximation, in which the cyclotron frequency does not depend upon the particle's speed or the radius of the particle's orbit, is valid.

When high energies per unit mass (i.e. 20-80 MeV/A) and a wide range of ion masses (e.g. from the lighter elements like He, Li, C, up to the mass of uranium) need to be accelerated, the superconducting technology allows to keep very compact the machine design , which need to work at a very high intensity magnetic fields, i.e. 4-6T [33]. In order to achieve such an intense magnetic field, the superconducting cyclotron is usually equipped with a series of superconductive coils and cooled down at the liquid helium (LHe) temperature of about 4.0K.

Synchrocyclotron

Synchrocyclotrons were developed to compensate for the relativistic effects occurring when the particles' velocity begins to approach the speed of light. Synchrocyclotrons are characterized by a varying RF driving the electric field. In these conditions, the relativistic mass can be rewritten as $m = \frac{m_0}{\sqrt{1-\beta^2}} = \gamma m_0$, where $\beta = v/c$, c is the light speed and m_0 is the particle rest mass. The relativistic frequency is thus$f = f_0/\gamma$, where f_0 is the cyclotron frequency in classical approximation. The main drawback of synchrocyclotrons is that, as a result of the variation in the frequency of the oscillating voltage supply, only a very small fraction of the ions leaving the source are captured in phase-stable orbits of maximum radius and energy. Therefore, as the average beam

current is only a small fraction of the instantaneous beam current, the machine produces high energy ions with comparatively low intensity.

Isochronous cyclotrons

In the isochronous cyclotrons a constant RF driving frequency is maintained and the relativistic effects are compensated by an increasing magnetic field with the radius. Isochronous cyclotrons are capable of producing much greater beam current than synchrocyclotrons but require azimuthal variations in the magnetic field strength to guarantee a strong focusing effect and keep the particles in the correct spiral trajectory. For this reason, an isochronous cyclotron is also called "AVF (azimuthal varying field) cyclotron". The radius of the circular motion of a charged particle in the presence of relativistic effects and a uniform magnetic field is $r = \frac{\gamma m_0 v}{qB}$ and the relativistic cyclotron frequency is $f = \frac{f_0}{\gamma}$. Choosing the magnetic field value $B = \gamma B_0$, the radius of the circular motion becomes equal to $r = \frac{m_0 v}{qB_0}$ and, like in the non-relativistic case, depends only on the velocity v. In this case, the cyclotron frequency is constant.

2.3 The use of cyclotrons in nuclear medicine

Medical cyclotrons can be divided in types according to the available projectile energy, as shown in Table 6.

Table 6: Overview of the medical cyclotrons available worldwide

Cyclotron type	Energy Range	Approximate number
Small medical cyclotron (SMC)	< 20 MeV	1050
Intermediate energy cyclotron	20-35 MeV	100
High energy cyclotron	> 35 MeV	50

The widely used cyclotrons used for nuclear medicine are the Small Medical Cyclotron (SMC) allowing beam energy up to 20 MeV. They offer proton beam currents typically in the range of 60-100 μA [34]. The SMC are mainly installed in hospitals and their number is still increasing: as an example, in 2015 almost 1000 SMCs were installed

worldwide [35]. Typically, SMCs accelerate protons and only in a few cases they are also capable of accelerating deuterons (at half of the specified proton energy). SMCs are commonly used to produce medical radionuclides for in-hospital use, in particular short-lived, standard radionuclides, basically for PET studies. Cyclotrons providing beam energy between 20 and 35 MeV are considered intermediate energy cyclotrons or medium energy cyclotrons, and normally accelerate protons or deuterons (very few of them offer also α beams option). They are installed in major commercial plants or research institutes to produce classical SPECT or novel PET radionuclides, as well as generator parent nuclides. Finally, high energy cyclotrons with beam energy above 35 MeV are found in large research institutes and can provide a wide variety of beams, in particular protons, deuterons and α beams. Such machines can be used to produce innovative and emerging radionuclides, for both diagnosis and therapy, as well as generators parent nuclides such as ^{82}Sr and ^{68}Ge.

2.3.1 The role of targets in radionuclide production

Whatever the manufacturing technique used, targets are hit by accelerated particle beams of given energies and intensity (or exposed to an intense neutron flux inside a reactor core channel) with the aim to yield the desired radionuclide, through the selected nuclear reaction route. Targets used for neutron irradiation have much larger size and masses than the accelerator targets, to enhance the reaction-rate during the irradiation time. That is because of the much longer mean free path (i.e. the inverse of the macroscopic cross section $1/\Sigma$) the neutrons have with respect to charged particles. For this reason, it would be preferable to avoid the use of isotope-enriched targets due to their very high cost.

However, during the bombardment, the heat deposited by the beam in the irradiated material is removed by a proper cooling system. After the irradiation, the target undergoes a radiochemical process to separate the desired element from the bulk material and all others produced contaminants. The optimized design of the target thus takes into account all these specific aspects and strongly depends on the specific radionuclide of interest. The target realization, therefore, requires specific studies to choose the right material and the proper manufacturing technique. An advantage of particle accelerators over nuclear reactors is that the target is usually a different chemical element from the desired product: this makes possible to find a suitable chemical separation process to extract and purify the radionuclide of interest. In the case

of accelerator-based production of radionuclides, by selecting the best target material and the beam energy range for the irradiation, it is also possible to reduce the coproduction of radioisotopic impurities. Standard radionuclides are mostly produced by using gas or liquid targets, while for novel radionuclides, solid targets are often used. Water targets (i.e. usually ^{18}O- or ^{16}O-enriched) are the most commonly used for the production of PET radionuclides, such as ^{18}F and ^{13}N [36].

Gas and liquid targets usually consist of a gas or fluid cell contained by a water-cooled target body and a thin foil (e.g. window) that encloses the target cell but still allows the beam penetration. The materials used for the body fabrication must be good mechanical properties, stand high pressures, chemically inert to basically all the reactive chemical species produced during the irradiation stage, have good thermal conductivity and they are also chosen to reduce as much as possible the production of long lived radioactivity in the target body during irradiation. The most used materials of the target body metals are aluminum, titanium, nickel, niobium, tantalum, and silver; in Table 7 are reported the principal physical characteristics.

Table 7: Target body materials properties for gas and liquid targets

Property	**Aluminum**	**Titanium**	**Nickel**	**Niobium**	**Tantalum**	**Silver**
Thermal conductivity ($W \cdot m^{-1} \cdot K^{-1}$)	237	21.9	90.9	53.7	57.5	429
Melting point (°C)	660.32	1668	1455	2477	3017	961.78
Heat capacity ($J \cdot mol^{-1} \cdot K^{-1}$)	24.2	25.06	26.07	24.6	25.36	25.35

Target windows are typically realized by thin sheets in metal havar, aluminum, niobium, and titanium. These selected materials are very strong in thin sheets and maintain their strength at elevated temperatures. The beam deposits energy on the target windows, causing a heat deposition that can be dissipated in different ways, depending upon the specific characteristics. It has also to be considered that the interaction of the thin foil with the beam may cause the production of contaminant radionuclides that can potentially end up in the final product due to some reactive chemical reactions and recoil effect. These additional impurities must be taken into account in the radiochemical purification phase after irradiation.

The main advantage of solid targets is the possibility to produce a larger amount of the desired radionuclide considering the higher density of the material, generally in the form

of foils or pressed metals (or metal oxide/carbides, etc.) powders. Moreover, more complex separation chemistry and the need of specific studies to determine the proper technological process to prepare of a few hundred μm thick layers have to be considered. Therefore, solid targets for the production of novel radionuclides are typically maintained and optimized in-house. It is worth reminding that common issues related to target preparation (solid, liquid or gas) concern:

- the use of expensive enriched materials to produce radionuclides with high radionuclidic purity;
- the mandatory cooling system optimized for the specific target configuration. As an example, often a tilted solid target is used to better spread the beam power heat spot hitting the target over a larger target surface area;
- the automation of the delivery line, typically by using a pneumatic system, that is necessary to reduce as much as possible the manual handling (especially when the target must be retrieved shortly after irradiation).

As an example, Table 8 reports the novel radionuclides produced in SMCs and used for diagnostic.

Table 8: Production of diagnostic radionuclides in small medical cyclotrons (SMCs) [34]

Radionuclide	**Imaging procedure**	**$T_{1/2}$**	**I**	**E_γ or $E_{av.\beta}$ (keV)**	**Feasible SMC nuclear reaction (E_p< 20 MeV)**	**Target type**
^{99m}Tc	SPECT	6.43 h	γ 99%	140.5	^{100}Mo(p,2n)^{99m}Tc	Solid
^{123}I	SPECT	13.2 h	γ 83%	158	^{123}Te(p,n)^{123}I	Solid
^{124}I	PET	4.18 d	β^+ 12% β^+ 11% γ 63%	687 975 603	^{124}Te(p,n)^{124}I	Solid
^{89}Zr	PET	78.4 h	β^+ 23% γ 99%	396 909	^{89}Y(p,n)^{89}Zr	Solid Liquid
^{64}Cu	PET	12.7 h	β^+ 18% β^- 39% γ 0.5%	278 190 134	^{64}Ni(p,n)^{64}Cu	Solid Liquid
^{68}Ga	PET	67.7 min	β^+ 88% γ 3%	836 1077	^{68}Zn(p,n)^{68}Ga	Solid Liquid
^{67}Ga	SPECT	78.3 h	γ 39% γ 21% γ 17%	93 185 300	^{68}Zn(p,2n)^{67}Ga ^{67}Zn(p,n)^{67}Ga	Solid
^{111}In	SPECT	67.3 h	γ 94%	245	^{111}Cd(p,n)^{111}In	Solid

Radionuclide	Imaging procedure	$T_{1/2}$	I	E_γ or $E_{av.\beta}$ (keV)	Feasible SMC nuclear reaction (E_p< 20 MeV)	Target type
			γ 91%	171		
^{86}Y	PET	14.7 h	β^+ 12% β^+ 6% γ 83%	535 681 1077	^{86}Sr(p,n)^{86}Y	Solid Liquid
^{44}Sc	PET	3.97 h	β^+ 94% γ 100%	632 1157	^{44}Ca(p,n)^{44}Sc	Solid Liquid

2.4 Generator-based production

A radionuclide generator is a device, nowadays commonly available in nuclear medicine departments of hospitals all over the world, able to provide the radioactive amount needed for the preparation of radiopharmaceuticals for imaging procedures every day. A radionuclide generator contains a long-lived radionuclide (parent), which decays into a short-lived (daughter) radionuclide of interest. The parent/daughter radionuclides separation can be done by following different strategies, such as solvent extraction, ion exchange, adsorption chromatography, electrochemistry, and sublimation [37]. A radionuclide generator useful for medical applications involves a radioactive equilibrium (Appendix B) in which the parent has a half-life significantly longer than that of the daughter, allowing daily availability of the isotope of interest directly in the hospital by repeated elution [38]. This device is particularly interesting for those nuclear medicine hospitals that do not have a cyclotron or that are located far from the production site, causing long distances and expensive distribution costs. Some generator systems relevant to life-science applications are listed in Table 9.

The most important radionuclide generator for radiopharmaceutical preparation is the ^{99}Mo → ^{99m}Tc system. The parent radionuclide ^{99}Mo ($T_{1/2}$ = 66 hours), which produces by decay the radioactive daughter ^{99m}Tc ($T_{1/2}$ = 6 hours). A decay chain equilibrium is established between the parent and the daughter, known as transient equilibrium. The transient equilibrium is achieved in about 4 daughter half-lives, i.e. 24 hours in case of ^{99m}Tc.

Table 9: Generator systems relevant for life-sciences applications (f fission; β^+ positrons; β^- beta electrons; EC electron capture; ERT endoradiotherapy) [38]

Generator system	Parent nuclide			Daughter nuclide		
	$T_{1/2}$	Production route	Main decay	$T_{1/2}$	Main emission	Application
$^{47}Ca/^{47}Sc$	4.536 d	Reactor	β^-	3.341 d	γ, β^-	ERT
$^{44}Ti/^{44}Sc$	60.3 y	Accelerator	EC	3.927 h	β^+	PET
$^{52}Fe/^{52m}Mn$	8.28 h	Accelerator	β^+	21.1 min	β^+	PET
$^{68}Ge/^{68}Ga$	270.8 d	Accelerator	EC	1.135 h	β^+	PET
$^{82}Sr/^{82}Rb$	25.6 d	Accelerator	EC	1.273 min	β^+	PET
$^{90}Sr/^{90}Y$	28.5 y	Reactor, f	β^-	2.671 d	β^-	ERT
$^{99}Mo/^{99m}Tc$	2.7477 d	Reactor, f	β^-	6.006 h	γ	SPECT

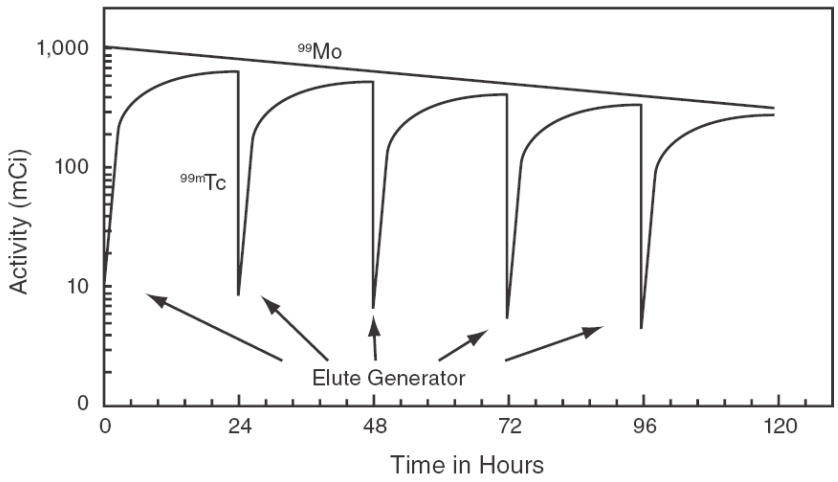

Figure 7: ^{99m}Tc in-growth and elution in a generator system

As shown in Figure 7, the relative activity of ^{99m}Tc in the generator decreases each time the generator is eluted and subsequently grows back in as the ^{99}Mo decays. Technetium generators are commonly available on the market in different ^{99}Mo activity amounts and are typically eluted once per day for 1 to 2 weeks; after this time, the amount of technetium is not enough to satisfy the demands of a hospital.

3 THEORY OF RADIOISOTOPE PRODUCTION

Radioisotopes production, both for diagnostic imaging and/or therapeutic treatments, is achieved through specific nuclear reactions in reactors or from particle accelerators. The main reactor-based mass production is indeed through the selection (i.e. radiochemical separation/purification process) of fission fragments produced by neutron-induced fission reactions on HEU targets. For some radionuclides the alternative way (usually for limited yields) is instead based upon the use of the intense neutron flux levels that may be achieved inside the reactor core volume (in one of the reactor channels available) in order to exploit the different neutron capture reaction routes.

Instead, in accelerators the standard charged particle reactions utilize protons and, when necessary, deuterons, $^{3}He^{2+}$, and $^{4}He^{2+}$. The accelerator produced radioisotopes are currently becoming more popular because of the ageing of the reactor facilities available, next to be permanently shutdown, and the number of running reactors used for radioisotopes production is becoming smaller than the number of available cyclotrons [32].

3.1 Nuclear reaction models

A nuclear reaction is a process in which two nuclear particles (two nuclei or a nucleus and a nucleon) interact to produce two or more nuclear particles and/or γ/X-rays. The equation for a generic nuclear reaction is:

$$a + A = b_i + B_i + Q \tag{3.1}$$

where a is the incident particle, A is the target nucleus in the ground state, b_i is the outgoing particle (or particles), B_i are the residual nuclei and Q represents the energy released in the reaction. The energy released in a nuclear reaction can appear mainly in one of three ways: as kinetic energy of the products, as emission of gamma rays by unstable nuclei in their transition from a high energy state to a lower state (γ-decay) or with the population of metastable energy levels. For a general A(a, b)B nuclear reaction,

the energy balance in the reaction in the laboratory reference frame (in which the target nucleus is at rest) is:

$$m_a c^2 + T_a + m_A c^2 = \sum_i m_{b_i} c^2 + T_{b_i} + \sum_i m_{B_i} c^2 + T_{B_i} \quad (3.2)$$

where T_i is the kinetic energy of the *i-th* particle and m_i represents its mass.

The Q-value is calculated as the difference between the sum of the masses of the initial reactants (*a* and *A*) and the sum of the masses of the final products (b_i and B_i), but it can also be defined in terms of energy gained or lost in a specific nuclear reaction. The Q-value is given by:

$$Q \stackrel{\text{def}}{=} \left[m_a + m_A - \left(\sum_i m_{b_i} + \sum_i m_{B_i} +\right)\right]c^2 = \sum_i T_{b_i} + \sum_i T_{B_i} - T_a \quad (3.3)$$

which, can also be expressed in terms of kinetic energy *T* considering the target nucleus not at rest:

$$Q = \sum_i T_{b_i} + \sum_i T_{B_i} - (T_a + T_A) = T_{final} - T_{initial} \quad (3.4)$$

The Q-value is positive for exothermic reactions (spontaneous reactions) or negative for endothermic reactions; in this case, a net energy input is required. However, it must be considered that before hitting the nucleus, the incident particle must overcome the barrier due to the repulsive Coulomb force between the particle and the nucleus. Since the incident particle loses energy due to the Coulombian force, its initial central of mass energy (threshold) must exceed the Q-value [5]. In a nuclear reaction, the nucleus can decompose along several exit channels and each one is characterized by a given Q-value and Threshold energies.

The probability that a certain nuclear reaction occurs is called nuclear reaction cross section σ and has the unit of a surface area: in fact, it describes the probability that a particle will interact per unit surface area of a target. The geometrical cross section of a uranium nucleus is approximately 10^{-28} m^2 and this area has been chosen to define the unit called barn ($1\ b = 1 \times 10^{-24} cm^2$). The barn is not an International System of Units but it is normally used to describe reaction probabilities in atomic and nuclear physics [5].

The exact mechanism of nuclear reactions is not yet completely understood, but some approximations can be used to visualize the process, i.e. the compound nucleus reaction, the direct nuclear reaction, and the pre-equilibrium nuclear reactions [39] (described hereafter).

Compound nuclear reactions

The formation of a "compound nucleus" and its subsequent decomposition has been proposed by N. Bohr in 1936. This model assumes that the incident particle and the target nucleus become indistinguishable after the collision, forming a particular excited state of the nucleus (many nucleon-nucleon interactions), indicated as the compound nucleus. When the incident nuclear particle combines with the target nucleus it loses its identity, becoming indistinguishable particles. The total energy is shared among all nucleons until a nucleon, or a group of nucleons, receives enough energy to escape; this continues until the energy becomes lower than the particle emission threshold. This compound system is a relatively long-lived intermediate state of the particle-target composite system (about 10^{-18} s) [5] and is predominant at low energies (below 10 MeV) [39].

The following process in a nuclear reaction is the decay of the compound nucleus that can take place by numerous paths, usually called exit channels. These channels are constrained by the conservation of mass-energy, charge, spin, angular and total momentum but they do not depend on how the nucleus was formed. The ejected particles are emitted with an almost isotropic angular distribution. The formation of a compound nucleus and its following decay are considered as independent processes.

Direct nuclear reactions

At the other extreme, direct nuclear reactions occur when the incident particle interact on the surface of a target nucleus (single-nucleon interaction) and the incoming energy is directly transferred to a nucleon with the consequent emission of two particles [5]. The direct nuclear reactions are faster (about 10^{-22} s, which is approximately the time that an incident particle takes to traverse the target nucleus) than compound nuclear reactions. Direct nuclear reactions occur for incident energies above about 10 MeV and the two particles are emitted with an angular distribution peaked in the forward direction [39]. Then, the compound nucleus component is dominant at low energies while the direct contribution increases with energy, as more channels become available.

Pre-equilibrium nuclear reactions

The separation of nuclear reaction mechanisms into direct and compound results to be too simplistic. Indeed, the phenomenon called pre-equilibrium emission takes place after the first stage of the direct reaction but before the equilibrium of the compound nucleus is attained [39]. Pre-equilibrium processes are relevant in the description of the reaction cross section for incident energies between 10 and at least 200 MeV. It is possible to imagine that the incident particle step-by-step creates more complex states of the compound system and gradually loses its memory of the initial energy and direction. Direct particles are emitted predominantly in the same direction as the incident particle, whereas in the case of compounds reactions the particles are emitted in all directions. The transition between the two extreme situations occurs gradually as is evident from Figure 8 in which it can be noted a gradual transition to isotropy for decreasing outgoing energies.

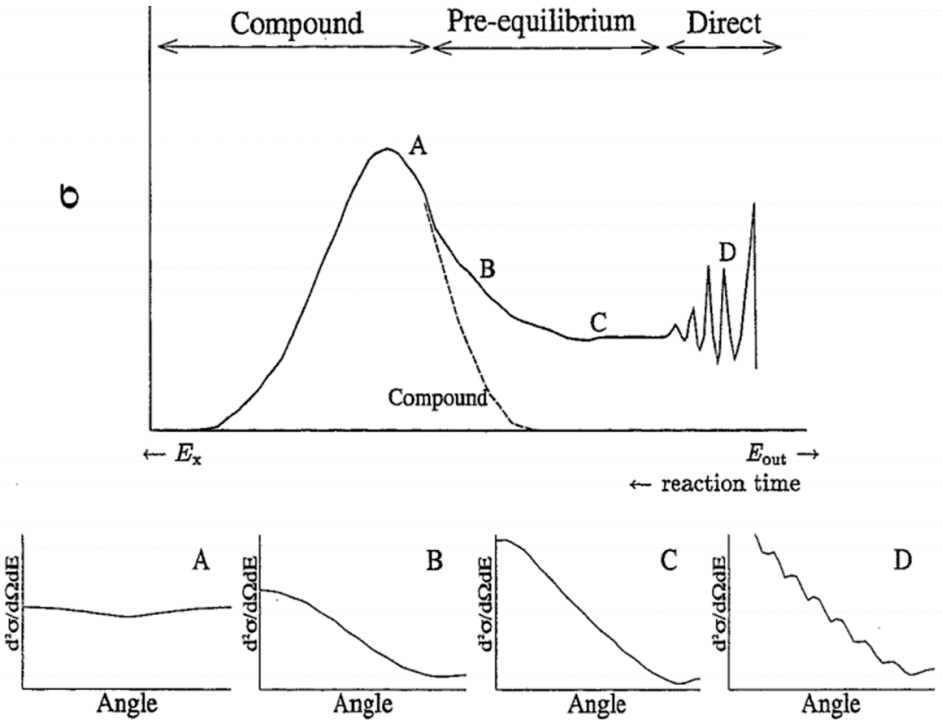

Figure 8: Typical energy spectrum of a reaction A(a,b)B with an incident energy of several tens of MeV [39]

The different nuclear reaction mechanisms described are included in different nuclear reaction codes, such as TALYS, EMPIRE, FLUKA, MCNPX, etc., usually used to estimate the trend of the nuclear reactions that are not measured yet. In this context, it is worth mentioning an ongoing collaboration with a group of phenomenological

analysts (L. Canton INFN-PD and A. Fontana INFN-PV) to identify the validity limits of the entire set of models present in the TALYS and other nuclear reaction codes. This work is particularly important to predict the production of stable isotopes that are difficult to be measured but affect the isotopic or radionuclidic purity of the final product.

3.2 Experimental determination of the cross-sections

By definition, the cross section is the probability of a specific nuclear reaction occur (i.e. the interaction of one bombarding particle and one target atom). Given N_b the number of bombarding particles [particle/s], and N_t the number of target atoms [atoms/cm^2] expressed as $N_t = \frac{N_A \rho P x}{A}$, where N_A is the Avogadro constant [1/mol], A is the mass number [g/mol], P the purity, x the thickness [cm] and ρ the mass target density [g/cm^3], it is possible to write the following differential equation of simple activation:

$$\frac{dN}{dt} = N_t N_b \sigma - \lambda N \tag{3.5}$$

where N is the number of produced particles, characterized by the decay constant λ [1/s]. The solution of this equation gives the number of radionuclides $N(t_{EOB})$ present in the target at the End Of Bombardment (EOB) after the irradiation time t_{irr}:

$$N(t_{EOB}) = N_t N_b \sigma \frac{1}{\lambda}\left(1 - e^{-\lambda t_{irr}}\right) \tag{3.6}$$

Accordingly, the activity (i.e. the number of nuclide decays per unit time) of the radionuclides produced at EOB is given by:

$$A(t_{EOB}) = N_t N_b \sigma\left(1 - e^{-\lambda t_{irr}}\right) \tag{3.7}$$

The number of decays ΔN occurred during the measuring time t_m can be determined by integrating the activity of the radionuclide of interest, considering the decay time t_D between the EOB and the beginning of the measurement:

$$\Delta N = N_t N_b \sigma \frac{1}{\lambda}\left(1 - e^{-\lambda t_{irr}}\right) e^{-\lambda t_D}\left(1 - e^{-\lambda t_m}\right) \tag{3.8}$$

The activity of the radionuclides of interest can be determined by detecting the emitted radiation (α, β, γ and X); in this work I have measured γ-emitting radionuclides by using a High Purity Germanium (HPGe) detector. The counts ΔC in the net peak area registered by the detector are given by:

$$\Delta C = \varepsilon_d I \, \Delta N \tag{3.9}$$

where ε_d is the detector efficiency, I is the intensity of the γ-ray considered (usually given as number of γ photons yielded normalized per 100 decays), ΔN the number of decay occurred during the measuring time. Usually, the measuring system automatically corrects the net area for the detector dead time (the minimum time interval that two consecutive counts must be separated in order to be recorded as two different events), providing the real time (t_r) and the live time (t_l) of the measurement.

From the above equations the cross section σ [cm^2] can be expressed as:

$$\sigma = \frac{\Delta C \, \lambda}{\varepsilon_d I N_t N_b (1-e^{-\lambda t_{irr}}) e^{-\lambda t_D} (1-e^{-\lambda t_r})} \tag{3.10}$$

The cross section $\sigma(E)$ is a function of the energy and for this reason, it is necessary to determine the correct energy to associate to the target foil considered. The energy E is calculated as the average of the incoming (E_{IN}) and outcoming (E_{OUT}) particle energy, $E = \frac{(E_{IN}+E_{OUT})}{2}$, if the cross section changing (approximately) linearly in the E_{IN}-E_{OUT} energy interval. In order to experimentally evaluate the cross section $\sigma(E)$ for a given nuclear reaction, it is necessary to irradiate a thin target foil with a well-characterized particle beam. When the energy loss inside the target is negligible compare to the beam energy (i.e. $\Delta E/E \sim 0.01 - 0.05$) [40], it is possible to use the expression "thin target". In the case of a thin target, the energy loss is negligible and can be assumed $\sigma(E_{IN}) = \sigma(E_{OUT}) = \sigma(E)$.

In the real-case, in order to determine the proton energy in each foil, the *Stopping and Range of Ions in Matter* (SRIM[4]) software [41] can be used. The SRIM code bases the calculations of the energy loss of the ions in the matter on the well-known Bethe-Bloch formula and related corrections, especially at low energy (Appendix C). SRIM code provides tables of stopping power values, ranges, and straggling distributions for any projectile ion at any energy in any target material. This software can also have a multi-

[4] The software SRIM is available at www.srim.org

layer target configuration input and allows to associate the two energies, E_{IN} and E_{OUT}, to each layer.

The cross section is calculated by integrating with respect to the measuring and irradiation time the equation 3.10, that can be also written as:

$$\sigma = \frac{Act_{EOIB} \cdot A}{N_b \cdot N_A \cdot \rho \cdot P \cdot x} \tag{3.11}$$

where the activity at the End Of Instantaneous Bombardment [42] is defined as:

$$Act_{EOIB} = \frac{C}{\varepsilon_d(E_\gamma) I(E_\gamma) t_l} \cdot e^{\lambda t_D} \cdot \left(\frac{\lambda t_{irr}}{1 - e^{-\lambda t_{irr}}}\right)\left(\frac{\lambda t_r}{1 - e^{-\lambda t_r}}\right) =$$

$$= Act_{meas} \cdot e^{\lambda t_D} \cdot \left(\frac{\lambda t_{irr}}{1-e^{-\lambda t_{irr}}}\right)\left(\frac{\lambda t_r}{1-e^{-\lambda t_r}}\right) \tag{3.12}$$

The previous formula shows that the activity measured (Act_{meas}) depends on the net photopeak at the energy E (numbers of counts C) measured by the HPGe detector, the detector efficiency $\varepsilon_d(E_\gamma)$, the intensity $I(E_\gamma)$ of the γ-emission at the energy E_γ and the live time t_l of the measurement. In the case of radionuclides with two or more γ-lines without interference, with the aim to reduce the error associated, the Act_{meas} is calculated considering a weighted mean value by using the following equations [43]:

$$Act^*_{meas} = \frac{\sum_i Act_i/\Delta(Act)_i^2}{\sum_i 1/\Delta(Act)_i^2} \qquad \Delta(Act^*_{meas}) = \sqrt{\frac{1}{\sum_i 1/\Delta(Act)_i^2}} \tag{3.13}$$

The uncertainty $\Delta(Act)_i$ is calculated with the quadratic sum formula since all parameters are independent $\left(\frac{\Delta Act_i}{Act_i}\right)^2 = \sum_q \left(\frac{\Delta q_x}{q_x}\right)^2$ where q are the parameters (C, ε, I, t_l).

Once the activity Act_{EOIB} is determined and the characteristics of the target (ρ, P and x) and the incident beam flux (N_b) are known, it is possible to calculate the cross section by applying the equation 3.10. If it is not possible to know the incident beam flux with high precision, the cross section of interest is calculated by using a well-known nuclear reaction $\sigma'(E')$ evaluated and recommended by the IAEA [44] [45]. In this case, it is necessary to irradiate a multi-layer target with at least two foils (one target and one monitor foil), assuming that the beam flux is the same in both layers. I have always used this strategy in the experiments performed: at least one monitor foil was always associated to each irradiated target foil; when possible, two monitor foils were used.

The cross section of the radionuclide of interest, as a function of energy, is then calculated by the following equation (the superscript is used to indicate what concerns the monitor foils):

$$\sigma(E) = \sigma'(E)\frac{Act_{EOIB}\ A\ \rho'\ P'\ x'\ \lambda'}{Act'_{EOIB}\ A'\ \rho\ P\ x\ \lambda} \tag{3.14}$$

The previous equation, as proposed by Otuka et al. [46], can also be written as

$$\sigma_x = \sigma_r \frac{C_x\ N_r\ \varepsilon_r\ I_r\ f_r}{C_r\ N_x\ \varepsilon_x\ I_x\ f_x} \tag{3.15}$$

where the subscripts *x* and *r* are used to indicate what concerns the radionuclide of interest and monitor reaction respectively. The time factor f is equal to

$$f = \left(1 - e^{-\lambda t_{irr}}\right)e^{-\lambda t_D}\left(1 - e^{-\lambda t_r}\right)/\lambda \tag{3.16}$$

and *N* is the number of atoms in the target per area (as previously indicated N_t).

The uncertainty in $\Delta\sigma_x$ is calculated with the quadratic sum formula if all parameters are independent:

$$\left(\frac{\Delta\sigma_x}{\sigma_x}\right)^2 = \sum_q \left(\frac{\Delta q_x}{q_x}\right)^2 + \sum_q \left(\frac{\Delta q_r}{q_r}\right)^2 + \left(\frac{\Delta\sigma_r}{\sigma_r}\right)^2 \tag{3.17}$$

where q are the parameters (*C, n, ε, I, f*) [46].

The time factor f contains five sources of uncertainties: $t_{irr}, t_D, t_r, \lambda_r$ and λ_x. Even if the uncertainties in t_{irr}, t_D and t_r are considered negligible, it is not possible to include the uncertainties in λ_r and λ_x by using the standard quadratic sum formula because the decay constant is related to the cross section through the exponential function. For this reason, the uncertainty in the time factors should be propagated from the uncertainties in the decay constants calculated with the following equations [46]:

$$\left(\frac{\Delta f}{f}\right)^2 = S_{f\lambda}^2\left(\frac{\Delta\lambda}{\lambda}\right)^2$$

$$S_{f\lambda} = \frac{\lambda}{f}\frac{\partial f}{\partial\lambda} = \left(\frac{\lambda t_{irr}e^{-\lambda t_{irr}}}{1-e^{-\lambda t_{irr}}} - \lambda t_D + \frac{\lambda t_r e^{-\lambda t_r}}{1-e^{-\lambda t_r}} - 1\right) \tag{3.18}$$

$$\Delta\lambda = (ln2 \cdot \Delta\tau_{1/2})/\tau_{1/2}^2$$

The uncertainties of the half-lives can be obtained from the NuDat database [7].

3.3 Saturation factor and thick target yield

By using thin targets, the flux and energy of the projectiles' beam do not change significantly during passage through them. Instead, in a thick target, the projectile energy changes considerably and it is more complicated to calculate the activity produced since the variation of energy with the target thickness and the variation of cross section with the energy must be also considered. Indeed, the total activity of a given radionuclide produced with a proton beam on thick target at the End of Bombardment (Y_{EOB}), which also depends on the irradiation time, is calculated considering the following formula reported in the IAEA Technical report [47]:

$$Y_{EOB} = \frac{N_A N_b}{A_T}\left(1 - e^{-\lambda t_{irr}}\right)\int_{E_e}^{E_i} \sigma_T(E)\frac{dE}{S_T(E)} \tag{3.19}$$

where:

- Y_{EOB} is the thick target Yield (Y) at the End of Bombardment (EOB);
- A_T is the atomic weight of the target material [g];
- $S_T(E)$ is the stopping power of the particle beam through the target material at the energy E, usually expressed as dE/dx.

The term $\left(1 - e^{-\lambda t_{irr}}\right)$ is called saturation factor (SF) and takes into account both the production of nuclei due to the nuclear reaction considered and the decay of the nuclei that have been already produced. The SF limits the practical production of a given radionuclide, which is determined by its half-life $\tau_{1/2}$ ($\tau_{1/2} = \ln 2/\lambda$). The SF dependence on irradiation time, expressed in terms of the half-life $\tau_{1/2}$, is shown in Figure 9.

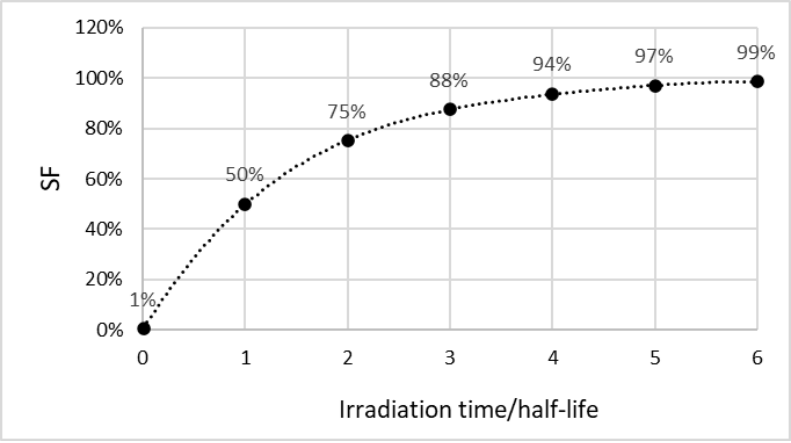

Figure 9: Saturation Factor dependence on irradiation time, expressed in terms of half-lives

Figure 9 shows that for an irradiation time of one half-life (t = $T_{1/2}$), it is possible to obtain 50% of the saturation yield, that is half of the maximum radionuclide production achievable from that target; for a 2 half-lives irradiation (t = $2T_{1/2}$), one obtains 75%, and so on. For an infinitely long irradiation time the number of radionuclides produced equals the number of nuclides decaying:

$$SF = \lim_{t_{irr}\to\infty}\left(1 - e^{-\lambda t_{irr}}\right) = 1 \tag{3.20}$$

For practical reasons, irradiations rarely exceed three half-lives (a saturation of about 90%), except for the shortest lived radioisotopes for which it is possible to achieve saturation with short irradiation times. An example for that is the production of the ^{15}O (half-life of about 2.04 minutes) through the $^{16}O(p,pn)^{15}O$ nuclear reaction by using a SMC. The short half-life of ^{15}O allows reaching saturation in about 13 minutes.

Thick targets are used for the production of a large amount of the activity of the desired radionuclide by exploiting the production cross section in a wide energy range. In order to use the activity produced in the preclinical and clinical applications, it is necessary to respect the legislative prescriptions. For this reason, the product obtained must be characterized by evaluating:

- The Specific Activity A_s [Bq/g], or the activity concentration for a given radionuclide at time t, is by definition the activity of the radioisotope ^{k}X divided by the cumulative mass of all radioactive and stable isotopes ^{i}X (if yielded or already present) which are isotopic with the element X involved :

$$A_s(t)_{k_X} = \frac{A_{k_X}(t)}{\left[\frac{\sum_i N_{i_X}(t)}{NA}\right]\cdot A} \tag{3.21}$$

  where N_A is the Avogadro constant [1/mol], A is the mass number [g/mol].

- The Radio Nuclidic Purity (RNP) is the percentage ratio, versus time, between the activity of radionuclide ^{k}X and the entire radioactivity of all radionuclides ^{i}X (including ^{k}X) isotopic with element X:

$$RNP_X(t) = \frac{A_{k_X}(t)}{\sum_i A_{i_X}(t)} \cdot 100 \tag{3.22}$$

  RNP is important in radiopharmacy since any radionuclidic impurities may increase the radiation dose increase imparted by the patient and may also give rise to a degradation of the quality of any imaging procedure performed;

- The Isotopic Purity (*IP*) is the percentage ratio, versus time, between the number of ^{k}X radionuclides available versus all the isotopes (both radioactive and stable) isotopic with element X:

$$IP_X(t) = \frac{N_{k_X}(t)}{\sum_i N_{i_X}(t)} \cdot 100 \tag{3.23}$$

4 – THE LARAMED PROJECT

The Legnaro National Laboratory (LNL) is one of the four major research centers of the Italian National Institute for Nuclear Physics (INFN). The main researches carried out at LNL are in the field of fundamental nuclear physics and nuclear astrophysics. The SPES project (Selective Production of Exotic Species) is one of the main initiatives of the LNL with the purpose to provide high intensity and high-quality beams of neutron rich nuclei to perform basic research in nuclear structure and reaction dynamics as well as to interdisciplinary applications, ranging from the production of radionuclides of medical interest to the generation of neutrons for material studies, thanks to the recent installation of a new 70p cyclotron. In the framework of the SPES project, LARAMED (LAboratory of RAdioisotopes for MEDicine) is an award-winning government-funded (MIUR) interdisciplinary project granted within the so-called PREMIUM PROJECTS 2012. The goals of this project include research on different fields: from both theoretical and experimental nuclear physics activities to radiochemistry aspects, technical R&D on mechanical engineering and materials science, up to issues close to nuclear medicine.

The presence of the new proton-cyclotron at LNL will have a strong influence on the research programs that will be carried out in the next coming years by the LARAMED group. This explains why the ongoing research is focused on medical radioisotopes production by using only proton beams. For this reason, in parallel with the scientific research, the whole group constantly follows all the infrastructure constructions currently underway (realization of dedicated bunkers, laboratories, etc.), the purchase and installation of the beam lines, the hot-cells, and all the equipment necessary to carry out the experiments. This chapter, then, presents the context in which my Ph.D. research activities have been carried out and reports the work, still in progress, conducted by me and the LARAMED group in order to start the facility operations at LNL as soon as possible.

4.1 The Legnaro National Laboratory and the SPES facility

The core of the SPES project is the model 70p cyclotron installed at LNL in May 2015 (Figure 10), manufactured by BEST^{TM} Theratronics (Canada). It is a dual-beam operational cyclotron, with the proton beam energy tunable in the range 70-35 MeV and with high output current (up to 750 μA). The maximum allowed beam current at any of the two exit ports has been fixed at 500 μA for Radiation Protection (RP) issue. The cyclotron is positioned in the central bunker at the underground floor of the SPES building (Figure 11).

Figure 10: The new high-energy (35-70 MeV) and high-current (up to 750 μA) proton-beam cyclotron installed at INFN-LNL (Legnaro, Padua, Italy)

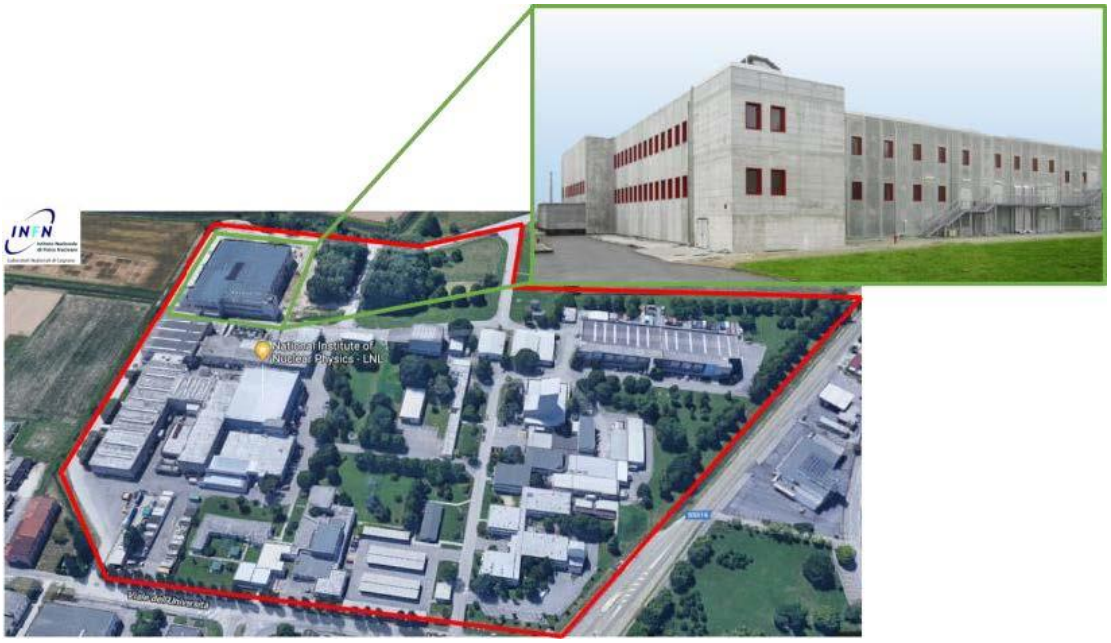

Figure 11: Areal view of INFN-LNL (left) and a zoom on the SPES building (right).

The SPES project has been organized into four operative stages that are shortly summarized as follows:

- SPES-α: This stage, close to its completion, involves the acquisition, installation, and commissioning of the high-performance cyclotron with high output current (0.75 mA) and high energy (from 35 up to 70 MeV), together with the related infrastructure for the accelerator and experimental stations. One of the two beams will be devoted to the ISOL facility, producing mainly neutron-rich Radioactive Ion Beams (RIBs) from a Uranium Carbide target [48]; the second will be dedicated to applied physics;
- SPES-β: This stage comprises the production of radioactive ion beams that, once selected with the high-resolution mass spectrometer, will be re-accelerated into the ALPI superconducting linac, already operative since the end of ’90, to collide onto specific targets for studies in nuclear physics and astrophysics;
- SPES-γ: The goal is to evaluate the accelerator-based production of emerging radionuclides to produce innovative radiopharmaceutical both for LARAMED (LAboratory for the production of RAdioisotopes of MEDical interest) [49] and ISOLPHARM (ISOL technique for radioPHARMaceuticals) projects [50].
- SPES-δ: This long-term stage aims at the development of an intense neutron source copying the atmospherics spectrum (due to the interaction of high-energy cosmic rays with the atmosphere), up to 70 MeV. It will be dedicated to multidisciplinary studies, such as Single Event Effects (SEE) studies on electronics/detectors for high-energy physics apparatuses, aerospace industry nuclear astrophysics, characterization of nuclear waste [51] [52].

Figure 12 shows the layout of the SPES building [49] at the underground level, where the cyclotron is placed in the center of the floor. The double extraction system is further split by two switching magnets into additional sub-lines carrying the proton beams in bunkers dedicated to different research activities. The area is divided into two separate parts: the LARAMED section (highlighted in blue), comprising four irradiation bunkers (RI#1, RI#2, RI#3 and A9c) dedicated to radioisotopes research/production activities, and the SPES bunkers (highlighted in gray), dedicated to the production of neutron-rich unstable nuclei for research in fundamental nuclear physics and radioisotopes production using the ISOL technique.

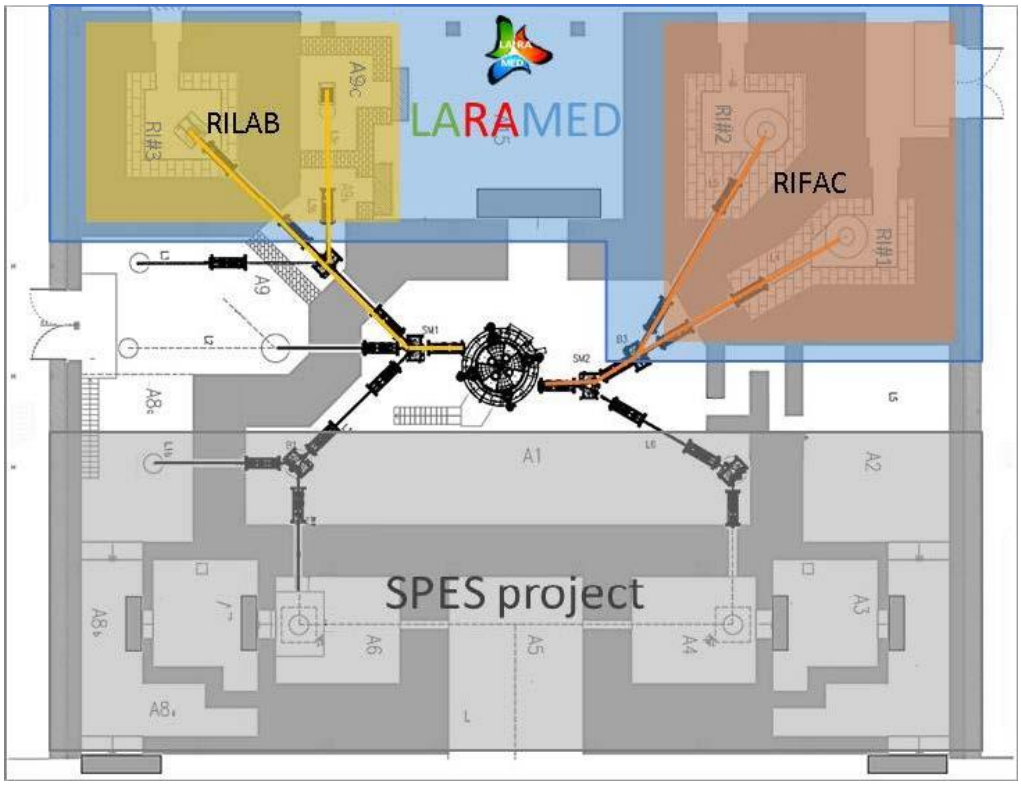

Figure 12: The layout of the SPES building (underground level) showing the cyclotron with outward beam lines. The LARAMED section (highlighted in blue) is divided into two separate sections: The RadIoisotopes LABoratory (RILAB) and the RadioIsotope FACtory (RIFAC). The exit beamlines of SPES bunkers (highlighted in gray) will be connected to the existing ALPI-PIAVE accelerators

4.2 The LARAMED facility

The main focus of the LARAMED project [49] is the study and development of efficient methods for the production of medical radionuclides, by using the high-beam-current and high-energy cyclotron recently installed at LNL. To achieve these goals, as shown in Figure 12, four bunkers (RI#1, RI#2, RI#3, and A9c) were assigned to the project. The LARAMED facility is dived into two separate sections: The RadioIsotope FACtory (RIFAC), comprising RI#1 and RI#2 bunkers, and the RadIoisotopes LABoratory (RILAB), comprising RI#3 and A9c bunkers. The RIFAC laboratory will be used, after an agreement with a private company, to produce massive amounts of radioisotopes to be distributed to hospitals. In the RILAB section, the RI#3 bunker will be used to produce limited amounts of novel radioisotopes for research purposes (i.e. support other research centers, as well as research studies at preclinical level) by using high-current

proton beam while the A9c bunker will be used for experimental nuclear physics activities (i.e. mainly cross-section measurements) by using a maximum current of 100 nA (Table 10).

At the time being, the RILAB is under completion and the current status is summarized below:

- the RI#3 bunker infrastructure completed. The walls are 4 meters thick to guarantee safety outside the bunker from a radioprotection (RP) point of view. Surface finishing work underway on the internal bunker walls;
- the beamline for RI#3 bunker is purchased and next to be fully installed;
- the civil construction for the A9c bunker completed, as shown in Figure 13. The walls and the roof are 1 meter thick to guarantee safety outside the bunker from a radioprotection point of view. Surface finishing work underway on the internal bunker walls;
- the beamline for A9c bunker is next to be purchased;
- the final part of the beamline, with a double Kapton foil septum for safety reasons, in order to have an extracted proton beam devoted to cross section measurements (100 nA), already designed;
- the target station for cross section measurements has been already designed at LNL and built, ready to be installed;
- the beam-dump for A9c bunker is in an advanced design phase;
- the walls of both bunkers must be covered with a special paint to reduce dust that could be activated with the start of the research activity;
- all shielding doors are next to be purchased.

Figure 13: Civil works in progress for the A9c bunker previous the installation of the roof (may 2019) and completion of the whole structure (late summer 2019)

The main features of the proton beams planned for each of the four beamlines of the LARAMED facility are listed in Table 10.

Table 10: Proton-beam characteristics of the four LARAMED beamlines.

	RIFAC		**RILAB**	
Bunkers	RI#1	RI#2	RI#3	A9c
Expected current	500 µA	500 µA	300 µA	100 nA
Expected energy	35-70 MeV	35-70 MeV	35-70 MeV	35-70 MeV

My role in the facility design process has been to fix the main specifications expected for the beam dump and target station in the A9c bunker, with all the supporting systems for their operation (electrical power, gas, and cooling water circuits). The L3c is dedicated to nuclear physics experiments (e.g. cross section measurements). The

limitation to a maximum current of 100 nA is necessary to observe the regulation imposed by the LNL RP unit, considering the thickness of the bunker's walls (1 meter in A9c instead of 4 meters in the RI#3 bunker). During my Ph.D. I was charged to constantly follow the progress of the civil works, plus plant installations, thanks to periodic meetings with the LNL technical services responsible for the construction of the infrastructure, the necessary services, the installation of the beam-lines and the rRP service.

To carry out research and development of efficient methods to produce medical radionuclides, in addition to the dedicated bunkers, it is necessary to have a laboratory for the targets manufacturing and a compound dedicated to the radiochemical separation and characterization of the obtained product. Figure 14 reports a schematic summary layout of the LARAMED laboratories on the second floor of the SPES building [49].

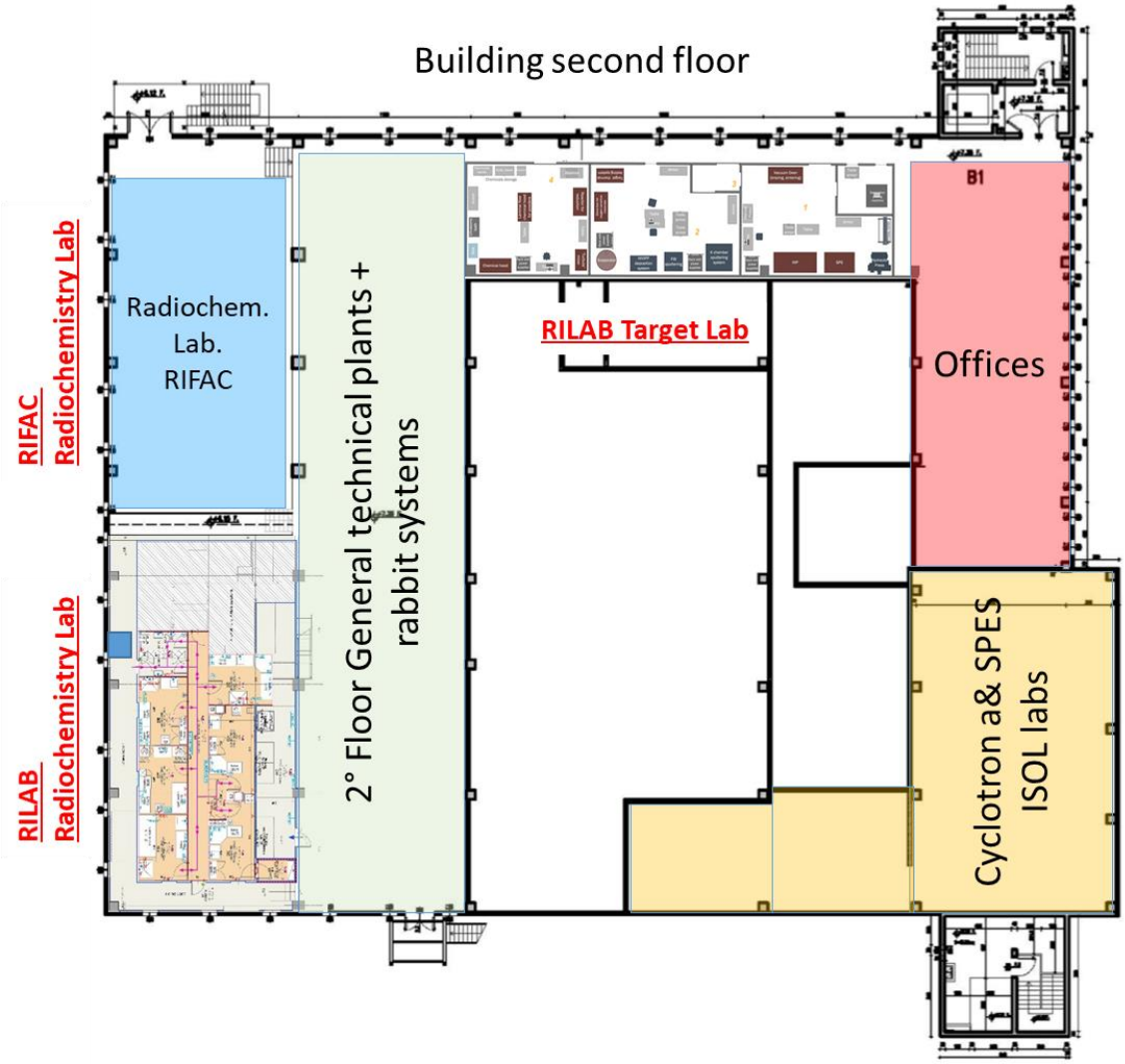

Figure 14: Layout of the LARAMED laboratories at the second floor of the SPES building

As shown in Figure 14, the LARAMED laboratories include:

- the **RIFAC Laboratory** for radioisotopes/radiopharmaceutical production, currently not designed yet;
- the **RILAB Target Laboratory**, designed for manufacturing solid targets, exploiting standard as well as unconventional techniques that will be developed, that will be irradiated in the RI#3 and A9c bunkers at the underground level, for both nuclear physics and medical radioisotopes production purposes;
- the **RILAB Radiochemistry Laboratory** designed for R&D activities on the processing of the irradiated targets, separation, purification, and chemical and physical quality controls of the final product. In this laboratory, it will be possible to carry out these research activities because its layout and infrastructure are suitable for managing radioactive materials. RILAB Laboratories will be equipped with HVAC system (Heating, Ventilation and Air Conditioning) designed to avoid the dispersion of radioactive material, as well as with electrical, gas, water supplies, and the necessary radiological and environmental protection system.

The realization of the RILAB Radiochemistry Laboratory has actively involved me for some years in the decisions taken concerning the realization of the whole compound, with particular attention to the gamma and beta spectroscopy laboratory. I contributed to define the instrumentation necessary to allow the operation of a laboratory with the aim to get a full characterization of the radioisotopes produced. The main instruments that will be present in the spectroscopy laboratory will be two HPGe detectors, shielded with 10 cm of lead, with an electrically cooled cryostat. I personally wrote the technical specifications and followed the whole process of their purchase. The acceptance test phase of the instrumentation was carried out in December 2017 followed by a consequent familiarization of the efficiency and energy calibration procedures with the related software. The laboratory is also designed to host a detector dedicated to β-spectroscopy, and, one to perform alpha spectrometry as well.

A hot-cell, with lead shielding, for radioisotope manipulation with high activity levels and related radiochemistry is already installed in the RILAB radiochemistry laboratory. The hot-cell is equipped both with telemanipulators (Figure 15-A) and with manual manipulation, supplied with the black protective gloves (Figure 15-B). The back of the cell is very bulky (Figure 15-C) and this makes it clear the importance of a correct

evaluation and design of the entire compound. In fact, adequate space must be provided for this encumbrance outside the compound, as well as for a comfortable maneuvering space for the maintenance activities that will take place at the back of the cell. In June 2019, me and the LARAMED group that will be involved in the practical work in the compound following the course to be trained in the use of the cell, as shown in Figure 15-D.

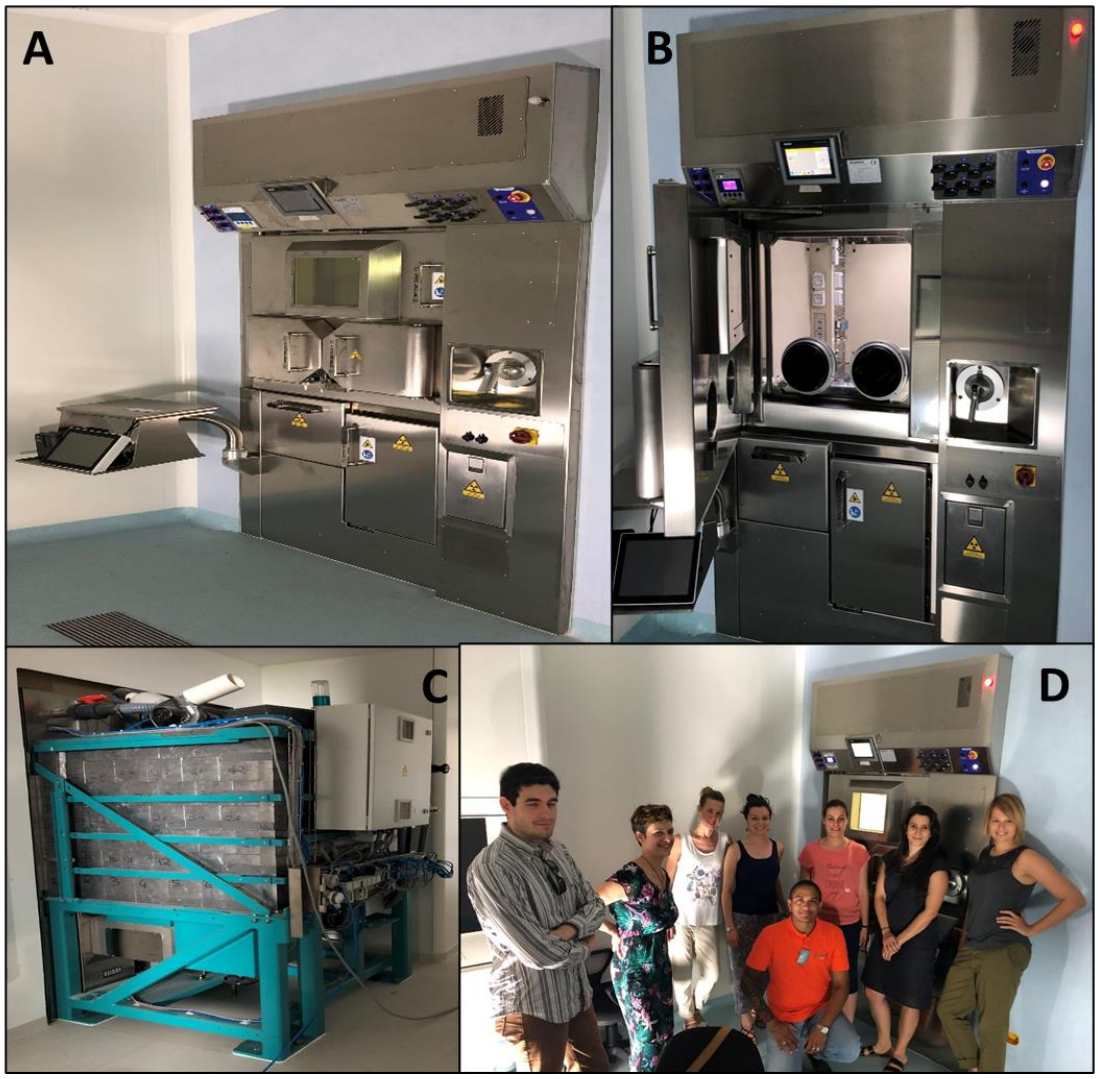

Figure 15: The hot-cell for radioisotope manipulation installed in the RILAB laboratory

4.3 The LARAMED project

As mentioned before, the aim of the LARAMED project will be entirely focused on the utilization of the high performance BEST 70p cyclotron, to study unexplored production routes and the technological development for the production of novel radionuclides useful in nuclear medicine [49]. As already described in the previous paragraph, since the infrastructures and laboratory facilities are not yet completed, some research lines were carried out, or are still underway, in collaboration with several laboratories or hospitals in Italy and abroad. Thanks to this strategy, it was possible to start the LARAMED program by working on cyclotron production of conventional and emerging radionuclides with several projects, listed in Table 11. Except for the APOTEMA project, I was involved in all other research activities listed in Table 11. The approach of the LARAMED team to the data analysis, and in particular for the cross section measurements, requires at least two persons that perform independently the analysis of the same data and, at the end, a comparison of results obtained. In this way, eventual discrepancies can be checked by at least two researchers and, at the end of the process, discussed with the entire LARAMED team in a dedicated meeting. This method was always applied for the results described in my Ph.D. thesis, carried out by me and in close collaboration with G. Pupillo.

Table 11: List of past and running LARAMED's satellite projects

Project name	INFN already funded/running projects
APOTEMA (2012-2014) TECHNOSP (2015-2017)	Accelerator-**Tc-99m** alternative (direct) production route through hospital cyclotrons
COME (2016)	COpper MEasurement (**Cu-67**)
PASTA (2017-2018)	Production with Accelerator of **Sc-47** for Theranostic Applications
TERABIO (2016-2019)	High Power **Target** concepts R&D ($^{64/67}$Cu)
E_PLATE (2018-2019)	High intensity vibrational powder plating (**Target**)
METRICS (2018-2020)	Multimodal pET/mRi Imaging with Cyclotron-produced **Mn-52/51** and stable paramagnetic Mn iSotopes

The goals and main characteristics of each project are briefly reported below.

4.3.1 APOTEMA and TECHN-OSP

Technetium-99m (^{99m}Tc; $t_{½}$ =6h, E_{γ}=140 keV) was the first radionuclide investigated in the framework of the LARAMED project, aimed at the study of radionuclides cyclotron production, with two INFN projects respectively named APOTEMA (Accelerator-based Production Of TEchnetium/-Molybdenum for medical Applications, funded in 2012-2014 by INFN SCN5) and TECHN-OSP (TECHNetium direct-production in hOSPital, founded in 2015-2017 by INFN CSN5).

^{99m}Tc still has a fundamental role in nuclear medicine imaging worldwide, being the most important γ-emitting medical radionuclide employed in nearly 85% of all diagnostic nuclear medicine procedures carried out every year [53]. The conventional supply chain of ^{99m}Tc is based on the β^- decay of the nuclear reactor produced ^{99}Mo ($t_{½}$=66 h). The unplanned, relatively long term, shut down of some of the few reactors authorized in the period 2009–2010 has forced the scientific community to investigate alternative production routes for ^{99m}Tc and its precursor ^{99}Mo [54] [55] [56] [6] [57]. The direct cyclotron-based production of ^{99m}Tc, already evaluated as feasible alternative since 1971 [58], is considered as potential replacement of the reactor-based technology [59] [60] [61] [62] [54] [63] [42] [56] [64].

Since to date more than 40 cyclotrons are already present in Italy [65], the idea behind the research activities carried out is to realize the technology to allow the direct production of ^{99m}Tc in every medical cyclotron, potentially in the easiest way and with automatic procedures. To achieve this goal, the following items were studied:

- Evaluation of the cross sections of the most promising nuclear reactions to produce ^{99m}Tc; in particular, the ^{100}Mo(p,2n)^{99m}Tc reaction [66] [54];
- Development of a procedure for the realization of ^{100}Mo targets to be used in hospital cyclotrons;
- Development of a chemical separation/purification process for the extraction of Tc from the Mo target [67];
- Development of a Mo recovery procedure to re-use the enriched material to produce new targets [68];
- Determination of the ^{99g}Tc/^{99m}Tc isomeric ratio and other Tc-contaminants expected in the cyclotron-produced ^{99m}Tc;
- Determination of the conformity with the European Pharmacopea as well as the radiolabeling efficiency and imaging quality [69] [70].

In addition to these items, radiopharmaceuticals and preclinical studies were performed with the cyclotron-produced ^{99m}Tc [69] [71] [72].

Its noteworthy that, following the new trends for non-HEU-based radionuclide production methods, based upon alternative, cyclotron-driven routes, the APOTEMA-TECHNOSP research activities have become part of a larger international collaborative effort under a coordinated research project (CRP F22062), launched by IAEA in 2011, the results of which have been recently issued [73].

4.3.2 COME: COpper MEasurement

The COME project, proposed in the framework of the LARAMED project at LNL in collaboration with the INFN-FE department and the ARRONAX facility (Nantes, France) [74], is focused on ^{67}Cu production. Thanks to its peculiar physicochemical characteristics, ^{67}Cu is one of the most important emerging isotopes in nuclear medicine, and for this reason, it was included by the IAEA in the Coordinated Research Project (CRP) on "Therapeutic Radiopharmaceuticals Labelled with New Radionuclides such as Astatine-211, Copper-67, Lead-212/Bismuth-212" [75] and in the recent CRP focused on the study of "^{67}Cu, ^{186}Re and ^{47}Sc as Emerging Theranostic Radionuclides" [76]. ^{67}Cu is the longest lived radionuclide of copper, with a half-life of 61.83 h and an emitting β^- and γ radiation [7]. The energy of β^- particles is appropriate for therapy (140 keV as mean energy, corresponding to about 200-300 μm range in soft tissue), while the 185 keV photons are suitable for pre-therapy low dose imaging (SPECT or SPECT/CT). These physical characteristics allow the use of ^{67}Cu for both therapy and diagnostic applications, making ^{67}Cu a promising theranostic radionuclide.

The use of ^{67}Cu is actually curtailed by its low availability: until now its production was mainly based on high-energy accelerator (200 MeV protons), by using the ^{68}Zn(p,2p)^{67}Cu and ^{68}Zn(γ,p)^{67}Cu nuclear reactions [77] [78]. Another charged-particle induced reaction is the ^{70}Zn(p,α)^{67}Cu, measured during the '90s up to 35 MeV [79] [80], but no data at higher energy are available in the international database [7]. With the COME project, it was experimentally determined the cross section of ^{70}Zn(p,x)^{67}Cu reaction in the still unexplored proton energy region 45-70 MeV.

I actively participate in all the aspects of the COME project (described in detail in the following chapter), including planning, research funding, schedule of each experiment, data analysis, meeting organization and participation, reports, and article drafting.

4.3.3 PASTA: Production with Accelerator of Sc-47 for Theranostic Applications

Scandium-47 is one of the few radionuclides, together with ^{67}Cu, that is intrinsically suitable for both therapeutic and diagnostic purposes, thanks to its β^- and γ-radiation respectively useful for therapy and to perform SPECT/CT imaging studies. The main advantage of ^{47}Sc-labelled compounds, and theranostic radionuclides in general, is the possibility to perform low-dose imaging studies prior therapy with the same radiopharmaceutical, allowing the selection of patients with a significant chance of responding to the specific treatment. The production of ^{47}Sc in enough quantities and at a reasonable cost is challenging and the worldwide increasing interest on this topic is highlighted by the recent Coordinated Research Project (CRP), promoted by the International Atomic Energy Agency (IAEA), focused on the study of "*^{67}Cu, ^{186}Re and ^{47}Sc as Emerging Theranostic Radionuclides*" [76].

The aim of the PASTA project, proposed in the framework of LARAMED at LNL in collaboration with the INFN-FE, INFN-PD, and INFN-PV departments and the ARRONAX facility, is thus answering to the increasing request of ^{47}Sc production for clinical applications. The cross sections of the most promising proton-induced nuclear reactions to produce ^{47}Sc were measured. This work allowed to select the best irradiation parameters considering the co-production of contaminant radionuclides (such as ^{46}Sc) and to study a radiochemical process for the extraction and purification of ^{47}Sc.

Also for the PASTA project (described in detail in a following chapter), I actively participate to all the aspects of the experiment, including planning, research funding, schedule of each irradiation run, data analysis, meeting organization and participation, reports and article drafting. In this case, a master thesis in nuclear physics was also carried out in collaboration with the University of Bologna (Italy) [81], regarding the cross sections measurements with ^{nat}V targets. All the experimental data I collected post the planned irradiation runs were also provided to student L. De Dominicis who wasn't part of the experimental group. I explained every detail of the experiment and I taught her how to carry out all the data analysis in complete autonomy. Thanks to this work,

at the end of the process it was possible to compare her results with mine before drafting the scientific articles.

4.3.4 TERABIO innovative technologies for radionuclide ThERApy and BIOimaging

The TERABIO project [49], funded as a special project in 2016 by the Italian Ministry of Research (MIUR), aims to research innovative technological solutions in high power target realization for radionuclides production. Taking advantage of the presence of the 70p BEST cyclotron at LNL, this technological R&D aims to study new cyclotron solid targets by using increasingly proton current to produce medical radionuclides in enough quantities for preclinical and hopefully clinical trials.

Thanks to the outcomes of the COME project in which I had an active role, it was possible to patent the idea of an optimized layout for a target aimed at ^{67}Cu production, described in the International Patent n° WO 2019/220224 A1 (November 2019). I am the first author of these patents. This layout is the ground for the future work on zinc oxide targets, composed of different layers of enriched materials, which is going to be developed at LNL.

4.3.5 E_PLATE

The E_PLATE (Electrostatic Powder pLating for Accelerator TargEts) project [82] aims to study HIgh energy VIbrational Powder Plating (HIVIPP) technique to produce isotopic target useful for nuclear physics experiments, as measurements of cross sections. The HIVIPP method [83] allows to prepare thin targets from metallic powder material with high efficiency (95-98%) and high uniformity of the deposit. It is extremely useful in the case of enriched powders, thanks to the very small losses.

I participate to all the crucial aspects of the E_PLATE project, including comments on the proposal, participation in all the common meetings, and to the specific meetings regarding the realization of the titanium targets used in the PASTA project. I also contributed to the drafting of the scientific article, currently in press [84].

4.3.6 METRICS

The METRICS (Multimodal pET/mRi Imaging with Cyclotron-produced Mn-52/51 and stable paramagnetic Mn iSotopes) project [85] aims to achieve a real matching between both PET and MRI scans acquired by using a chemically identical contrast and radioactive agent. Manganese is a transition element with paramagnetic properties useful for MRI, with two β^+ emitter isotopes (^{51}Mn and ^{52}Mn) useful for PET. The METRICS project aims to study the development and optimization of ^{52}Mn cyclotron production and proper separation and purification method. Manganese production is followed by the study of stable Mn(II)-^{52}Mn complexes, carried out in collaboration with the INFN-Fe department and the University of Ferrara.

My contribution to the METRICS project has regarded all the gamma-spectrometry acquisitions and data analysis carried out at the Sacro Cuore Don Calabria hospital (Negrar, VR, Italy) over the years 2017-2020 years. In particular, irradiation runs were carried out at increasing proton currents to verify target thermo-mechanics behaviuor and its activation (2018-2019); during the years 2019-2020, several irradiation runs were carried out to develop an efficient radiochemical process to extract Mn-radionuclides from the ^{nat}Cr bulk. I scheduled all the data acquisition in collaboration with the staff of the hospital and I was charged for all data analysis. The experiments on radiochemistry are still underway.

5 THE COME PROJECT: ^{67}Cu PRODUCTION

The aim of the COME project (COpper MEasurement) is the measurements of the nuclear cross section to produce of ^{67}Cu by using proton accelerators. ^{67}Cu is part of a small number of radionuclides, listed in Table 2, that are of interest in theranostics thanks to their physical characteristics. Among them, ^{67}Cu is under the spotlight of the international community, as highlighted by the IAEA Coordinated Research Project (CRP) on "Therapeutic Radiopharmaceuticals Labelled with New Emerging Radionuclides (^{67}Cu, ^{186}Re, ^{47}Sc)" (IAEA CRP No. F22053), that started in 2016, in which I actively participated thanks to the research work carried out in this thesis on ^{67}Cu production. ^{67}Cu, with a 2.6 d half-life, is the longest-lived radioisotope of Cu. It is a very attractive theranostic radionuclide [21] [86] because it is a pure β^- emitter with also photon emission (Table 12). The medical interest is due to its long half-life, (suitable for imaging in vivo slow pharmacokinetics [21]), medium energy β^-emissions, significant biological roles in vivo and relatively easy labelling chemistry [22]. Moreover, the 185-keV γ-ray allows SPECT imaging of the uptake and biodistribution of the agent both before and during the therapy administration.

Table 12: Decay characteristics of ^{67}Cu as reported in NuDat database 2.7 (NNDC) [7]

^{67}Cu (half-life 61.83 h *12*)			
γ-radiation		**β^--radiation**	
Energy (keV)	Intensity (%)	End-point energy (keV)	Intensity (%)
91.266 *5*	7.00 % *10*	168.2 *15*	1.10 % *11*
93.311 *5*	16.10 % *20*	377.1 *15*	57 % *6*
184.577 *10*	48.7 % *3*	468.4 *15*	22.0 % *22*
208.951 *10*	0.115 % *5*	561.7 *15*	20.0 % *20*
300.219 *10*	0.797 % *11*		
393.529 *10*	0.220 % *8*		

^{67}Cu can also be paired with ^{64}Cu (12.7 h half-life and β^+ emitter [7]) to perform pretherapy biodistribution determinations and dosimetry using PET systems.

Production techniques for ^{64}Cu are well known and are usually based on the ^{64}Ni(p,n)^{64}Cu and ^{64}Ni(d,2n)^{64}Cu reactions [87]. Instead, the use of ^{67}Cu has been prevented by a lack of regular availability of sufficient quantities for preclinical and clinical studies. The investigation of ^{67}Cu production is, therefore, a crucial point. The production methods of ^{67}Cu are listed in Table 13.

Table 13: Production methods of ^{67}Cu [22]

^{67}Cu (half-life 61.83 h *12*)
Production method
^{67}Zn(n,p)^{67}Cu
^{70}Zn(d,αn) ^{67}Cu
^{64}Ni(α,p) ^{67}Cu
^{68}Zn(p,x) ^{67}Cu
^{70}Zn(p,α) ^{67}Cu
^{68}Zn(γ,p) ^{67}Cu

As described in the previous chapter, a new proton-beam cyclotron is present at LNL and for this reason, our research is focused on nuclear reactions induced by protons with a maximum energy of 70 MeV. As shown in Table 13, for our purposes I could investigate two different nuclear reactions by using enriched metal targets of ^{68}Zn and ^{70}Zn.

In the EXFOR database [88] all the measured and the evaluated cross sections are available. Looking at the ^{68}Zn(p,2p)^{67}Cu reaction (Figure 16), I found that it has been investigated since the 1950s. The ^{68}Zn(p,2p)^{67}Cu reaction has been evaluated by the IAEA in a Nuclear Data Section, where experts select the most reliable cross-section and decay data (Figure 17). From the selected data, in September 2008, the recommended cross-section value in the form of excitation functions was derived, according to the procedure described by F. T. Tárkányi et al. [89]. Consequently, publications after 2008 were not considered in the IAEA evaluation: for this reason, the data published also by me in G. Pupillo et al. (2018) [90] [91] are not included. Figure 16 and Figure 17 show the reaction on ^{68}Zn target, which reaches a maximum cross section value of about 10 mb at about 70 MeV.

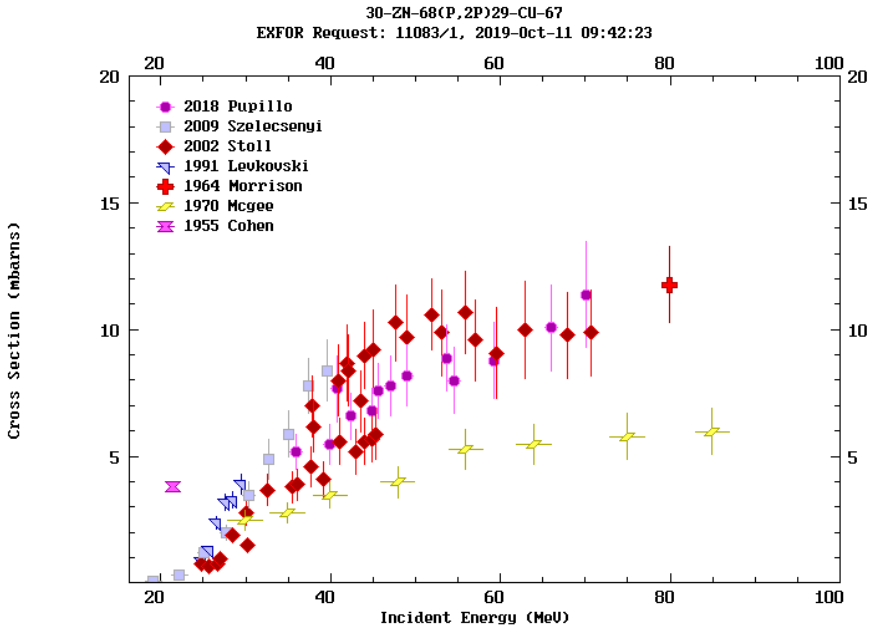

Figure 16: Data present in the EXFOR database for the nuclear reaction $^{68}Zn(p,2p)^{67}Cu$ [88]

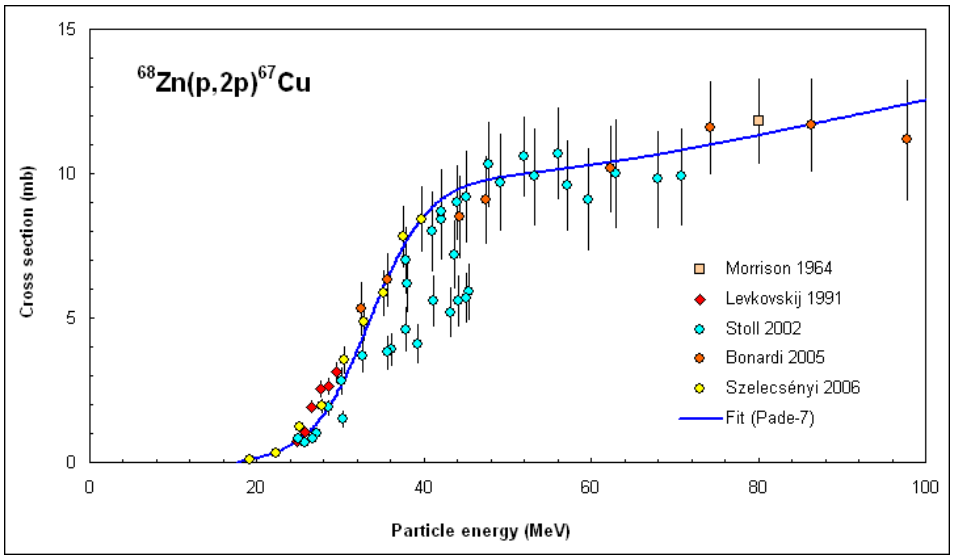

Figure 17: IAEA recommended cross sections for the $^{68}Zn(p,2p)^{67}Cu$ reaction [92]

The $^{68}Zn(p,2p)^{67}Cu$ reaction has a maximum cross section of about 10 mb, which does not easily allow for large-scale production. The challenge is to find an alternative nuclear reaction that makes the ^{67}Cu production feasible, in order to satisfy the request and hopefully to start large-scale pre-clinical tests.

The second interesting nuclear reaction for the cyclotron-based production of ^{67}Cu is the $^{70}Zn(p,\alpha)^{67}Cu$, measured up to 35 MeV (Figure 18) by V.N. Levkovskij (1991) and S. Kastleiner et al. (1999) so far [79] [80]. The $^{70}Zn(p,\alpha)^{67}Cu$ reaction has a maximum

cross section value of 15 mb at about 15 MeV but no data regarding energies higher than 35 MeV are available on the EXFOR database [88]. Considering the maximum energy available by using compact cyclotrons, as the one installed at INFN-LNL [52], the COME project aimed to measure the $^{70}Zn(p,x)^{67}Cu$ nuclear reaction up to 70 MeV, since at E_p > 35 MeV other ^{67}Cu production reaction channels are possible besides the highlighted (p,α) reaction (Table 15).

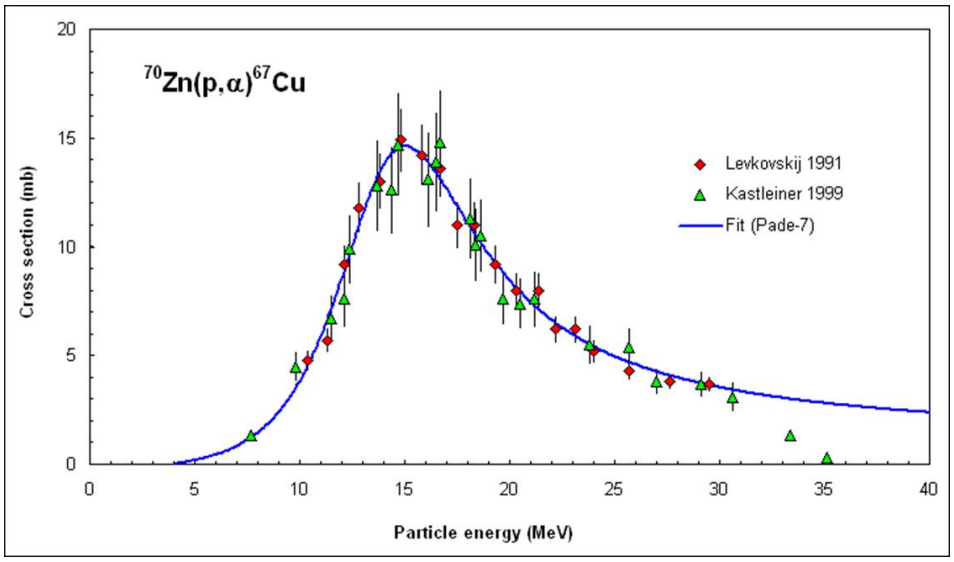

Figure 18: IAEA evaluation of the $^{70}Zn(p,\alpha)^{67}Cu$ reaction up to 35 MeV [93]

I actively participated to the COME project since its conceiving and drafting of the scientific proposal to INFN committee. I contributed to define the experiment plan, dividing the work into several steps, as listed below:

- literature study on ^{67}Cu production;
- identification of experimental problems (e.g co-production of the ^{67}Ga radionuclide, which presents the same gamma-lines as ^{67}Cu);
- purchase of enriched material (^{70}Zn) and thin monitor foils (^{nat}Al);
- design of the collimator and target-holder suitable for the beam-line used;
- study of the radiochemical procedure to separate Cu-isotopes from Ga-isotopes;
- planning and realization of the irradiation runs at different energies of the proton beam;
- dissolution and subsequent radiochemical separation of each irradiated ^{70}Zn and ^{nat}Al foils in collaboration with Dr. Martini;
- spectroscopy measurements of each solution obtained before and after the radiochemical process;

- data analysis carried out independently both by me and by Dr. Pupillo, to obtain the ^{67}Cu production cross section values for different proton beam energies.

5.1 Evaluation of the ^{70}Zn(p,x)^{67}Cu Reaction

Since there are no data for the ^{70}Zn(p,x)^{67}Cu reaction at energies higher than 35 MeV where, due to the higher proton energy, other production channels open in addition to (p,α), it was initially consulted the Q-calc tool of the NNDC website to know the Q-value and the threshold of all possible reactions on ^{70}Zn. In the case of production for medical use, Cu-isotopes produced in the ^{70}Zn(p,x) reaction, can be (in theory) separated from all the different chemical elements with an appropriate radiochemical separation and purification procedure. In general, if the purpose of an irradiation is to measure the cross sections and each element of interest produced is easily identifiable with γ-spectroscopy measurements, a chemical separation is not necessary. The case of the reaction under study is similar to the ^{68}Zn(p,2p)^{67}Cu reaction, whose measurement was published in 2018 [91]. Thanks to the previous work, it was already known that, among the variety of radionuclides produced during the bombardment of a zinc target, the ^{67}Ga (half-life 3.2617 d) is particularly relevant: it presents the same γ-lines of ^{67}Cu, since they both decay into ^{67}Zn (Table 14) [94]. Moreover, they have a similar half-life, and therefore it is not possible to infer the precise activity of one radionuclide waiting for the decay of the other one. For these reasons, a radiochemical procedure aimed at the separation of copper from gallium elements is necessary to carry out cross section studies on ^{67}Cu production. The COME project was scheduled in order to measure also the cross section of the ^{64}Cu co-produced. This result is possible by using an enriched ^{63}Cu foil instead of a ^{nat}Cu foil to be used during the following separation process as a source of the tracer radionuclide of copper-isotopes, ^{61}Cu. The COME experiments were not planned with the aim to measure all the produced radionuclides, but only the isotopes of interest: ^{67}Cu, ^{64}Cu (to optimize ^{67}Cu production), ^{67}Ga, ^{66}Ga (to avoid γ-interferences), ^{65}Zn (to estimate the activation of enriched material in view of a future recovery and reuse). The whole experimental details are described hereafter.

Table 14: ^{67}Cu and ^{67}Ga γ-emission lines [94]

γ radiation	**^{67}Cu ($T_{1/2}$=61.83 h)**	**^{67}Ga ($T_{1/2}$=3.2617 d)**
Energy (keV)	Intensity (%)	Intensity (%)
91.266	7.00	3.11
93.311	16.10	38.81
184.577	48.7	21.410
208.951	0.115	2.460
300.219	0.797	16.64
393.529	0.220	4.56

Table 15 reports the Q-value and the threshold energies for the isotopes of copper and gallium produced in the ^{70}Zn(p,x) reactions.

Table 15: Threshold energies to produce the radionuclides of interest from ^{70}Zn targets [94]

	Reaction channel on ^{70}Zn target	**Q-value (MeV)**	**Threshold (MeV)**
^{67}Cu	p,α	2.619	0
	p,p+t	-17.195	17.443
	p,n+^{3}He	-17.959	18.218
	p,2d	-21.228	21.534
	p,n+p+d	-23.452	23.790
	p,2n+2p	-25.677	26.047
^{64}Cu	p,3n+α	-23.490	23.829
	p,n+2t	-34.822	35.324
^{61}Cu	p,4n+2t	-62.477	63.377
^{67}Ga	p,4n	-27.682	28.081
^{66}Ga	p,5n	-38.909	39.469
^{69m}Zn	p,d	-6.994	7.094
	p, n+p	-9.218	9.351
^{65}Zn	p,3n+t	-35.528	36.039

Preliminary estimations of the cross sections trends have also been carried out by using two nuclear codes, TALYS [95] and PACE4, included in LISE++ package [96], obtaining contrasting results (Figure 19). The TALYS code has also been used with a set of specific parameters that have been previously optimized by C. Duchemin et al (2015) [97], by comparing simulations with experimental values for many nuclear reactions (proton- and deuteron-beams, up to 70 MeV and 35 MeV respectively, with ^{227}Th, ^{232}Th and ^{225}Ac targets). The combined parameters that showed good reproducibility for the different nuclear reactions studied are the exciton model for pre-

equilibrium reaction, numerical transition rates with an optical model for collision probability, and the microscopic level densities (Skyrme force) from Hilaire's combinatorial tables [95]. Results of the TALYS code run with this new set of parameters are indicated under the name "TALYS*" [97].

Figure 19 shows that the cross section predictions at energies higher than 35 MeV differ significantly from each other, suggesting a possible higher cross section with respect to the ^{68}Zn isotope. Hence the need for a precise experimental measurement of the ^{70}Zn(p,x)^{67}Cu reaction above 35 MeV. The knowledge of the ^{70}Zn(p,x)^{67}Cu cross section will provide a new tool to define the best production route of ^{67}Cu, possibly giving the opportunity to make this radionuclide available to the scientific community. A collaboration with a group of theoretical nuclear physicist (L. Canton INFN-PD and A. Fontana INFN-PV) is ongoing with the aim to compare the results obtained and the theoretical trends to identify the validity limits of the entire set of models present in TALYS and in other nuclear reaction codes.

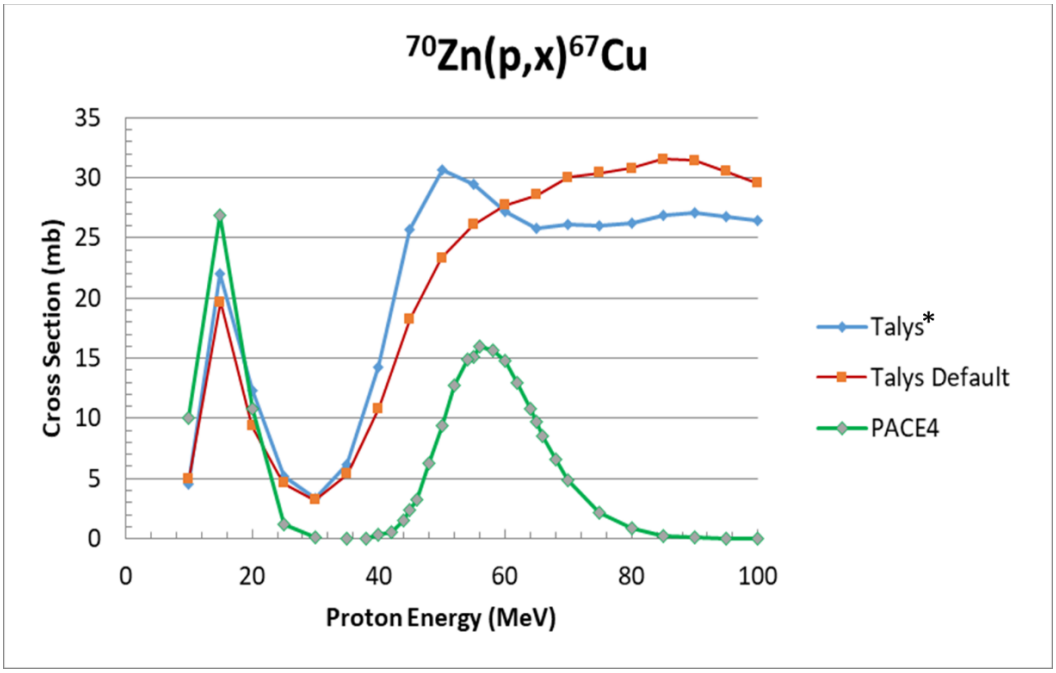

Figure 19: Theoretical estimations of the ^{70}Zn(p,x)^{67}Cu reaction by using PACE4 and TALYS

Theoretical calculations have been also used to predict copper and gallium isotopes production in order to better plan the experimental part of the COME project (Figure 20). Among the different possibilities, TALYS* has been selected since it is the one that better described the experimental data for the ^{68}Zn(p,2p)^{67}Cu reaction [90], without performing an ad-hoc optimization.

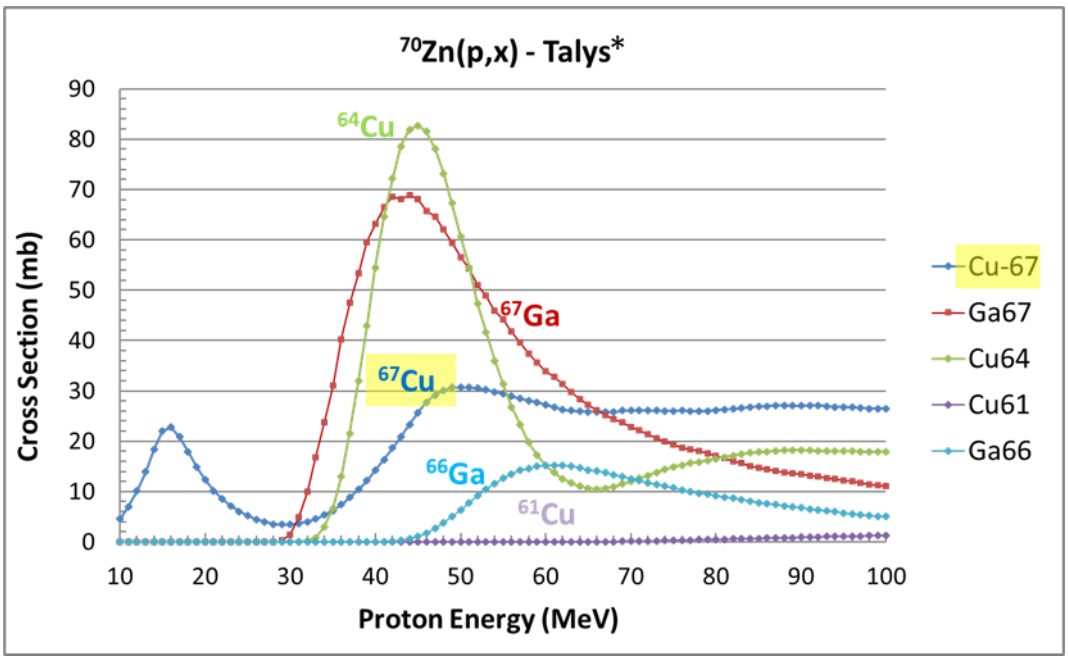

Figure 20: TALYS cross section estimation for $^{70}Zn(p,x)^{xx}Cu,^{xx}Ga$ reactions*

5.2 Experimental description

As the dedicated LARAMED infrastructure is currently under development, the cross section measurements were performed in collaboration with the ARRONAX facility (Nantes, France) [74].

5.2.1 The ARRONAX facility

The ARRONAX facility is based on a multi-particle, high-energy and high-intensity IBA cyclotron (Cyclone 70), installed at Nantes (France) in 2007 and fully operational since January 2011 [74]. This facility is funded by the Regional Council of Pays de la Loire, the University of Nantes, the French government (with the Centre National de la Recherche Scientifique, CNRS, and the Institut National de la Santé et de la Recherche Médicale, INSERM) and the European Union. The aim of ARRONAX is the production of radionuclides for diagnostic and therapeutic applications. Figure 21 reports the scheme of the ARRONAX facility without the laboratories around the vaults.

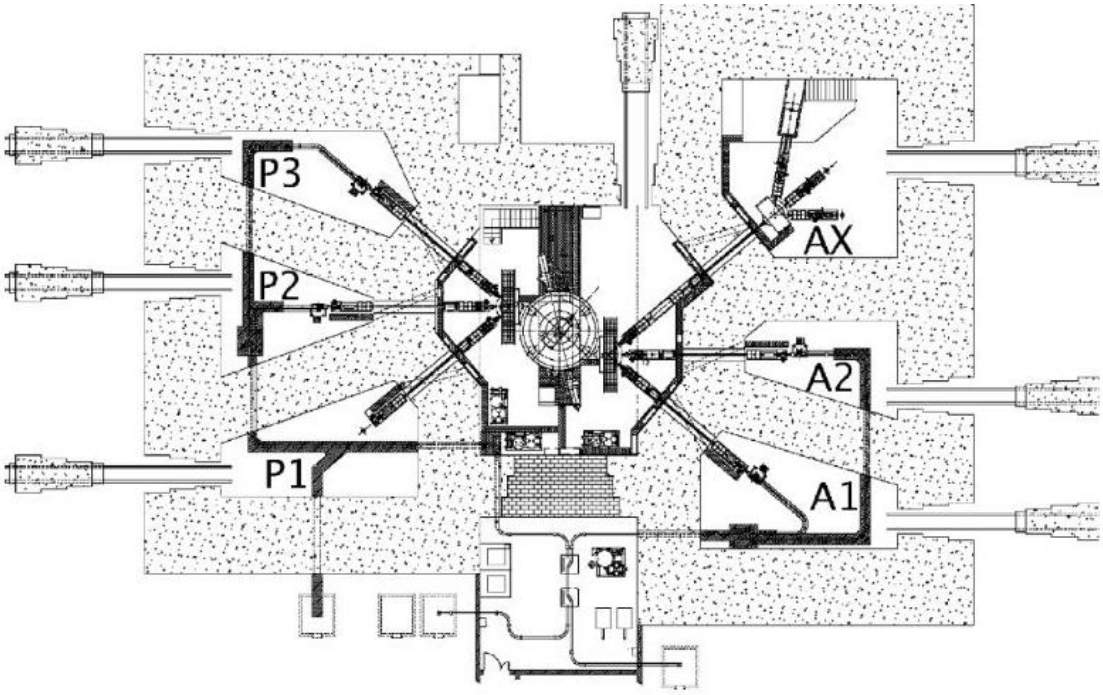

Figure 21: Scheme of the ARRONAX facility without the laboratories around the vaults [74]

Four vaults (A1, A2, P2, and P3) are devoted to isotope production and are connected to hot cells through a pneumatic system; vault P1 is dedicated to the development of a

neutron activator system; vault AX is devoted to research in physics, radiolysis and radiobiology [74].

The cyclotron can accelerate both positive and negative ions up to 70 MeV. All the available beams at ARRONAX and their main characteristics are reported in Table 16.

Table 16: Characteristics of the available beams at ARRONAX [74]

Beam	Accelerated particles	Energy range (MeV)	Intensity (μA)	Dual beam
Protons	H^-	30-70	< 350	Yes
Protons	HH^+	17.5	< 50	No
Deuterons	D^-	15-35	< 50	Yes
α particles	He^{++}	70	< 35	No

Positive ions are extracted with an electromagnetic septum which allows only fixed energy for HH^+ or α particle beams. Negative ions are extracted using the stripper foil technique which offers a wide range of usable energy, from 30 MeV up to 70 MeV. This is the technique used to generate the proton beam used in cross section measurements of the COME project.

5.2.2 Target preparation and stacked-foils target technique

The well-known *Stacked-foils target technique* was used in the cross section measurements performed in this work [98]. This technique allows for bombarding many target foils, thus obtaining several cross section values at different energy in the same irradiation run. As described in the section 3.2, the energy E is calculated as the average of the incoming (E_{IN}) and outcoming (E_{OUT}) particle energy in each foil, $E = \frac{(E_{IN}+E_{OUT})}{2}$. Since all the irradiations were performed at the ARRONAX facility, the stacked-foils technique was chosen in order to optimize the number of irradiations and consequently travel expenses. Considering the time needed by the radiochemical process and the spectroscopy measurements of all the solutions obtained, only two ^{70}Zn target foils were included in each stacked-foils target.

For each run a stacked-foils target (Figure 22) was irradiated containing [66]:

- two target foils of ^{70}Zn, 10 μm thick (Znx1 and Znx2);

- two aluminum monitor-catcher foils (Nickel in the run #5) (20 μm thick) placed right after each Zn foil (Alx1 and Alx2); since in the beam-line dedicated to research at ARRONAX it is not possible to know the incident flux on the target with sufficient precision, Al monitor foils were used to measure the effective beam flux by considering the well-known $^{27}Al(p,x)^{24}Na$ (and $^{nat}Ni(p,x)^{57}Ni$) reference reactions recommended by the IAEA [99] [100];
- an aluminum foil (2 mm thick) placed among the first Al-monitor and the second Zn-target (Al) acting as energy degrader;
- a ^{63}Cu foil (enrichment 99.7%, about 10 μm thick) to produce the Cu element tracer ^{61}Cu (Cux1) (the presence of the ^{63}Cu foil is better explained in the description of the radiochemical separation procedure);
- the aluminum foil (100 μm thick) placed at the end of the stack-structure, used as support to give more rigidity and strength to the Zn_{x2}, $Al_{x2,}$ and $Cu63_x$ thin foils.

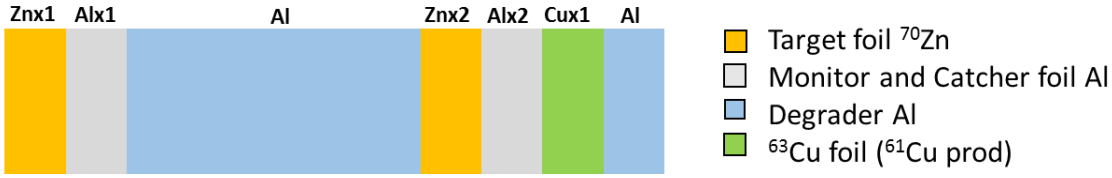

Figure 22: Graphical representation of the staked foil target configuration

Target foils of ^{70}Zn were produced at LNL by lamination from highly pure enriched powder purchased by Trace (Trace Science International Inc., Delaware, USA) and by Chemotrade (Chemotrade GmbH, Dusseldorf, Germany) companies, with the isotopic composition reported in Table 17. Both companies supplied zinc with enrichment greater than 95% in ^{70}Zn. The main contaminant is ^{68}Zn and its contribution is taken into account in the cross section calculation, since the radionuclides of interest in this work ($^{67/64}Cu$, $^{67/66}Ga$ and ^{65}Zn) are also produced from the ^{68}Zn material. Therefore, if the presence of ^{68}Zn in the target is not taken into account, the cross sections associated with the reactions on ^{70}Zn would have been incorrect.

Table 17: Isotopic composition of the ^{70}Zn powder purchased by Trace and by Chemotrade

	Trace	**Chemotrade**
Element	Enrichment (%)	
Zn-70	95.42	95.47
Zn-64	< 0.02	0.05
Zn-66	< 0.02	0.27
Zn-67	0.13	0.07
Zn-68	4.45	4.14

All foils were cut in a circular shape of 12 mm diameter; the mean thickness was calculated by knowing the diameter and the mass of each foil, weighted by using a precision scale. Figure 23 reports an example of target foils used in the 5th irradiation.

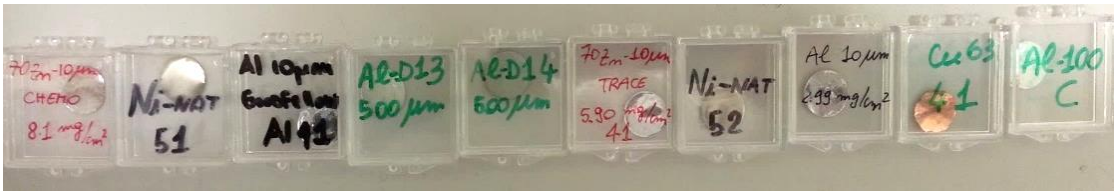

Figure 23: Picture of target foils used in the 5th irradiation run

A dedicated target holder was designed and realized in aluminum at INFN-LNL with a maximum thickness for the stacked-foils assembly of 2 mm (Figure 24). This device can fit the target station of the research beam-line at our disposal at the ARRONAX facility (vault AX) and it is optimized for the small dimensions (12 mm in diameter) of the enriched and costly materials used during these experiments (^{70}Zn and ^{63}Cu).

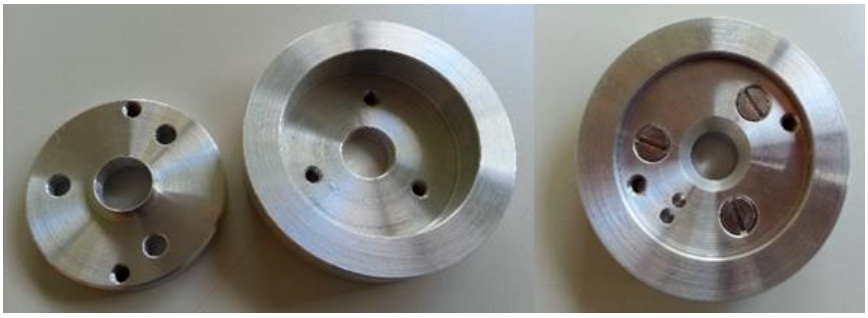

Figure 24: Picture of the dedicated target holder (open and closed)

A dedicated collimator in graphite (cylinder 4 cm long with hole diameter 9 mm) and its plastic support were also designed and built at INFN-LNL. Before each irradiation run, the target holder and the collimator were aligned on the beam-line of the AX vault (Figure 25). The alignment procedure and the collimator, with a smaller hole than the

size of the foils, ensure that the proton beam hits exclusively the stacked-foils target, thus avoiding the activation of the target holder. As shown in Figure 25, the target holder was placed under normal atmosphere downstream at the end of the beam line. The beam line was kept under vacuum and closed with a 75 μm thick Kapton foil. The target station, in which we place our target-holder, is not fixed and for each irradiation run it was necessary to place it again in front of the beam line and assure correct alignment. For this reason, the distance from the target holder to the Kapton foil was accurately measured for each run, ranging from 14.5 cm to 17.1 cm. The structure of the target station does not allow to approach further reduce this distance.

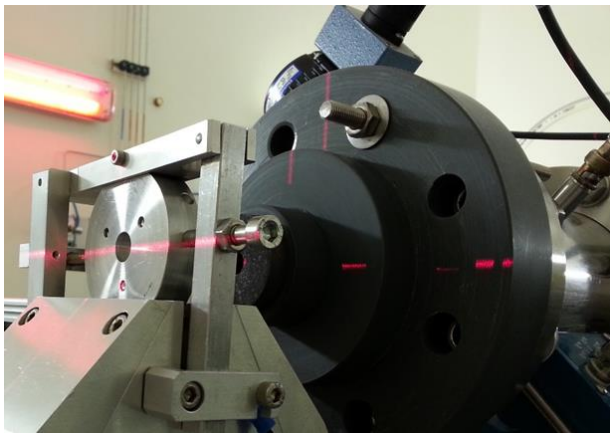

Figure 25: Picture of the target holder, the collimator and its support, installed on the dedicated beam-line at the AX vault, during the alignment procedure

This information allows us to estimate the energy of the beam in each foil included in the stacked-target by using the SRIM [41] software, as already described in the chapter 3. SRIM allows to include configurations of multi-layers targets that, in our case, was always composed by Kapton, air layer, Zn_{x1}, Al_{x1}, $Al_{degrader}$, Zn_{x2}, $Al_{x2,}$ and $Cu63_{x}$. The energy *E* associated with each layer was calculated for each experiment, considering the exact thicknesses of all the foils used, previously measured by weighting the foils and assuming the standard density (except for enriched materials whose density was rescaled considering the isotopic composition). The energy uncertainty for each foil was obtained by considering the uncertainty on extracted energy from the cyclotron (±500 keV) and calculating with SRIM code the energy straggling through each layer of the stacked-target; we obtained a maximum value for the beam energy uncertainty of 750 keV.

5.2.3 Radiochemical separation procedure ^{xx}Zn/^{xx}Ga/^{xx}Cu

As previously described, the reaction ^{70}Zn(p,x) produces ^{67}Cu and ^{67}Ga isotopes that have the same γ-lines, since they both decay into ^{67}Zn (Table 14) [94]. They have also a similar half-life and for these reasons, a radiochemical procedure, aimed at the separation of copper from gallium elements, was developed by the LARAMED chemist team at the Ferrara University in collaboration with the Department of Nuclear Medicine of the Ospedale Sant'Orsola of Bologna. It was also chosen to include the separation of zinc isotopes for the future development of the recovery of the irradiated ^{70}Zn. To measure the efficiency of the radiochemical separation, it is necessary to use tracer radionuclides. For this purpose, it is required to have isotopes of copper, gallium, and zinc elements that present characteristic γ-rays with no interferences with the different γ-lines emitted by the co-produced radionuclides. In the case of gallium and zinc elements, the selected tracer isotopes are ^{66}Ga ($T_{1/2}$=9.49 h) and ^{69m}Zn ($T_{1/2}$=13.756 h), which are directly produced during the proton irradiation of ^{70}Zn target. In the case of copper elements, we preferred not to use the ^{64}Cu produced in the target, since its 1345.77 keV line has low intensity (0.475%) [94], forcing the need of very long spectra acquisition times. In order to reduce the time of the spectra acquisition, ^{61}Cu ($T_{1/2}$=3.339 h) was selected as tracer radionuclide of copper elements (Table 18). However, as ^{61}Cu should not be directly produced in the ^{70}Zn target in the entire energy-range of interest, as predicted by the TALYS code and shown in Figure 20, an enriched ^{63}Cu foil was added to the stacked-target (Figure 22) and used as a source of ^{61}Cu [80]. By dissolving the ^{63}Cu target after irradiation and adding an aliquot of it in the ^{70}Zn dissolved target before the separation procedure, we introduced the tracer for the Cu element. By using an enriched ^{63}Cu foil (99.7%; ^{65}Cu ≤ 0.3%) the co-production of additional ^{64}Cu is avoided, thus allowing also a clean measurement of the ^{70}Zn(p,x)^{64}Cu reaction. The production of ^{64}Cu was of particular interest because it is the only copper radionuclide that may affect the radionuclidic purity (RNP) of ^{67}Cu-labelled radiopharmaceuticals.

Table 18: ^{61}Cu γ-emission lines [94]

^{61}Cu ($T_{1/2}$ = 3.339 h *8*)	
γ-emission Energy [keV]	**Intensity [%]**
283	12.2
656	11
67	4.2
1185.2	3.7
373	2.1
588	1.1

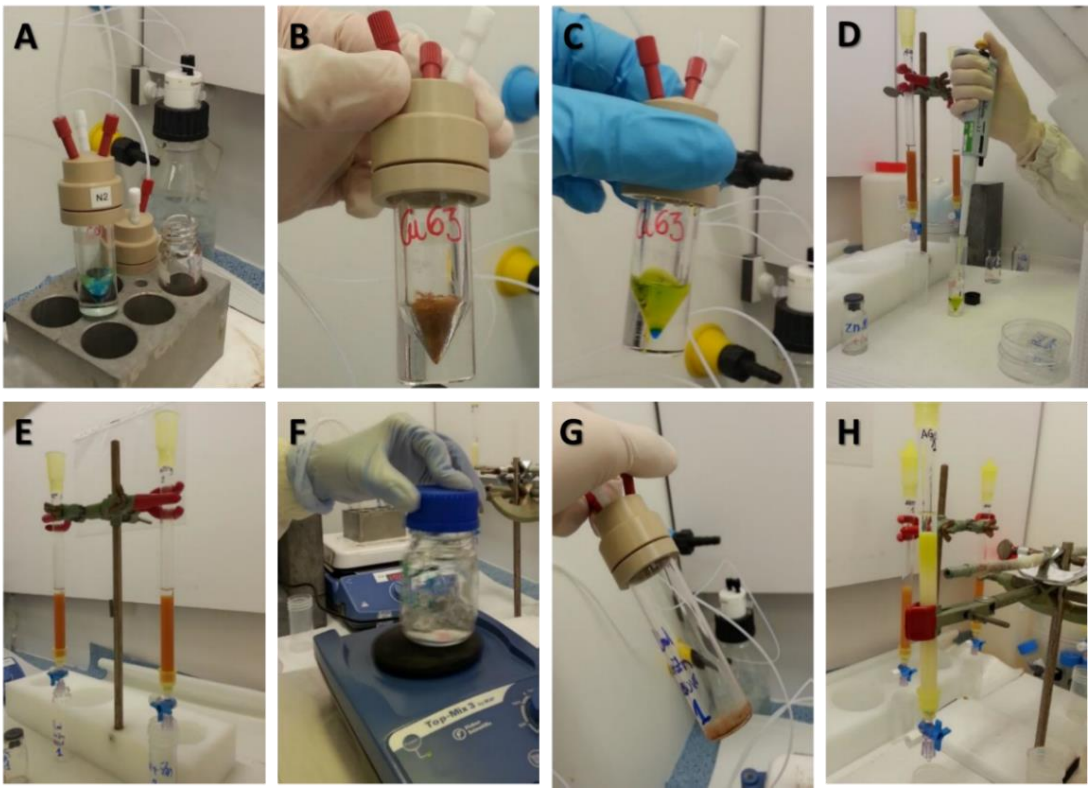

Figure 26: Schematic representation with pictures of main steps of the separation procedure applied to the irradiated targets

The basic steps of the developed radiochemical procedure, having a total duration of about 4 hours, are (Figure 26):

- **A**, **B** and **C**: dissolution of the ^{63}Cu foil in HNO_3 6 M and consequent evaporation, dissolution in HCl 10 M (repeated twice);
- **D**: dissolution of the ^{70}Zn target in HCl 10M and addition of a 0.5mL ^{63}Cu aliquot to the dissolved zinc thus becoming the "MIX" solution containing all Cu, Ga and Zn isotopes;
- **E**: Simultaneous treatment of MIX solution by the cation exchange resin in which gallium isotopes are retained (^{66}Ga and ^{67}Ga) while Cu and Zn isotopes are left to flow through the resin;
- **F**: the "xGa" solution eluted from the cation exchange resin under stirring by means of a mechanical vortex to ensure the homogeneity of the solution (about 20 mL) before aliquoting (xGa-Aliquot 5mL);
- **G**: the eluted Cu-Zn solution under evaporation before dilution in HCl 2 M (repeated twice);

- **H**: simultaneous treatment of Cu-Zn 2 M HCl solution by the anion exchange resin in which Zn isotopes are retained (^{62}Zn, ^{65}Zn and ^{69}Zn) while all other elements produced, including Cu isotopes (^{67}Cu, ^{64}Cu and ^{61}Cu), are left to flow through the resin in the final "xCu" solution; "xZn" solution is then obtained by eluting the column with HCl 0.005M. Both solutions of about 20 mL were aliquoted for gamma spectrometry analysis (xCu- and xZn-Aliquot 5 mL each).

All monitor foils (both aluminum and nickel) were dissolved in 10 M HCl directly in a 5 mL vial suitable for the subsequent spectrometry measurement. It was chosen to dissolve also the monitor foils in order to use the same geometry and thus the same efficiency of the target foils. The yield of the chemical separation is given in the section 5.3, and reported in Table 21.

5.2.4 Irradiation runs and acquisition data

Six irradiation runs were performed at the ARRONAX facility using a proton beam with tunable energy (35−70 MeV) and stacked-foils targets, allowing the simultaneous bombardment of a set of thin metallic foils (Table 19). The energy of the proton beam in the different runs is changed by the cyclotron operators by varying the position of the stripper foil. The duration of typical irradiation was 1.5 hours with a constant current flow of about 100 nA.

At the end of each irradiation, the activated target was disassembled behind a leaded glass to ensure the radiation protection to the operator. Each foil has been separated and stored in a lead radiation shielding container. The next phase was the start of the previously described chemical separation procedure in a dedicated laboratory.

Table 19: Irradiation parameters of irradiation runs performed at ARRONAX facility (Nantes, Francia) to study the ^{67}Cu production

Irradiation run #	Proton energy (MeV)	Irradiation time (s)	Mean current (nA)	^{70}Zn targets irradiated #
1	70.3	5390	98.8	2
2	56.0	5396	100.4	2
3	61.0	4895	110.5	2
4	68.0	5406	100.7	1
5	48.0	7270	102.5	2
6	56.0	5400	100.4	2

After each step of the chemical procedure, a spectrometry measurement was taken to follow the whole process by using the tracer radionuclides. For the γ-ray spectrometry was used a High Purity Germanium (HPGe) detector with low-background lead and copper shielding (10% relative efficiency, FWHM 1.0 keV at 122 keV, Canberra GC1020), available at the ARRONAX laboratories (Figure 27). The acquisition of the signals took place with an ORTEC's Multichannel Analyzers that analyzes a stream of voltage pulses and sorts them into a spectrum of a number of events, versus pulse-height, related to the energy of the γ-ray that has generated the signal. The spectra are displayed and saved with the program GammaVision.

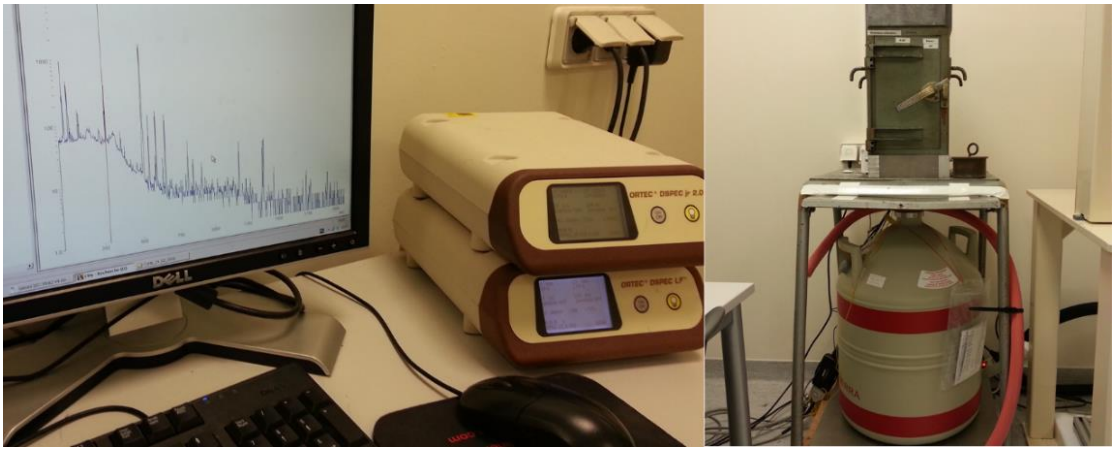

Figure 27: HPGe detector, a digital multichannel analyzer and the computer with the acquisition program, used at ARRONAX to acquire spectra

The HPGe detector is calibrated for two geometries: in contact with the detector (0 cm) or at a distance of 19 cm (Figure 28). To keep the acquisition geometry constant, 5 mL of each solution was always measured in a dedicated plastic vial, as the one shown in the image on the right in Figure 28. For both possible acquisition geometries, it was provided to us the efficiency of the detector associated with a liquid sample in a vial containing 5 mL of a solution whose activity was known for each isotope present. The function used for the efficiency calibration is

$$\epsilon(E) = \exp\left(c_1 \cdot E + c_2 + \frac{c_3}{E} + \frac{c_4}{E^2} + \frac{c_5}{E^3} + \frac{c_6}{E^4}\right) \quad (5.1)$$

where the energies E are expressed in MeV and $c_{1\text{-}6}$ are the parameters determined by applying a fitting curve to some measured efficiency value, relative to specific energies, obtained by using 5 mL of a reference multi-peak liquid source, purchased to Cerca-Lea, France, containing the reference radionuclides ^{241}Am, ^{109}Cd, ^{57}Co, ^{139}Ce, ^{51}Cr,

^{113}Sn, ^{85}Sr, ^{137}Cs, ^{88}Y, and ^{60}Co. The values calculated by the fitting procedure are reported, for both geometries, in Table 20.

Table 20: Values of the coefficients c_x present in the efficiency formula 5.1 for the geometry in contact (g0) and at 19 cm (g1)

Coefficient	Value (g0)	Value (g1)
c_1	-0.391791000	-0.270847000
c_2	-4.863400000	-8.438260000
c_3	0.756183000	0.713157000
c_4	-0.099995300	-0.095606200
c_5	0.006460440	0.005762700
c_6	-0.000159407	-0.000129671

Usually, the MIX vials, which contain all the activity produced during the irradiations, were measured at a distance of 19 cm from the HPGe detector to reduce the dead time. The solutions xCu, xGa and xZn were always measured at contact with the HPGe detector since they contained only an aliquot of the total activity of the single radionuclide (5 mL out of 20 mL).

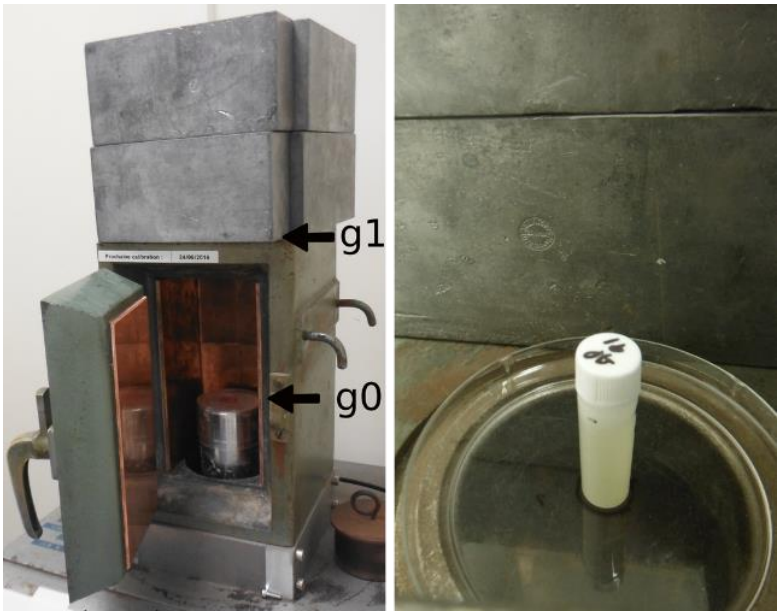

Figure 28: HPGe detector used at ARRONAX to acquire spectra with indicated geometry in contact (g0) and at 19 cm (g1). On the right an example of a vial in the g1 position

During the first irradiation, the measurement of the vial called MIX, containing the dissolved ^{70}Zn foil and the ^{61}Cu aliquot, was not carried out. Although all the other acquisitions have been made, the reference of the initial activity before the

radiochemical separation procedure was missing. In the second irradiation run the zinc foil was dissolved into a glass vial and only later it was moved into a γ-spectrometry vial. A fraction of the activity has remained attached to the walls of the glass vial so even if in this case the γ-spectrometry of the MIX was made, we did not have a reference to the total initial activity.

From the third irradiation, the zinc foil was dissolved directly into the γ-spectrometry vial allowing the measurement of the total initial activity. For this reason, in the data analysis, we considered only four irradiations out of the performed six.

5.3 Data analysis

All the spectra acquired at the ARRONAX facility were analyzed by using the jRadView software, developed at LNL. As an example, in Figure 29, a spectrum obtained after the dissolution phase of the target and the three spectra obtained after the chemical separation, are shown. Since the logic of the radiochemical separation carried out is aimed exclusively at the measurement of the cross section, the solution called xCu, in addition to Cu-isotopes, contains also different elements such as nickel and cobalt. This explains the reason why in the spectrum related to the xCu solution there are many γ-lines not referable to copper isotopes. Since a tracer was not used for each element produced in the ^{70}Zn(p,x) reaction, it was possible to calculate the cross sections only for the isotopes of copper (excluding the ^{61}Cu added to the initial solution), gallium and zinc.

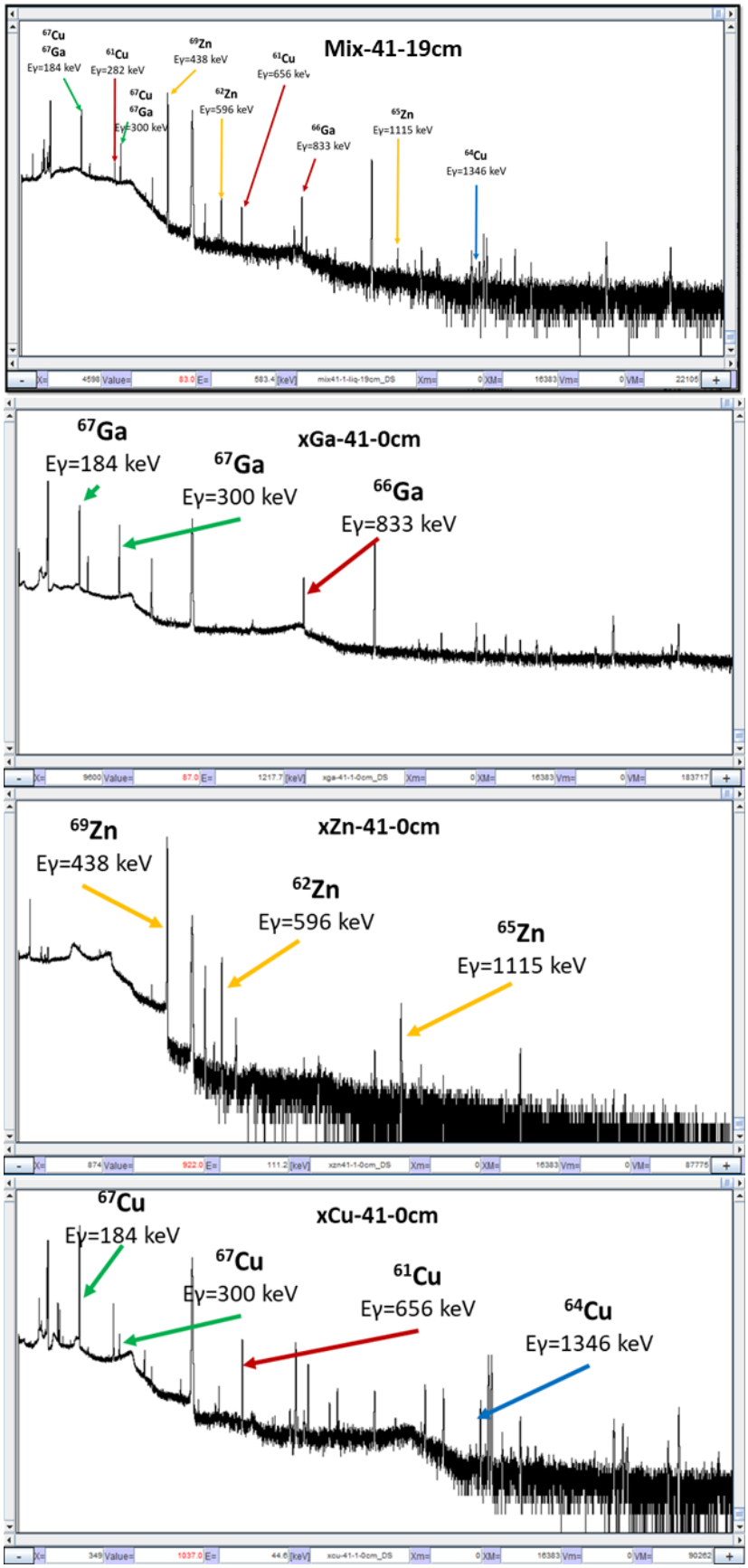

Figure 29: Spectra obtained in the fourth irradiation run, before ("Mix") and after ("xGa", "xZn" and "xCu") the radiochemical separation

The recovery yield of each tracer in the solutions, listed in Table 21, was derived from the analysis of the spectra evaluating the tracer fraction in each solution compared to the total present in the MIX, as shown in the following equations:

$$Act^{I}_{tracer} : Act^{I}_{nuclide} = Act^{F}_{tracer} : Act^{F}_{nuclide}$$

$$Act^{I}_{nuclide} = Act^{F}_{nuclide} \cdot \frac{Act^{I}_{tracer}}{Act^{F}_{tracer}} \quad (5.2)$$

where $Act^{I}_{nuclide}$ and $Act^{F}_{nuclide}$ represent the activity before and after the separation.

The recovery yield allowed me to correct the activities of the radionuclides of interest obtained from the xCu, xGa and xZn solutions to obtain the total activity produced in the irradiation run.

Table 21 Mean purification yield evaluated on all eleven samples expressed in percentage. ND= Not Determinable since isotopes characteristic peaks have not been observed in the spectra (peaks assessed below the minimum detectable activity)

%	Gallium solution	Copper solution	Zinc solution
Ga-66	79 ± 11	2 ± 1	ND
Cu-61	ND	95 ± 2	ND
Zn-69	ND	ND	84 ± 2

While Cu is all recovered in the Cu solution and no Cu traces were found in the other samples, a small amount of ^{66}Ga was found in the Cu solution (2 ± 1 % of the total ^{66}Ga activity present in the MIX solution before the separation procedure). This means that the first cation exchange resin did not trap efficiently Ga. The presence of ^{66}Ga in the copper solution indicates the consequent presence of ^{67}Ga which must be taken into account in the cross section determination by using the branching ratio correction (BR = branching ratio). Starting from the formula to calculate the activity from the spectra $Act_{meas} = \frac{C}{\varepsilon(E) I(E) t_L}$ and knowing the total number of counts attributed to the 184 keV and 300 keV γ-lines (C^{184} and C^{300}), due only to the ^{67}Cu and ^{67}Ga activities (Act_{Cu67} and Act_{Ga67}), the BR correction consisted in the solution of the following two equation system [101]:

$$\begin{cases} C^{184} = k_1 Act_{Cu67} + k_2 Act_{Ga67} \\ C^{300} = k_3 Act_{Cu67} + k_4 Act_{Ga67} \end{cases}$$

$$\begin{aligned} k_1 &= \varepsilon^{184} I_{Cu67}^{184}\, t_L \quad k_2 = \varepsilon^{184} I_{Ga67}^{184}\, t_L \\ k_3 &= \varepsilon^{300} I_{Cu67}^{300}\, t_L \quad k_4 = \varepsilon^{300} I_{Ga67}^{300}\, t_L \end{aligned} \tag{5.3}$$

$$Act_{Ga67} = \frac{k_1 C^{300} - k_3 C^{184}}{k_4 k_1 - k_3 k_2}$$
$$Act_{Cu67} = \frac{k_4 C^{184} - k_2 C^{300}}{k_4 k_1 - k_3 k_2}$$

The BR correction, as the other described below, is taken into account in the uncertainty calculation of the final cross section value.

Also the kinematic recoil effect must be considered in the activity estimation. In fact, some atoms jump out one foil and they are trapped in the following one; this effect is particularly evident in thin foils (thickness in the order of 10 μm) and light atoms, as in case of ^{24}Na produced in the ^{nat}Al monitor foil and caught by the ^{63}Cu foil (Figure 30). For ^{24}Na, the maximum value of the recoil effect was 21.1%, for Ga and Cu radionuclides was 2.6% and 2.3% for ^{69m}Zn. The activities of the radionuclides of interest were corrected for the recoil effect in order to consider the total number of the atoms of each radionuclide produced in the irradiation.

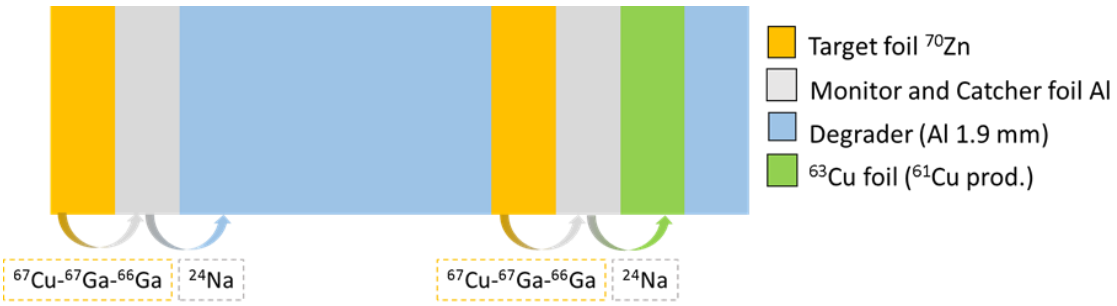

Figure 30: Graphical representation of the Recoil effect in a typical stacked-foils target

If necessary, the activity must be further corrected for the Weight Factor to consider that the γ-spectrometry is performed only on 5 mL out of 20 mL. The final activity at EOIB was calculated by using the Formula 3.12 and, when necessary, applying the corrections of the Recoil Effect, Chemical Yield, Branching Ratio, and Weight Factor (Table 22).

Table 22: Corrections to the activity at EOIB for each solution

	Solution	Recoil effect	Chemical Yield	BR method	Weight factor
^{67}Cu	xCu	*x*	*x*	*x*	*x*
^{64}Cu	xCu	*x*	*x*		*x*
^{67}Ga	xGa	*x*	*x*		*x*
^{66}Ga	MIX	*x*			
^{69m}Zn	MIX	*x*			
^{65}Zn	xZn	*x*	*x*		*x*

Since in the beam line used it is not possible to know with sufficient precision the beam flux, a ^{nat}Al foil was used for this purpose by referring to the well-known ^{nat}Al(p,x)^{24}Na monitor reaction recommended by the International Atomic Energy Agency (IAEA) [99]. As shown in Figure 30, a ^{nat}Al foil was placed immediately after each ^{70}Zn target in all irradiation runs, also acting as a catcher. In this way, having two adjacent thin foils, it was assumed that the beam flux through them is the same. The cross sections, as a function of energy, were then calculated by using the equation 3.14.

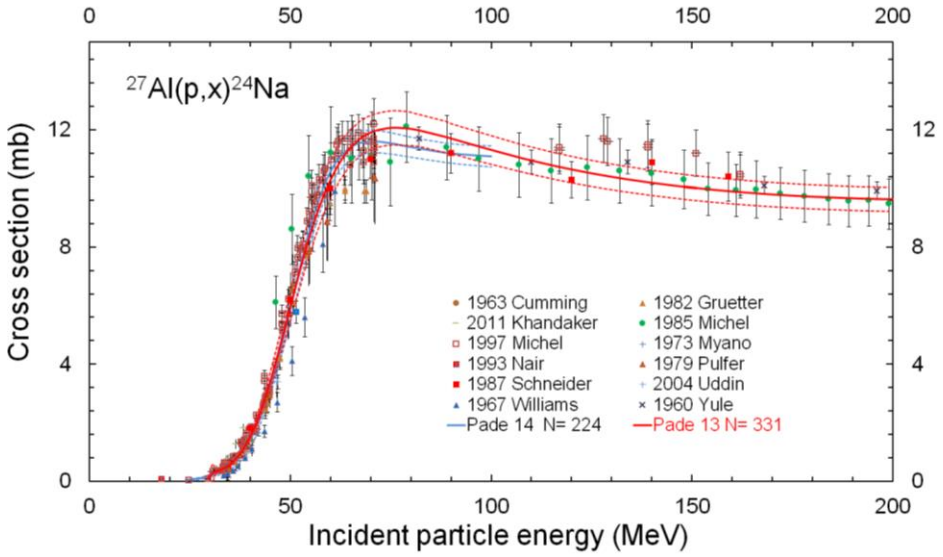

Figure 31: Recommended cross section for the ^{27}Al(p,x)^{24}Na reaction with uncertainties [99]

The values of the reference cross section used, with related uncertainty, are reported in Table 23 [99]. The uncertainty varies from 5% to 8% and this is the major contribution to the uncertainty of the measured cross section.

Table 23: The IAEA $^{nat}Al(p,x)^{24}Na$ monitor reaction values and related uncertainties [99]

Energy [MeV]	Reference cross section [mb]
44.4 ± 0.7	2.9 ± 0.7
47.5 ± 0.6	4.4 ± 0.3
50.7 ± 0.5	6.3 ± 0.5
55.7 ± 0.5	9.0 ± 0.6
56.0 ± 0.8	9.2 ± 0.7
60.7 ± 0.5	10.8 ± 0.5
67.7 ± 0.6	11.6 ± 0.5

The nuclear data used in the data analysis performed to obtain the ^{67}Cu, ^{64}Cu, ^{67}Ga, ^{66}Ga, ^{65}Zn, and ^{69m}Zn cross sections are reported in Table 24.

The results obtained are corrected for the contribution due to the presence of ^{68}Zn (about 4%) in the target (Table 17) [101]. In the case of ^{67}Cu, ^{67}Ga, and ^{66}Ga radionuclides, the most recently measured values of the excitation functions from ^{68}Zn targets were considered [90].

Table 24: Nuclear data used in the ^{67}Cu, ^{64}Cu, ^{67}Ga, ^{66}Ga, ^{65}Zn and ^{69m}Zn cross section calculations [7]

Isotope	Half-life	Energy [keV]	Intensity [%]
^{67}Cu	61.83 h *12*	184.577 *10*	48.7 *3*
		300.219 *10*	0.797 *11*
^{64}Cu	12.701 h *2*	1345.77 *6*	0.475 *11*
^{67}Ga	3.2617 d *5*	184.576 *10*	21.410 *10*
		300.217 *10*	16.64 *12*
^{66}Ga	9.49 h *3*	833.5324 *21*	5.9 *3*
		1039.220 *3*	37.0 *20*
^{65}Zn	243.93 d *9*	1115.539 *2*	50.04 *10*
^{69m}Zn	13.756 h *18*	438.634 18	94.85 *7*

For the ^{64}Cu, the IAEA recommended cross section was used [102] and for the ^{65}Zn radionuclide was used the only available experimental data on the EXFOR database [103] [88]. The ^{69m}Zn radionuclide is not produced by proton-beams in ^{68}Zn targets and for this reason, this correction is not necessary. For the ^{67}Cu, ^{64}Cu and ^{67}Ga radionuclides the correction due to ^{68}Zn presence in the target is lower than 4%. Final results for all the measured ^{70}Zn(p,x)^{67}Cu, ^{64}Cu, ^{67}Ga, ^{66}Ga, ^{69m}Zn, ^{65}Zn cross sections are rescaled to 100% enriched ^{70}Zn and listed in Table 25. In the calculation of the final error, all the corrections that had to be applied were considered. This work is also described in a dedicated paper we have published [101].

Table 25: Cross sections of the $^{70}Zn(p,x)^{67}Cu$, ^{64}Cu, ^{67}Ga, ^{66}Ga, ^{69m}Zn, ^{65}Zn reactions referred to 100% enriched ^{70}Zn targets

Energy [MeV]	^{67}Cu [mb]	^{64}Cu [mb]	^{67}Ga [mb]	^{66}Ga [mb]	^{69m}Zn [mb]	^{65}Zn [mb]
44.7 ± 0.7	8.0 ± 1.3	48.0 ± 4.6	281.2 ± 42.8	3.2 ± 0.6	84.3 ± 7.4	6.2 ± 1.2
47.7 ± 0.6	10.8 ± 1.9	57.3 ± 5.3	214.0 ± 33.8	4.1 ± 0.8	71.5 ± 6.3	7.1 ± 1.3
50.8 ± 0.5	12.7 ± 2.2	51.1 ± 5.3	172.1 ± 27.0	11.4 ± 2.1	66.5 ± 5.6	8.2 ± 1.5
55.8 ± 0.5	16.8 ± 3.0	45.2 ± 4.0	120.1 ± 18.6	31.4 ± 6.1	60.5 ± 4.7	11.9 ± 2.1
56.0 ± 0.8	18.7 ± 3.4	48.0 ± 4.5	135.6 ± 21.0	37.2 ± 7.3	68.6 ± 5.1	14.3 ± 2.6
60.8 ± 0.5	20.1 ± 3.6	33.0 ± 2.7	97.3 ± 14.2	46.8 ± 8.5	65.7 ± 4.1	28.2 ± 4.7
67.8 ± 0.6	21.5 ± 4.0	23.2 ± 1.7	59.7 ± 7.7	34.5 ± 5.1	54.8 ± 2.8	65.3 ± 10.5

Our experimental data were compared with the calculations obtained using the TALYS nuclear code (version 1.9) [23]. TALYS was used with the default set of parameters and by using a different set of parameters proposed by C. Duchemin et al. [97] (indicated with TALYS* on the legend of each graph).

5.3.1 $^{70}Zn(p,x)^{67}Cu$, ^{64}Cu cross sections

Results obtained for the $^{70}Zn(p,x)^{67}Cu$ nuclear reaction are illustrated in Figure 32. No literature data are available in the energy range investigated (45-70 MeV) [88]. This nuclear reaction was already measured up to 35 MeV [79] [80] and evaluated by the IAEA up to 40 MeV [93] (Figure 18); these data are reported in Figure 32 for completeness. Different irradiation runs showed a regular increasing trend of the reaction in the energy range investigated (45-70 MeV) that is well described by the TALYS calculation with the default set of parameters, even if with an overestimation of the cross section. At this moment, it is not possible to predict the entire trend of the reaction and it would be necessary to perform a dedicated measurement in the energy range 30-45 MeV in order to link our new data with the previous estimation of the (p,α) channel. It was not possible to investigate also this energy range due both to the limited time duration of the project and the limited funds assigned to the COME project to cover all expenses.

The experimental values obtained by S. Kastleiner et al. [79] (enrichment of the ^{70}Zn 85.03%) well reproduced by the IAEA fit up to 33 MeV while in the energy range 33-35 MeV there is a discrepancy not only with the IAEA fit but also with the TALYS results obtained with both set of parameters (Figure 32). Following the method

described by S.M. Qaim et al. [104], data by V.N. Levkovski [80] are rescaled by a factor of 0.77 to consider the recent IAEA evaluation [44] [45] of the $^{nat}Mo(p,x)^{96g+m}Tc$ monitor cross section used by the author (250 mb *vs* 192.82 mb at E_P = 30 MeV). The new data by V.N. Levkovsky (Figure 32) are not in agreement either with the IAEA fit or with TALYS results obtained with both set of parameters.

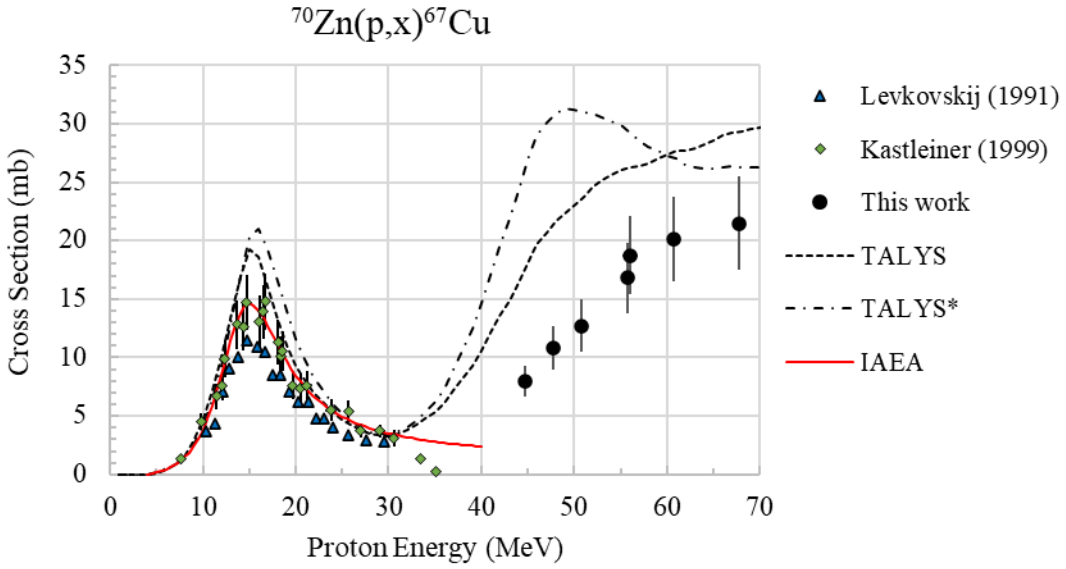

Figure 32: Results of the $^{70}Zn(p,x)^{67}Cu$ nuclear cross section

Figure 33 reports the first experimental data of the $^{70}Zn(p,x)^{64}Cu$ nuclear reaction, showing a regular trend in the energy range investigated. In this case, there is an evident discrepancy between the TALYS calculations and the measured values.

In Figure 34 it is evident that the trend of the $^{70}Zn(p,x)^{64}Cu$ reaction declines when E_P > 48 MeV, whereas for the $^{70}Zn(p,x)^{67}Cu$ reaction it increases in the entire energy range investigated. However, the cross section values for ^{64}Cu production are always higher than those of ^{67}Cu, as shown in Figure 34.

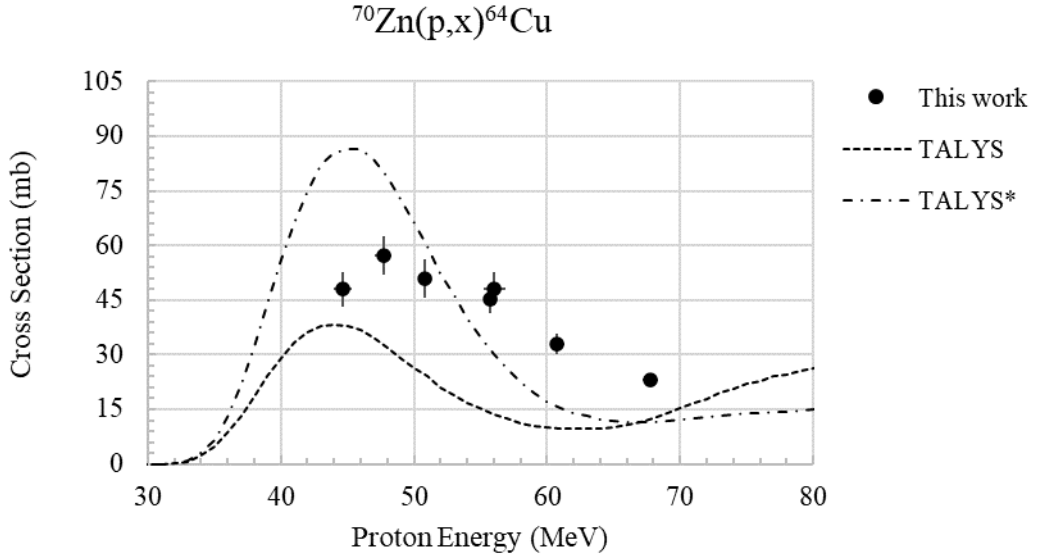

Figure 33: Results of the $^{70}Zn(p,x)^{64}Cu$ nuclear cross section

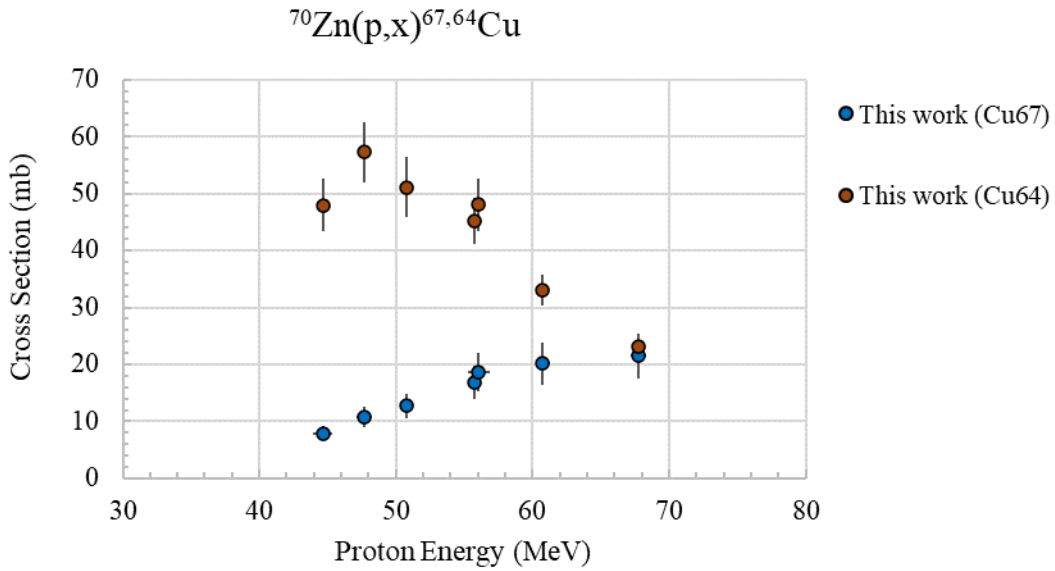

Figure 34: Results of the $^{70}Zn(p,x)^{67,64}Cu$ nuclear cross sections

5.3.2 $^{70}Zn(p,x)^{67}Ga$, ^{66}Ga cross sections

In view of a potential use of enriched ^{70}Zn targets to produce ^{67}Cu, it is important to be able to estimate the production of ^{66}Ga and ^{67}Ga radionuclides since they must be considered in the optimization of the radiochemical procedure necessary for copper separation and purification. In Figure 35 and Figure 36 are reported the results of the $^{70}Zn(p,5n)^{66}Ga$ and $^{70}Zn(p,4n)^{67}Ga$ cross sections. The ^{66}Ga reaction cross section

shows a 50 mb peak around 61 MeV, while the ^{67}Ga reaction cross section apparently has a peak at lower energy (E_P < 45 MeV). As in the case of ^{64}Cu, the experimental trend is not properly described by TALYS estimations.

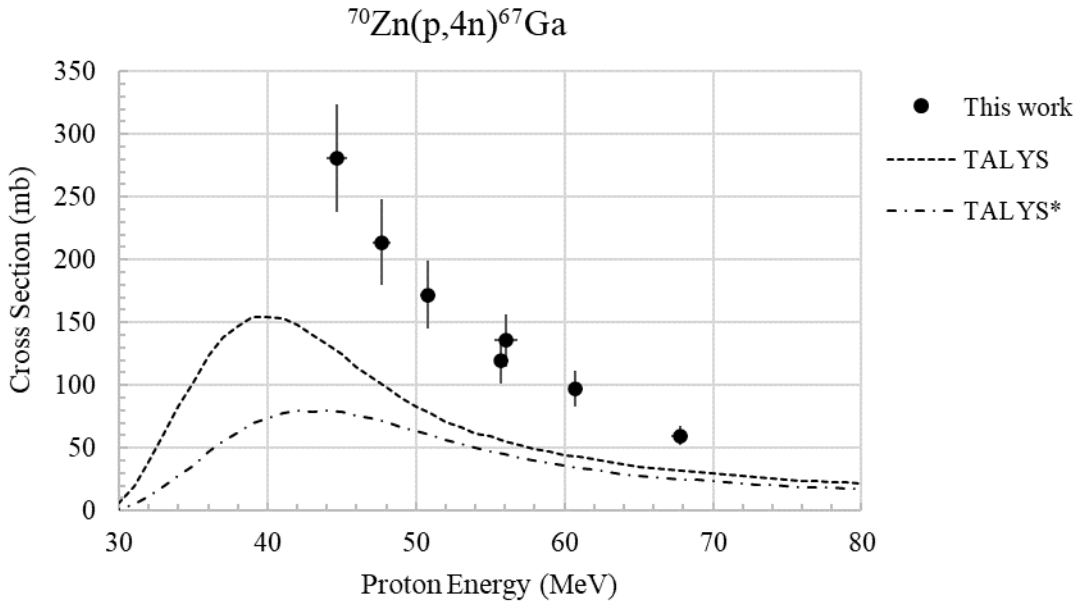

Figure 35: Results of the ^{70}Zn(p,4n)^{67}Ga nuclear cross section

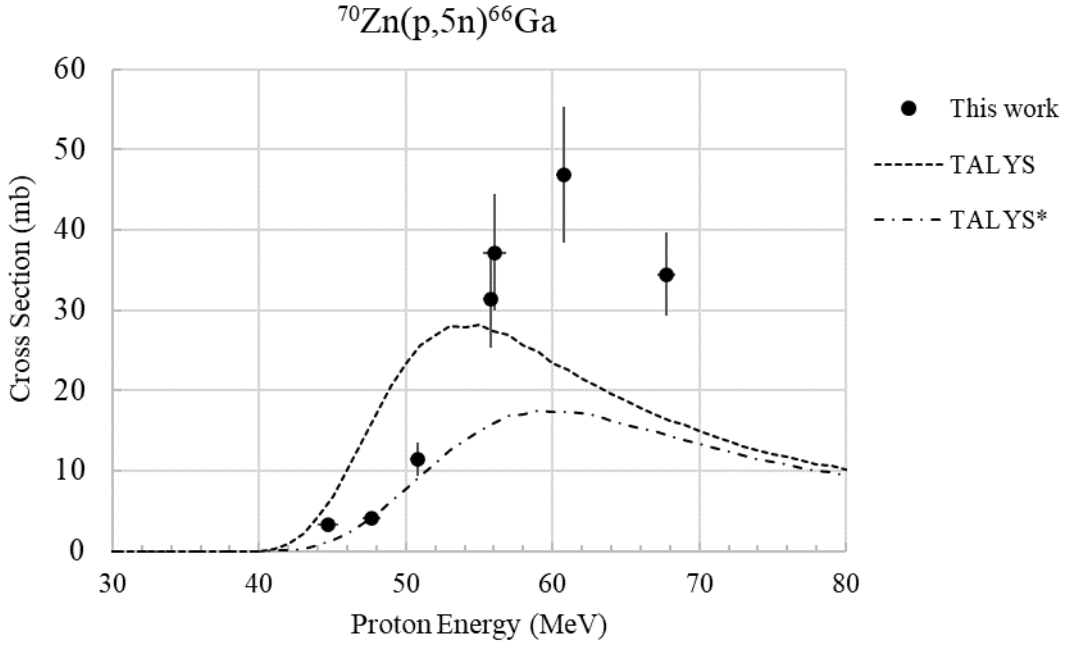

Figure 36: Results of the ^{70}Zn(p,5n)^{66}Ga nuclear cross section

5.3.3 ^{70}Zn(p,x)^{65}Zn,^{69m}Zn cross sections

The first measurement of the ^{70}Zn(p,x)^{65}Zn cross section is reported in Figure 37. The measurement of ^{65}Zn production is of particular interest in the case of the optimization of the ^{70}Zn recovery process since it is the longest-lived radioactive contaminant present in the irradiated material. The amount of ^{65}Zn product allows to estimate a suitable decay time before reprocessing of the irradiated material. As the ^{65}Zn activity is measured from the xZn solution containing only zinc isotopes, no interference with the 1115 keV γ-line from ^{65}Ni can occur. The experimental data showed a regular increasing trend of the reaction in the energy range investigated (45-70 MeV) which, however, is not properly described by the theoretical calculation, although TALYS reproduces the general trend better than TALYS*. There is however an evident discrepancy in the initial trend of the reaction, which has 36 MeV as threshold energy with the ^{70}Zn(p,3n+t)^{65}Zn channel (Table 15). Indeed, in the two lower energy points (44.7 and 47.7 MeV) the measured cross section is between 6 and 7 mb, while both TALYS and TALYS* predict the start of the cross-section trend at around 47 MeV (Figure 37). This could be due to reactions on other Zn-isotopes present as impurities in the enriched material (Table 17), even if the contribution due to the ^{68}Zn was already corrected. It has to be noted that the ^{64}Zn, ^{66}Zn and ^{67}Zn isotopes have negligible abundance in the target materials used. The reaction channel ^{70}Zn(p,6n)^{65}Ga→^{65}Zn has a threshold of 48.7 MeV and cannot explain the obtained value of about 6 mb at 44.7 MeV. In addition, despite the lowest threshold value for the ^{70}Zn(p,x)^{65}Zn reaction is 36 MeV, the production of ^{65}Zn from ^{70}Zn target was also observed in the energy range between 12 and 45 MeV by Schwarzbach in 2001 [105].

Figure 38 reports the results of the ^{70}Zn(p,x)^{69m}Zn cross section, together with TALYS estimations and literature data [80]. Also in this case, the data by V.N. Levkovskij was rescaled by a factor of 0.77 (as previously described for the ^{70}Zn(p,x)^{67}Cu reaction). There is a general agreement in the trend of the ^{70}Zn(p,x)^{69m}Zn cross section between TALYS* and our measurements. It would be interesting to complete the entire trend with new data in the 30-45 MeV energy range.

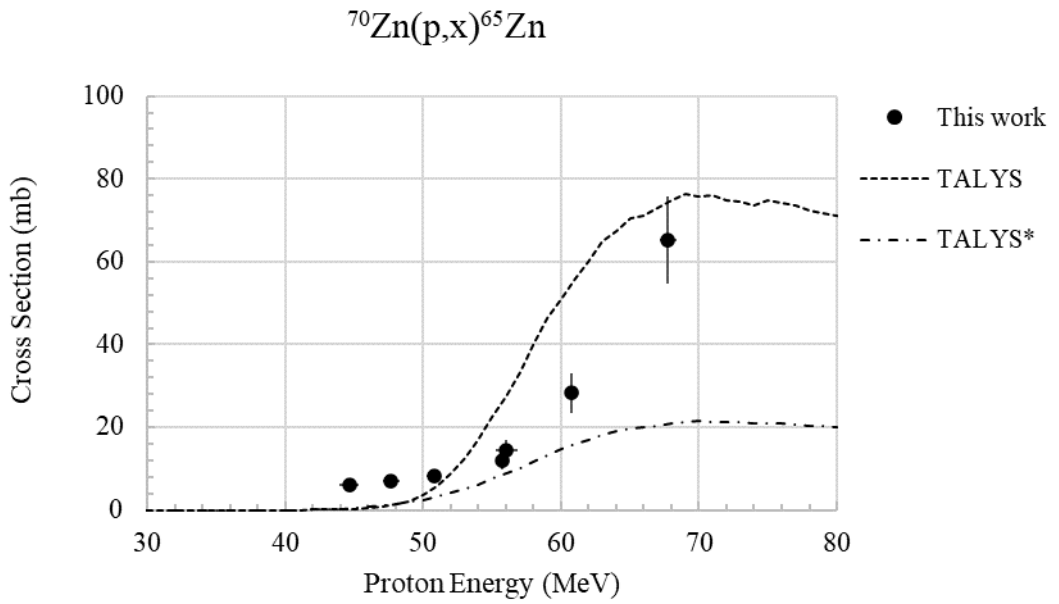

Figure 37: Results of the $^{70}Zn(p,x)^{65}Zn$ nuclear cross section

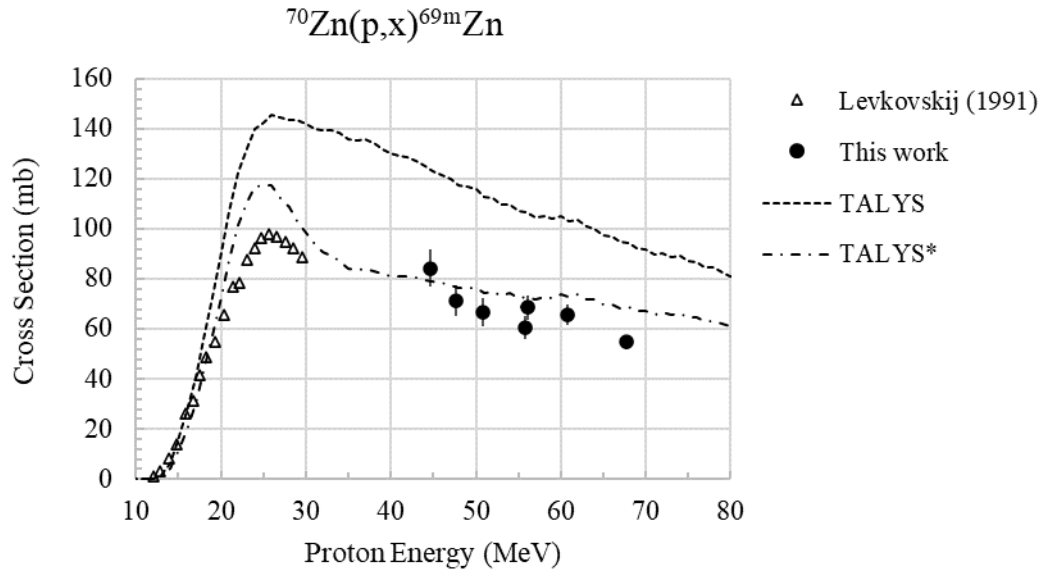

Figure 38: Results of the $^{70}Zn(p,x)^{69m}Zn$ nuclear cross section

5.4 Comparison of ^{67}Cu production by using ^{70}Zn and ^{68}Zn targets

The new results obtained for the ^{70}Zn(p,x)^{67}Cu nuclear reaction were compared with the well-known ^{68}Zn(p,x)^{67}Cu nuclear reaction to understand which is the most convenient route to produce ^{67}Cu. The comparison between the two proton-induced nuclear reactions is shown in Figure 39. It is evident that for E_p > 48 MeV the reaction with ^{70}Zn target has a higher yield: for example, at 70 MeV the cross section value is almost twice than the recommended one regarding ^{68}Zn targets. To quantify the ^{67}Cu activity produced with a proton beam in the 45-70 MeV energy range I performed thick target yield (TTY) calculations following the Formula 3.18, reported in the IAEA Technical report series n° 468 [47]. The ^{67}Cu production yield in the energy range investigated considering I=1 μA and T_{irr}=62 h (about 1 half-life of ^{67}Cu) is 70% higher by using ^{70}Zn target instead of ^{68}Zn target, as shown in Table 26.

In the case of ^{67}Cu production with simultaneous minimization of ^{64}Cu co-production, the irradiation parameters can be optimized. The comparison between the ^{70}Zn(p,x)^{64}Cu and ^{68}Zn(p,x)^{64}Cu nuclear cross sections are shown in Figure 40, where it can be noted that in the energy range investigated the reaction with ^{70}Zn target is decreasing while it is increasing with ^{68}Zn target.

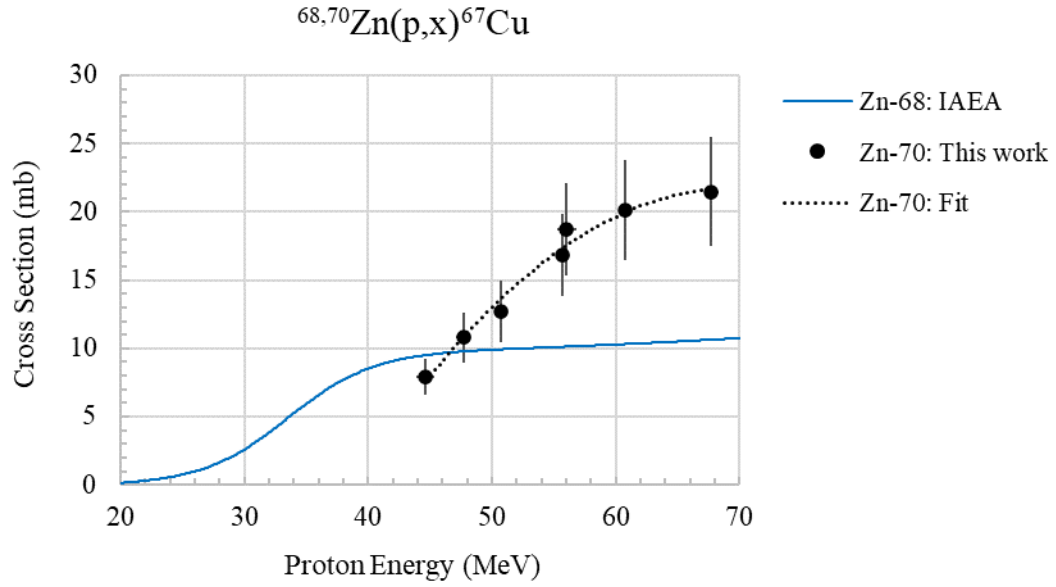

Figure 39: Comparison between the ^{70}Zn(p,x)^{67}Cu and ^{68}Zn(p,x)^{67}Cu nuclear cross sections

Table 26: Comparison between ^{67}Cu production yield in the 45-70 MeV energy range for $^{68/70}Zn$ targets (I=1 μA; T_{irr}=62 h)

Irradiation parameters	Target	Isotope	MBq/μA	mCi μA	$^{70}Zn/^{68}Zn$
45-70 Mev	^{68}Zn	^{67}Cu	1007	27	1.7
T_{irr} = 62 h	^{70}Zn		1718	46	

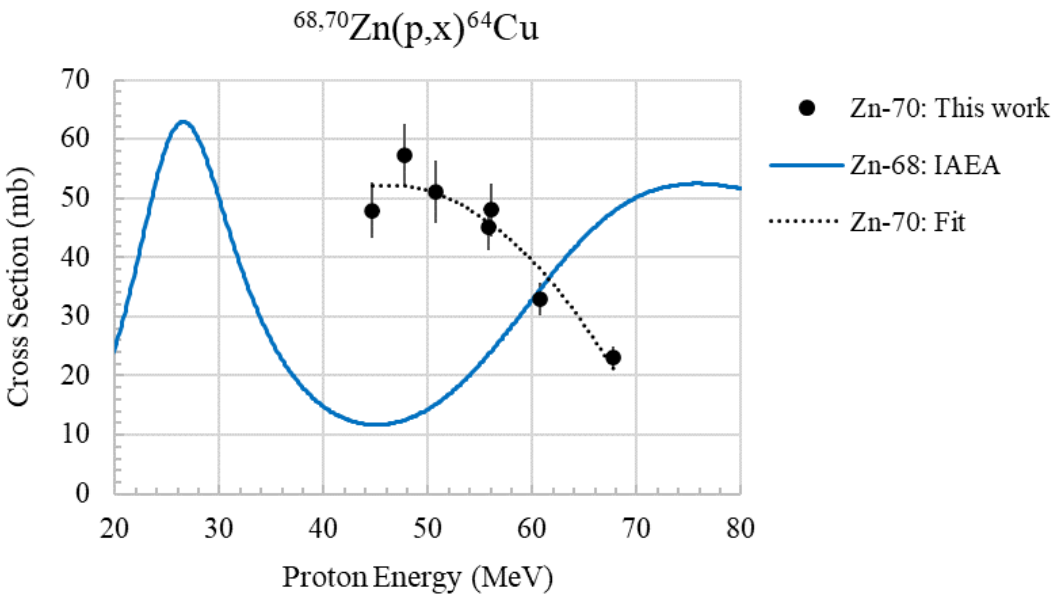

Figure 40: Comparison between the $^{70}Zn(p,x)^{64}Cu$ and $^{68}Zn(p,x)^{64}Cu$ nuclear cross sections

The ratio $^{67}Cu/^{64}Cu$ of nuclear cross sections obtained with ^{68}Zn and ^{70}Zn targets is presented in Figure 41. This graph is useful to identify the energy ranges in which is maximized the production of ^{67}Cu and minimizes ^{64}Cu.

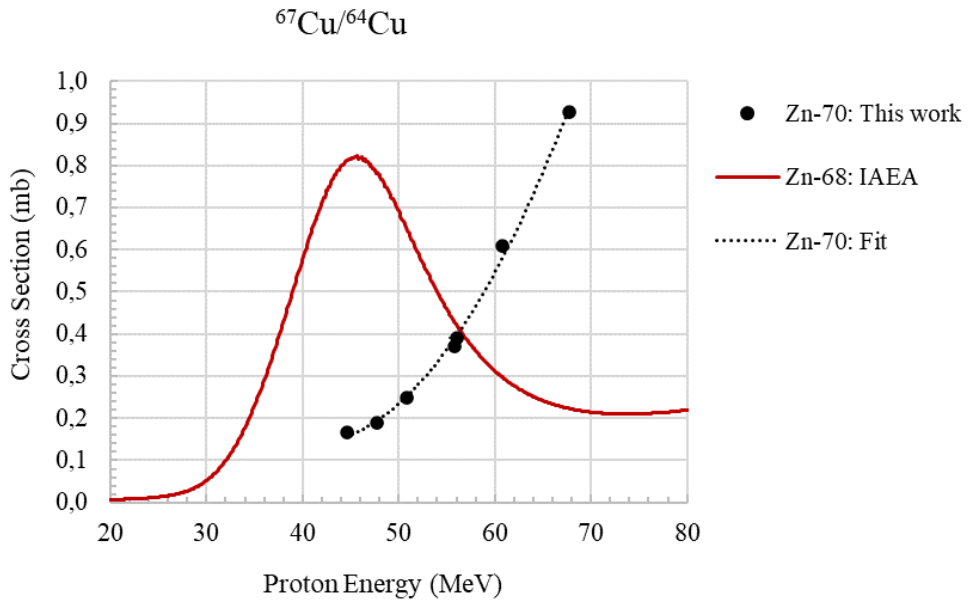

Figure 41: Comparison between the ratio $^{67}Cu/^{64}Cu$ of nuclear cross sections obtained with ^{68}Zn and ^{70}Zn targets

The result reported in Figure 41 allowed us to identify the optimal energy ranges to produce ^{67}Cu using the two different target materials. Up to an energy of 56 MeV it is convenient to use ^{68}Zn target, while for energies higher than 56 MeV it is convenient ^{70}Zn target (Figure 41). This multi-layer target configuration is described in the International Patent n° WO 2019/220224 A1 (November 2019), shown in Figure 42. The calculated yield of ^{67}Cu and ^{64}Cu radionuclides in the energy range 35-70 MeV are presented in Table 27 and Table 28, respectively for a multi-layer target (^{70}Zn and ^{68}Zn) and a thick ^{68}Zn target, considering in both cases I=1 μA and T_{irr}=62 h.

Table 27: ^{67}Cu and ^{64}Cu production yields for the two energy ranges (35-56 MeV and 56-70 MeV) for a multi-layer $^{70}Zn/^{68}Zn$ target configuration (I=1 μA; T_{irr}=62h)

T_{irr} = 62 h	Target	Isotope	MBq/μA	TOT (MBq/μA)	mCi/μA
35-56 MeV	**^{68}Zn**	^{67}Cu	591	1800	49
56-70 MeV	**^{70}Zn**		1209		
35-56 MeV	**^{68}Zn**	^{64}Cu	3540	5400	146
56-70 MeV	**^{70}Zn**		1879		

Table 28: ^{67}Cu and ^{64}Cu production yields in the 35-70 MeV energy range for ^{68}Zn target (I=1 μA; T_{irr}=62h)

T_{irr} = 62 h	Target	Isotope	MBq/μA	mCi/μA
35-70 MeV	**^{68}Zn**	^{67}Cu	1246	34
		^{64}Cu	6491	175

Table 27 and Table 28 show that a multi-layer $^{70}Zn/^{68}Zn$ target produces 45% more ^{67}Cu and 17% less ^{64}Cu in comparison with thick ^{68}Zn targets, for the same energy range and irradiation parameters. These theoretical results allowed me to propose a multi-layer target structure in which is present a second ^{70}Zn layer to exploit the $^{70}Zn(p,\alpha)^{67}Cu$ reaction in the energy range 25-10 MeV, as schematized in Figure 42.

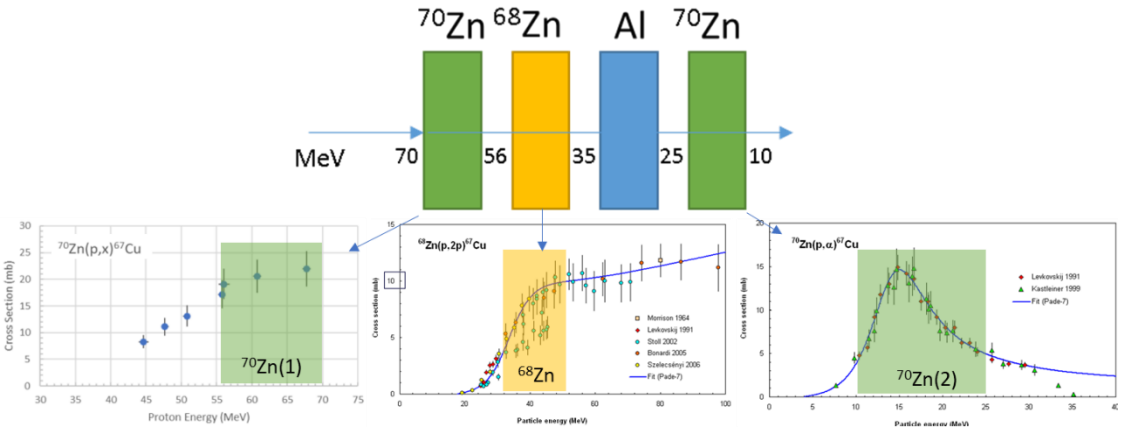

Figure 42: Schematic description of the multi-layer target configuration as proposed in the International Patent n° WO 2019/220224 A1 (November 2019)

In the energy range 25-35 MeV the ^{67}Cu production cross section is low for both targets and a degrader has been proposed to cover this energy range. The ^{67}Cu and ^{64}Cu production yields for this multi-layer target configuration (I=1 μA; T_{irr}=62 h) are reported in Table 29.

Table 29: ^{67}Cu and ^{64}Cu production yields for a multi-layer target configuration (I=1 μA; T_{irr}=62 h)

T_{irr} = 62 h	Target	Isotope	MBq/μA	TOT (GBq/μA)	mCi/μA
56-70 MeV	**^{70}Zn**		1209		
35-56 MeV	**^{68}Zn**	^{67}Cu	591	≈ 2	53
10-25 MeV	**^{70}Zn**		226		
56-70 MeV	**^{70}Zn**		3540		
35-56 MeV	**^{68}Zn**	^{64}Cu	1879	≈ 5.4	146
10-25 MeV	**^{70}Zn**		0		

Since the TTY is directly proportional to the beam current, one of the main objectives in the near future will be the development of the technology for the production of enriched zinc targets capable of withstanding enough high current to ensure a sufficient ^{67}Cu production for medical applications.

The importance of this goal is underlined by the theraputic studies carried out with [^{64}Cu]$CuCl_2$ in which a single therapeutic dose is about 100 mCi [106].

The LARAMED group is going to explore the entire production cycle of ^{67}Cu by developing the technology for target production, the main challenge for the large-scale production, the chemical separation, the purification procedure and the target recovery. Hopefully, studies on the realization of thick Zn targets will begin in 2021; to date, some

unconventional manufacturing techniques are under investigation to work out the technological challenge to get the assembly of the different layers requested. To recover the irradiated Zn it will be necessary to provide a separation between the two different isotopes used in the multi-layer target described: this aspect is an additional challange to carefully analyse. Indeed, the target recovery will be a fundamental step due to the price of enriched zinc. The market prices of enriched materials vary depending on the request and the difficulty in obtaining the required enrichment. As an example, Table 30 shows the offer obtained by the CHEMOTRADE company in March 2018 for ^{70}Zn and ^{68}Zn.

Table 30: Offer obtained by CHEMOTRADE company in March 2018 for ^{70}Zn and ^{68}Zn in metal powder

Isotope	Natural abundance [%]	Enrichment [%]	Form	Quantity (mg)	€/mg
^{68}Zn	18.5	99.2	oxide	100	5.8
			metal	100	5.8
^{70}Zn	0.6	98.7	oxide	100	23
		95.4	metal	100	23

Furthermore, a collaboration with experts in dosimetric calculations (L. Melendez-Alafort IOV and L. De Nardo INFN-PD) is ongoing, with the goal of finding out the effective dose due to the administration of ^{67}Cu and ^{64}Cu radionuclides both for the $CuCl_2$ form and for specific Cu-labelled radiopharmaceuticals.

6 THE PASTA PROJECT

The aim of the PASTA project (Production with Accelerator of Sc-47 for Theranostic Applications), developed in the framework of LARAMED [49] at INFN-LNL, is to study the production of ^{47}Sc by using proton accelerators. ^{47}Sc is one of the radionuclides of interest in theranostic thanks to its β^- and γ-radiation (Table 31) which make it suitable for both therapeutic and diagnostic purposes. The interest on ^{47}Sc, suggested as emerging theranostic radionuclide in the IAEA CRP started in 2016 [76], is also due to the possibility to pair it with a β^+ emitter isotope, such as ^{44g}Sc and ^{43}Sc, allowing to carry out also PET screenings [107].

Table 31: Nuclear data of ^{47}Sc [7]

Isotope	Half-life	Energy [keV] (Intensity [%])	β^- Mean energy [keV] (Intensity [%])
^{47}Sc	3.3492 d *6*	159.381 *15* (68.3 % *4*)	162.0 *21* (100 % *8*)

The limiting factor for clinical and preclinical studies with ^{47}Sc-labeled radiopharmaceuticals is the lack of ^{47}Sc availability. ^{47}Sc can be produced via different nuclear reaction routes by using cyclotrons, nuclear reactors, and electron linear accelerators. In all cases, it is possible to produce ^{47}Sc, either directly, or by the decay of a parent ^{47}Ca radionuclide, as shown in Table 32.

Table 32: Direct and indirect reactions to produce ^{47}Sc with the nuclear reactions induced by charged particles or neutrons

	Target	Cyclotrons/Electron Linac			Nuclear reactor
		p	d	α	n
Direct reactions	**Ti**	^{50}Ti(p,α) ^{47}Sc ^{49}Ti(p,2pn) ^{47}Sc ^{48}Ti(p,2p) ^{47}Sc	^{50}Ti(d,αn) ^{47}Sc ^{49}Ti(d,α)^{47}Sc ^{48}Ti(d,2pn)^{47}Sc ^{47}Ti(d,2p)^{47}Sc		^{47}Ti(n,p)^{47}Sc (fast neutrons)
	Ca	^{48}Ca(p,2n) ^{47}Sc	^{48}Ca(d,3n)^{47}Sc ^{46}Ca(d,n)^{47}Sc	^{44}Ca(α,p)^{47}Sc	
	V	^{51}V(p,αp) ^{47}Sc			
Indirect reactions	**Ti**	^{50}Ti(p,3pn)^{47}Ca→^{47}Sc ^{49}Ti(p,3p)^{47}Ca→^{47}Sc	^{50}Ti(d,αp)^{47}Ca→^{47}Sc		
	Ca	^{48}Ca(p,pn)^{47}Ca→^{47}Sc	^{48}Ca(d,p2n)^{47}Ca→^{47}Sc ^{46}Ca(d,p)^{47}Ca→^{47}Sc		^{46}Ca(n,γ)^{47}Ca→^{47}Sc (thermal neutrons)

Among all the possible ^{47}Sc production reactions, the LARAMED group, stimulated by the presence of the new proton-cyclotron at LNL, is interested in the study of the different reactions induced by proton beams. As in the case of the COME project, I was involved since the conception of the PASTA project and I took part in every step of the experiment. I actively participated in the writing phase of the project and I contributed to defining the structure of the experiment by dividing the work into several phases, shown below:

- study of literature on ^{47}Sc production;
- purchase of target materials (enriched Ti-metallic powders and ^{nat}V foils) and thin monitor foils (^{nat}Al and ^{nat}Ni);
- realization of the targets;
- planning and realization of the irradiation runs at different energies of the proton beam;
- γ-spectroscopy measurements of each irradiated foil;
- data analysis to obtain the ^{47}Sc production cross section for different proton beam energies and different target materials.

Considering the medical application of ^{47}Sc, the main purpose of the PASTA project is therefore to find the best proton-induced nuclear reaction and the optimal energy range that allows an enough ^{47}Sc production and a simultaneous minimization of the co-production of all possible contaminants [108] [109]. Particular attention must be paid to the other Sc-isotopes since they cannot be chemically separated from the produced ^{47}Sc. Among the Sc-isotopes, the most critical is the ^{46}Sc as it has a longer half-life (half-life 83.79 d) than the ^{47}Sc (half-life 3.3492 d).

Observing the natural abundances of the target materials that allow for the production of ^{47}Sc with proton beams, reported in bold in Table 33, and taking into account the cost of enriched materials as well, it was chosen to avoid the use of calcium targets and to focus the project on the titanium isotopes and natural vanadium.

Table 33: Natural abundance of target materials that allow the production of scandium isotopes considering a 70 MeV proton beam (^{47}Sc is produced from bold isotopes) [7]

Target	Abundance (%)
^{51}V	**99.750** ***2***
^{50}V	**0.250** ***2***
^{50}Ti	**5.18** ***2***
^{49}Ti	**5.41** ***2***
^{48}Ti	**73.72** ***3***
^{47}Ti	7.44 *2*
^{46}Ti	8.25 *3*
^{48}Ca	**0.187** ***21***
^{46}Ca	**0.004** ***3***
^{44}Ca	2.09 *11*
^{43}Ca	0.135 *10*
^{42}Ca	0.647 *23*
^{40}Ca	96.94 *16*

The composition of the ^{nat}V validates the use of easily available commercial foils to study ^{47}Sc production. Instead, in the case of natural titanium, the most abundant isotope is ^{48}Ti but with a percentage far from 100%. Considering the composition of ^{nat}Ti (Table 33) it is not possible to extract from the whole cross sections the contribution of each titanium isotope to the production of the specific radionuclides of interest. Indeed, the ^{nat}Ti(p,x)^{47}Sc reaction has been widely studied by many research groups, but no energy range has been found in which the ^{47}Sc, and not the ^{46}Sc, is produced, as shown in Figure 43 and Figure 44 [88]. For these reasons, one of the aims of the PASTA project is to study the reactions on different Ti-isotopes separately that have been barely investigated: indeed, no data are available for the ^{49}Ti(p,x)^{47}Sc cross section and a few data sets are published for the ^{50}Ti(p,x)^{47}Sc and ^{48}Ti(p,2p)^{47}Sc reactions, as reported in Figure 45 and Figure 46 [110] [80].

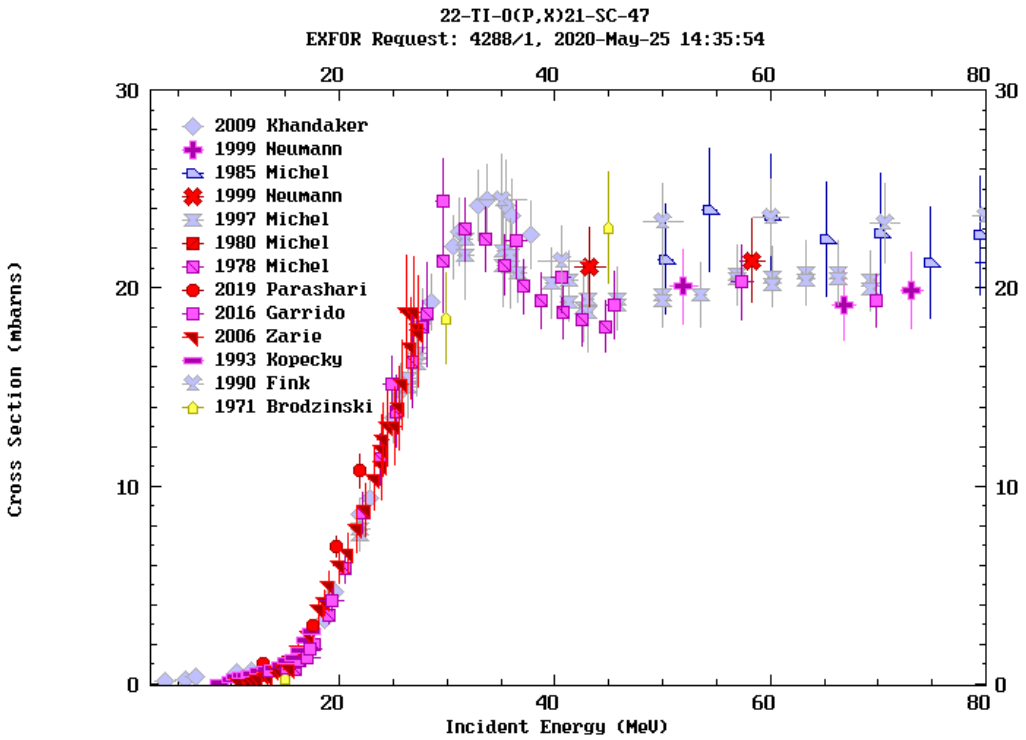

Figure 43: Cross section for $^{nat}Ti(p,x)^{47}Sc$ reaction extracted from the EXFOR DataBase [88]

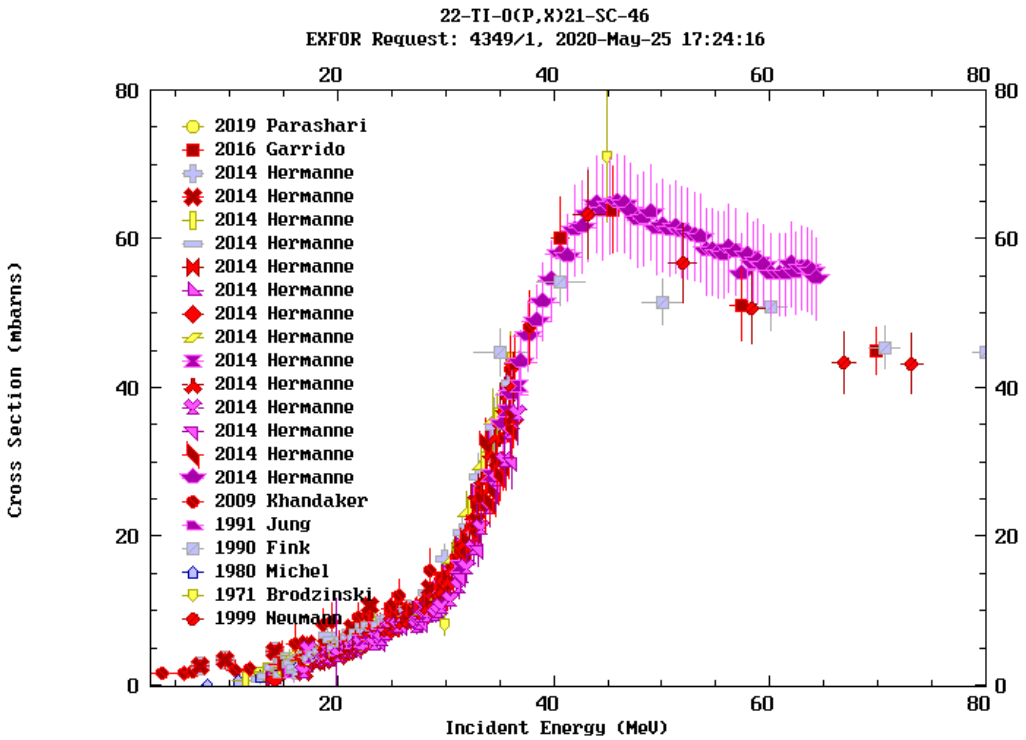

Figure 44: Cross section for $^{nat}Ti(p,x)^{46}Sc$ reaction extracted from the EXFOR DataBase [88]

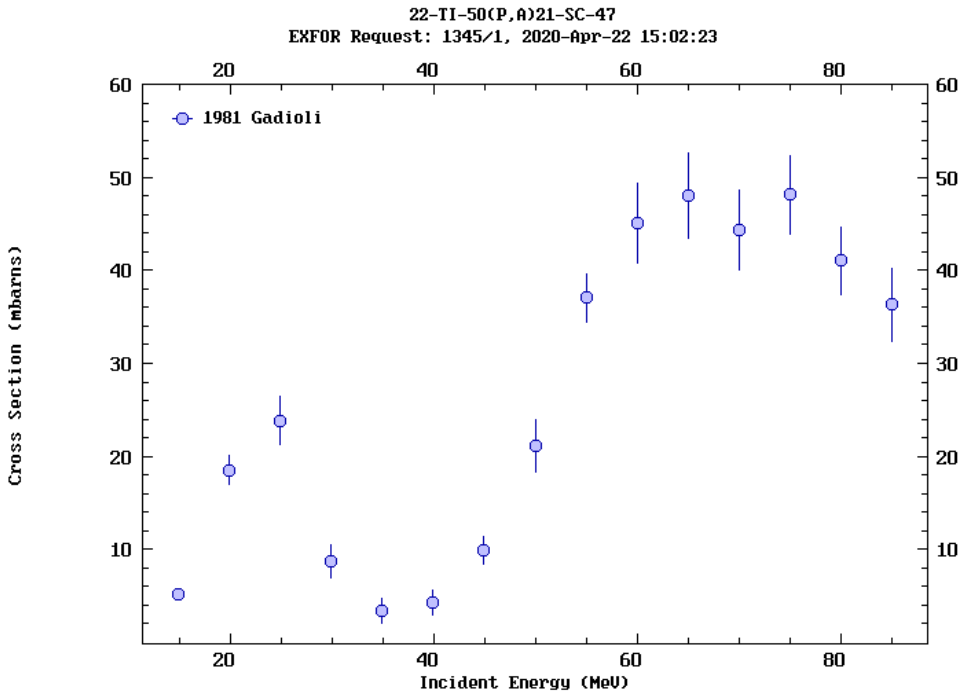

Figure 45: Cross section for $^{50}Ti(p,\alpha)^{47}Sc$ reaction extracted from the EXFOR DataBase [88]

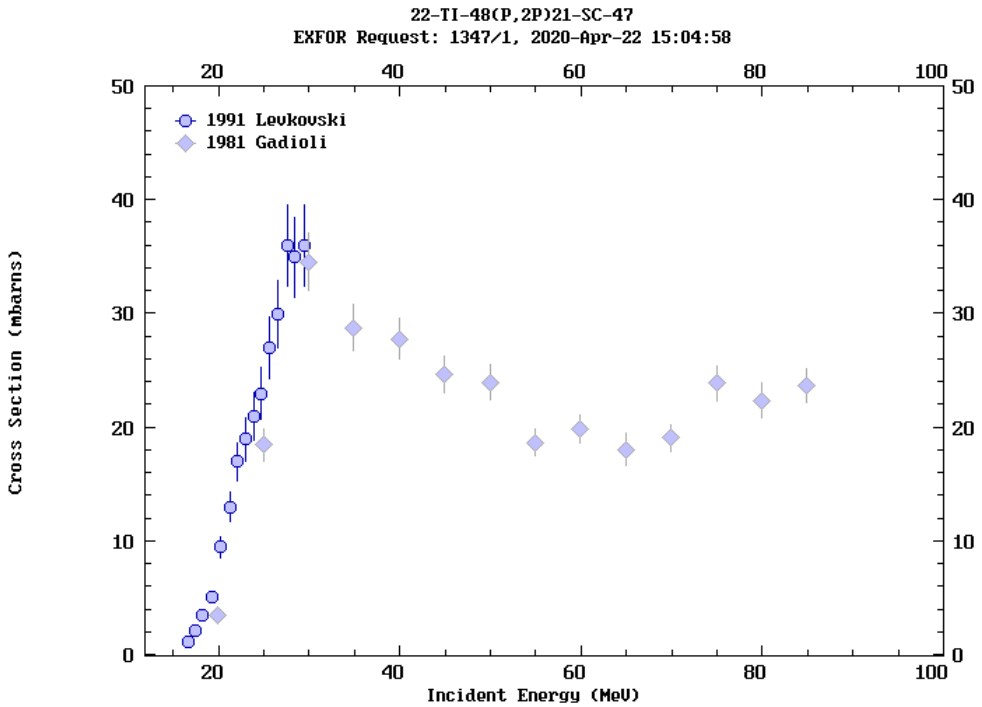

Figure 46: Cross section for $^{48}Ti(p,2p)^{47}Sc$ reaction extracted from the EXFOR DataBase [88]

On the contrary, the nuclear reactions induced on ^{nat}V targets (Figure 47) have been measured by many authors, as reported in literature [111] [112] [113] [114] [115] [116].

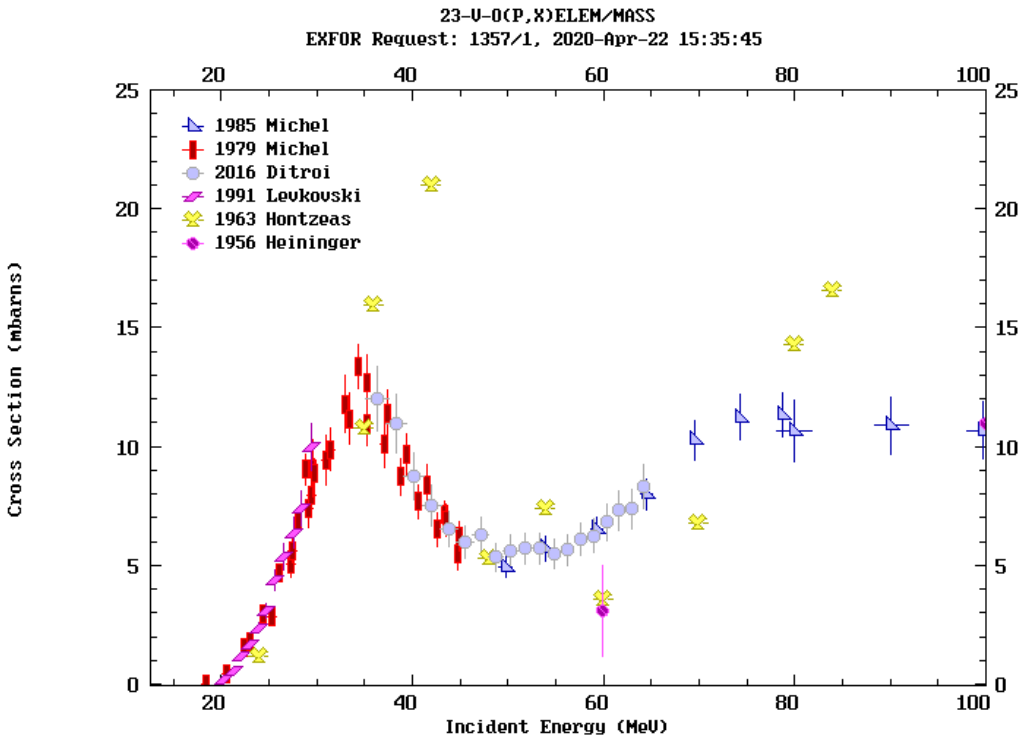

Figure 47: Cross section for $^{nat}V(p,x)^{47}Sc$ reaction extracted from the EXFOR DataBase [88]

To better plan the experiments, the National Nuclear Data Center (NNDC) database was consulted to identify the main radionuclides produced with the chosen targets and a 70 MeV proton beam. Table 34 reports the Q-values and the lower thresholds of possible reactions on ^{51}V to produce the radionuclides of interest.

Table 35, Table 36, and Table 37 report the Q-value and the lower threshold of possible reactions on ^{50}Ti, ^{49}Ti, and ^{48}Ti to produce the same radionuclides.

Table 34: Threshold energies to produce the radionuclides of interest from ^{51}V targets with proton bombardment [94]

	Reaction channel on ^{51}V target	**Q-value (keV)**	**Threshold (keV)**
^{48}Sc	p+^{3}He	-22631.22 *4.97*	23078.8 *5.07*
	2p+d	-28124.7 *4.97*	28680.92 *5.07*
	n+3p	-30349.26 *4.97*	30949.48 *5.07*
^{47}Sc	p+α	-10292.17 *1.97*	10495.72 *2.01*
	d+^{3}He	-28645.22 *1.97*	29211.74 *2.01*
	2p+t	-30106.03 *1.97*	30701.44 *2.01*
	n+p+^{3}He	-30869.79 *1.97*	31480.3 *2.01*
	p+2d	-34138.7 *1.97*	34813.86 *2.01*
	n+2p+d	-36363.26 *1.97*	37082.42 *2.01*
	2n+3p	-38587.83 *1.97*	39350.98 *2.01*
^{46}Sc	d+α	-18714.293 *0.792*	19084.408 *0.808*

	n+p+α	-20938.86 *0.792*	21352.97 *0.808*
	t+^{3}He	-33034.684 *0.792*	33688.016 *0.808*
^{44}Sc	n+t+α	-32544.93 *1.8*	33188.58 *1.84*
	2n+d+α	-38802.16 *1.8*	39569.55 *1.84*
	3n+p+α	-41026.73 *1.8*	41838.12 *1.84*
^{43}Sc	2n+t+α	-42244.13 *1.91*	43079.6 *1.94*
	3n+d+α	-48501.36 *1.91*	49460.58 *1.94*
	4n+p+α	-50725.92 *1.91*	51729.14 *1.94*
^{43}K	p+2α	-20478.287 *0.573*	20883.29 *0.585*
	d+^{3}He+α	-38831.34 *0.573*	39599.312 *0.585*
	2p+t+α	-40292.15 *0.573*	41089.01 *0.585*
^{42}K	d+2α	-27878.402 *0.415*	28429.758 *0.423*
	n+p+2α	-30102.967 *0.415*	30698.318 *0.423*
	t+3He+α	-42198.79 *0.415*	43033.36 *0.423*
^{48}V	n+t	-23458.3 *1.05*	23922.24 *1.08*
	2n+d	-29715.54 *1.05*	30303.22 *1.08*
	3n+p	-31940.1 *1.05*	32571.78 *1.08*
^{51}Cr	n	-1534.794 *0.213*	1565.148 *0.217*
^{49}Cr	3n	-23795.77 *2.28*	24266.38 *2.32*
^{48}Cr	4n	-34378.12 *7.33*	35058.02 *7.48*

Table 35: Threshold energies to produce the radionuclides of interest from ^{50}Ti targets with proton bombardment [94]

	Reaction channel on ^{50}Ti target	**Q-value (keV)**	**Threshold (keV)**
^{49}Sc	2p	-12159.0 3.0	12405.0 3.0
^{48}Sc	^{3}He	-14570.0 5.0	14864.0 5.0
	p+d	-20064.0 5.0	20468.0 5.0
	n+2p	-22288.0 5.0	22738.0 5.0
^{47}Sc	α	-2231.0 1.9	2276.0 2.0
	p+t	-22044.9 1.9	22489.6 2.0
	n+^{3}He	-22808.6 1.9	23268.7 2.0
	2d	-26077.5 1.9	26603.6 2.0
	n+p+d	-28302.1 1.9	28873.0 2.0
	2n+2p	-30526.7 1.9	31142.5 2.0
^{46}Sc	n+α	-12877.7 0.7	13137.5 0.7
	d+t	-30467.0 0.7	31081.6 0.7
	n+p+t	-32691.6 0.7	33351.0 0.7
^{44}Sc	3n+α	-32965.6 1.8	33630.6 1.8
	n+2t	-44297.6 1.8	45191.2 1.8
	2n+d+t	-50554.9 1.8	51574.7 1.8
^{43}Sc	4n+α	-42664.8 1.9	43525.4 1.9
	2n+2t	-53996.8 1.9	55086.1 1.9
	3n+d+t	-60254.1 1.9	61469.6 1.9
^{43}K	2α	-12417.1 0.4	12667.6 0.4
	p+t+α	-32231.0 0.4	32881.2 0.4
	n+^{3}He+α	-32994.8 0.4	33660.3 0.4
^{42}K	n+2α	-22041.81 0.16	22486.45 0.16
	d+t+α	-39631.11 0.16	40430.58 0.16
	n+p+t+α	-41855.68 0.16	42700.02 0.16
^{48}V	3n	-23878.9 1.0	24360.6 1.0

Table 36: Threshold energies to produce the radionuclides of interest from ^{49}Ti targets with proton bombardment [94]

	Reaction channel on ^{49}Ti target	Q-value (keV)	Threshold (keV)
^{48}Sc	2p	-11349.0 *5.0*	11583.0 *5.0*
^{47}Sc	^{3}He	-11869.4 *1.9*	12113.8 *2.0*
	p+d	-17362.9 *1.9*	17720.3 *2.0*
	n+2p	-19587.5 *1.9*	19990.7 *2.0*
^{46}Sc	α	-1938.5 *0.7*	1978.4 *0.7*
	p+t	-21752.4 *0.7*	22200.1 *0.7*
	n+^{3}He	-22516.1 *0.7*	22979.6 *0.7*
^{44}Sc	2n+α	-22026.4 *1.8*	22479.8 *1.8*
	2t	-33358.5 *1.8*	34045.1 *1.8*
	n+d+t	-39615.7 *1.8*	40431.1 *1.8*
^{43}Sc	3n+α	-31725.6 *1.9*	32378.6 *1.9*
	n+2t	-43057.7 *1.9*	43943.9 *1.9*
	2n+d+t	-49314.9 *1.9*	50330.0 *1.9*
^{43}K	^{3}He+α	-22055.6 *0.4*	22509.5 *0.4*
	p+d+α	-27549.0 *0.4*	28116.1 *0.4*
	n+2p+α	-29773.6 *0.4*	30386.5 *0.4*
^{42}K	2α	-11102.62 *0.16*	11331.15 *0.16*
	p+t+α	-30916.49 *0.16*	31552.86 *0.16*
	n+^{3}He+α	-31680.24 *0.16*	32332.34 *0.16*
^{48}V	2n	-12939.8 *1.0*	13206.1 *1.0*

Table 37: Threshold energies to produce the radionuclides of interest from ^{48}Ti targets with proton bombardment [94]

	Reaction channel on ^{48}Ti target	Q-value (keV)	Threshold (keV)
^{47}Sc	2p	-11445.1 *1.9*	11685.6 *2.0*
^{46}Sc	^{3}He	-14373.7 *0.7*	14675.8 *0.7*
	p+d	-19867.2 *0.7*	20284.7 *0.7*
	n+2p	-22091.8 *0.7*	22556.0 *0.7*
^{44}Sc	n+α	-13884.0 *1.8*	14175.7 *1.8*
	d+t	-31473.3 *1.8*	32134.6 *1.8*
	n+p+t	-33697.9 *1.8*	34405.9 *1.8*
^{43}Sc	2n+α	-23583.2 *1.9*	24078.7 *1.9*
	2t	-34915.3 *1.9*	35648.9 *1.9*
	n+d+t	-41172.5 *1.9*	42037.6 *1.9*
^{43}K	2p+α	-21631.2 *0.4*	22085.7 *0.4*
	2^{3}He	-34490.8 *0.4*	35215.5 *0.4*
	P+d+^{3}He	-39984.3 *0.4*	40824.4 *0.4*
^{42}K	3He+α	-23537.85 *0.15*	24032.45 *0.16*
	p+d+α	-29031.32 *0.15*	29641.36 *0.16*
	n+2p+α	-31255.89 *0.15*	31912.67 *0.16*
^{48}V	n	-4797.4 *1.0*	4898.2 *1.0*

6.1 Target preparation

Highly pure metal ^{nat}V foils are available commercially, while enriched titanium is available only in the form of a metallic powder or as titanium dioxide. For this reason, at INFN-LNL a new technique was developed in the framework of LARAMED R&D activities aimed at the targets manufacturing suitable for cross section measurements within the E_PLATE project (INFN-LNL, 2018/2019, PI Ms. H. Skliarova) [49] [117] [84]. The project is devoted to R&D on HIgh energy VIbration Powders Plating (HIVIPP) technique, proposed by I. Sugai [83], for accelerator target production starting from enriched powder materials. The HIVIPP technique allows to prepare targets of enriched materials, comprising refractories, some other metals, and even non-metallic materials with high efficiency, i.e. no losses of material during the process. This method is based on the powder's motion in an electric field. Two target substrates are placed in contact with two electrodes, at the top and bottom; between them, a quartz cylinder, isolating the powder of the material to deposit, is inserted. This system is placed in a vacuum chamber and a high voltage (>3 kV) is applied to the electrodes. Due to the electric field, the powder starts to be charged and to quickly move towards the electrode having opposite charge. When the acquired kinetic energy of the particle is enough, it is deposited onto the substrate surface (usually >10 kV). Within the HIVIPP method, two targets are deposited simultaneously.

In this work, thin ^{48}Ti metal targets were produced by using the HIVIPP technique and enriched metal powders purchased by TRACE (Richmond Hill, Ontario, Canada). A quartz cylinder of 1 cm height and an internal diameter of 14 mm, in order to minimize the consumption of the isotopically enriched material, was used. Al foils, 25 μm thick, and 99% purity (Goodfellow, Cambridge Ltd, UK) were used as substrates to use them also as reference monitors of the particle flux during the cross-section measurements. The depositions were carried out in a vacuum of $1 \cdot 10^{-7}$ mbar and at 15 kV. A scheme of the experimental set up used to realize the ^{48}Ti metal targets is shown in Figure 48. More details on the target realization and analysis are described in dedicated works published [117] [84].

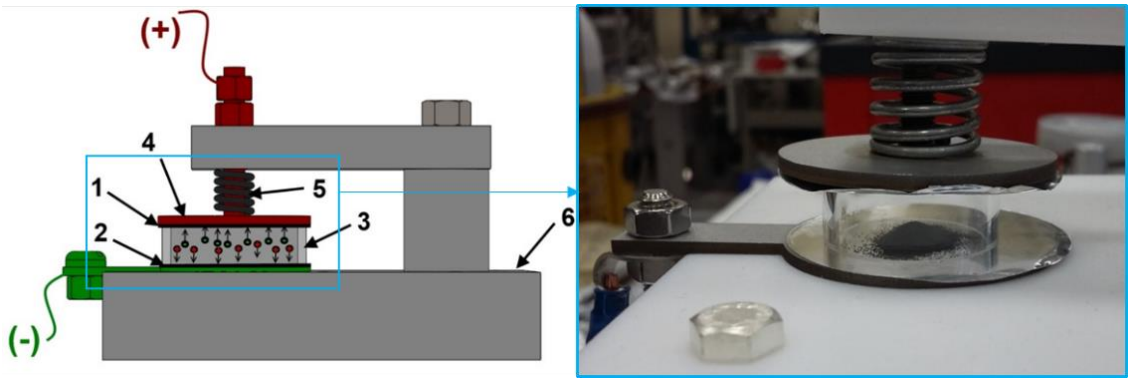

Figure 48: Scheme (left) and photo (right) of the HIVIPP experimental set up carried out at LNL-INFN: 1-Backing (upper electrode, cathode), 2-Backing (lower electrode, anode), 3-Quartz cylinder, 4–Pressing plate, 5-Spring, 6– Teflon holder

The material not deposited can be recovered making this technique useful for enriched and expensive materials. An example of ^{48}Ti metal target realized is shown in Figure 49. The ^{48}Ti metal target was cut with a 12 mm die to fit the target holder (described in the previous chapter) and it is evident from the image on the right that the target withstood the irradiation conditions without damage.

Figure 49: ^{48}Ti target realized (left), cut with a 12 mm die fitting the target-holder dimensions (middle) and the irradiated target without visible damages (right)

For the cross section measurements, it is essential to know the quantity of material deposited (mg/cm^2) on the aluminum support. For this reason, the samples were analyzed by the Elastic Backscattering Spectrometry (EBS), at the LNL AN2000 Accelerator, using a proton beam of 1 mm diameter at 1.8 MeV and 10-20 nA current intensity [84]. The analysis of the obtained spectra performed under the E_PLATE project allows to get the deposited material amount. Figure 50 shows that the deposited titanium is obtained from the fit (black line) of the experimental data (red dots) taking into account the contribution due to the presence of the aluminum substrate (blue line), titanium (gray line) and oxygen (purple line) due to the titanium oxidation, by

minimizing the sum of the square difference between the calculated and measured channel values. The long tail of low concentration is due to the roughness induced by Ti grain dimensions. The presence of Al on the surface is shown by the high energy edge in blue line.

The EBS analysis gives a more precise evaluation of the deposited Ti (mg/cm^2) than the value obtained from the simple weighing of the aluminum support before and after the deposition. From the weight it is not possible to discriminate the contribution of the amount of oxygen, in the partially oxidized target, and this entails an overestimation of the deposited amount. On the other hand, the analysis with EBS technique refers only to the area hit by the proton beam. Therefore, in order to have a representative value of the whole target set, it would be desirable to average the EBS results obtained from several measurements in different areas of the same target. However, complete scans of only two targets were performed to check the uniformity of the deposition; additional information on EBS analysis can be found in the dedicated article recently published [84]. To date we have not been able to analyze all the ^{48}Ti targets that have already been irradiated; the measures of the remaining targets are planned by 2020.

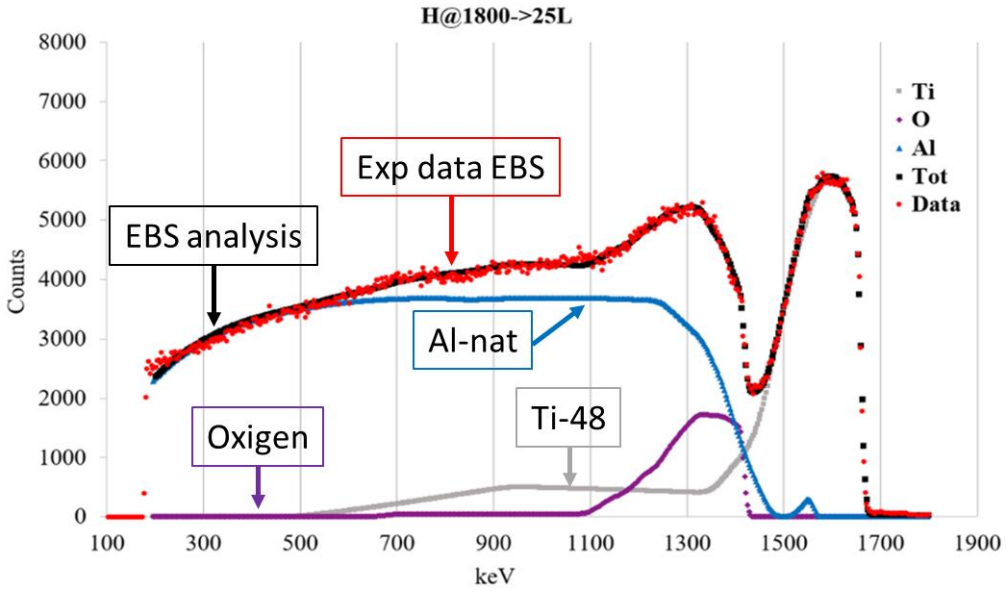

Figure 50: Example of an analysis procedure of the EBS spectrum of ^{48}Ti on Al target

The batches of enriched ^{49}Ti and ^{50}Ti powders were purchased from the Oak Ridge National Laboratory (Oak Ridge TN, USA). Unfortunately, the enriched materials received were not in the form of metallic powder, but in the form of metal sponge having different grain sizes and shapes, being the maximum size of the metal sponge 2 mm.

Figure 51 shows the case of enriched ^{49}Ti, with a picture of the received vial and a picture obtained with a Scanning Electron Microscope (SEM) analysis.

The deposition with the HIVIPP technique starting directly from the untreated materials resulted inefficient, even selecting the smallest powder. Two targets were realized as test: the obtained deposits were inhomogeneous, as shown in Figure 52. The deposit is composed by grains of variable size between a few µm up to about 100 µm, making the sample impossible to be used for nuclear cross section measurements.

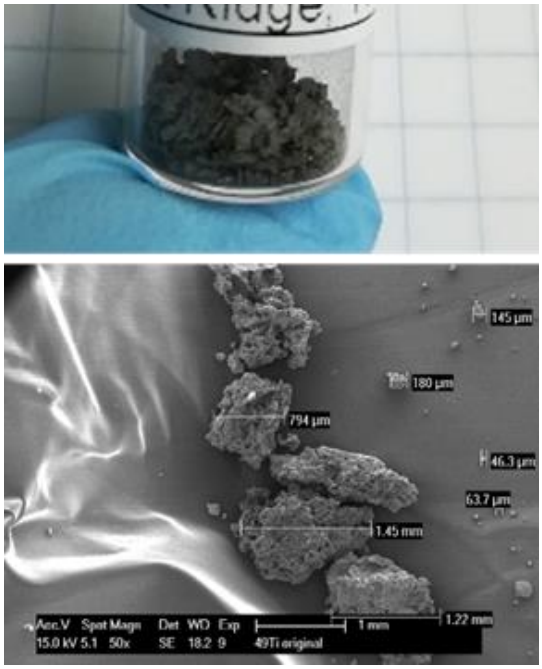

Figure 51: Enriched ^{49}Ti: picture of the material (top); SEM image (bottom)

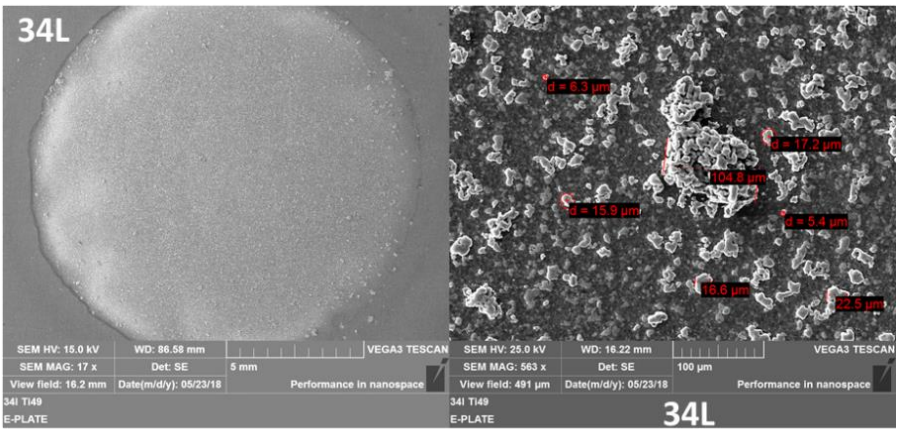

Figure 52: ^{49}Ti target realized with the HIVIPP technique by using the smallest grains of the material received in metallic sponges

For this reason, a method to treat the materials and reduce homogeneously the size of the powder to be deposited was developed. A cryomilling procedure, able to apply a multidirectional impact on the powder, was optimized using ^{nat}Ti material, with stainless-steel jar and spheres of the cryomilling system. The ^{nat}Ti material was purchased in a form as much as similar to the ^{49}Ti shape, in order to simulate the procedure as much as possible. Figure 53 shows the results of the optimized procedure. The powder size resulting after the cryomilling was less than 20 μm, like the ^{48}Ti powder used successful manufactured for the realization of the targets mentioned above.

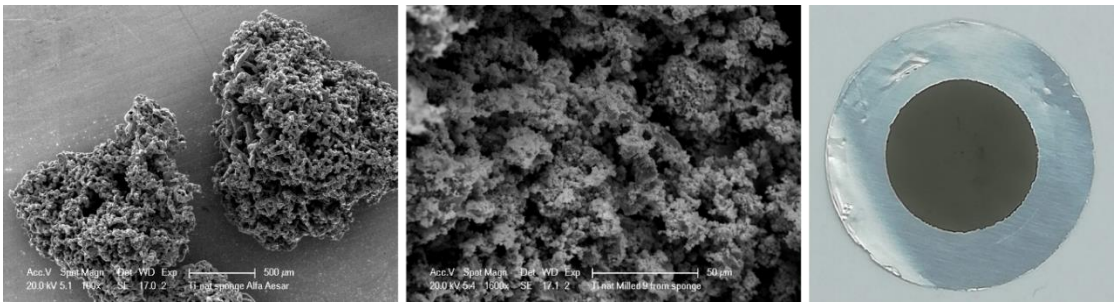

Figure 53: SEM images of ^{nat}Ti material before (left) and after (middle) cryomilling process. Target realized by HIVIPP technique with cryomilled ^{nat}Ti powder (right)

During 2020 it is expected to optimize the process to realize the ^{49}Ti targets and complete the characterization of the ^{48}Ti targets; ^{50}Ti targets are expected to be manufactured by 2021.

6.2 Experimental description

As in the case of ^{67}Cu, the irradiation runs are performed at the ARRONAX facility and the stacked-foils target method is used. When possible, ^{nat}V (purity > 99.8%, 20 μm thick) and ^{48}Ti (purity > 99.3%, thick < 3 μm) targets were irradiated at the same time, as in the case shown in Figure 54. The distribution of the different foils (targets and related monitor foils) in the stacked-foils target was chosen to be able to quantify the recoil effect that has to be taken into account in the data analysis. In these experiments, a radiochemical treatment of the irradiated targets is not necessary, and after the target disassembling, it was possible to start immediately the γ-spectroscopy measurements. For this reason, it was possible to irradiate up to 5 targets simultaneously; several targets of the same material were separated with two different Al degraders, thus identifying

three different energy ranges (Figure 54). A monitor and at least one target foil were positioned in each energy range identified, and their order was chosen to allow the quantification of the recoils of the different isotopes produced.

The first experiments were carried out exclusively with ^{nat}V targets due to the technical time needed to purchase the enriched ^{48}Ti and for the realization of the targets with the HVIPP technique.

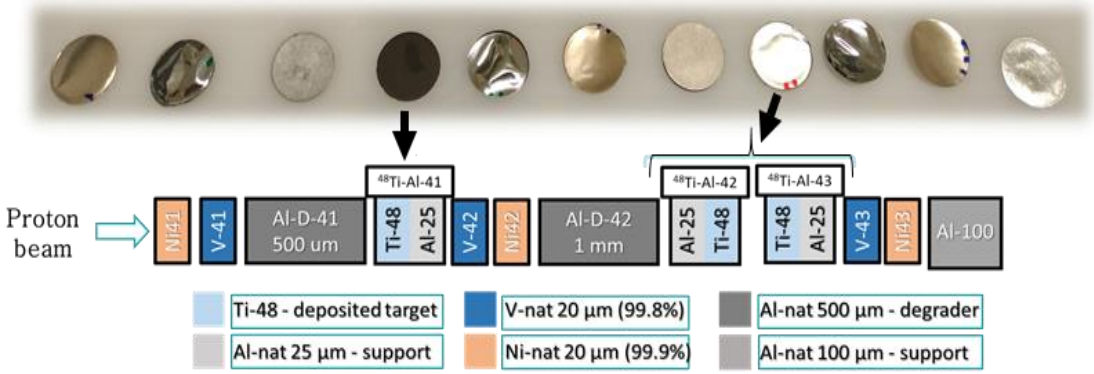

Figure 54: Schematic structure of the stacked-foils target used in the IV irradiation run

Six irradiation runs were performed at the ARRONAX facility using a proton beam with tunable energy (34–70 MeV); the duration of typical irradiation was 1.5 hours with a constant current flow of about 100 nA. The irradiation parameters of the irradiation runs performed to study the ^{47}Sc production are reported in Table 38.

Table 38: Parameters of irradiation runs performed to study the ^{47}Sc production

Irradiation run #	**Proton energy (MeV)**	**Irradiation time (minutes)**	**Mean current (nA)**	**Reaction**	**Irradiated targets #**
1	70.3	90	≈ 100	$^{nat}V(p,x)^{47}Sc$	3
2	54.0	90	≈ 100	$^{nat}V(p,x)^{47}Sc$	3
3	61.0	90	≈ 100	$^{nat}V(p,x)^{47}Sc$	3
4	34.0	90	≈ 120	$^{48}Ti(p,x)^{47}Sc$ $^{nat}V(p,x)^{47}Sc$	2 3
5	40.0	50	≈ 130	$^{48}Ti(p,x)^{47}Sc$ $^{nat}V(p,x)^{47}Sc$	4 1
6	34.0	90	≈ 100	$^{48}Ti(p,x)^{47}Sc$ $^{nat}V(p,x)^{47}Sc$	3 1

At the end of each irradiation, the activated target was disassembled and each target was measured via γ-spectrometry. Unlike the measurements to study the production of ^{67}Cu,

since there are no interferences with the ^{47}Sc γ-lines, it was not necessary to apply a chemical separation procedure to the irradiated targets. The γ-spectrometry measurements were performed with a High Purity Germanium Detectors (HPGe) at a distance of 19 cm from the detector (geometry named g1). For the acquisition geometries g1 the efficiency of the detector was obtained by using the formula 5.1 and a reference ^{152}Eu point-like solid source, provided by ARRONAX (purchased by CERCA-LEA, Site Nucléaire du Tricastin, France). Before the sixth irradiation, the calibration procedure was repeated. For this reason, only in this case a different calibration curve, indicated with g1*, was used. Both values are reported in Table 39.

Table 39: Values of the coefficients c_x present in the efficiency formula (5.1) for the geometry at 19 cm (g1 and g1)*

Coefficient	Value (g1)	Value (g1*)
c_1	-0.17327000	-0.17217200
c_2	-8.58062000	-8.49034000
c_3	1.24848000	1.07953000
c_4	-0.31971600	-0.22201400
c_5	0.04463840	0.02420220
c_6	-0.00238326	-0.00105495

The first γ-acquisition of each foil started 2-3 hours after the EOB and lasted for 15 minutes. In the days following the irradiation, we have carried out γ-spectrometry measurements (usually 2-3 hours long) to follow the decay of the produced radionuclides. It was also performed an additional acquisition of each foil about 2-3 months after the EOB. In this way, we measured the activity of the long-lived isotopes, such as ^{46}Sc (83.79 d [7]), with a larger precision due to the reduction of the compton component in the spectrum. Altogether, at least 5 acquisitions of each irradiated sample were performed. The repeated acquisitions also allow to verify potential discrepancies at specific γ-lines due to expected interference between two different elements. The cross sections, as a function of energy, were then calculated by using the procedure described by N. Otuka et al. [46] (equation 3.15). As in the case of ^{67}Cu, to be able to know with sufficient precision the beam flux, ^{nat}Al and ^{nat}Ni foils were used by referring to the well-known ^{nat}Al(p,x)^{24}Na and ^{nat}Ni(p,x)^{57}Ni monitor reactions recommended by the IAEA [99] [100].

In the irradiations with the beam energy lower than 40 MeV it was chosen to use as a monitor reaction the one on ^{nat}Ni target because it has the highest cross section in

comparison with the one on ^{nat}Al (Figure 55). The values of the reference cross section used, with related uncertainty, are reported in Table 40. The uncertainty varies from 5% to 8% and this is the major contribution to the uncertainty of the measured cross section.

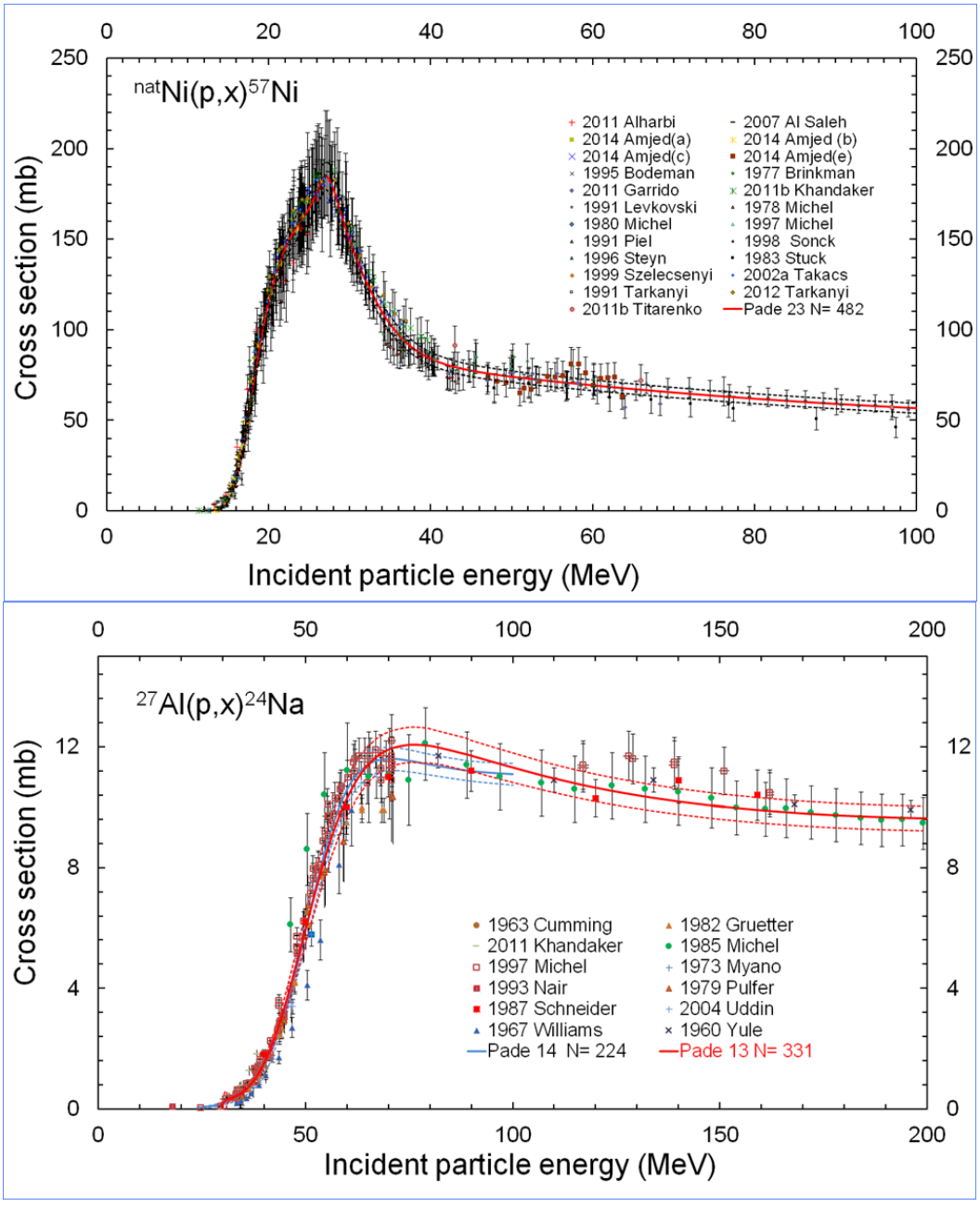

Figure 55: Recommended cross section for ^{27}Al(p,x)^{24}Na and ^{nat}Ni(p,x)^{57}Ni reactions [99] [100]

The nuclear data used in the data analysis performed to obtain the ^{48}Sc, ^{47}Sc, ^{46}Sc, ^{44}Sc, ^{44m}Sc, ^{43}Sc, ^{48}V, ^{43}K, ^{42}K, ^{48}Cr, ^{49}Cr, and ^{51}Cr cross sections are extracted from the NuDat 2.7 database [94] and reported in Table 41.

Table 40: The $^{nat}Al(p,x)^{24}Na$ and $^{nat}Ni(p,x)^{57}Ni$ monitor reaction values used [99] [100]

Energy [MeV]	Reference radionuclide	Reference cross section [mb]
26.3 ± 0.9	^{57}Ni	180.2 ± 7.5
29.0 ± 0.8	^{57}Ni	162.9 ± 6.8
31.1 ± 0.7	^{57}Ni	136.6 ± 5.7
33.5 ± 0.6	^{57}Ni	113.9 ± 4.8
39.3 ± 0.6	^{57}Ni	85.6 ± 3.6
48.1 ± 0.8	^{24}Na	4.8 ± 0.3
50.9 ±0.7	^{24}Na	6.4 ±0.5
53.7 ±0.5	^{24}Na	8.0 ±0.6
55.6 ±0.8	^{24}Na	9.0 ±0.6
58.2 ±0.7	^{24}Na	10.0 ±0.7
60.7 ±0.5	^{24}Na	10.8 ±0.5
65.5 ±0.8	^{24}Na	11.4 ±0.5
67.7 ±0.7	^{24}Na	11.6 ±0.5
70.0 ± 0.5	^{24}Na	11.6 ± 0.4

Table 41: Nuclear data used in the cross section calculations [7]

Isotope	Half-life	Energy [keV]	Intensity [%]
^{48}Sc	43.67 h *9*	1037.522 *12*	97.6 *7*
^{47}Sc	3.3492 d *6*	159.381 *15*	68.3 *4*
^{46}Sc	83.79 d *4*	889.277 *3*	99.9840 *10*
^{44}Sc	3.97 h *4*	1157.020 *15*	99.9 *4*
^{44m}Sc	58.61 h *10*	1157.002 *3* 271.241 *10*	1.20 86.7 *3*
^{43}Sc	3.891 h *12*	372.9 *3*	22.5
^{43}K	22.3 h *1*	372.760 *7*	86.80
^{42}K	12.355 h *7*	1524.6 *3*	18.08
^{48}Cr	21.56 h *3*	308.24 *6*	100
^{49}Cr	42.3 m *1*	152.928 *2*	30.3 *11*
^{51}Cr	27.7025 d *24*	320.0824 *4*	9.910 *10*

The different acquisitions permit to have several cross section estimations for the same sample and the same radionuclide. The final cross section was calculated as the weighted average of the single values. The resulting uncertainty, calculated by using the equation 3.17, is thus smaller than those obtained through every single measurement. The uncertainty of the monitor cross section, reported in Table 40, is the most important systematic error and it is added at the end of this calculation. The data analysis was performed by me and the final results for all the 12 radionuclides produced were compared with the results obtained by L. De Dominicis *[81]*. The measured $^{nat}V(p,x)^{48}Sc$, ^{47}Sc, ^{46}Sc, ^{44g}Sc, ^{44m}Sc, ^{43}Sc, ^{48}V, ^{43}K, ^{42}K, ^{48}Cr, ^{49}Cr, ^{51}Cr cross sections

are listed in Table 42. The uncertainty of the proton energy considers the uncertainty on the extracted proton beam (± 500 keV) and the energy straggling calculated with the SRIM software *[41]*, giving a maximum value of ± 800 keV. The results on ^{nat}V targets are always compared with TALYS calculations and literature data extracted from the EXFOR database *[88]*. The older data are reported in the following graphs as extracted from EXFOR. As already described in chapter 5, data by V.N. Levkovski *[80]* were corrected by a factor of 0.77 *[101]* (indicated in the graphs by adding a star next to the author's name). All the error bars available on EXFOR are also reported in the following figures. The TALYS code was used both with default parameters and with a set of specific parameters that have been previously optimized by comparing simulations with experimental values for many nuclear reactions under the name "TALYS*" *[97]*.

Table 42: Measured cross sections of the $^{nat}V(p,x)$ ^{48}Sc, ^{47}Sc, ^{46}Sc, ^{44g}Sc, ^{44m}Sc, ^{43}Sc, ^{48}V, ^{43}K, ^{42}K, ^{48}Cr, ^{49}Cr, ^{51}Cr reactions

Energy [MeV]	**^{48}Sc [mb]**	**^{47}Sc [mb]**	**^{46}Sc [mb]**	**^{44g}Sc [mb]**	**^{44m}Sc [mb]**	**^{43}Sc [mb]**	**^{48}V [mb]**	**^{43}K [mb]**	**^{42}K [mb]**	**^{48}Cr [mb]**	**^{49}Cr [mb]**	**^{51}Cr [mb]**
70.0 ± 0.6	2.3 ± 0.2	8.0 ± 0.4	16.4 ± 0.9	8.7 ± 0.6	8.0 ± 0.4	0.4 ± 0.1	72.4 ± 6.7	0.27 ± 0.02	2.0 ± 0.1	1.1 ± 0.1	6.2 ± 1.0	10.9 ± 1.0
67.8 ± 0.7	2.4 ± 0.2	7.7 ± 0.5	16.7 ± 1.0	7.3 ± 0.6	7.0 ± 0.4	0.3 ± 0.1	79.0 ± 7.2	0.30 ± 0.02	2.0 ± 0.1	1.3 ± 0.1	6.8 ± 1.1	11.7 ± 1.1
65.5 ± 0.8	2.3 ± 0.2	6.8 ± 0.4	16.7 ± 1.0	5.7 ± 0.5	5.2 ± 0.3	0.1 ± 0.1	80.9 ± 11.2	0.32 ± 0.02	1.9 ± 0.1	1.4 ± 0.1	7.2 ± 0.8	11.8 ± 0.9
60.7 ± 0.6	1.9 ± 0.1	5.1 ± 0.3	18.6 ± 1.2	2.1 ± 0.2	1.9 ± 0.1	0.3 ± 0.3	91.8 ± 7.6	0.39 ± 0.03	1.3 ± 0.1	1.7 ± 0.1	9.1 ± 1.0	16.5 ± 1.2
58.3 ± 0.7	1.8 ± 0.1	5.0 ± 0.4	21.6 ± 1.8	1.2 ± 0.1	1.1 ± 0.1	0.1 ± 0.1	103.3 ± 10.6	0.43 ± 0.04	0.9 ± 0.1	1.9 ± 0.2	10.6 ± 1.3	18.3 ± 1.6
55.7 ± 0.8	1.4 ± 0.1	4.4 ± 0.4	23.0 ± 1.9	0.6 ± 0.1	0.47 ± 0.04	0.05 ± 0.03	100.9 ± 9.8	0.42 ± 0.04	0.48 ± 0.05	1.9 ± 0.2	11.2 ± 1.2	18.4 ± 1.7
53.6 ±0.6	1.0 ± 0.1	4.1 ± 0.3	25.1 ± 2.0	0.35 ± 0.03	0.25 ± 0.02	0.07 ± 0.04	100.8 ± 9.8	0.41 ± 0.03	0.26 ± 0.03	1.8 ± 0.1	12.1 ± 1.5	16.8 ± 1.4
51.0 ±0.7	0.7 ± 0.1	4.1 ± 0.3	27.8 ± 2.3	0.19 ± 0.04	0.13 ± 0.01	0.1 ± 0.1	91.1 ± 9.3	0.32 ± 0.03	0.07 ± 0.01	1.5 ± 0.1	14.2 ± 1.7	17.3 ± 1.6
48.1 ±0.8	0.37 ± 0.03	4.6 ± 0.3	30.8 ± 2.4	0.17 ± 0.05	0.05 ± 0.01	0.4 ± 0.2	74.5 ± 7.3	0.20 ± 0.02		1.0 ± 0.1	18.3 ± 2.6	19.7 ± 1.8
39.5 ±0.6		8.3 ± 0.5	18.6 ± 1.1				8.3 ± 0.8				28.9 ±2.8	25.7 ± 1.6
33.3 ±0.6		10.9 ± 0.6	2.6 ± 0.2				2.4 ± 0.2				25.3 ± 2.6	32.3 ± 1.9
31.2 ±0.7		9.0 ± 0.5	0.6 ± 0.1				1.2 ± 0.1				17.2 ± 1.7	34.1 ± 2.0
29.2 ±0.8		7.4 ± 0.5					0.40 ± 0.02				8.3 ± 0.9	33.7 ± 2.2
26.5 ± 0.8		4.3 ± 0.2					0.15 ± 0.02				0.7 ± 0.1	46.2 ± 2.9

6.3 Results and discussion

In this paragraph, all the results obtained within the PASTA project will be described in detail.

6.3.1 ^{48}Ti(p,x)^{47}Sc, ^{46}Sc, ^{44}Sc, ^{44m}Sc cross sections

The first data obtained for the ^{48}Ti(p,x)^{47}Sc, ^{46}Sc, ^{44g}Sc, ^{44m}Sc cross sections are reported in Figure 56. As already mentioned, the characterization tests of the ^{48}Ti deposit on the Al support are not yet completed. Some samples have still to be measured and it is planned to do it before the end of 2020. The information on the deposition thickness (mg/cm^2) is essential to be able to correctly calculate the cross sections. The data reported in Table 43 were calculated by using the approximate value obtained from the difference of the simple weighing of the aluminum support, before and after the deposition. When the EBS analyses of the irradiated samples will be completed, the new thickness values, taking onto account the oxygen amount in each target foil, will be used. As the thickness of ^{48}Ti deposited also affects the beam energy loss, even the energy associated with each point in the graph may undergo small changes. The provisional thicknesses of the ^{48}Ti targets used in the first data analysis are shown in Table 44. The uncertainty on the target foil thickness is not taken into account in the error calculation.

Table 43: Measured cross sections of the ^{48}Ti(p,x) ^{47}Sc, ^{46}Sc, ^{44g}Sc, ^{44m}Sc reactions

Energy [MeV]	^{47}Sc [mb]	^{46}Sc [mb]	^{44g}Sc [mb]	^{44m}Sc [mb]
39.6 ± 0.6	19.4 ± 0.9	55.0 ± 3.4	17.4 ± 1.4	9.0 ± 0.4
37.6 ± 0.7	20.5 ± 0.9	44.1 ± 2.8	22.6 ± 2.8	11.4 ± 0.5
35.5 ± 0.8	21.3 ± 1.1	32.3 ± 3.1	29.0 ± 2.0	12.5 ± 0.7
33.0 ± 0.6	24.6 ± 0.9	16.0 ± 1.7	42.1 ± 2.8	16.2 ± 0.8
31.4 ± 0.7	28.6 ± 1.3	10.8 ± 0.7	54.3 ± 4.2	19.6 ± 0.9
26.8 ± 0.8	35.1 ± 2.6		83.0 ± 6.6	24.4 ± 1.8

Table 44: Thicknesses of the ^{48}Ti targets obtained by weighing and used in the data analysis

E (MeV)	26.8	31.4	33.0	35.5	37.6	39.6
Thickness (µm)	1.6	1.5	1.6	1.6	1.3	1.3

The results obtained using the non-definitive target thickness are presented in Figure 56, showing a regular trend that is quite in agreement with the previous experimental data [80] [110]. In the case of ^{44m,g}Sc pair the procedure proposed by Otuka et al, described in detail in paragraph 6.3.3, was followed.

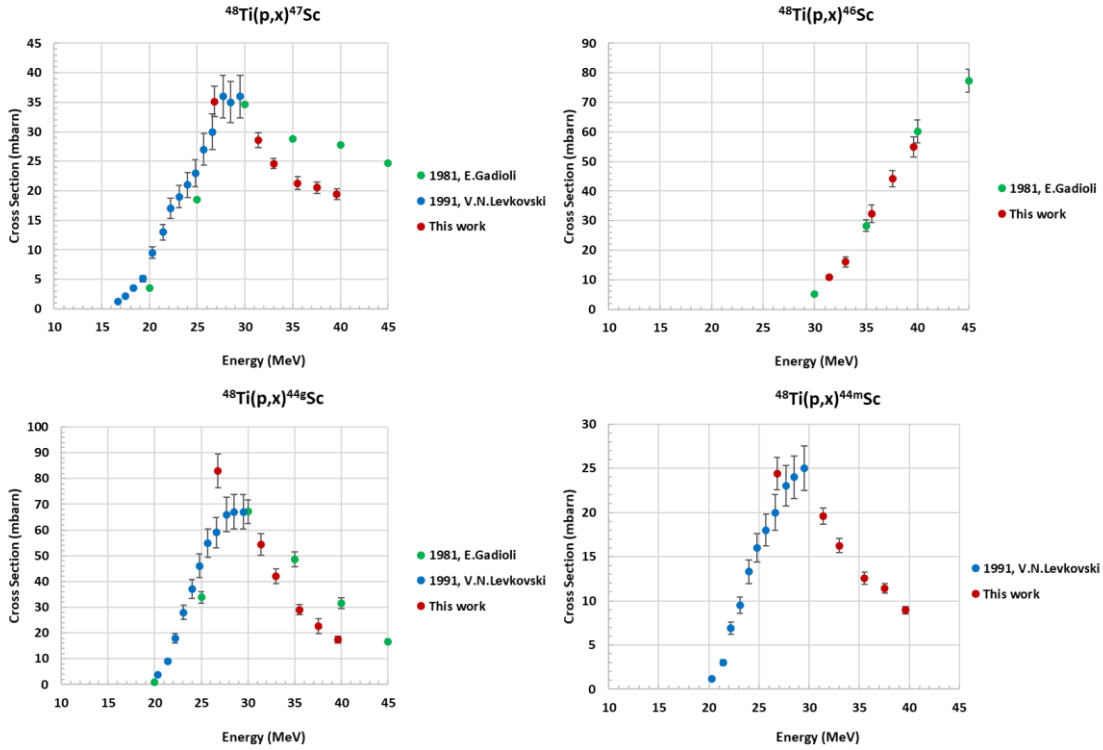

Figure 56: Results of the ^{48}Ti(p,x)^{47}Sc, ^{46}Sc, ^{44g}Sc, ^{44m}Sc nuclear cross sections, compared with literature data [80] [110]

6.3.2 The case of $^{nat}V(p,x)^{43}Sc$ and $^{nat}V(p,x)^{43}K$

The nuclear data used in the data analysis performed to obtain the ^{43}Sc and ^{43}K cross sections are reported in Table 45. ^{43}Sc and ^{43}K are both produced by proton-beams in ^{nat}V targets, since the threshold energies on ^{51}V are 43.08 MeV ($^{43}Sc+2n+t+\alpha$) and 20.88 MeV ($^{43}K+p+2\alpha$) respectively, as reported in Table 34.

Table 45: Nuclear data for ^{43}Sc and ^{43}K [7]

Isotope	Half-life	Eγ [keV]	Iγ [%]
^{43}Sc	3.891 h *12*	372.9 *3*	22.5
^{43}K	22.3 h *1*	372.760 *7*	86.8
		617.490 *6*	79.2 *6*

Figure 57 reports the experimental data of the $^{nat}V(p,x)^{43}K$ nuclear reaction obtained using only the γ-line at 617 keV in the spectrum analysis since it does not interfere with other γ-rays emitted both from co-produced radionuclides and from the background. The results are reported together with the TALYS estimations and the literature data [111] [112] [113] [114], extracted from the EXFOR database [88].

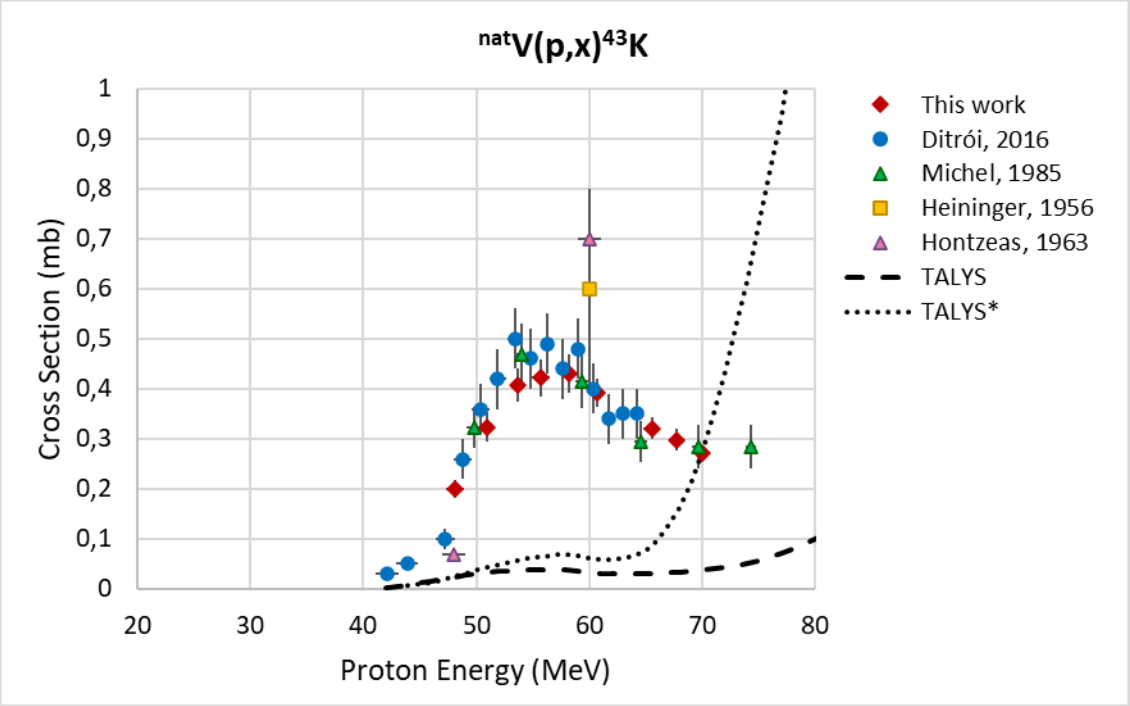

Figure 57: Cross section for the reaction $^{nat}V(p,x)^{43}K$ compared with the TALYS and TALYS calculations and with the literature data [111] [113] [112] [114]*

The new data obtained in this work agree with the one by R. Michel et al. (1985) [114] and by F. Ditrói et al (2016) [111]; on the contrary, for energies higher than 60 MeV, there is a discrepancy with the data by C.G. Heininger et al. (1956) and by S. Hontzeas et al. (1963). Both the TALYS and TALYS* calculations underestimate the experimental data and do not properly describe the measured trend (Figure 57).

It is evident that our results are completely different from those recently published by F. Ditrói et al (2016) [111] while our data for ^{43}K agree with those previous data (Figure 57). Also, the data published by S. Hontzeas et al. (1963) [112] are not in agreement with our results: their values show an increasing trend of the cross section at $E_P < 60$ MeV while our data show a growing trend only at $E_P > 65$ MeV. In the Hontzeas' work, the correction for the interference with ^{43}K was not necessary as two different γ-lines are used to identify the two isotopes. Moreover, it should be considered that, besides using obsolete nuclear data (e.g. 4 h instead of 3.891 h of ^{43}Sc half-life), only the 511 keV emission from positron annihilation was used to identify the ^{43}Sc.

Both the TALYS and TALYS* predictions agree with our experimental data at $E_P < 65$ MeV (Figure 58). At higher energies the TALYS calculation seems to better describe our measured trend. The difference between our data and those recently published by F. Ditrói et al (2016) [111] is probably due to the lack of correction for the ^{43}K contribution to the 373 keV γ-line [118].

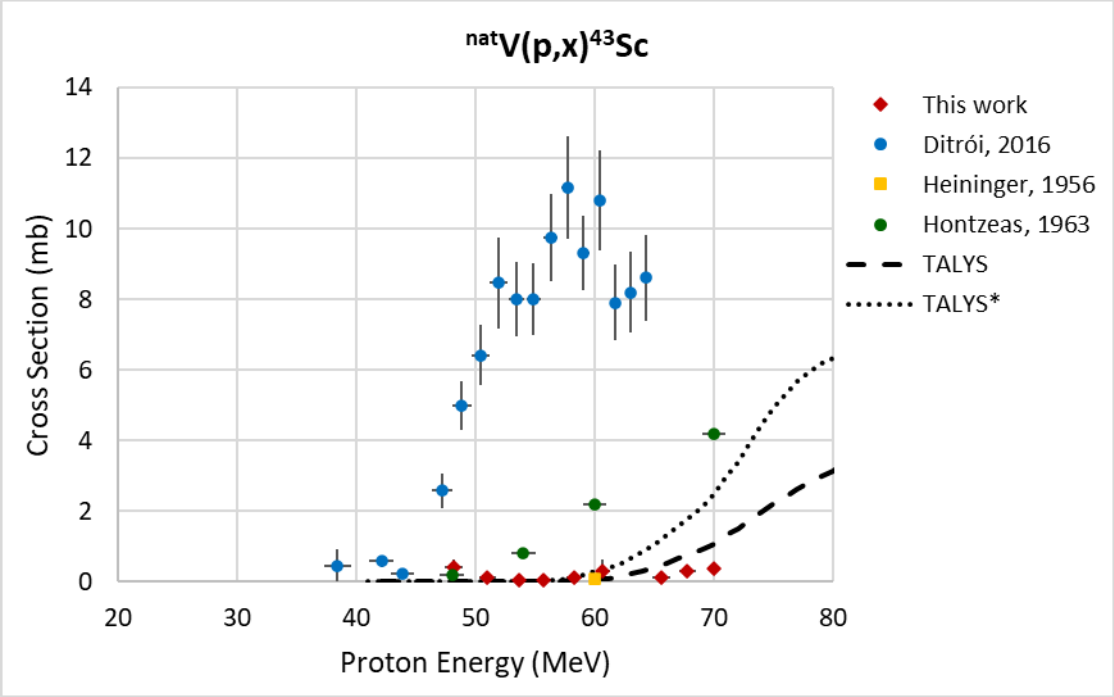

Figure 58: Cross section for the reaction $^{nat}V(p,x)^{43}Sc$ compared with the TALYS and TALYS calculations and with the literature data [111] [113] [112]*

6.3.3 The case of $^{nat}V(p,x)^{44m}Sc$ and $^{nat}V(p,x)^{44g}Sc$

The case of ^{44}Sc is particularly complex because this isotope has a metastable and a ground state, as shown in the decay scheme reported in Figure 59.

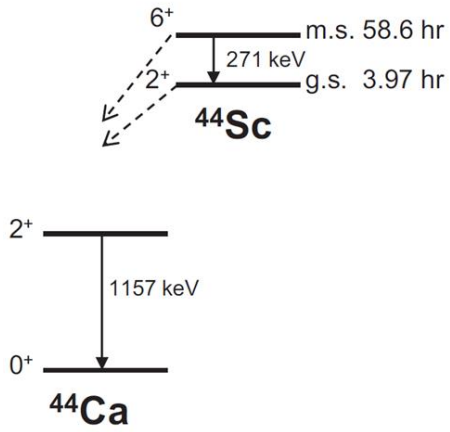

Figure 59: Decay scheme of ^{44g}Sc (half-life 3.97 h) and ^{44m}Sc (half-life 58.61 h)

The ^{44m}Sc cross section was easily calculated starting from its unshared 271.241 keV γ-line using the Formula 3.14. In case of the ^{44g}Sc cross section, the only usable γ-line (E_γ =1157 keV; I_γ=99.9%) is also emitted by the metastable state (I_γ=0.012%); ground and metastable states are connected by the isomeric transition b_{IT}=0.988 [119]. Since the ^{44m}Sc has a longer half-life then ^{44g}Sc (58.61 h and 3.97 h respectively), the ^{44m}Sc decay contributes to increase the ^{44g}Sc population which has one component directly produced during the bombardment and another one due to the decay of the metastable state. The ^{44g}Sc can also be produced by the decay of the ^{44}Ti but, since it has a long half-life ($T_{1/2}$ = 60 y [7]), its contribution to ^{44g}Sc formation can be considered negligible seeing that the irradiation time was about 1 hour.

In order to calculate the cross section associated with ^{44g}Sc production, it is thus necessary to discriminate between the three different contributions to the counts relating to the γ-line at 1157 keV; for this purpose, we have chosen to follow the formulation proposed by N. Otuka [46]:

$$C_{1157,i} = n\phi\varepsilon_{1157}\left[\sigma_{g,i}I_{1157,g}f_g + \sigma_{m,i}I_{1157,m}f_m + \sigma_{m,i}b_{IT}I_{1157,g}\frac{\lambda_m\lambda_g}{\lambda_m-\lambda_g}\left(\frac{f_g}{\lambda_g}-\frac{f_m}{\lambda_m}\right)\right] \quad (6.2)$$

where the first term is related to the directly produced ground state, the second term is related to the emission from the metastable state, and the third term is related to the emission from the ground state produced from the isomeric transition of the metastable state; *f* is the time factor as reported in formula 3.16. The beam flux was obtained from the monitor cross sections (^{nat}Al(p,x)^{24}Na and ^{nat}Ni(p,x)^{57}Ni) with the following formula:

$$\phi = \frac{1}{\sigma_r} \frac{C_r}{n_r \, \varepsilon_r I_r \, f_r} \tag{6.3}$$

Combining the Formulas 3.8, 6.3, and 6.4 we obtain the formula that allows the calculation of the ^{44g}Sc cross section:

$$\sigma_g = \frac{1}{n \, \phi \, I_{1157,g} \, f_g} \left[\frac{C_{1157}}{\varepsilon_{1157}} - \frac{C_{271}}{\varepsilon_{271}} \frac{I_{1157,m}}{I_{271}} - \frac{C_{271}}{\varepsilon_{271}} \frac{b_{IT} I_{1157,g}}{I_{271} f_m} \frac{\lambda_m \lambda_g}{\lambda_m - \lambda_g} \left(\frac{f_g}{\lambda_g} - \frac{f_m}{\lambda_m} \right) \right] = \alpha \, (\beta - \gamma - \delta) \tag{6.3}$$

The uncertainty associated to the ^{44g} Sc cross section was obtained by the following formulas:

$$\left(\frac{\Delta \sigma_g}{\sigma_g} \right)^2 = \sum_k s_k^2 \left(\frac{\Delta x_k}{x_k} \right)^2 \tag{6.4}$$

$$s_k = \left(\frac{x_k}{\sigma_g} \right) \left(\frac{\partial \sigma_g}{\partial x_k} \right) \tag{6.5}$$

We assume that these parameters at given energy are independent of each other. The explicit forms of the relative sensitivity coefficients s_{ik} are:

$$\begin{gathered}
\left(n/\sigma_{g,i}\right)\left(\partial \sigma_{g,i}/\partial n\right) = 1, \quad \left(\Phi/\sigma_{g,i}\right)\left(\partial \sigma_{g,i}/\partial \Phi\right) = 1, \\
\left(\varepsilon_{1157}/\sigma_{g,i}\right)\left(\partial \sigma_{g,i}/\partial \varepsilon_{1157}\right) = -\alpha\beta/\sigma_{g,i}, \\
\left(\varepsilon_{271}/\sigma_{g,i}\right)\left(\partial \sigma_{g,i}/\partial \varepsilon_{271}\right) = \left(\alpha/\sigma_{g,i}\right)(\gamma + \delta), \\
\left(C_{1157,i}/\sigma_{g,i}\right)\left(\partial \sigma_{g,i}/\partial C_{1157,i}\right) = \left(\alpha/\sigma_{g,i}\right)\beta, \\
\left(C_{271,i}/\sigma_{g,i}\right)\left(\partial \sigma_{g,i}/\partial C_{271,i}\right) = -\left(\alpha/\sigma_{g,i}\right)(\gamma + \delta), \\
\left(I_{1157,g}/\sigma_{g,i}\right)\left(\partial \sigma_{g,i}/\partial I_{1157,g}\right) = -\left(\alpha/\sigma_{g,i}\right)(\beta - \gamma), \\
\left(I_{1157,m}/\sigma_{g,i}\right)\left(\partial \sigma_{g,i}/\partial I_{1157,m}\right) = -\left(\alpha/\sigma_{g,i}\right)\gamma, \\
\left(I_{271}/\sigma_{g,i}\right)\left(\partial \sigma_{g,i}/\partial \, I_{271}\right) = \left(\alpha/\sigma_{g,i}\right)(\gamma + \delta), \\
\left(b_{IT}/\sigma_{g,i}\right)\left(\partial \sigma_{g,i}/\partial b_{IT}\right) = -\left(\alpha/\sigma_{g,i}\right)\delta,
\end{gathered} \tag{6.6}$$

Figure 60 reports the results obtained for the $^{nat}V(p,x)^{44g}Sc$ cross section compared with the TALYS and TALYS* calculations and with the literature data [111] [112].

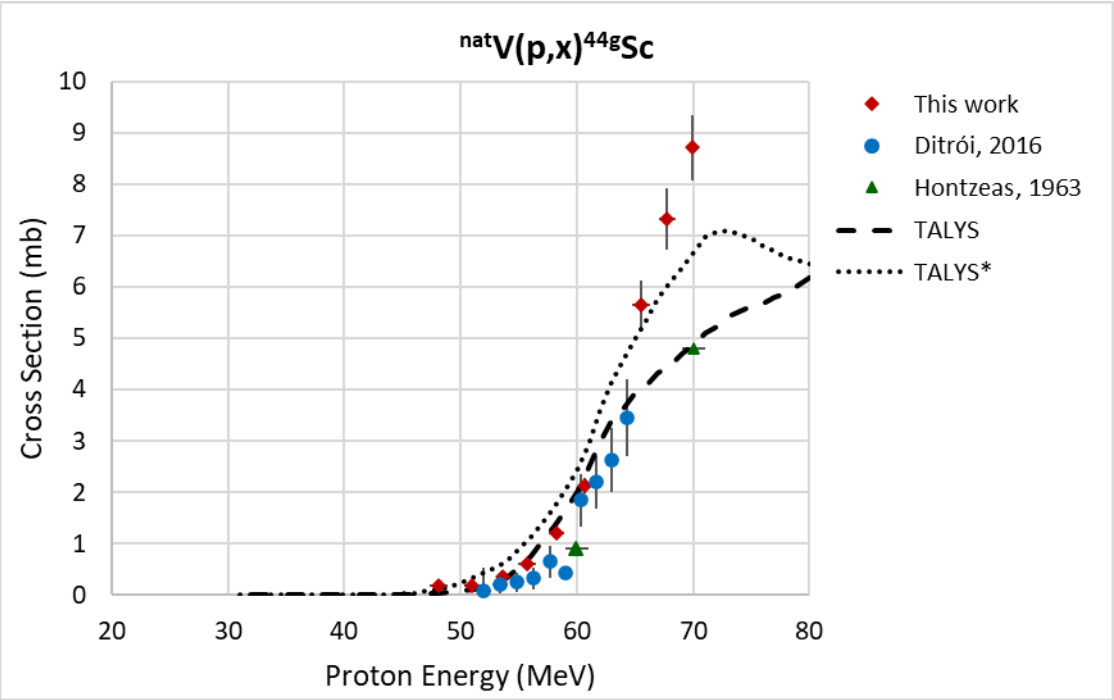

Figure 60: Cross section for the $^{nat}V(p,x)^{44g}Sc$ reaction compared with the TALYS and TALYS calculations and with the literature data [111] [112]*

Our results are sufficiently in agreement with both the TALYS* calculation and the data published by F. Ditrói et al (2016) [111]. There is a disagreement with the data by S. Hontzeas et al. (1963) [112] at E = 70 MeV.

Figure 61 shows the results obtained for the $^{nat}V(p,x)^{44m}Sc$ cross section compared with the TALYS and TALYS* calculations and with the literature data [111] [112] [114].

Our results are enough in agreement with both the TALYS* calculation and the data published by F. Ditrói et al (2016) [111] and by R. Michel et al. (1985) [114]. The trend of the data published by S. Hontzeas et al. (1963) [112] for $E_p < 60$ MeV is in agreement with all the other literature data while there is a difference at $E_p = 70$ MeV. There is also a large discrepancy with the expected trend obtained with the TALYS calculation that underestimates the experimental data for $E_p > 60$ MeV.

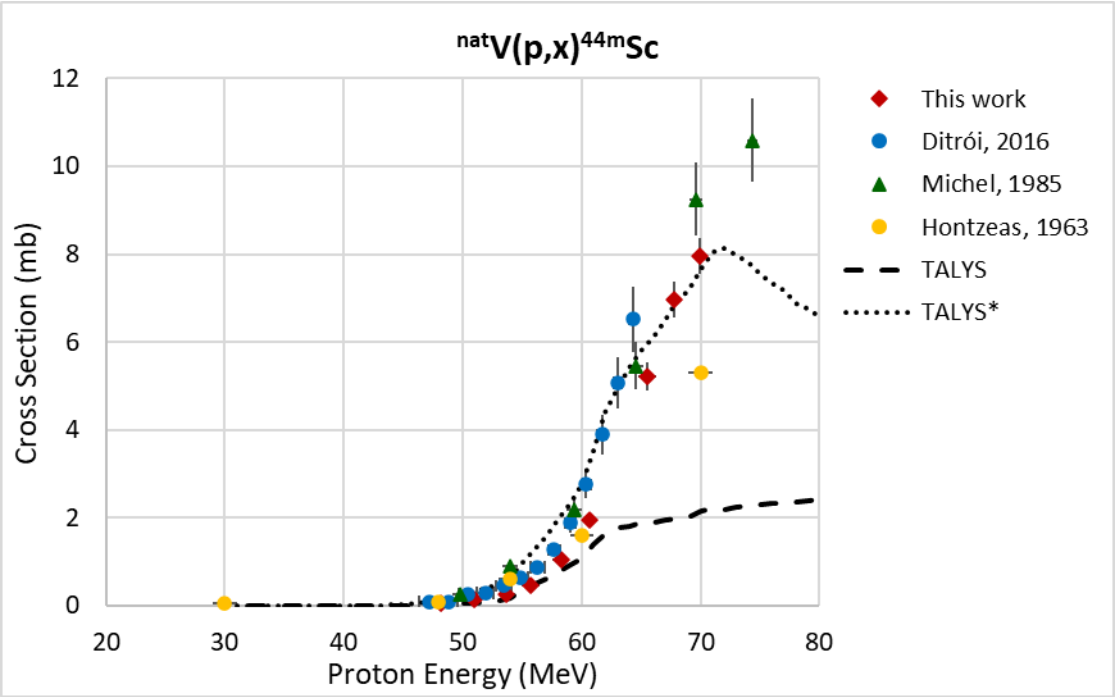

Figure 61: Cross section for the reaction $^{nat}V(p,x)^{44m}Sc$ compared with TALYS and TALYS calculations and with the literature data [111] [112] [114]*

6.3.4 $^{nat}V(p,x)^{43,46,47,48}Sc,^{42}K,^{48}V,^{48,49,51}Cr$ cross sections

Results obtained for the $^{nat}V(p,x)$ ^{48}Sc, ^{47}Sc, ^{46}Sc, ^{44}Sc, ^{44m}Sc, ^{43}Sc, ^{48}V, ^{43}K, ^{42}K, ^{48}Cr, ^{49}Cr, ^{51}Cr cross sections are shown from Figure 62 to Figure 69.

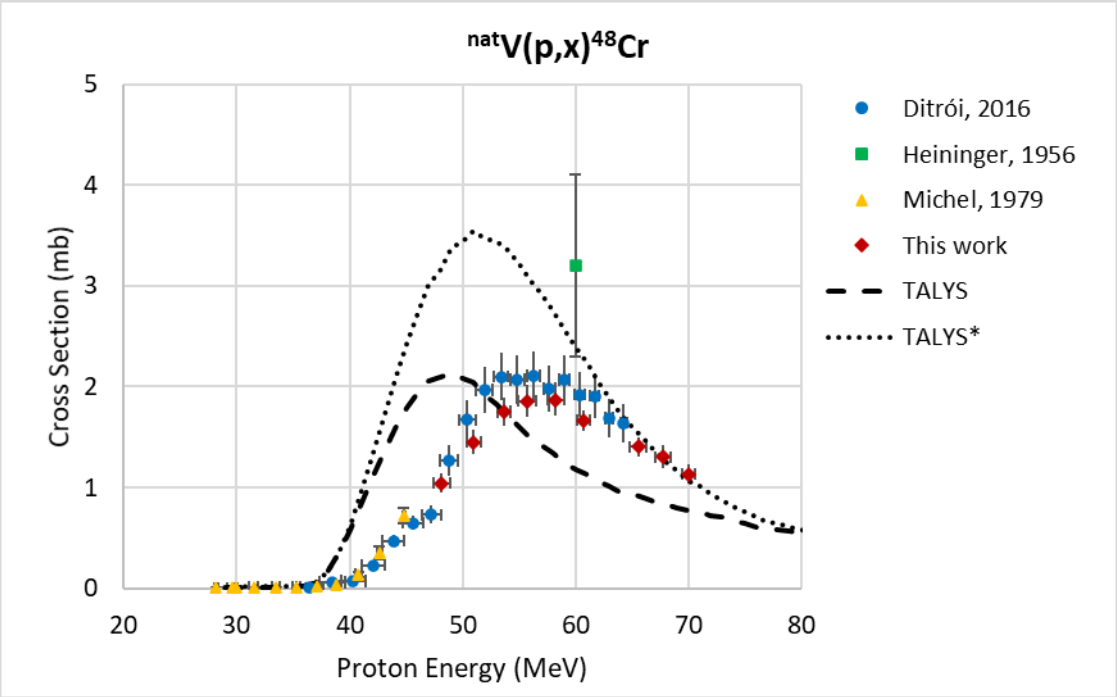

Figure 62: Cross section for the reaction $^{nat}V(p,x)^{48}Cr$ with the TALYS and TALYS codes and comparison with the experimental data [111] [113] [115]*

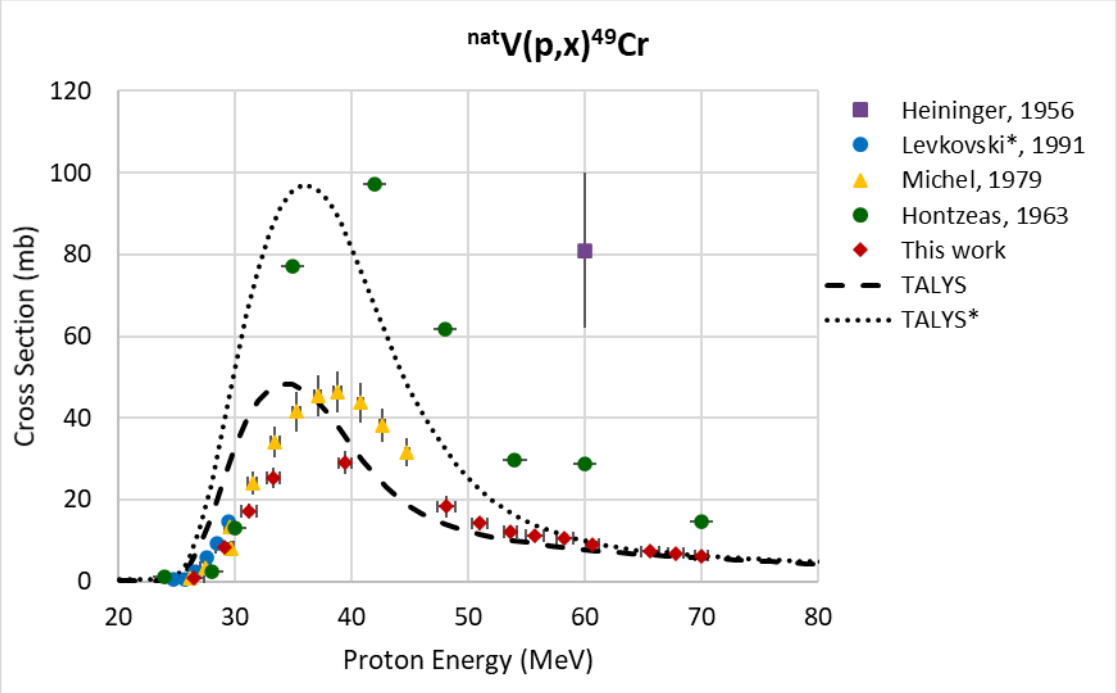

Figure 63: Cross section for the reaction $^{nat}V(p,x)^{49}Cr$ compared with the TALYS and TALYS calculations and with the literature data [80] [112] [113] [115]*

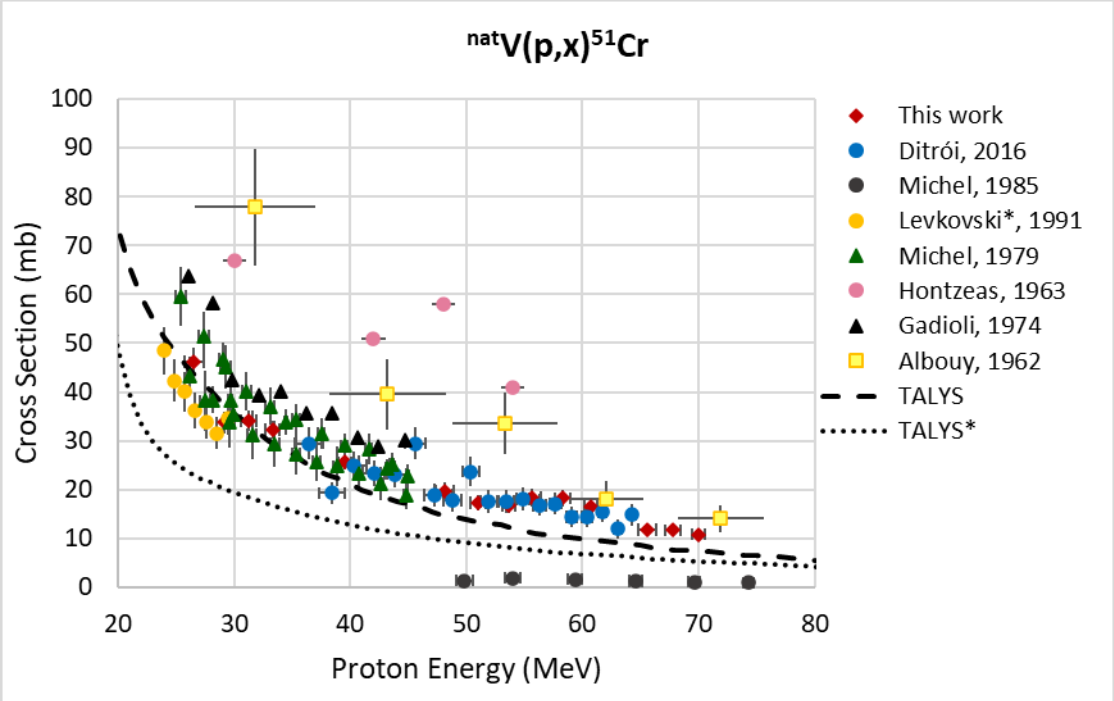

Figure 64: Cross section for the reaction $^{nat}V(p,x)^{51}Cr$ compared with the TALYS and TALYS calculations and with the literature data [80] [110] [111] [112] [114] [115]*

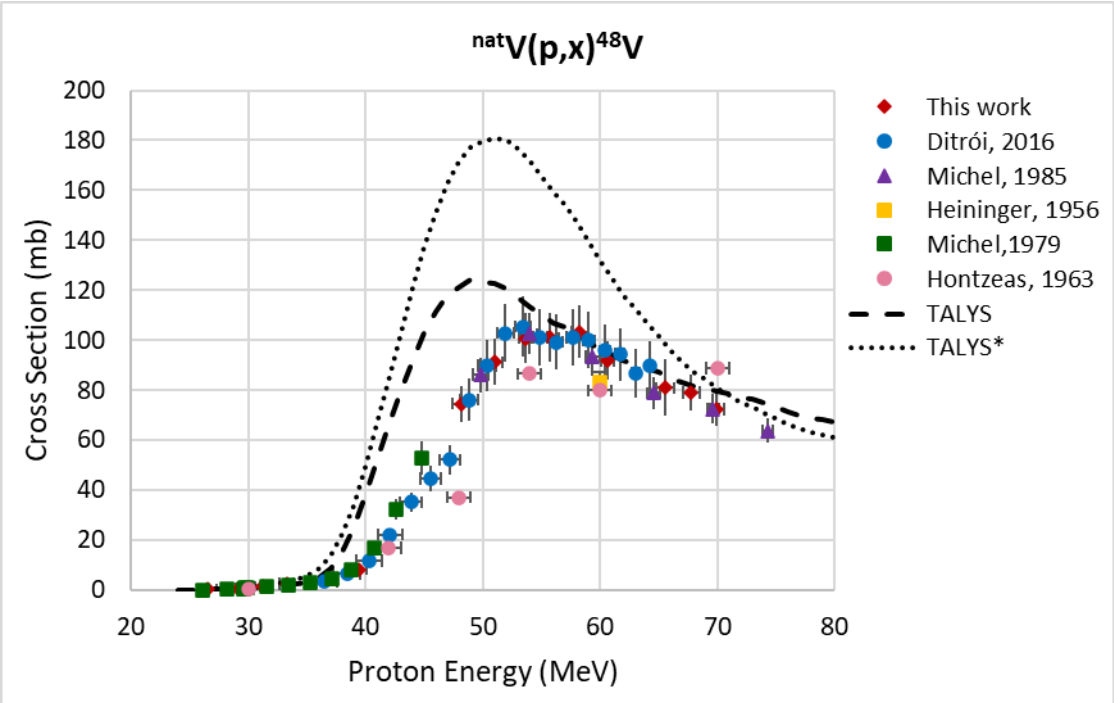

Figure 65: Cross section for the reaction $^{nat}V(p,x)^{48}V$ compared with the TALYS and TALYS calculations and with the literature data [111] [112] [113] [114] [115]*

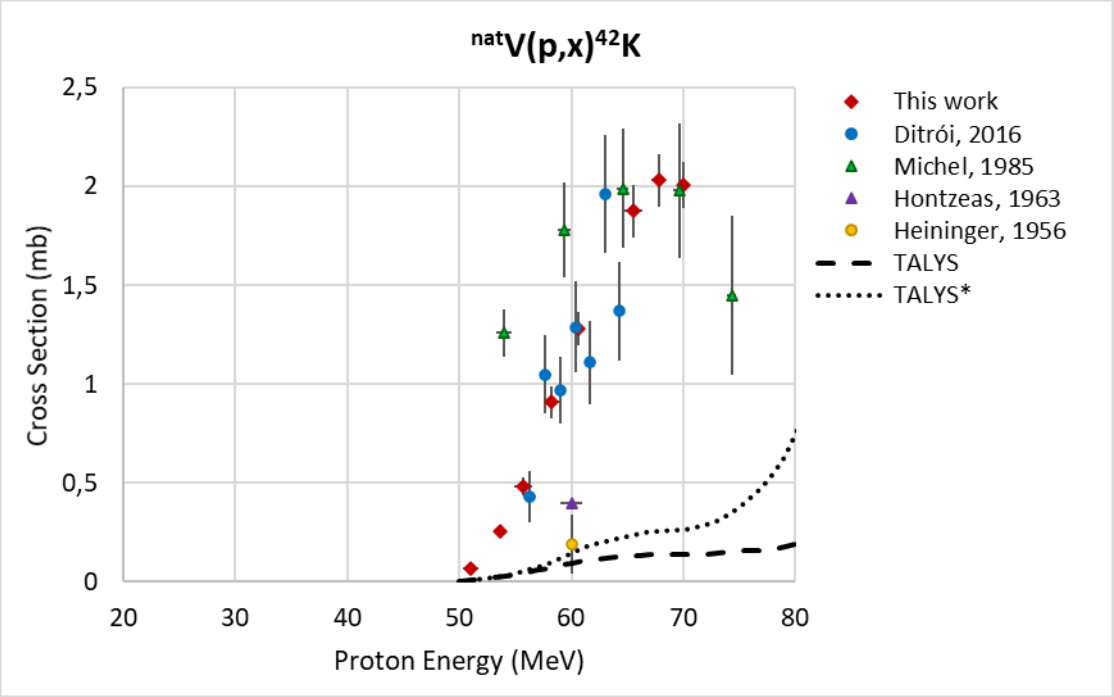

Figure 66: Cross section for the $^{nat}V(p,x)^{42}K$ reaction compared with the TALYS and TALYS calculations and with the literature data [111] [112] [113] [114]*

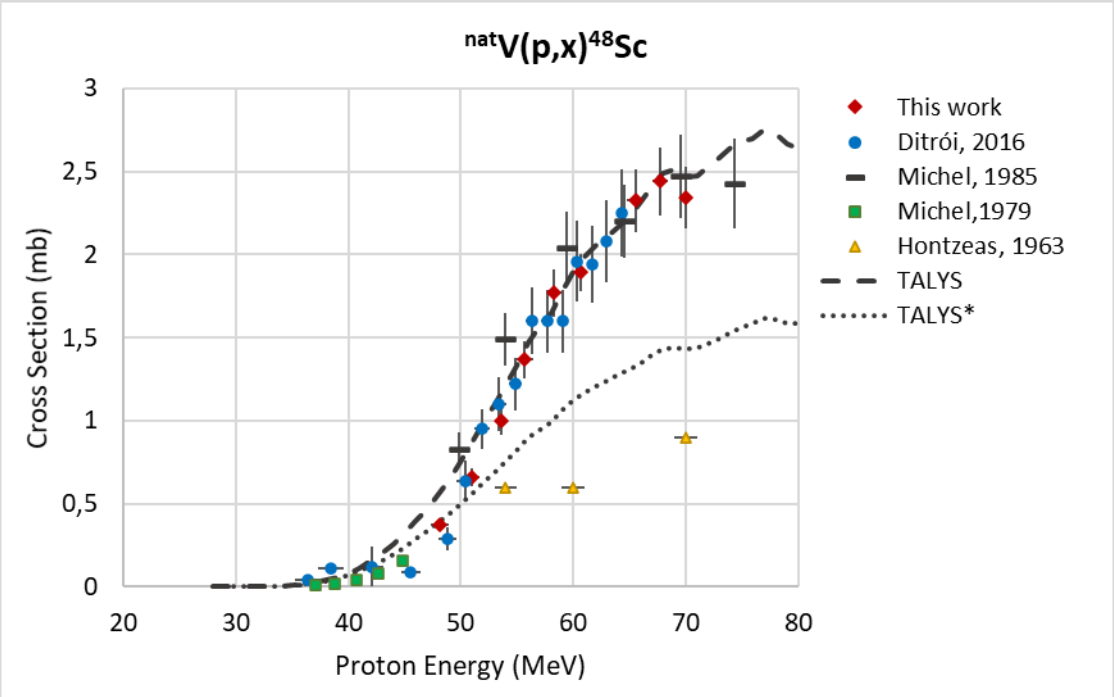

Figure 67: Cross section for the $^{nat}V(p,x)^{48}Sc$ reaction compared with the TALYS and TALYS calculations and with the literature data [111] [112] [114] [115]*

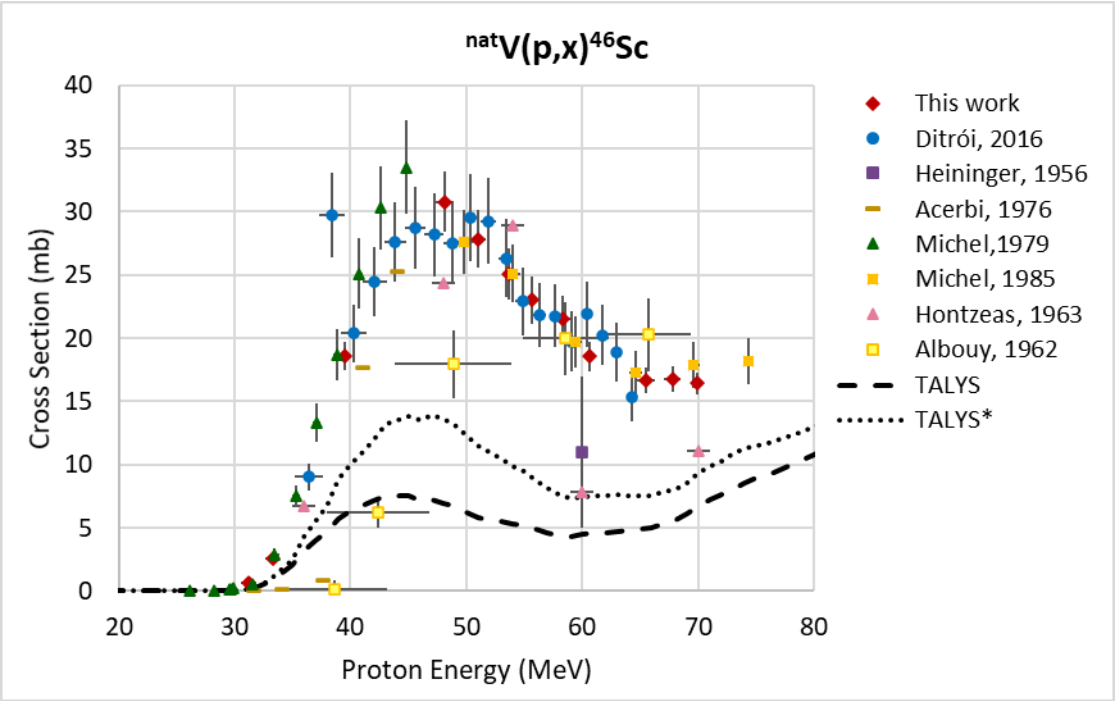

Figure 68: Cross section for the $^{nat}V(p,x)^{46}Sc$ reaction compared with the TALYS and TALYS calculations and with the literature data [111] [112] [113] [114] [115] [116]*

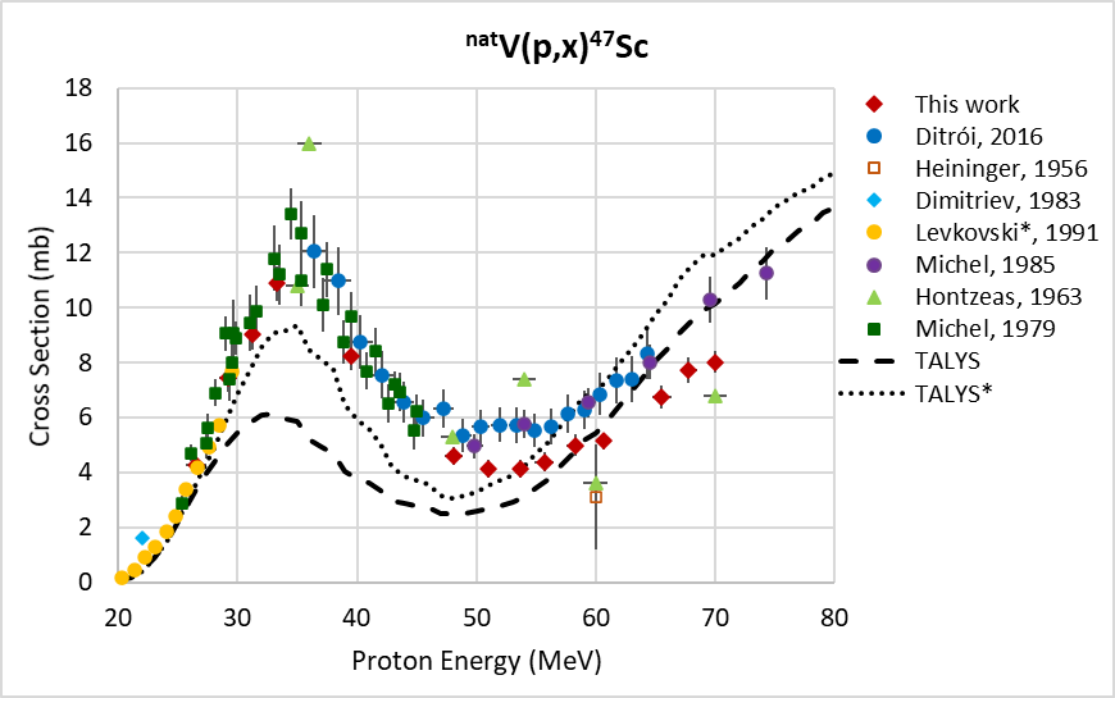

Figure 69: Cross section for the $^{nat}V(p,x)^{47}Sc$ reaction compared with the TALYS and TALYS calculations and with the literature data [111] [112] [113] [114] [115] [116]*

From the results obtained for the $^{nat}V(p,x)^{48}Sc$, ^{47}Sc, ^{46}Sc, ^{44}Sc, ^{44m}Sc, ^{43}Sc, ^{48}V, ^{43}K, ^{42}K, ^{48}Cr, ^{49}Cr, ^{51}Cr cross sections, shown in Figure 57-Figure 69, it is possible to observe that:

- for all the measured isotopes, always a regular trend was obtained in our results;
- the uncertainties associated with the values of the cross section are lower than those relating to the literature data. This is due to the applied experimental procedure which allowed us to obtain the value of the cross section for each target foil as weighted average on the statistical error of the obtained values (as previously described, at least 5 acquisitions of each irradiated sample were performed);
- the trend obtained for each radionuclide generally agrees with the other literature data. However, there are some exceptions, as in the case of ^{47}Sc and ^{49}Cr.
  - In the case of ^{47}Sc there is a good agreement of our data below 40 MeV with previous results by V.N. Levkovsky et al. [80], by R. Michel et al. (1985) [114] and by F. Ditrói et al (2016) [111]. However, the cross section values obtained in this work for $E_p > 40$ MeV are 20-30% lower than previous data [108];
  - In the case of ^{49}Cr radionuclide the maximum peak value is lower than that obtained by R. Michel et al. (1979) [115]. The correction for the data by Michel et al. (1979) is instead expected to be so small that it is useless to calculate it. In fact, they used old nuclear data (42 min half-life, 29.5% intensity line at about 153 keV), which are slightly different from the actual data (42.3 min half-life, 30.3% intensity line at about 153 keV). This eventual correction will not explain the discrepancy in the peak value from our measurement and the data by Michel (1979);
- for all the studied nuclear reactions the TALYS and TALYS* calculations correctly describe the initial trend near the reaction thresholds;
- the TALYS and TALYS* estimations are not always able to reproduce the trend of the experimental data. Three different behaviors were observed:
  - the theoretical trend is correct for the whole energy range studied (as in the case of ^{48}Sc and ^{51}Cr radionuclides);
  - the theoretical trend is correct but with a shift in energy (as in the case of ^{48}Cr and ^{48}V radionuclides);

- the theoretical trend is correct but underestimates the experimental data (as in the case of ^{46}Sc and ^{42}K radionuclides).

From the comparison between the results obtained and the trends predicted by the TALYS and TALYS* calculations it is plain that, except in the case of ^{48}Cr and ^{48}V, the theoretical predictions do not reproduce the experimental trends of the nuclear reactions studied.

6.4 TTY of the reactions ^{nat}V(p,x)^{47,46}Sc for E_p < 35 MeV

Considering the melting temperature of metallic ^{nat}V (about 1900°C) and the easy availability of highly pure material on the market at low cost, I focused my study on this production route in view of a small-scale production at INFN-LNL. Among all the co-produced Sc-isotopes, the one that mostly affects and limits the use of ^{47}Sc in medical applications is ^{46}Sc ($T_{1/2}$=83.79 d), since it has a longer half-life than ^{47}Sc ($T_{1/2}$=3.3492 d). For this reason, it is necessary to find an energy range in which the ^{47}Sc is produced with the minimum co-production of ^{46}Sc. To identify the energy range that satisfies this request with the ^{nat}V(p,x) reaction, the cross section ratio between ^{47}Sc and ^{47}Sc plus ^{46}Sc is shown in Figure 70; when the ratio is equal to 1 only the ^{47}Sc is produced. This condition is achieved for energies lower than 30 MeV, but it is important to note that the ^{47}Sc cross section is lower than 9 mb (Figure 69). Despite both estimates obtained by the TALYS and TALYS* calculations do not correctly reproduce the experimental data, these results both agree in identifying the optimal energy range for E_p<30 MeV. All other Sc-isotopes are produced at higher energies, as it is possible to note in Figure 58, Figure 60, Figure 61, and Figure 67.

The estimation of the Tick Target Yield (TTY) was performed, following the formula 3.19, for ^{47}Sc and ^{46}Sc radionuclides by considering a polynomial fit of the experimental data for E_p <35 MeV (Figure 71).

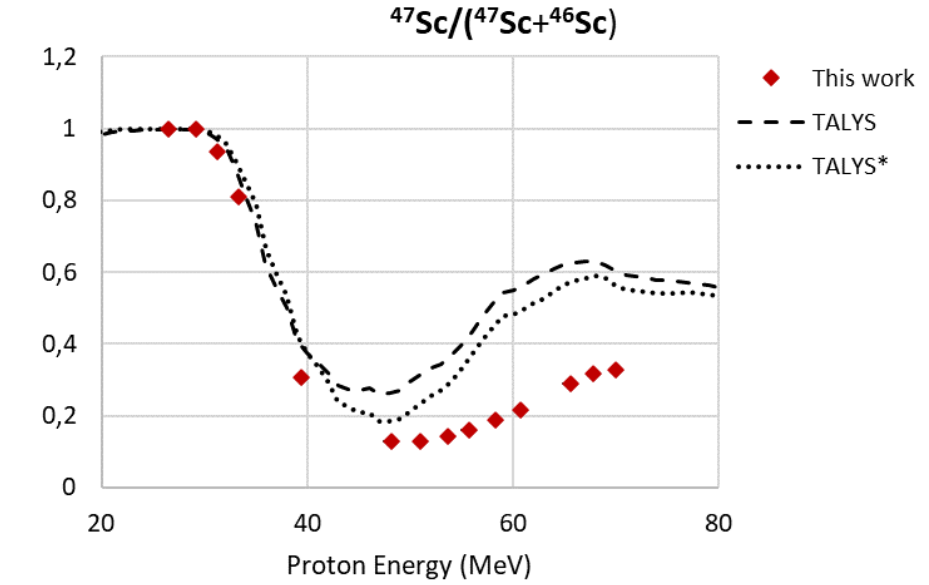

Figure 70: Cross section ratio between ^{47}Sc production and ^{46}Sc plus ^{47}Sc obtained from the measured data and the TALYS and TALYS estimations*

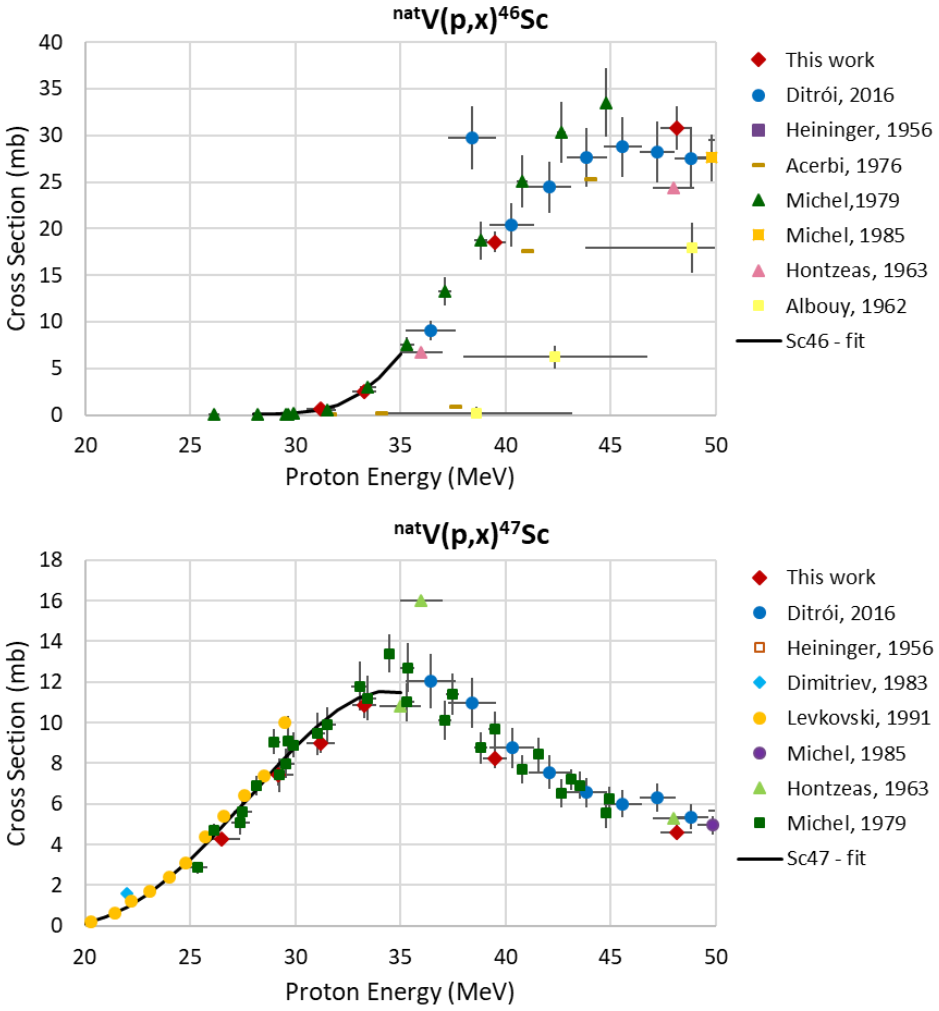

Figure 71: Polynomial fit of the ^{46}Sc and ^{47}Sc experimental data for E_p < 35 MeV

Assuming an irradiation of a thick ^{nat}V target with a proton beam with $E_P < 34$ MeV (energy easily available at the ARRONAX facility), using the SRIM software [41] it was estimated that a thickness of 1.5 mm is sufficient to maximize the ^{47}Sc production. Thanks to the low cost of the ^{nat}V material, it is therefore possible to exploit all the low energy trend of the ^{47}Sc cross section: considering an incident proton beam energy of 34 MeV, the energy loss in the 1.5 mm thick vanadium is about 12 MeV.

The calculated yields of ^{47}Sc and ^{46}Sc radionuclides for E_p=34 MeV and a 1.5 mm thick ^{nat}V target are presented in Table 46 for an irradiation time of 1 h, 24 h, and 80 h (i.e. about one half-life of ^{47}Sc).

Table 46: ^{47}Sc and ^{46}Sc production yields obtained from the calculations, based on experimental results, for thick ^{nat}V target (E_p= 34 MeV; I=1 μA; T_{irr}=1 h, 24 h, and 80 h)

Target	Thickness (μm)	T_{irr} (h)	Isotope	MBq	mCi
^{nat}V	1500	1	^{47}Sc	4	0.1
			^{46}Sc	0.01	0.0003
		24	^{47}Sc	87	2.3
			^{46}Sc	0.3	0.008
		80	^{47}Sc	232	6.3
			^{46}Sc	0.98	0.03

To verify the theoretical TTY obtained and reported in Table 46, a dedicated experiment was carried out.

6.4.1 Experimental measure of the ^{47}Sc yield by using thick ^{nat}V target

In order to measure the amount of ^{47}Sc produced by using a thick ^{nat}V target, it was realized an additional irradiation run in November 2019 at the ARRONAX facility. The distribution of the different foils in the stacked-foils target was chosen to be able to quantify the ^{46}Sc contribution that is expected to be present mainly in the first layer of ^{nat}V (named V-71), that is 500 µm thick (Figure 72). For this purpose, thin ^{nat}Ni and ^{nat}Al foils (used as monitor and catcher foils) were placed to separate the first thick ^{nat}V layer from the other two (named V-72+V-73). The thickness of the targets (calculated considering the bulk density of the material, the weight and the area of the foil) and the relative beam energies are reported in Table 47. As previously described, the beam energy loss was calculated with the SRIM software [41], also taking into account the Kapton foil (75 µm thick) at the end of the beamline, and the air layer (132.7 mm thick) before the target structure. For the thick targets the energy input (E_{IN}) and output (E_{OUT}) are reported separately; for the thin targets it is reported the energy associated with the center of the foil, as the difference between incoming and outgoing energy is small compared to the initial uncertainty associated with the beam energy.

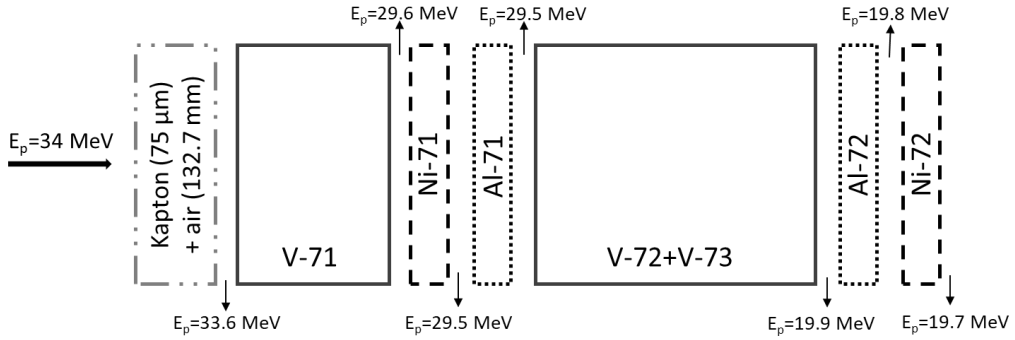

Figure 72: Stacked-foils target structure used in the irradiation run with thick ^{nat}V target

Table 47: Beam energies associated with the foils composing the target structure

Target	Thickness (µm)	E_{IN} (MeV)	E_{OUT} (MeV)	E (MeV)
V_{71}	541.5	33.59	29.63	
Ni_{71}	9.2			29.58
Al_{71}	9.8			29.50
V_{72}+V_{73}	1080.8	29.48	19.90	
Al_{72}	9.9			19.88
Ni_{72}	9.3			19.78

The experiment was carried out with 34 MeV proton beam energy, a nominal 100 nA current, and an irradiation time of one hour. The activity produced in thick targets is expected to be so high that it does not allow γ-spectrometry measurements directly with solid targets. For this reason, a chemical dissolution procedure was applied to the irradiated targets. The V_{71} and V_{72}+V_{73} targets were dissolved in separated solutions (each of 30 mL of HNO_3 4M), in order to measure the activities of the radionuclides produced in the two energy ranges. For these thick targets, the γ-spectrometry measurements were performed with an aliquot of the total solution (5 mL out of 30 mL); the weight correction was considered in the data analysis. All thin ^{nat}Ni and ^{nat}Al foils were dissolved in 5 mL HCl 9M and 5 mL HCl 10M respectively, directly in the 5 mL vial suitable for the subsequent spectrometry measurement.

The monitor reaction selected, the IAEA ^{nat}Ni(p,x)^{57}Ni [100], was used to obtain the effective value of the proton beam current on the target by knowing the ^{57}Ni activity produced (also considering the recoil in the ^{nat}Al target) and the tabulated cross section value corresponding to the beam energy on ^{nat}Ni foil. The effective proton beam current obtained is 92.9 nA.

Results, obtained considering the corrections due to the recoil effect and that the γ-spectroscopy measurement was carried out only on an aliquot of the total solution, are reported in Table 48.

Table 48: Experimental results at EOB for the ^{48}Sc, ^{47}Sc and ^{46}Sc production yields for a multi-layer ^{nat}V target configuration (E_p= 34 MeV; I=92.9 nA; T_{irr}=1 h)

Target (^{nat}V)	Isotope	kBq
V_{71}	^{48}Sc	4.30E-01 ± 1.89E-02
V_{72}+V_{73}		1.04E+00 ± 3.08E-02
V_{71}	^{47}Sc	1.97E+02 ± 7.03E+00
V_{72}+V_{73}		1.26E+02 ± 4.50E+00
V_{71}	^{46}Sc	5.97E-01 ± 2.13E-02
V_{72}+V_{73}		5.02E-02 ± 1.97E-03

Surprisingly not only ^{46}Sc and ^{47}Sc but also a small amount of ^{48}Sc was produced. Indeed, as shown in Figure 67, the ^{48}Sc cross section should be zero for E<35 MeV. The activity was obtained by analyzing three different γ-lines excluding those that have interference with other radionuclides (Table 49). The values obtained from the three γ-lines differ from each other up to 40%. The final value of the ^{48}Sc activity was obtained with the weighed average; the determining value of the result is that obtained from the

γ-ray at 1037 keV which, having a higher intensity, has a high statistic and consequently a small error.

Table 49: γ-lines [7] used for the ^{48}Sc activity obtained directly from the spectra analysis

Energy (keV)	Intensity (%)	Comments	V-71 ^{48}Sc activity (Bq)	V-72+V-73 activity (Bq)
175.361 *5*	7.48 *10*	No interferences, γ-line used for ^{48}Sc activity	4.96E02 ± 2.15E01	1.07E03 ± 6.84E01
983.526 *12*	100.1 *6*	Interference with ^{48}V; not used for ^{48}Sc activity		
1037.522 *12*	97.6 *7*	*No interferences*, γ-line used for ^{48}Sc activity	4.06E02 ± 2.15E01	9.78E02 ± 4.98E01
1212.880 *12*	2.38 *4*	No interferences, γ-line used for ^{48}Sc activity	6.29E02 ± 1.25E02	1.33E03 ± 1.15E02
1312.120 *12*	100.1 *7*	Interference with ^{48}V; not used for ^{48}Sc activity		
			weighed mean value of ^{48}Sc [Bq]	
			4.30E02 ± 1.89E01	1.04E03 ± 3.80E01

The ^{48}Sc activity could be due to the presence of 0.25% of ^{50}V in the ^{nat}V used since the corresponding threshold energy is lower than in the case of ^{51}V (Table 50).

Table 50: Proton-induced reactions Q-values for the ^{48}Sc production for ^{50}V and ^{51}V targets (E_p=35 MeV) [94]

Target	Reaction Products	Q-value (keV)	Threshold energy (keV)
^{51}V	**^{48}Sc+p+^{3}He**	-22631	23079
	^{48}Sc+2p+d	-28125	28681
	^{48}Sc+n+3p	-30349	30949
^{50}V	**^{48}Sc+3p**	-19298	19687

To verify this hypothesis, the TENDL-2019 nuclear data library [120] [121] was consulted considering separately the contributions due to the ^{50}V and ^{51}V targets in the assumption of 100% abundance for both isotopes (Figure 73). In the case of ^{51}V, all three production channels of ^{48}Sc, i.e. (p,p+3He), (p,2p+d) and (p,n+3p), were taken into account. As expected from the thresholds energies (Table 50), the ^{48}Sc production cross section starts at lower energies in the case of the ^{50}V; however, it should be taken into account that the result must be scaled by a factor of 0.25%, i.e. the ^{50}V natural abundance. However, in Figure 73, it can be noted that both the TENDL trends provide a zero cross section value for E<30 MeV. An additional unexpected result is the highest

^{48}Sc activity value in the lowest energy range. Until now no explanation has been found for the experimental result obtained for the ^{48}Sc activity.

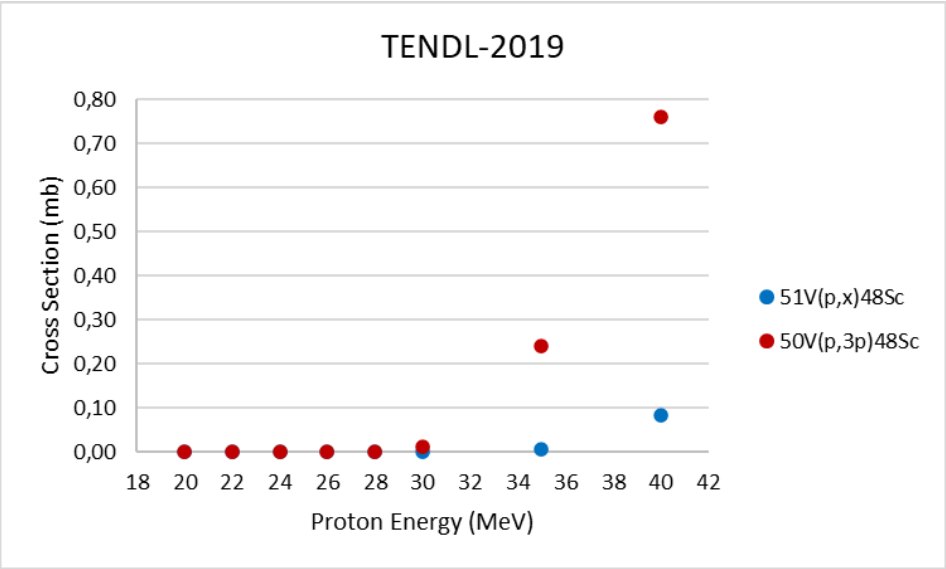

Figure 73: TENDL-2019 estimations for the ^{48}Sc production considering ^{50}V and ^{51}V targets with 100% abundance [120] [121]

Table 51 reports the experimental values reported in Table 48 rescaled to 1 µA and 24 h irradiation, a reasonable irradiation time. The data were also compared with the theoretical yield calculations obtained from the fit of the experimental data shown in Figure 71. The comparison shows that the results have the same orders of magnitude despite experimental results are always slightly lower than the theoretical estimations, except in the case of the ^{46}Sc in the lower energy range. It must be considered that it is easy to not properly fit the ^{46}Sc cross section for E<30 MeV since it is very close to zero. As previously discussed, there are no experimental data for the ^{48}Sc production at energies below 35 MeV and therefore it is not possible to estimate its production.

Table 51: Comparison between experimental results at EOB and theoretical estimations for the ^{48}Sc, ^{47}Sc and ^{46}Sc production yields for a multi-layer ^{nat}V target configuration (E_p= 34 MeV; I=1 µA; T_{irr}=24 h)

	Energy range (MeV)	Exp [Bq]	Calc [Bq]	Exp/Calc
^{48}Sc [Bq]	33.6 – 29.6	9.3E+04 ± 4.1E+03		
	29.5 – 19.9	2.3E+05 ± 8.2E+03		
^{47}Sc [Bq]	33.6 – 29.6	4.6E+07 ± 1.6E+06	4.8E+07	96 %
	29.5 – 19.9	2.9E+07 ± 1.1E+06	3.4E+07	85 %
^{46}Sc [Bq]	33.6 – 29.6	1.5E+05 ± 5.5E+03	2.1E+05	71 %
	29.5 – 19.9	1.3E+04 ± 5.1E+02	8.7E+03	149 %

Beyond the anomalies found in the ^{48}Sc activity, a second unexpected result was found by analyzing ^{nat}Al monitor foils: in fact, the ^{24}Na radionuclide is present in both foils (Table 52). The ^{nat}Al(p,x)^{24}Na reaction is well known being one of the monitor reactions suggested by the IAEA [99] and the lowest cross section value provided (0.05 mb) corresponds at 24 MeV. Moreover, ^{24}Na should not be produced in the Al_{72} foil also because the lowest energy threshold is 24.6 MeV, as reported in Table 53.

Table 52:Experimental results at EOB for the ^{24}Na production from thin ^{nat}Al foils

	Energy (MeV)	^{24}Na [Bq]
Al_{71}	29.50	2,38E+02 ± 1,09E+01
Al_{72}	19.88	2,15E+02 ± 8,64E+00

Table 53: Threshold energies to produce ^{24}Na from ^{nat}Al targets for E_p=35 MeV [94]

Reaction channel on ^{nat}Al target	Q-value (keV)	Threshold energy (keV)
^{24}Na+p+^{3}He	-23710.18 *0.05*	24595.56 *0.05*
^{24}Na+2p+d	-29203.65 *0.05*	30294.17 *0.05*
^{24}Na+n+3p	-31428.22 *0.05*	32601.81 *0.05*

A possible explanation for the ^{24}Na production at low energy could be an incorrect beam energy provided by the ARRONAX cyclotron operators. To check the beam energy it is possible to exploit the presence of the ^{nat}Ni monitor foils by using the method proposed by Piel et al. [122], which takes advantage of two monitor reactions. The idea is to compare the ratio between the tabulated cross section values and the ratio of the activities measured experimentally. Since the two ratios are proportional, it is possible to evaluate the beam energy incident on the monitor foil. This method makes sense only if, in the energy range of interest, the trends of the two cross section are different and at least two monitor reactions are available. In the ^{nat}Ni foil there is only the ^{nat}Ni(p,x)^{57}Ni monitor reaction but, following the suggestions of F. Tárkányi et al. [123], the reaction ^{nat}Ni(p,x)^{55}Co was used as an additional reference reactions. This allowed me to have two cross sections as monitors related to two different isotopes produced in the same foil. To construct the function describing the ^{nat}Ni(p,x)^{55}Co cross section trend, the data available in the EXFOR database were used. Data collected were then fitted to have the cross section as a function of the energy (Figure 74).

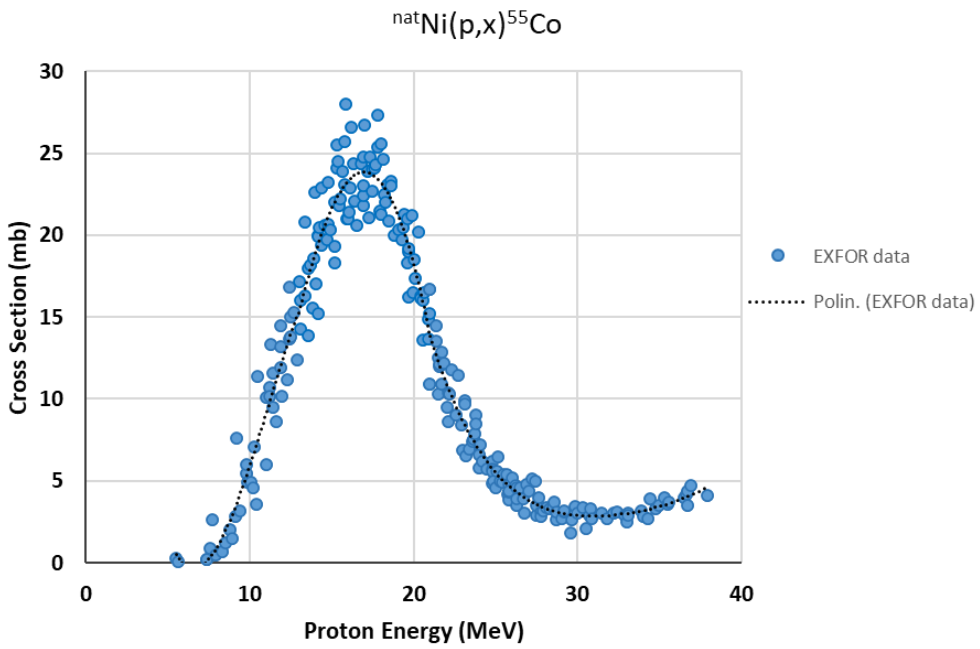

Figure 74: Cross section trend of the $^{nat}Ni(p,x)^{55}Co$ reaction obtained fitting the data available in the EXFOR database [88]

It is, therefore, possible to calculate the two ratios following the equation:

$$\frac{\sigma_{Ni-57}}{\sigma_{Co-55}} = \frac{A_{EOB,Ni-57}(1 - e^{-\lambda_{Co-55}t})}{A_{EOB,Co-55}(1 - e^{-\lambda_{Ni-57}t})}$$

The ratio between the $^{nat}Ni(p,x)^{57}Ni$ and $^{nat}Ni(p,x)^{55}Co$ reference cross sections as a function of the energy is shown in Figure 75.

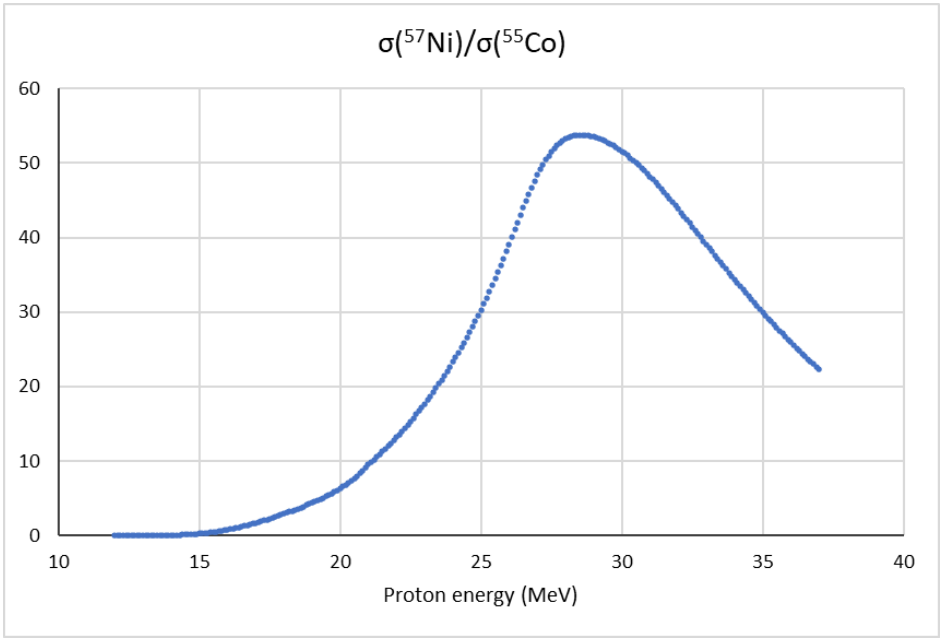

Figure 75: Ratio between the $^{nat}Ni(p,x)^{57}Ni$ and $^{nat}Ni(p,x)^{55}Co$ reference cross sections

Once the ratio between the experimental activities was calculated, by looking for the obtained value on the y-axis of Figure 75, it was possible to determine the corresponding value of the beam energy in the ^{nat}Ni foil. This procedure was repeated for both the ^{nat}Ni foils present in the stack and the results obtained are reported in Table 54.

Table 54: Comparison between the energy associated with the two ^{nat}Ni foils obtained with the SRIM code and with the ratio between the two reference cross sections

	Energy_SRIM (MeV)	Energy_estimated (MeV)
Ni_{71}	29.6	32.1 26.7
Ni_{72}	19.8	19.2

In the case of the Ni_{71} foil, the ratio of the experimental activities corresponds to two different energy values; this is due to the trend of the ratio between the cross section monitors which has a maximum value of about 28.5 MeV (Figure 75). The two values both differ at least 2.5 MeV from the value calculated with the SRIM code. Despite, the energy value obtained for the Ni_{72} foil is close to the value calculated with the SRIM code, it was not possible to associate a unique value to the beam energy in the Ni_{71} foil.

All the inconsistencies found lead me to repeat the experiment, hopefully by 2020.

6.4.2 Consideration on the ^{47}Sc dosimetry

To establish which is the maximum acceptable contamination of ^{46}Sc without increasing too much the dose given to the patient, a collaboration with experts in dosimetry (L. Melendez-Alafort, Istituto Oncologico Veneto – IOV, and L. De Nardo, University and INFN-PD) department has started. The first step was to carry out the dosimetric calculations by using the theoretical $^{47/46}$Sc production estimates and not the experimental results. In general, the presence of contaminant isotopes in the solution used to label a radiopharmaceutical does not affect the labelling efficiency, the radiochemical purity, or the biological behavior after administration [124]. However, the presence of contaminants affects the total radiation dose administered to the patient (Appendix A). The dose must be determined for each radiopharmaceutical because it is directly related to its kinetics [125]. One of the ^{47}Sc-complexes better described in the literature is the DOTA-folate conjugate cm10 ([^{47}Sc]-cm10) with an albumin-binding entity. The well-known [^{47}Sc]-cm10 biodistribution based on SPECT/CT images shows

a high localization in the tumor site [126] which allows determining the pharmacokinetic[5] data. The [^{47}Sc]-cm10 complex was thus chosen as an example of radiopharmaceutical to evaluate the dose increase due to the presence of the ^{46}Sc contaminant. The activity curves in the main male human organs were extrapolated from biodistribution data in KB[6] tumor-bearing nude mice to which [^{47}Sc]-cm10 was injected [126]. This calculation was made with the mass scaling method, which takes into account the difference in human and animal organs masses considering the total body masses [127]. Dosimetric calculations were performed using the OLINDA (Organ Level Internal Dose Assessment) software code version 2.1.1 [128] [129]. For each ^{xx}Sc-radioisotope *i*, in addition to the absorbed dose for each target organ, the total effective dose *EDi* imparted to the body was also calculated (the total effective dose is defined in Appendix A). The total effective dose (ED_t) produced by all ^{xx}Sc radioisotopes present in the radiopharmaceutical was calculated for different injection times.

The input data were obtained from the theoretical yield calculations at EOB for ^{47}Sc and ^{46}Sc in two different energy ranges, considering 1 μA of beam current and an irradiation time of 24 hours and 80 hours (Table 55).

Table 55: Production yields at EOB of ^{47}Sc and the contaminant ^{46}Sc, calculated for 1 μA proton beam impinging on ^{nat}V thick target for different energy ranges and irradiation times

Irradiation time: t = 24 hours (^{47}Sc SF = 19%)			
Energy range (MeV)	**^{47}Sc (Bq)**	**^{46}Sc (Bq)**	**^{47}Sc RNP (%)**
35-19	1.05 E+08	6.45 E+05	99.39
30-19	4.15 E+07	1.49 E+04	99.96
Irradiation time: t = 80 hours (^{47}Sc SF = 50%)			
Energy range (MeV)	**^{47}Sc (Bq)**	**^{46}Sc (Bq)**	**^{47}Sc RNP (%)**
35-19	2.79 E+08	2.13 E+06	99.24
30-19	1.11 E+08	4.92 E+04	99.96

[5] Pharmacokinetic: the characteristic interactions of a drug and the body in terms of its absorption, distribution, metabolism, and excretion

[6] KB cells: cervical tumor cells with a high expression of folate receptors therefore, they has been used as standard model for preclinical investigations of folate-based (radio) conjugates

The ^{47}Sc RNP plotted as a function of time post irradiation is shown in Figure 76 and it obviously decreases over time. When the proton energy range is 35-19 MeV, the RNP is higher than 90% up to 320-350 hours post EOB, while for 30-19 MeV RNP is higher than 97% up to 500 hours post EOB.

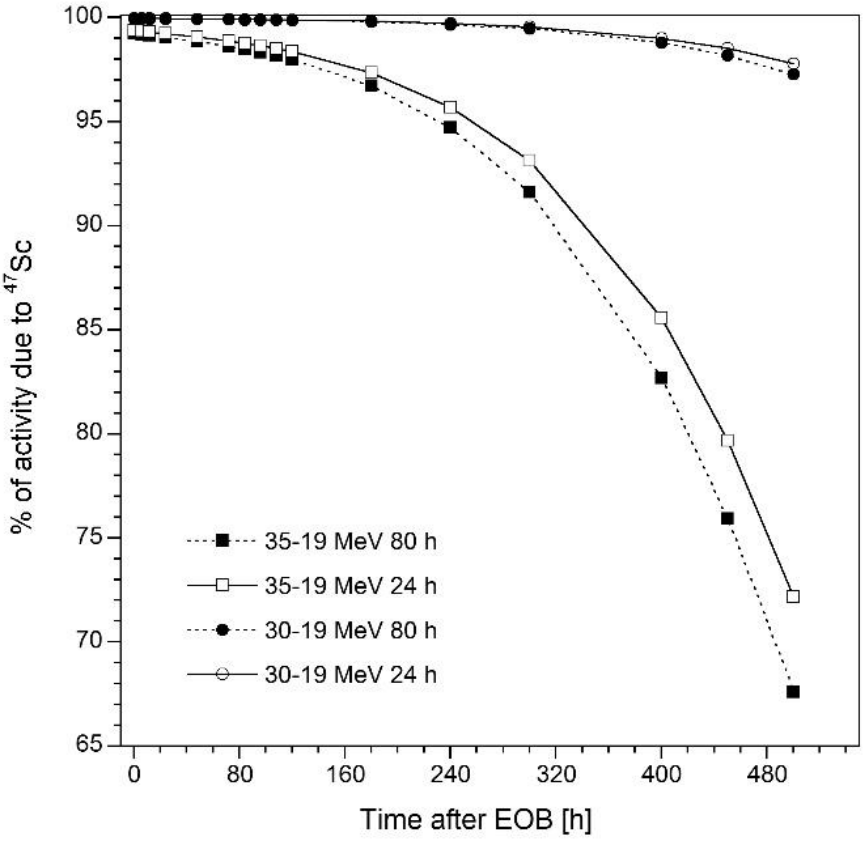

Figure 76: Percentage of activity due to ^{47}Sc as a function of time post-irradiation for two different energy ranges and two irradiation times (80 h: full symbols, 24 h: empty symbols)

The total ED (EDt) for ICRP 89 male phantoms was therefore calculated per unit of administered activity of the $^{47/46}$Sc-cm10 radiopharmaceutical, considering the injection immediately after labelling with the mixtures of Sc-radioisotopes present at the different times after EOB. The contribution of ^{47}Sc to the EDt decreases with time due to the increasing contribution of the long-lived ^{46}Sc contaminant (Figure 77).

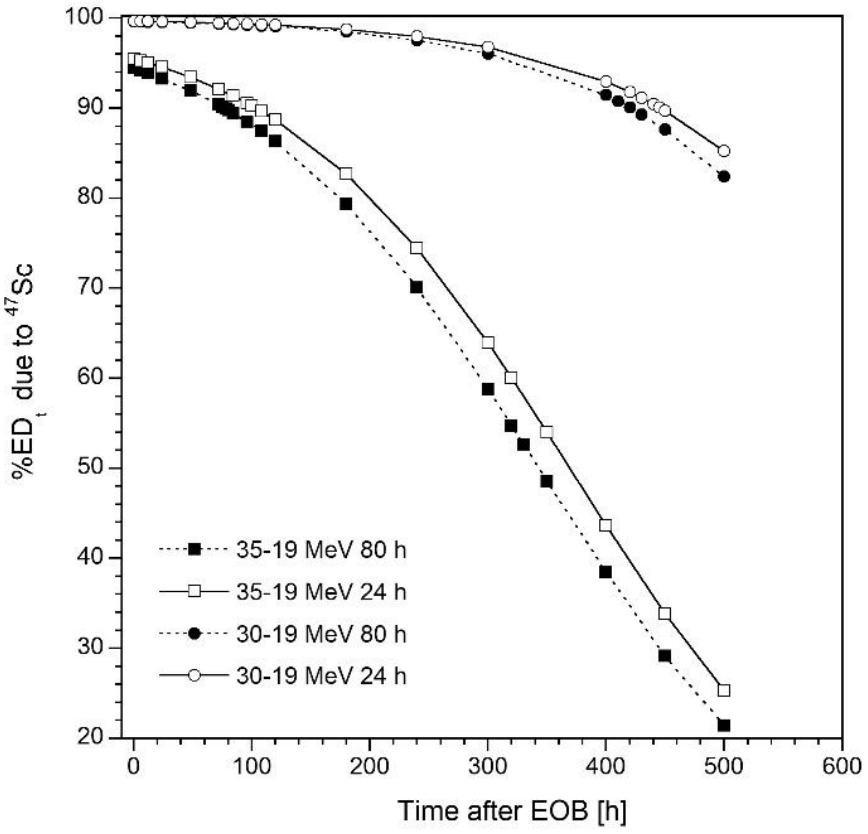

Figure 77: Contribution of Sc-radioisotopes to the total ED (EDt) using the male adult ICRP 89 phantom, at different times after EOB, for the two different energy ranges and two irradiation times (80 h: full symbols and 24 h: empty symbols)

The effective Dose Increase (DI) was calculated to verify that the DI value due to the presence of contaminants was maintained within the 10% limit required for clinical use [130]. This limit is fulfilled for both energy ranges considered; however, as shown in Figure 77, in case of $E_P < 30$ MeV the radionuclidic purity is higher and therefore, the contribution of other Sc-radioisotopes to the total ED is minimal even 500 h after the EOB. This outcome is useful in case of long transportation times, i.e. for a centralized production. If the amount of ^{47}Sc produced is a priority with respect of having a long useful time window after the EOB in which a ^{47}Sc-labeled radiopharmaceutical could be injected (t_{max}), the wider energy window 35-19 MeV should be preferred to the energy range 30-19 MeV. In both cases, an irradiation time of 80 h is preferable to 24 h, because the amount of ^{47}Sc produced is much higher while the time window (t_{max}) is only slightly shorter.

CONCLUSIONS AND PERSPECTIVES

This Ph.D. thesis here reported describes the work I have performed in the framework of the LARAMED (LAboratory of RAdioisotopes for MEDicine) project. My Ph.D. aimed to study efficient production routes for the ^{67}Cu and ^{47}Sc radionuclides, considering the 70 MeV proton cyclotron installed at INFN-LNL. ^{67}Cu and ^{47}Sc are γ- and β^- emitters, allowing for the selection of patients that have a good chance to respond to the specific radiopharmaceutical with SPECT imaging prior therapy. Moreover, they can be also paired to β^+ emitter isotopes (such as ^{64}Cu and $^{43/44}$Sc) to perform also low dose PET studies. Worldwide a real problem to be solved is the lack of ^{67}Cu and ^{47}Sc availability, as underlined by the IAEA CRP focused on the production of the theranostic radionuclides ^{67}Cu, ^{47}Sc and ^{186}Re (IAEA CRP No. F22053 for the years 2016-2019). For these reasons, among the goals of LARAMED, the production of these theranostic is a priority. The accurate knowledge of the reaction cross section is the first step in the optimization of radioisotope production. Since the LARAMED beam-line devoted to cross section measurements is not ready yet, the experiments were designed in Italy but they were carried out at the ARRONAX facility (Nantes, France).

The most used reaction for ^{67}Cu production is based on the use of ^{68}Zn target but, in the framework of the COME project, I measured the promising ^{70}Zn(p,x) nuclear reaction in the unexplored energy above 35 MeV. It is envisaged from the theoretical estimations that up to 70 MeV, there is a co-production of ^{67}Ga radionuclide: since ^{67}Cu and ^{67}Ga both decay in ^{67}Zn they have the same γ-lines. Moreover, such radionuclides have a similar half-life and thus it is not possible to deduce the precise activity of one radionuclide, waiting for the decay of the other one. For these reasons, with the purpose to study the ^{70}Zn(p,x)^{67}Cu nuclear cross section, a radiochemical procedure aimed at the separation of copper from gallium elements was developed in collaboration with the University of Ferrara and the S. Orsola hospital (Bologna, Italy). I planned and performed six irradiation runs at different energies by using the stacked-foils target technique; the intensity of the proton beam was stable during the irradiation at about 100 nA. The developed radiochemical process was always applied to irradiated targets

and the solutions obtained after the chemical separation were measured by using a HPGe detector. The values of the cross sections for ^{67}Cu and the contaminants were obtained by considering in the data analysis, when necessary, several corrections (Recoil Effect, Chemical Yield, Branching Ratio, and Weight Factor). I corrected all results for the contribution due to the presence of ^{68}Zn in the target (< 5%) and I rescaled them to 100% enriched ^{70}Zn. The major outcome of the COME project was the first measurement of the ^{70}Zn(p,x)^{67}Cu, ^{64}Cu, ^{67}Ga, ^{66}Ga, ^{65}Zn, and ^{69m}Zn cross sections in the 45-70 MeV energy range. A dedicated article describing the measurement in detail was published [101]. Results of the COME project allowed me to compare the ^{70}Zn and ^{68}Zn nuclear reactions to produce ^{67}Cu, also minimizing the co-production of ^{64}Cu. Neglecting the different costs of the enriched materials, results showed that for E_P < 55 MeV it is better to use ^{68}Zn while from 55 to 70 MeV it is better to use ^{70}Zn. This multi-layer target configuration is described by me and the co-authors in the International Patent n° WO 2019/220224 A1 (November 2019). In addition to this, the use of ^{70}Zn targets in the entire 45-70 MeV range provides a 70% increased production of ^{67}Cu. However, it has to be noted that the cost of ^{70}Zn is about four times larger than the one of ^{68}Zn, considering similar enrichments.

I studied the production of the theranostic ^{47}Sc in the framework of the PASTA project. Several target materials (^{48}Ti, ^{49}Ti, ^{50}Ti, and ^{nat}V) were selected in order to compare and choose the reaction that maximizes the production of ^{47}Sc and at the same time minimizes the co-produced contaminants. The enriched ^{48}Ti is very expensive and it was not easy to realize thin targets suitable for cross section measurements. To achieve this goal, the HIVIPP technique was developed with the E_PLATE project to obtain a thin deposit on metallic supports, starting from enriched titanium metallic powder. The characterization of the ^{48}Ti targets to quantify the deposited material, in mg/cm^2, was also carried out by using the EBS technique, obtaining the additional information of the oxygen present in the targets. The EBS measurements on the ^{48}Ti irradiated targets are yet not complete and, for this reason, the results regarding the cross sections measurements performed are given by using the weight of the samples. The enriched ^{49}Ti and ^{50}Ti materials were delivered in the form of inhomogeneous metal sponges, ranging from a few μm up 2 mm diameter. It was necessary to treat the material in order to reduce the size of grains into homogeneous metallic powder. I expect that the realization and characterization of the ^{49}Ti and ^{50}Ti targets will be completed within 2020 and, subsequently, it will be possible to measure for the first time the ^{49}Ti(p,x)^{47}Sc cross section. During the PASTA project, the irradiation of ^{nat}V targets was carried out

more easily, since this material is available on the market with the desired thickness and purity at low cost. I performed six irradiation runs at the ARRONAX facility by using different incident proton energies and stacked-foils targets. In total n°14 ^{nat}V and n° 9 ^{48}Ti targets were irradiated and no chemical process was applied after bombardment. The cross sections values obtained for the ^{48}Ti(p,x) ^{47}Sc, ^{46}Sc, ^{44}Sc, ^{44m}Sc nuclear reactions show a regular trend, in agreement with the previous experimental data. The results of the ^{nat}V(p,x) ^{48}Sc, ^{47}Sc, ^{46}Sc, ^{44}Sc, ^{44m}Sc, ^{43}Sc, ^{51}Cr, ^{49}Cr, ^{48}Cr, ^{48}V, ^{43}K, ^{42}K cross sections were also obtained and compared with the literature and theoretical calculations. All the twelve measured isotopes show a regular cross section trend. Particular attention was given to the case of ^{43}Sc, since a large discrepancy was noted with literature values. The reason for such disagreement in the trend of the cross section may be due to the interference with the γ-line emitted by the co-produced ^{43}K. My data for ^{43}Sc and ^{43}K production were also supported by the theoretical predictions: this work led to a dedicated article [118]. For all the nuclear reactions studied with ^{nat}V targets, the calculations obtained with the TALYS code, run with the default parameters and a new set of parameters, correctly describe the initial trends near the reaction thresholds. Depending on the specific radionuclide, the TALYS and TALYS* estimations were not always able to reproduce the trend of the experimental data; for this reason, a collaboration with experts in nuclear models is ongoing.

Considering the melting temperature of metallic ^{nat}V (about 1900°C) and the easy availability of thick foils with high purity at low cost, I focused on this production route in view of a small-scale production at INFN-LNL. Among all the co-produced Sc-isotopes, the one that mostly affects and limits the use of ^{47}Sc in medical applications is the ^{46}Sc radionuclide since it has a longer half-life than ^{47}Sc. Based on the experimental trends of the ^{nat}V(p,x)^{47}Sc, ^{46}Sc reactions [108], the Thick Target Yield (TTY) was calculated up to 34 MeV and compared with the real production obtained in dedicated irradiation performed in November 2019. Results showed that the amount of ^{47}Sc and ^{46}Sc produced were adequately in agreement with the expected activity, but surprisingly ^{48}Sc activity was also found. An additional experiment is foreseen by 2020. The theoretical results obtained with ^{nat}V target led us to extend the collaboration with experts in dosimetry, already ongoing on ^{67}Cu and ^{64}Cu radionuclides, to establish which is the maximum acceptable contamination of ^{46}Sc without increasing too much the dose given to the patient, considering a specific radiopharmaceutical. Considering the DOTA-folate conjugate cm10 ([^{47}Sc]-cm10), was found that the increase of the

Effective Dose due to the presence of the ^{46}Sc was maintained within the 10% limit required for clinical use for $E_P < 35$ MeV.

Similar calculations are already ongoing for the case of $^{67/64}CuCl_2$ and are envisaged for different ^{67}Cu-labelled radiopharmaceuticals.

The perspective for the LARAMED project at INFN-LNL is to establish regular small-scale productions of emerging and innovative radionuclides, with high priority to the theranostic ^{67}Cu and ^{47}Sc, by using the new high-performance proton cyclotron. The fruitful network of national and international collaborations will permit to test the efficacy of the developed radiopharmaceuticals with dedicated in-vitro and in-vivo preclinical studies. This thesis on nuclear physics is the ground of a complex interdisciplinary work that may hopefully soon be an additional step forward for a better cancer treatment.

APPENDIX A

Basic principles of dosimetry

Dosimetry is the measure of the quantities that allow to calculate the biological damage due to exposure (external or internal) to the different types of ionizing radiation [131]. The biological effects of radiation are considered to be at zero threshold, as even small doses have a probability, however small, of producing damage. For this reason, it is required that the use of radiogenic sources, called practice, are justified and optimized.

To understand the calculation of the absorbed dose in humans due to the injection of a radiopharmaceutical is necessary to report some basic definitions of three different radiation dose quantities.

Absorbed dose

The absorbed dose (D) is the energy absorbed per unit mass of any material by ionizing radiation, and is measured in gray (Gy), where 1 Gy = 1 J Kg^{-1}.

$$D = \frac{dE}{dm}$$

Equivalent dose

Equivalent dose (H_T) is the absorbed dose modified by a factor accounting for the effectiveness of type of radiation in producing biological damage to a specific tissue. Because of that, absorbed doses of equal values do not necessarily have a equal biological effects. A radiation weighting factor (w_R) is a dimensionless factor, and it is used to equate different types of radiation with different levels of biological effectiveness. The resulting weighted is thus the organ- or tissue equivalent dose:

$$H_T = \sum_R w_R D_{T,R}$$

where:

- $D_{T,R}$ is the dose delivered by radiation type R averaged over a tissue or organ T;
- w_R is the radiation weighting factor for radiation type R (Table 56).

The factor w_R is dimensionless. Therefore, the fundamental units of equivalent dose are the same as those for absorbed dose. Operationally, however, they are distinguish using the special units: H (rem) = D (rad)×wR, H (Sv) = D (Gy)×wR and 1Sv = 100 rem.

Table 56: Radiation weighting factor recommended from the International Commission on Radiological Protection (ICRP) [132]

Radiation type and energy range	**Radiation weighted factor, w_R**
Photons, all energies	1
Electrons and muons, all energies	1
Protons, other than recoil protons, E>2MeV	5
Alpha particles, fission fragments, heavy nuclei	20
Neutrons	A continuous function of neutron energy

$$w_R = \begin{cases} 2.5 + 18.2e^{-[ln(E_n)]^2/6}, & E_n < 1\ MeV \\ 5.0 + 17.0e^{-[ln(2E_n)]^2/6}, & 1\ MeV \le E_n \le 50\ MeV \\ 2.5 + 3.25e^{-[ln(0.04E_n)]^2/6}, & E_n > 50\ MeV \end{cases}$$

The equivalent dose to total body is the average of all the energy absorbed by all tissues divided by the mass of the entire body.

Effective dose

Certain organs are more sensitive to the effect of ionising radiation. Therefore, The International Commission on Radiological Protection (ICRP) assigned a dimensionless weighting factors to the organs, which are a function of their relative radiosensitivity for expressing fatal cancers or genetic defects. Multiplying an organ's dose equivalent by its assigned weighting factor gives a weighted dose equivalent. The sum of weighted dose equivalents for a given exposure to radiation is the effective dose (ED):

$$ED = \sum_T w_T H_T$$

where:

- H_T is the equivalent dose;
- w_T is the tissue weighting factor (Table 57).

Table 57: Some tissue weighting factor recommended from the International Commission on Radiological Protection (ICRP) [132]

Organ	Tissue weighted factor, w_T
Gonads	0.08
Bone marrow	0.12
Lung	0.12
Breast	0.12
Thyroid	0.04
Bone Surfaces	0.01
Colon	0.12
Stomach	0.12
Bladder	0.4
Liver	0.4
Esophagus	0.4
Skin	0.1
Salivary glands	0.1
Brain	0.1

APPENDIX B

Secular and Transient Equilibrium

Equilibrium is a condition occurring when a parent(P)/daughter(D) mixture is present and the daughter's half-life is shorter than the parent's one.

The parent nucleus decays according to the following equation of radioactive decay

$$A_P = -\frac{dN_P}{dt} = \lambda_P N_P$$

where $N_P = N_P^0 e^{-\lambda_P t}$ and $A_P = A_P^0 e^{-\lambda_P t}$.

The amount of daughter nuclei is determined by two processes, the radioactive decay and the radioactive growth by decay of the parent nuclei, described by the equation:

$$\frac{dN_D}{dt} = -\lambda_D N_D + \lambda_P N_P$$

which is solved as:

$$N_D = \frac{\lambda_P}{\lambda_D - \lambda_P} N_P^0 \left(e^{-\lambda_P t} - e^{-\lambda_D t}\right) + N_D^0 e^{-\lambda_D t}$$

The decay of the amount of daughter nuclide present at the time t = 0 ($N_2^0 = 0$) is:

$$A_D = \lambda_D N_D = \frac{\lambda_D}{\lambda_D - \lambda_P} A_P^0 \left(e^{-\lambda_P t} - e^{-\lambda_D t}\right)$$

The ratio between λ_D and λ_P is the dominant factor that determines the daughter activity in time.

Secular equilibrium

When the half-life of the parent nuclide is infinitely larger than that of the daughter nuclide ($\lambda_P \ll \lambda_D$), the activity of the daughter species can be described as:

$$A_D = A_P^0 \left(e^{-\lambda_P t} - e^{-\lambda_D t}\right)$$

For $\lambda_P = 0$ the growth of the daughter activity in time is:

$$A_D = A_P^0 \left(1 - e^{-\lambda_D t}\right)$$

For $t \to \infty$ the daughter activity reaches a value of:

$$A_D = A_P^0 \, e^{-\lambda_P t} = A_P$$

and the parent and daughter activities become equal. This means that in the secular equilibrium mixture, the daughter follows the decay of the parent with its half-life (Figure 78).

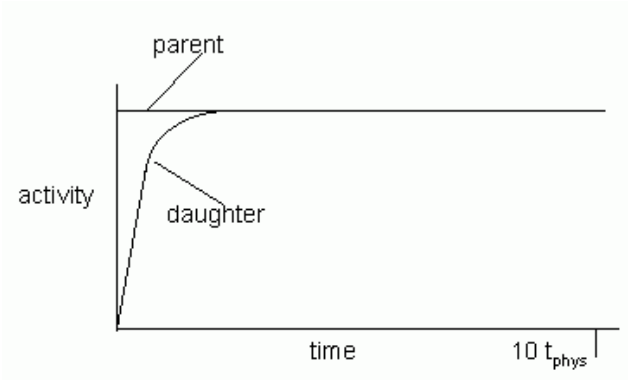

Figure 78: Relation between the activities of a P/D nuclides in the case of secular equilibrium

Transient equilibrium

When the half-life of the daughter nuclide is not negligible compared to parent's half-life ($\lambda_P < \lambda_D$), a stationary state is reached after sufficient time in which the daughter activity is larger than the parent activity (Figure 79).

$$A_D = \frac{\lambda_D}{\lambda_D - \lambda_P} A_P^0 \, e^{-\lambda_P t} = \frac{\lambda_D}{\lambda_D - \lambda_P} \, A_1$$

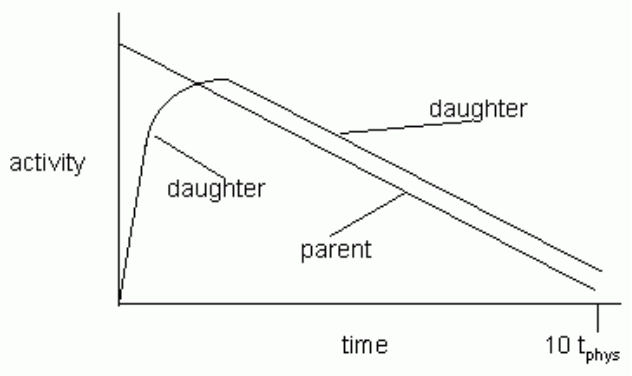

Figure 79: Relation between the activities of a P/D nuclide in case of transient equilibrium

APPENDIX C

Bethe-Bloch formula

Charged particles moving through matter interact with electrons of atoms in the material causing the excitation or ionization of the atoms. These interactions lead to a loss of energy of the traveling particles. The energy loss by the ions per distance travelled in matter is described by the Bethe-Bloch formula:

$$-\frac{dE}{dx} = 2\pi r_e^2 m_e c^2 \frac{z^2 Z}{\beta^2} \frac{\rho N_A}{A}\left[ln\left(\frac{2m_e v^2\gamma^2 T_{max}}{I^2}\right) - 2\beta^2\right] = \kappa\frac{z^2 Z}{\beta^2} \frac{\rho N_A}{A}\left[ln\left(\frac{2m_e v^2\gamma^2 T_{max}}{I^2}\right) - 2\beta^2\right]$$

where:

- r_e is the classic electron radius ($2.817 \cdot 10^{-13}$ cm);
- m_e is the electron rest mass;
- N_A is the Avogadro Number ($6.022 \cdot 10^{-13}$ mol^{-1});
- c is the speed of light;
- $\kappa = 2\pi N_A r_e^2 m_e c^2 = 0.1535\ MeV\ cm^2/g$
- I is the mean excitation potential of the target, approximately given by $I = (10\ eV)\cdot Z$;
- Z is the atomic number of the target material;
- A is the relative atomic mass of the target material;
- ρ is the density of the target material;
- z is the charge of the particle (in multiples of the electron charge);
- $\beta = v/c, \gamma = 1/\sqrt{1-\beta^2}$;
- T_{max} is the maximum energy transferred in a single collision, equal to $T_{max} = \frac{2m_e(c\beta\gamma)^2}{1+(m_e/M)\sqrt{1+(\beta\gamma)^2}+(m_e/M)^2} \approx 2m_e(c\beta\gamma)^2$ for $M \gg 2\gamma m_e$.

Comparing the experimental data and the theoretical trend obtained by the Bethe-Bloch formula, an evident discrepancy at low energies is observed. As an example, the Figure 80 shows the case of protons crossing an aluminum target. The discrepancy makes it necessary to bring some corrections to the Bethe's formula:

$$-\frac{dE}{dx} = \kappa\frac{z^2 Z}{\beta^2} \frac{\rho N_A}{A}\left[ln\left(\frac{2m_e v^2\gamma^2 T_{max}}{I^2}\right) - 2\beta^2 - \delta - 2\frac{C}{Z}\right]$$

where δ and C are the density and shell correction, respectively. The density correction is due to the shielding induced by the interaction with the electrons of the material; it is important at high energies and grows with the density of the material crossed. The shell correction must be taken into account when the velocity of the incident particle is lower than that the orbital velocity of the bound electrons. Figure 80 shows that the agreement between experimental data and the theoretical trend is better when these corrections are applied.

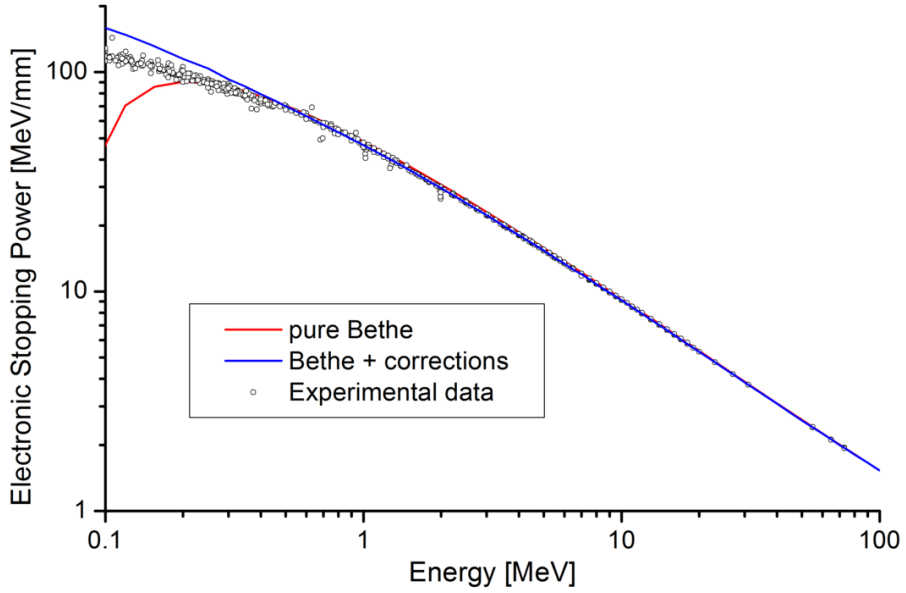

Figure 80: Stopping power of Aluminum for protons versus proton energy, and the Bethe formula without (red) and with corrections (blue)

FIGURE CAPTIONS

TABLE CAPTIONS

BIBLIOGRAFIA

[1] R. J. Kovalsky and S. Falen, "Radiopharmaceuticals in Nuclear Pharmacy and Nuclear medicine," *Ed. Appleton and Lange,* 2004.

[2] IAEA, «Cancer diagnosis,» [Online]. Available: https://www.iaea.org/topics/cancer-diagnosis.

[3] World-Nuclear-Association, «Radioisotope in Medicine,» February 2019. [Online]. Available: https://world-nuclear.org/information-library/non-power-nuclear-applications/radioisotopes-research/radioisotopes-in-medicine.aspx.

[4] S. R. Cherry, J. A. Sorenson. e M. E. Phelps, Physics in Nuclear Medicine, IV a cura di, 2012, pp. 209-231.

[5] IAEA, Nuclear Medicine Physics: A Handbook for Teachers and Students, Technical Editors: D.L. Bailey, J.L. Humm, A. Todd-Pokropek, A. van Aswegen, 2014.

[6] S. M. Qaim, "The present and future of medical radionuclide production.," *Radiochimica Acta,* vol. 100, pp. 635-651, 2012.

[7] NNDC, «National Nuclear Data Center,» NuDat 2.7, [Online]. Available: http://www.nndc.bnl.gov/nudat2/.

[8] S. Adak, R. Bhalla, K. K. VijayaRaj, S. Mandal, R. Pickett e S. K. Luthra, «Radiotracers for SPECT imaging: current scenario and future prospects,» *Radiochimica Acta,* vol. 100, pp. 95-107, 2012.

[9] J. Bushburg, The Essential Physics of Medical Imaging, Lippincott Williams & Wilkins, 2002.

[10] A. Rahmim e H. Zaidai, «PET versus SPECT: Strengths, Limitations and Challenges,» *Nuclear Medicine Communications,* vol. 29, p. 193–207, 2008.

[11] C. Pascali, A. Bogni, F. Crippa e E. Bombardieri , Concetti Generali sulla produzione di radiofarmaci emettitori di positroni, Milano: Aretré, 1999.

[12] S. M. Qaim, «Decay data and production yields of some non-standard positron emitters used in PET,» *Q. J. Nucl. Med. Mol. imaging Off. Publ. Ital. Assoc. Nucl. Med. [and] Int. Assoc. Radiopharmacol. (IAR), [and] Sect. Soc. of..,* vol. 52, n. 2, pp. 111-120, 2008.

[13] S. M. Qaim, «Development of novel positron emitters for medical applications: nuclear and radiochemical aspects,» *Radiochimica Acta,* vol. 99, pp. 611-625, 2011.

[14] R. Boellaard e H. H. Quick, «Current Image Acquisition Options in PET/MR,» *Seminars in Nuclear Medicine,* vol. 45, n. 3, pp. 192-200, 2015.

[15] IAEA, «Radiation and radionuclides in medicine,» IAEA Bulletin, December 2014. [Online]. Available: https://www.iaea.org/sites/default/files/55405810507.pdf.

[16] Radiology-Key, «Radionuclides: Production, Physical Characteristics, and Applications,» [Online]. Available: https://radiologykey.com/radionuclides-production-physical-characteristics-and-applications/.

[17] S. Qaim, «Therapeutic radionuclides and nuclear data,» *Radiochim. Acta.,* vol. 89, pp. 207-302, 2001.

[18] S. Qaim, F. Tárkányi e R. Capote, «Nuclear Data for the Production of Therapeutic Radionuclides,» IAEA Technical Report No. 473, 2011.

[19] S. V. Gudkov, N. Y. Shilyagina, V. A. Vodeneev e A. V. Zvyagin, «Targeted Radionuclide Therapy of Human Tumors,» *International Journal of Molecular Sciences,* vol. 28, 2015.

[20] C. Yeong, M. Cheng e K. NG, «Therapeutic radionuclides in nuclear medicine: current and future prospects,» *Journal of Zhejiang University-SCIENCE B (Biomedicine & Biotechnology),* vol. 15, n. 10, pp. 845-863, 2014.

[21] S. Srivastava, «A Bridge not too Far: Personalized Medicine with the use of Theragnostic Radiopharmaceuticals,» *Journal of Postgraduate Medicine, Education and Research,* vol. 47, pp. 31-46, 2013.

[22] R. Mikolajczak, N. P. v. d. Meulen e S. E. Lapi, «Radiometals for imaging and theranostics, current production, and future perspectives,» *J Label Compd Radiopharm.,* vol. 62, pp. 615-634, 2019.

[23] K. Willowson, «Production of radionuclides for clinical nuclear medicine,» *European Journal of Physics,* 2019.

[24] «NIDC National Isotope Development Center,» [Online]. Available: https://www.isotopes.gov/sites/production.html.

[25] NEA-NuclearEnergyAgency, «The Supply of Medical Radioisotopes: 2019 Medical Isotope Demand and Capacity Projection for the 2019-2024 Period,» 2019. [Online]. Available: https://www.oecd-nea.org/med-radio/docs/sen-hlgmr2019-1.pdf.

[26] IAEA, «Trends in Radiopharmaceuticals (ISTR-2005). Proceedings of an International Symposium. Vol. 1:14–18,» Vienna, 2007a.

[27] machinedesign, «What are the Differences Between Linear Accelerators, Cyclotrons and Synchrotrons?,» Technology Editor, [Online]. Available: http://machinedesign.com.

[28] BNL, «Brookhaven National Laboratory - Radioisotope Production,» [Online]. Available: https://www.c-ad.bnl.gov/esfd/BLIP%20Group/Radioisotope%20Production.htm.

[29] R. Aliev, S. Belyshev, A. Kuznetsov e al., «Photonuclear production and radiochemical separation of medically relevant radionuclides: 67Cu,» *Journal of Radioanalytical and Nuclear Chemistry,* n. 321, pp. 125-132, 2019.

[30] M. Inagaki, S. Sekimoto, W. Tanaka e al., «Production of 47Sc, 67Cu, 68Ga, 105Rh, 177Lu, and 188Re using electron linear accelerator,» *Journal of Radioanalytical and Nuclear Chemistry,* n. 322, p. 1703–1709, 2019.

[31] C. Loveless, L. Radford, S. Ferran e al., «Photonuclear production, chemistry, and in vitro evaluation of the theranostic radionuclide 47Sc,» *EJNMMI Research,* 2019.

[32] IAEA, «Cyclotron produced radionuclides: Principles and Practice,» IAEA Technical Reports Series No. 465, Vienna, Austria, 2008a.

[33] lns.infn, «Superconducting Cyclotron,» Laboratori Nazionali del Sud, [Online]. Available: https://www.lns.infn.it/en/accelerators/superconducting-cyclotron.html.

[34] Synowiecki, «Production of novel diagnostic radionuclides in small medical cyclotrons,» *EJNMMI Radiopharmacy and Chemistry,* 2018.

[35] P.-E. Goethals e R. Zimmermann, «Cyclotrons used in Nuclear Medicine World Market Report & Directory,» 2015.

[36] IAEA, «Cyclotron Produced Radionuclides: Operation and Maintenance of Gas and Liquid Targets,» [Online]. Available: https://www-pub.iaea.org/MTCD/Publications/PDF/Pub1563_web.pdf.

[37] IAEA, Production of Long Lived Parent Radionuclides for Generators: 68Ge, 82Sr, 90Sr and 188W, Vienna: IAEA RADIOISOTOPES AND RADIOPHARMACEUTICALS SERIES No.2, 2010.

[38] F. Roesch e F. j. Knapp, «Radionuclide Generators, Volume 4, Chapter 3,» in *Handbook of Nuclear Chemistry*, Amsterdam, A. Vertes, N.S. Klencsar, Publishers: Kluwer Academic, 2003, pp. 81-118.

[39] A. Koning e H. Akkermans, «PRE-EQUILIBRIUM NUCLEAR REACTIONS: An introduction to classical and quantum-mechanical models,» in *Proceedings of the Workshop: Nuclear reaction data and nuclear reactors*, 1999, pp. 143-158.

[40] M. Bonardi, «The contribution to nuclear data for biomedical radioisotope production from the Milan Cyclotron Laboratory.,» *Consultants meeting on data requirements for medical radioisotope production,* pp. 98 - 115, 1988.

[41] J. Ziegler, M. Ziegler e J. Biersack, «SRIM – the stopping and range of ions in matter,» *Nucl Instrum Methods Phys Res, Sect B,* vol. 268, pp. 1818-1823, 2010.

[42] S. Manenti, U. Holzwarth, M. Loriggiola, L. Gini, J. Esposito, F. Groppi e F. Simonelli, «The excitation functions of Mo-100(p,x)Mo-99 and Mo-100(p,2n)Tc-99m,» *Appl Radiat Isot,* vol. 94, pp. 344-348, 2014.

[43] R. L. William, Techniques for Nuclear and Particle Physics Experiments, Springer-Verlag, 1987.

[44] IAEA, «Monitor Reactions,» 2007. [Online]. Available: https://www-nds.iaea.org/medical/monitor_reactions.html.

[45] A. Hermanne e al., «Reference Cross Sections for Charged-particle Monitor Reactions,» *Nuclear Data Sheets,* vol. 148, pp. 338-382, 2018.

[46] N. Otuka, Uncertanty propagation in activation cross section measurements, Radiation Physics and Chemistry, 2017, pp. 502-510.

[47] IAEA, «Technical Report N.468 - Cyclotron Produced Radionuclides: Physical Characteristics and Production Methods,» IAEA, Vienna, Austria, 2009.

[48] A. Andrighetto, M. Manzolaro, S. Corradetti, D. Scarpa, A. Monetti, M. Rossignoli, M. Ballan, F. Borgna, F. D'Agostini, F. Gramegna, G. Prete, G. Meneghetti, M. Ferrari e A. Zenoni, «Spes: An intense source of Neutron-Rich Radioactive Beams at Legnaro,» *J. Phys. Conf. Ser.,* vol. 966, 2018.

[49] J. Esposito e e. al, «LARAMED: a LAboratory for RAdioisotopes of MEDical interest,» *molecules,* vol. 24, p. 20, 2018.

[50] A. Andrighetto e e. al., «The ISOLPHARM project: A New ISOL production method of high specific activity beta-emitting radionuclides as radiopharmaceutical precursor,» *Int. J. Mod. Phys. Conf. Ser.,* vol. 48, 2018.

[51] M. Maggiore, D. Campo, P. Antonini, A. Lombardi, M. Manzolaro, A. Andrighetto, A. Monetti, D. Scarpa, .. Esposito e L. Silvestrin, «SPES: A new cyclotron-based facility for research and applications with high-intensity beams,» *Modern physics letters A,* vol. 17, n. 32, p. 1740010, 2017.

[52] D. Bisello, E. Fagotti, .. Esposito, C. Loong, M. Maggiore, P. Mastinu, G. Prete, L. Silvestrin e J. Wyss, «LINUS, the Integrated LNL Neutron Source facility,» *Journal of Physics: Conference Series,* vol. 1, n. 1021, p. 012010, 2018.

[53] S. V. Selivanova, E. Lavallée, H. Senta, L. Caouette, A. J. B. McEwan, B. Guérin, R. Lecomte e E. Turcotte, «Clinical trial using sodium pertechnetate Tc-99m produced with medium-energy cyclotron: biodistribution and safety assessment in patients with abnormal thyroid function,» *J Nucl Med,* vol. 58, p. 791–798, 2017.

[54] J. Esposito, G. Vecchi, G. Pupillo, A. Taibi, L. Uccelli, A. Boschi e M. Gambaccini, «Evaluation of Mo-99 and Tc-99m Productions Based on a High-Performance Cyclotron,» *Sci Technol Nucl Ins,* pp. 1-14, 2013.

[55] L. Metello, «99mTc-tecnetium shortage: old problems asking for new solutions,» *J Med Imag Radiat Sci,* vol. 46, p. 256–261, 2015.

[56] M. Pillai, A. Dash e F. J. Knapp , «Sustained availability of 99mTc: possible paths forward,» *J Nucl Med,* vol. 54, p. 313–323, 2013.

[57] S. van der Marck, A. Koning e K. Charlton, «The options for the future production of the medical isotope 99Mo,» *Eur J Nucl Med Mol Imag,* vol. 37, p. 1817–1820, 2010.

[58] J. E. Beaver e H. B. Hupf, «Production of Tc-99m on a medicalcyclotron: a feasibility study,» *J Nucl Med,* vol. 12, p. 739–741, 1971.

[59] S. Qaim, «Nuclear data for medical radionuclides,» *J Radioanal Nucl Chem,* vol. 305, p. 233–245, 2015.

[60] X. Hou, J. Tanguay e K. R. Buckley, «Molybdenum target specifications for cyclotron production of Tc-99m based on patient dose estimates,» *Phys Med Biol,* vol. 61, p. 542–553, 2016 a.

[61] A. Boschi, P. Martini, M. Pasquali e L. Uccelli, «Recent achievements in Tc-99m radiopharmaceutical direct production by medical cyclotrons,» *Drug Development and Industrial Pharmacy,* vol. 43, pp. 1402-1412, 2017.

[62] R. Boyd, «Technetium Generators: Status and Prospects,» *Radiochim Acta,* vol. 41, p. 59−64, 1987.

[63] X. Hou, J. Tanguay, M. Vuckovic, K. Buckley, P. Schaffer, F. Bénard, T. J. Ruth e A. Celler, «Imaging study of using radiopharmaceuticals labeled with cyclotron-produced Tc-99m,» *Phys Med Biol,* vol. 61, p. 8199–8213, 2016 b.

[64] T. Ruth, «Accelerating production of medical radioisotopes,» *Nature,* vol. 437, p. 536–537, 2009.

[65] IAEA, «Cyclotrons used for Radionuclide Production,» [Online]. Available: https://nucleus.iaea.org/sites/accelerators/Pages/Cyclotron.aspx.

[66] G. Pupillo, J. Esposito, M. Gambaccini, F. Haddad e N. Michel, «Experimental cross section evaluation for innovative Mo-99,» *J Radioanal Nucl Chem,* n. DOI 10.1007/s10967-014-3321-9., 2014.

[67] P. Martini, A. Boschi, G. Cicoria, L. Uccelli, M. Pasquali, A. Duatti, G. Pupillo, M. Marengo, M. Loriggiola e J. Esposito, «A solvent-extraction module for cyclotron production of high-purity 405 technetium-99m,» *Appl. Radiat. Isot.,* 2016.

[68] H. Skliarova, P. Buso, S. Carturan, C. R. Alvarez, S. Cisternino, P. Martini, A. Boschi e J. Esposito, «Recovery of Molybdenum Precursor Material in the Cyclotron-Based Technetium-99m Production Cycle,» *Instruments,* 2019.

[69] L. Uccelli, A. Boschi, M. Pasquali, A. Duatti, G. Di Domenico, G. Pupillo, J. Esposito, M. Giganti, A. Taibi e M. Gambaccini, «Influence of the Generator in-Growth Time on the Final Radiochemical Purity and Stability of Tc-99m Radiopharmaceuticals,» *Sci. Technol. Nucl. Ins.,* pp. 1-7, 2013.

[70] N. Uzunov, L. Melendez-Alafort, M. Bello, G. Cicoria, F. Zagni, L. D. Nardo, A. Selva, L. Mou, C. R. Alvarez, G. Pupillo e e. al., «Radioisotopic purity and imaging properties of cyclotron-produced 99mTc using direct 100Mo(p,2n) reaction,» *Phys. Med. Biol.,* vol. 63, pp. 1-20, 2018.

[71] J. Esposito, M. Bello, A. Boschi, G. Cicoria, L. De Nardo, G. Di Domenico, A. Duatti, M. Gambaccini, M. Giganti, L. Gini e e. al., «IAEA,» 2018. [Online]. Available: https://www-pub.iaea.org/MTCD/Publications/PDF/SupplementaryMaterials/P1743_Supporting_material_web.pdf.

[72] P. Martini, G. Pupillo e A. Boschi, «First Accelerator-Based Tc-99m GBq Production Levels and in-vivo Imaging Tests for APOTEMA Experiment,» 2015. [Online].

[73] IAEA, «Cyclotron Based Production of Technetium-99m,» *Radioisotopes and Radiopharmaceuticals Reports No. 2,* 2017.

[74] F. Haddad, L. Ferrer, A. Guertin, T. Carlier, N. Michel, J. Barbet e J. F. Chatal, «ARRONAX, a high-energy and high-intensity cyclotron for nuclear medicine,» *European Journal of Nuclear Medicine and Molecular Imaging,* vol. 35, pp. 1377-1387, 2008.

[75] IAEA, *International Atomic Energy Agency, Therapeutic Radiopharmaceuticals Labelled with New Radionuclides such as Astatine-211, Copper-67, Lead-212/Bismuth-212, http://cra.iaea.org/crp/project/ProjectDetail?projectId=2073&lastActionName=OpenedCRPList,* 2015.

[76] IAEA, «Therapeutic Radiopharmaceuticals Labelled with New Emerging Radionuclides (Cu-67, Re-186, Sc-47) Coordinated Research Project,» 2015. [Online]. Available: http://cra.iaea.org/cra/stories/2015-09-30-F22053-New_Emerging_Radionuclides.html. [Consultato il giorno 20 11 2019].

[77] D. Medvedev e e. al., «Development of a large scale production of 67Cu from 68Zn at the high energy proton accelerator: Closing the 68Zn cycle.,» *Appl Radiat Isotopes 1,* pp. 31-46, 2012.

[78] V. N. Starovoitova, P. L. Cole e T. L. Grimm, «Accelerator-based photoproduction of promising beta-emitters 67Cu and 47Sc,» *J Radioanal Nucl Chem,* 2015.

[79] S. Kastleiner, H. H. Coenen e Q. S. M., «Possibility of production of 67-Cu at a small-sized cyclotron via the (p,α) reaction on enriched 70-Zn,» *Radiochimica Acta,* vol. 84, p. 107, 1999.

[80] V. Levkovskij, Cross sections of medium mass nuclide activation (A=40-100) by medium energy protons and alpha-particles (E=10-50 MeV, Moscow , 1991.

[81] L. D. Dominicis, *Master thesis: Proton-induced cross section on natV target: focus on 47Sc production,* University of Bologna (Italy), AA 2018/2019.

[82] Skliarova, «Annual Report,» Laboratori Nazionali di Legnaro, 2018. [Online]. Available: http://www.lnl.infn.it/~annrep/read_ar/2018/contributions/pdfs/166_D_14_D009.pdf.

[83] I. SUGAI, «An application of a new type deposition method to nuclear target preparation,» *Nucl. Instr. and Meth. A,* vol. 397, pp. 81-90, 1997.

[84] H. Skliarova, S. Cisternino, L. Pranovi, L. Mou, G. Pupillo, V. Rigato e C. Rossi-Alvarez, «HIVIPP deposition and characterization of isotopically enriched 48Ti targets for nuclear cross-section measurements,» *Nuclear Instruments and Methods in Physics Research Section A: Accelerators, Spectrometers, Detectors and Associated Equipment,* 2020, In press.

[85] J. Esposito, E. Cazzola, S. Cisternino, G. Gorgoni, L. Mou, G. Pupillo e H. Skliarova, «First experimental outcomes on target irradiation tests for Mn52 production in METRICS research project,» [Online]. Available: http://www.lnl.infn.it/~annrep/read_ar/2018/contributions/pdfs/139_D_136_D131.pdf.

[86] S. C. Srivastava, «Theragnostic radiometals: getting closer to personalized medicine,» in *Mazzi U et al. Technetium and other radiometals in chemistry and nuclear medicine*, Padova, SG Editoriali, 2010, p. 553–568.

[87] IAEA, « Recommended cross sections for 64Ni(p,n)64Cu reaction,» Last updated: September 2008. [Online]. Available: https://www-nds.iaea.org/radionuclides/nip64cu0.html.

[88] EXFOR, «Experimental Nuclear Reaction Data (EXFOR),» National Nuclear Data Center, [Online]. Available: http://www.nndc.bnl.gov/exfor/exfor.htm.

[89] F. T. Tárkányi, A. V. Ignatyuk, A. Hermanne, R. Capote, B. Carlson, J. Engle, M. Kellett, T. Kibedi, G. Kim, F. G. Kondev, M. Hussain, O. Lebeda, A. Luca, Y. Nagai, H. Naik, A. L. Nichols, F. M. Nortier, S. V. Suryanarayana, S. Takács e M. Verpelli, «Recommended nuclear data for medical radioisotope production: diagnostic gamma emitters,» *Journal of Radioanalytical and Nuclear Chemistry,* 2018.

[90] G. Pupillo, T. Sounalet, N. Michel, L. Mou, J. Esposito e F. Haddad, «New production cross sections for the theranostic radionuclide 67Cu,» *Nuclear Inst and Methods in Physics Research B ,* vol. 415 , p. 41–47, 2018.

[91] G. Pupillo, T. Sounalet, N. Michel, F. Haddad, L. Mou, L. Canton, A. Fontana, J. Esposìto e A. Duatti, «Cyclotron production of 67Cu: A new measurement of the 68Zn(p,2p)67Cu, 68Zn(p,2n)67Ga an d 68Zn(p,3n)66Ga nuclear cross sections,» *Nucleus,* vol. 63, 2018.

[92] IAEA, «Recommended cross section for 68Zn(p,2p)67Cu reaction,» Last updated september 2008. [Online]. Available: https://www-nds.iaea.org/radionuclides/zn867cu0.html.

[93] IAEA, «Emerging isotopes: Recommended cross sections for Zn-70(p,a)Cu-67 reaction,» 2008b. [Online]. Available: https://www-nds.iaea.org/medical/zn067cu0.html.

[94] NNDC, «Q-value Calculator,» [Online]. Available: https://www.nndc.bnl.gov/qcalc/.

[95] A. Koning e D. Rochman, «Modern Nuclear Data Evaluation with the TALYS Code System,» *Nuclear Data Sheets,* vol. 113, n. 12, pp. 2841-2934, 2012.

[96] B. Tarasov, «PACE4 code,» *Nucl Instrum Meth B,* vol. 204, pp. 174-178, 2003.

[97] C. Duchemin, A. Guertin, F. Haddad, N. Michel e V. Métivier, «Production of medical isotopes from a thorium target irradiated by light charged particles up to 70 MeV,» *Phys Med Biol,* vol. 60, p. 931–946, 2015.

[98] H. Piel, S. Quaim e G. Stöcklin, «Excitation functions of (p,xn)-reactions on natNi and highly enriched 62Ni: possibility of production of medically importantradioisotope 62Cu at a small cyclotron.,» *Radiochimica Acta,* 1992.

[99] IAEA, «Monitor Reaction: Recommended cross sections for 27Al(p,x)24Na reaction with estimated uncertainties,» [Online]. Available: https://www-nds.iaea.org/medical/alp24na0.html.

[100] IAEA, «Monitor Reaction: Recommended cross sections for natNi(p,x)57Ni reaction with estimated uncertainties,» [Online]. Available: https://www-nds.iaea.org/medical/nip57ni0.html.

[101] G. Pupillo, L. Mou e al., «Production of 67Cu by enriched 70Zn targets: first measurements of formation cross sections of 67Cu, 64Cu, 67Ga, 66Ga, 69mZn and 65Zn in interactions of 70Zn with protons above 45 MeV,» *Radiochimica Acta,* 2019.

[102] IAEA, «Emerging isotopes: Recommended cross sections for 68Zn(p,x)64Cu reaction,» 2008. [Online]. Available: https://www-nds.iaea.org/medical/zn864cu0.html. [Consultato il giorno 10 2019].

[103] T.McGee, C.L.Rao, G.B.Saha e L.Yaffe, «Nuclear Interactions of 45Sc and 68Zn with Protons of Medium Energy,» *Nuclear Physics A,* vol. 150, p. 11, 1970.

[104] S. Qaim, S. Sudár, B. Scholten, A. Koning e H. Coenen, «Evaluation of excitation functions of 100Mo(p,d+pn)99Mo and 100Mo(p,2n)99mTc reactions: Estimation of long-lived Tc-impurity and its implication on the specific activity of cyclotron-produced 99mTc.,» *Appl Radiat Isot,* n. 85, pp. 101-113, 2014.

[105] R. Schwarzbach, K. Zimmermann, I. Novak-Hofer e P. Schubiger, «A COMPARISON OF 67CU PRODUCTION BY PROTON (67 TO 12 MEV) INDUCED REACTIONS ON natZN/70ZN,» *J. Labelled Cpd. Radiopharm.,* 2001.

[106] M. Avila-Rodriguez, C. Rios, J. Carrasco-Hernandez, J. C. Manrique-Arias, R. Martinez-Hernandez, F. García-Pérez, A. Jalilian, E. Martinez-Rodriguez, M. Romero-Piña e A. Diaz-Ruiz, «Biodistribution and radiation dosimetry of [64Cu]copper dichloride: first-in-human study in healthy volunteers,» *European Journal of Nuclear Medicine and Molecular Imaging,* 2017.

[107] C. Müller, K. Domnanich, C. Umbricht e N. Van Der Meulen, «Scandium and terbium radionuclides for radiotheranostics: current state of development towards clinical applications.,» *Br J Radiol.,* 2018.

[108] G. Pupillo, L. Mou, A. Boschi, S. Calzaferri, L. Canton, S. Cisternino, L. D. Dominicis, A. Duatti, A. Fontana, F. Haddad, P. Martini, M. Pasquali, H. Skliarova e J. Esposito, «Production of 47Sc with natural vanadium targets: results of the PASTA project,» *Journal of Radioanalytical and Nuclear Chemistry,* n. 3, p. 297, 2019.

[109] G. Pupillo, A. Fontana, L. Canton, F. Haddad, H. Skliarova, S. Cisternino, P. Martini, M. Pasquali, A. Boschi, J. Esposito, A. Duatti e L. Mou, «Preliminary results of the PASTA project,» *EuNPC 2018, IL NUOVO CIMENTO,* 2019.

[110] E.Gadioli, E.Gadioli-Erba, J.J.Hogan e K.I.Burns, «Emission of alpha particles in the interaction of 10-85 MeV protons with Ti-48,50,» *Jour: Zeitschrift fuer Physik A, Hadrons and Nuclei,* vol. 301, p. 289, 1981.

[111] F.Ditroi, F.Tarkanyi, S.Takacs e A.Hermanne, «Activation cross-sections of proton induced reactions on vanadium in the 37-65 MeV energy range,» *Nucl. Instrum. Methods in Physics Res., Sect.B,* vol. 381, p. 16, 2016.

[112] S.Hontzeas e L.Yaffe, «Interaction of Vanadium with Protons of Energies up to 84 MeV,» *Canadian Journal of Chemistry,* vol. 41, p. 2194, 1963.

[113] C.G.Heininger e E.O.Wiig, «Spallation of Vanadium with 60-, 100-, 175-, and 240-MeV Protons,» *Physical Review,* vol. 101, p. 1074, 1956.

[114] R.Michel, F.Peiffer e R.Stuck, «Measurement and Hybrid Model Analysis of Integral Excitation Functions for Proton-Induced Reactions on Vanadium, Manganese and Cobalt up to 200 MeV,» *Nuclear Physics, Section A,* vol. 441, p. 617, 1985.

[115] R.Michel, G.Brinkmann, H.Weigel e W.Herr, «Measurement and Hybrid-Model Analysis of Proton-Induced Reactions with V, Fe and Co,» *Nuclear Physics, Section A,* vol. 322, p. 40, 1979.

[116] G.Albouy, J.P.Cohen, M.Gusakow, N.Poffe, H.Sergolle e L.Valentin, «Reaction (p,3n+3p) between 30 and 150 MeV,» *Journal de Physique,* vol. 24, p. 67, 1963.

[117] H. Skliarova, S. Cisternino, G. Cicoria, E. Cazzola, M. M. Gorgoni e J. Esposito, «Cyclotron solid targets preparation for medical radionuclides production in the framework of LARAMED project,» *J. Phys.,* 2019 (submitted).

[118] G. Pupillo, L. Mou, F. Haddad, A. Fontana e L. Canton, «New results on the natV(p,x)43Sc cross section: analysis of the discrepancy with previous data,» *Nuclear Instruments and Methods in Physics Research Section B: Beam Interactions with Materials and Atoms,* vol. 464, pp. 32-35, 2019.

[119] J. A.Cameron, «Nuclear Data Sheets for A = 44,» *Nuclear Data Sheets,* n. 9, pp. 2357-2495, 2011.

[120] TENDL-2019, «TENDL-2019 Nuclear data library,» [Online]. Available: https://tendl.web.psi.ch/tendl_2019/tendl2019.html.

[121] A. Koning, D. Rochman, J. Sublet, N. Dzysiuk, M. Fleming e S. van der Marck, «TENDL: Complete Nuclear Data Library for Innovative Nuclear Science and Technology,» *Nuclear Data Sheets,* 2019.

[122] H. Piel, S. Quaim e G. Stöcklin, «Excitation Functions of (p,xn)-Reactions on natNi and Highly Enriched 62Ni: Possibility of Production of Medically Important Radioisotope 62Cu at a Small Cyclotron,» *Radiochimica Acta,* vol. 57, 1992.

[123] F. Tárkányi, F. Szelecsényi e P. Kopecky, «Excitation functions of proton induced nuclear reactions on natural nickel for monitoring beam energy and intensity,» *International Journal of Radiation Applications and Instrumentation. Part A. Applied Radiation and Isotopes,* vol. 42, n. 6, pp. 513-517, 1991.

[124] L. De Nardo, G. Pupillo, L. Mou, D. Furlanetto, A. Rosato, J. Esposito e L. Meléndez-Alafort, «Dosimetric studies to assess the feasibility of labelling radiopharmaceuticals with 47Sc cyclotron-produced via natV(p,x)47Sc reaction,» *Submitted to Physics in Medicine and Biology,* 2020.

[125] L.Melendez-Alafort, G.Ferro-Flores, L.DeNardo, M.Bello, M.Paiusco, A.Negri e al., «Internal radiation dose assessment of radiopharmaceuticals prepared with cyclotron-produced Tc-99m,» *Medical Physics,* 2019.

[126] C.Muller, M.Bunka, S.Haller, U.Koster, V.Groehn, P.Bernhardt e al., «Promising Prospects for Sc-44-/Sc-47-Based Theragnostics: Application of Sc-47 for Radionuclide Tumor Therapy in Mice,» *J Nucl Med.,* n. 55, pp. 1658-1664, 2014.

[127] R.Sparks e B.Aydogan, «Comparison of the effectiveness of some common animal data scaling techniques in estimating human radiation dose,» in *Sixth International Radiopharmaceutical Dosimetry Symposium*, 1999.

[128] M.Stabin e A.Farmer, «OLINDA/EXM 2.0: The new generation dosimetry modeling code,» *J. Nucl. Med.,* n. 53, pp. 585-585, 2012.

[129] M.G.Stabin, R.B.Sparks e E.Crowe, «OLINDA/EXM: The Second-Generation Personal Computer Software for Internal Dose Assessment in Nuclear Medicine,» *J Nucl Med. ,* n. 46, pp. 1023-1027, 2005.

[130] L. Melendez-Alafort, G. Ferro-Flores, L. DeNardo e al., «Internal radiation dose assessment of radiopharmaceuticals prepared with cyclotron-produced Tc-99m,» *Medical Physics,* vol. 46, n. 3, pp. 1437-1446, 2019.

[131] M. G. Stabin, Fundamentals of Nuclear Medicine Dosimetry, Springer, New York, NY, 2008.

[132] 2. ICRP, «The 2007 Recommendations of the International Commission on Radiological Protection,» *Annals of the ICRP,* n. ICRP Publication 103, 2007.

[133] «Nuclear Regulatory Commission (NRC),» [Online]. Available: https://www.nrc.gov./docs/ML1101/ML110100788.pdf.

Università degli Studi di Ferrara

Sezioni

Dottorati di ricerca

Il tuo indirizzo e-mail

liliana.mou@lnl.infn.it

Oggetto:

Dichiarazione di conformità della tesi di Dottorato

Io sottoscritto Dott. (Cognome e Nome)

Mou Liliana

Nato a:

Cagliari

Provincia:

Cagliari

Il giorno:

25/09/1981

Avendo frequentato il Dottorato di Ricerca in:

Fisica

Ciclo di Dottorato

32

Titolo della tesi:

Cyclotron production of theranostic radionuclides: 67Cu and 47Sc

Titolo della tesi (traduzione):

Produzione con ciclotroni di radionuclidi teranostici: Cu67 e Sc47

Tutore: Prof. (Cognome e Nome)

Duatti Adriano

Settore Scientifico Disciplinare (S.S.D.)

FIS07

Parole chiave della tesi (max 10):

Cu67, Sc47, theranostics radionuclides, cross-sections, proton-cyclotron, production, sezioni d'urto, protoni, ciclotrone, radionuclidi teranostici

Consapevole, dichiara

CONSAPEVOLE: (1) del fatto che in caso di dichiarazioni mendaci, oltre alle sanzioni previste dal codice penale e dalle Leggi speciali per l'ipotesi di falsità in atti ed uso di atti falsi, decade fin dall'inizio e senza necessità di alcuna formalità dai benefici conseguenti al provvedimento emanato sulla base di tali dichiarazioni; (2) dell'obbligo per l'Università di provvedere al deposito di legge delle tesi di dottorato al fine di assicurarne la conservazione e la consultabilità da parte di terzi; (3) della procedura adottata dall'Università di Ferrara ove si richiede che la tesi sia consegnata dal dottorando in 2 copie di cui una in formato cartaceo e una in formato pdf non modificabile su idonei supporti (CD-ROM, DVD) secondo le istruzioni pubblicate sul sito: http://www.unife.it/studenti/dottorato alla voce ESAME FINALE – disposizioni e modulistica; (4) del fatto che l'Università, sulla base dei dati forniti, archivierà e renderà consultabile in rete il testo completo della tesi di dottorato di cui alla presente dichiarazione attraverso l'Archivio istituzionale ad accesso aperto "EPRINTS.unife.it" oltre che attraverso i Cataloghi delle Biblioteche Nazionali Centrali di Roma e Firenze; DICHIARO SOTTO LA MIA RESPONSABILITA': (1) che la copia della tesi depositata presso l'Università di Ferrara in formato cartaceo è del tutto identica a quella

presentata in formato elettronico (CD-ROM, DVD), a quelle da inviare ai Commissari di esame finale e alla copia che produrrò in seduta d'esame finale. Di conseguenza va esclusa qualsiasi responsabilità dell'Ateneo stesso per quanto riguarda eventuali errori, imprecisioni o omissioni nei contenuti della tesi; (2) di prendere atto che la tesi in formato cartaceo è l'unica alla quale farà riferimento l'Università per rilasciare, a mia richiesta, la dichiarazione di conformità di eventuali copie; (3) che il contenuto e l'organizzazione della tesi è opera originale da me realizzata e non compromette in alcun modo i diritti di terzi, ivi compresi quelli relativi alla sicurezza dei dati personali; che pertanto l'Università è in ogni caso esente da responsabilità di qualsivoglia natura civile, amministrativa o penale e sarà da me tenuta indenne da qualsiasi richiesta o rivendicazione da parte di terzi; (4) che la tesi di dottorato non è il risultato di attività rientranti nella normativa sulla proprietà industriale, non è stata prodotta nell'ambito di progetti finanziati da soggetti pubblici o privati con vincoli alla divulgazione dei risultati, non è oggetto di eventuali registrazioni di tipo brevettale o di tutela. PER ACCETTAZIONE DI QUANTO SOPRA RIPORTATO

Firma del dottorando

Ferrara, li ___07/10/2020_____ (data) Firma del Dottorando

_____ Liliana Mou

Firma del Tutore

Visto: Il Tutore Si approva Firma del Tutore _____